PRECISE MEASUREMENT OF THE β-ASYMMETRY IN THE DECAY OF MAGNETO-OPTICALLY TRAPPED, SPIN-POLARIZED ^{37}K

A Dissertation
by
BENJAMIN BROWN FENKER

Submitted to the Office of Graduate and Professional Studies of
Texas A&M University
in partial fulfillment of the requirements for the degree of
DOCTOR OF PHILOSOPHY

Chair of Committee,	Dan Melconian
Committee Members,	John Hardy
	Charles M. Folden III
	Bhaskar Dutta
	Alexei Safonov
Head of Department,	Peter McIntyre

December 2016

Major Subject: Physics

ABSTRACT

Precise low-energy measurements in nuclear β-decay provide constraints on possible physics beyond the standard model complementary to high-energy collider experiments. This thesis describes the most precise measurement of the positron asymmetry from a polarized nucleus to date. At the TRIUMF Neutral Atom Trap, atoms of the positron emitter ^{37}K are confined in an alternating-current magneto-optical trap and spin-polarized to 99.13(9) % via optical pumping. The use of atom-trapping techniques allows for an exceptionally open geometry with the decay products escaping the trapping region unperturbed by the trapping potential. The emitted positrons are detected in a pair of symmetric detectors placed along the polarization axis to measure the asymmetry. The analysis was performed blind and considers β-scattering and other systematic effects. The result, $A_\beta\left(0\right) = -0.5707 \pm 0.0018$, places limits on the mass of a hypothetical W boson coupling to right-handed neutrinos to be $> 300\,\mathrm{GeV/c^2}$ at zero-mixing as well as contributes to an independent determination of the V_{ud} element of the CKM matrix.

DEDICATION

For Kim.

Dans les champs de l'observation le hasard ne favorise que les esprits préparés.

Fortune favors the prepared mind.

(Louis Pasteur - 1854)

ACKNOWLEDGEMENTS

First, I would like to thank my advisor, Dr. Dan Melconian, for all his expertise, support, and patience while working on this project. Dan, it was a true pleasure working with you. I would also like to thank John Behr for at times serving as a second advisor and for being absolutely dedicated to making the experiment a success. Additionally, the other members of the Trinat collaboration whom I have worked with over the years deserve a sincere thank you. Spencer Behling, Melissa Anholm, Alexandre Gorelov, Daniel Ashery, Michael Mehlman, Praveen Shidling, Iuliana Cohen, and a score of excellent undergraduate researchers have all contributed invaluably to this work and it was enjoyable to work with each of you. My committee members have also provided thoughtful comments on this thesis, for which I am thankful.

I would also like to acknowledge the excellent work of the staff at both the Cyclotron Institute and Triumf, without whose help this research would not be possible. In particular, Konstantin Olchanski proved himself a data acquisition wizard by constructing the trigger logic on extremely short notice. Additionally, the computation time to perform the simulations required in this work was provided by the Texas A & M University High Performance Research Computing group. I am grateful not only for the computation time, but also the assistance in adapting the simulation to such an environment.

I would like to thank my parents, Justine and Howard, as well as my brothers, Will and Alex, for always supporting me no matter what and for teaching me that it is okay to ask questions even if there is no immediate answer. Lastly, I would like to thank my wonderful wife Kim for all of her love and support. Kim, I do not have the words to express how grateful I am for your patience, understanding, and frequent help throughout the course of this project.

TABLE OF CONTENTS

Page

ABSTRACT ii

DEDICATION iii

ACKNOWLEDGEMENTS v

TABLE OF CONTENTS vi

LIST OF FIGURES ix

LIST OF TABLES xiii

1. INTRODUCTION 1

    1.1 β-decay 1
    1.2 TRINAT overview 5

2. THEORY 10

    2.1 β-decay 10
        2.1.1 Angular correlations 14
    2.2 ^{37}K decay 15
        2.2.1 Recoil-order corrections 17
    2.3 Physics beyond the standard model 19
        2.3.1 Limits for pure-Fermi decays 21
        2.3.2 Limits for pure-Gamow Teller decays 21
        2.3.3 Limits from mixed decays 22
        2.3.4 Other limits 24
    2.4 CVC and V_{ud} in mirror decays 27

3. ATOMIC INTERACTIONS 30

    3.1 Electronic structure of alkali atoms 30
        3.1.1 Hyperfine structure 30
    3.2 Magnetic field effects 34
        3.2.1 Aligned field 34
        3.2.2 Transverse magnetic field 36

3.3 Interaction with a radiation field 37
3.4 Magneto-optical traps 37
  3.4.1 Drag potential - Doppler cooling 38
  3.4.2 Trapping potential 38
  3.4.3 The alternating-current MOT 41
3.5 Optical pumping 42
  3.5.1 The rate equations - an intuitive picture 43
  3.5.2 Density matrix 47

4. EXPERIMENTAL OVERVIEW 50

4.1 Apparatus 50
4.2 Duty cycle 54
4.3 Run conditions 56
4.4 Data acquisition 58

5. ATOMIC MEASUREMENTS 61

5.1 Data selection 61
5.2 Cloud characterization 65
5.3 Shakeoff-electron measurements 70
5.4 Polarization 71
  5.4.1 Optics details 73
  5.4.2 Magnetic fields 78
  5.4.3 Photoionization light 79
  5.4.4 Coherent population trapping 80
  5.4.5 Polarization results 82
  5.4.6 Systematic uncertainties 89

6. SIMULATIONS 93

6.1 Backscattering coefficient 96

7. DETECTOR CALIBRATIONS 101

7.1 Electron microchannel plate and delay-line anode 101
  7.1.1 Position calibration 101
  7.1.2 Timing information and shakeoff electrons 103
7.2 Double-sided silicon-strip detectors 106
  7.2.1 Waveforms 106
  7.2.2 Energy calibration 109
  7.2.3 Energy agreement and resolution 115
  7.2.4 Event selection and position information 123
7.3 Plastic scintillators 130

7.3.1 Cosmic rays 138

8. POSITRON ASYMMETRY 141

8.1 Blinding 144
8.2 Asymmetry analysis 145
8.3 Background correction 156
8.4 Systematic uncertainties 163

9. CONCLUSIONS AND FUTURE WORK 169

9.1 Right-handed currents 169
9.2 V_{ud} element of the CKM matrix 171
9.3 Future work 172
9.3.1 Polarization improvements 173
9.3.2 Beta-asymmetry improvements 174

REFERENCES 178

LIST OF FIGURES

FIGURE Page

1.1 β^+-decay Feynman diagrams 3

1.2 Schematic diagram of an experiment to test for parity conservation . 4

1.3 The x2 MOT system at TRINAT 6

1.4 The main TRINAT detection chamber 8

2.1 Level scheme for the decay of ^{37}K 16

2.2 Standard model predictions for the β-asymmetry parameter 18

2.3 Limits on right-handed currents in the weak interaction 25

2.4 Current status of CVC test with mirror transitions 28

3.1 Atomic energy level diagram of ^{37}K 33

3.2 A simplified diagram showing the principle of MOT operation 40

3.3 Principle of AC-MOT operation 41

3.4 Principle of optical pumping measurement 44

4.1 TRINAT detector layout in measurement chamber 51

4.2 Diagram of plastic scintillator, light-guide and PMT readout 52

4.3 HEX75 delay-line anode layout 54

4.4 The atomic duty cycle for the TRINAT experiment 55

5.1 Photoion time-of-flight and position spectra 63

5.2 Relative timing of the rMCP and UV light signal 64

5.3 Trap position as a function of duty cycle 67

5.4 Shakeoff electron position spectrum 72

5.5 Optical pumping level diagram 75

5.6 Optical pumping frequency locking scheme 76

5.7 Optical elements creating the circularly polarized light 76

5.8 Coherent population trapping measurement 81

5.9 Typical polarization fit 82

5.10 Timing jitter in optical pumping signal 84

5.11 Polarization results - each dataset 86

5.12 Polarization results - global fit 87

5.13 Time dependence of the nuclear polarization 88

6.1 Comparison of backscattering between simulation and experiment . . 98

6.2 Comparison of backscattering coefficient simulation parameters 100

7.1 HEX75 off-line calibration procedure 102

7.2 Electron MCP timing spectrum with respect to the plastic scintillator 105

7.3 Shakeoff electron position while optical pumping 107

7.4 Sample BB1 waveforms 108

7.5 Simulated BB1 energy spectra 110

7.6 Samples of uncalibrated BB1 spectrum 111

7.7 Typical fits to the BB1 energy spectra 114

7.8 BB1 fit results, zoomed in 116

7.9 BB1 energy linearity and x-y comparison 118

7.10 BB1 energy resolution 123

7.11 BB1 waveform peak amplitude time spectra 125

7.12 BB1 detector energy agreement algorithm 126

7.13 BB1 detector position spectrum 129

7.14 Energy spectrum of BB1 detector compared to GEANT4 129

7.15 Mean LED pulse height throughout duty cycle 131

7.16 Raw scintillator spectrum 132

7.17 Result of calibration fit for set S2, upper scintillator 134

7.18 Result of calibration fit for set S2, lower scintillator 135

7.19 Scintillator spectrum in coincidence with BB1 - upper 136

7.20 Scintillator spectrum in coincidence with BB1 - lower 137

7.21 Cosmic ray events 139

8.1 Implementation of the blinding scheme 145

8.2 Shakeoff electron timing and scintillator energy cuts 147

8.3 Shakeoff electron time-of-flight spectrum 148

8.4 Asymmetry throughout the duty cycle 150

8.5 Scintillator energy spectrum: detector/polarization state 150

8.6 Luminosity super ratio 151

8.7 Detector super ratio 152

8.8 Physics super ratio compared to GEANT4 (EB) 154

8.9 Physics super ratio compared to GEANT4 (EC) 155

8.10 Physics super ratio compared to GEANT4 (ED) 155

8.11 Result of fitting g_A to experimental data 156

8.12 Shakeoff electron time-of-flight background correction results 160

8.13 Shakeoff electron time-of-flight spectrum - EA 161

8.14 Comparison of background correction with HEX75 position cut . . . 162

8.15 Summed energy asymmetry, angle dependence 164

9.1 Updated exclusion plot for the minimally $L-R$ symmetric model . . 170

9.2 Updated status of CVC test in mirror nuclei 172

LIST OF TABLES

TABLE Page

1.1 Interactions consistent with Lorentz invariance 3

2.1 Correlation coefficients values in the SM 16

2.2 Recoil-order correction form factors 18

4.1 Run conditions for the June 2014 experiment 57

4.2 Trigger menu for the June2014 experiment 59

5.1 Position and time-of-flight results for each dataset 65

5.2 Trap parameters in the $\hat{x}$-direction 69

5.3 Trap parameters in the $\hat{z}$-direction 69

5.4 Trap parameters in the $\hat{y}$-direction 70

5.5 Results of the measurement of the OP light polarization 78

5.6 Parameter values following global polarization fit 85

5.7 Uncertainty budget for the nuclear polarization measurement 91

6.1 Parameters used in the GEANT4 Monte Carlo simulation 96

7.1 Calibration results for the HEX75 detector 102

7.2 Shakeoff electron time-of-flight and position spectra 106

7.3 Energy calibration and resolution of upper DSSSD 119

7.4 Energy calibration and resolution of lower DSSSD 121

7.5 Calibration results for the plastic scintillators 135

8.1 Uncertainty budget for the β-asymmetry measurement 167

1. INTRODUCTION

The experiment described here probes the symmetry structure of the charged weak nuclear interaction by observing the decay of laser-cooled, radioactive ^{37}K. The standard model of particle physics (SM) makes definite predictions for the angular distribution of decay products with respect to each other and to the spin of the parent nucleus. A deviation from this prediction could indicate the existence of *new* physics beyond the standard model (BSM).

1.1 β-decay

In nuclear β-decay, a radioactive atom was originally observed to transmute into an isotope of a different element by the conversion, within the nucleus, of a proton into a neutron or a neutron into a proton. Simultaneously, either an electron (β^-) or a positron (β^+) is emitted in order to conserve electric charge. However, it was soon observed that the energy spectrum of the $\beta^\pm$ was not peaked as would be expected for a two-body decay, but broadly distributed. This discrepancy is resolved by postulating that a third particle, termed a neutrino (ν), takes part in the decay [1]. The existence of the neutrino was confirmed in 1956, some 25 years after it was proposed [2]. The basic processes underlying the β^+-decay of $^{37}_{19}\mathrm{K} \rightarrow {}^{37}_{18}\mathrm{Ar} + e^+ + \nu_e$ along with the related process of β^--decay can be written at the nucleon level as:

$$n \rightarrow p + e^- + \bar{\nu}_e \qquad \beta^- \text{ decay} \tag{1.1a}$$

$$p \rightarrow n + e^+ + \nu_e \qquad \beta^+ \text{ decay} \tag{1.1b}$$

or at the quark level as:

$$d \rightarrow u + e^- + \bar{\nu}_e \qquad \beta^-\text{decay} \tag{1.2a}$$

$$u \rightarrow d + e^+ + \nu_e \qquad \beta^+\text{decay.} \tag{1.2b}$$

Nuclear β-decay is in fact just one example, but the most abundant naturally occurring example, of a weak interaction. These interactions are defined by their relatively "weak" nature, i.e. long half-lives compared to strong or electromagnetic interactions. I will discuss how nuclear β-decay fits into the more general picture of weak interactions later. For now, the transition rate for β-decay can be calculated according to Fermi's Golden Rule [1]:

$$\Gamma = \frac{1}{\tau} = \frac{2\pi}{\hbar} |\mathscr{M}_{fi}|^2 \rho(E_f) \tag{1.3}$$

where $\rho(E_f)$ is the thermodynamic density of states available at a final energy E_f and $\mathscr{M}_{fi}$ is the matrix element connecting the final and initial states through an as-yet undetermined operator $\mathscr{O}$:

$$\mathscr{M}_{fi} = \int \psi_f^* \mathscr{O} \psi_i dV \tag{1.4}$$

The differential decay rate was calculated by Fermi using this expression and assuming a contact interaction such as in Figure 1.1a, that the mass of the neutrino, m_ν, is zero and that the mass of the recoiling daughter nucleus is infinite compared to the beta particle's mass. Although the observation of neutrino oscillations indicates $m_\nu > 0$, analysis of the β-spectrum shape in tritium (^{3}H) decay very close to the endpoint energy gives an upper limit of $m_\nu < 2.05\,\mathrm{eV}$ [3, 4]. Additionally an Ar nucleus is known to be $\approx 6.7 \times 10^4$ times more massive than an electron. The overall strength of the weak interaction is characterized by a constant, $G_F/(\hbar c)^3 = 1.166\,378\,7(6) \times 10^{-5}/\mathrm{GeV}^2$ [5], and the differential decay rate is [1]:

$$\frac{d^5W}{dE_e d\Omega_e d\Omega_\nu} = \frac{G_F^2}{(2\pi)^5} p_e E_e (E_0 - E_e)^2 F(E_e, Z') |\mathscr{M}_{fi}|^2 \tag{1.5}$$

where p_e and E_e are the final momentum and total energy of the $\beta^\pm$, E_0 is the total energy available for the decay, and $F(E_e, Z')$ is the Fermi function, which accounts for the Coulomb interaction of the $\beta^\pm$ with the electric field of the daughter nucleus, and Z' is the charge of the daughter nucleus. Equation 1.5 has simply evaluated $\rho\,(E_f)$ from Eq. 1.3. That the observed energy distribution of the emitted $\beta^\pm$ agrees well with this simple theoretical treatment is remarkable.

But what form does $\mathscr{O}$ take? With only the simple restriction that $\mathscr{O}$ respects Lorentz symmetry, there are only five linearly independent possibilities, shown in Table 1.1 along with their properties under a parity transformation, i.e. a reflection of the coordinate axes through the origin: $\vec{r} \to -\vec{r}$. In addition to Lorentz symmetry,

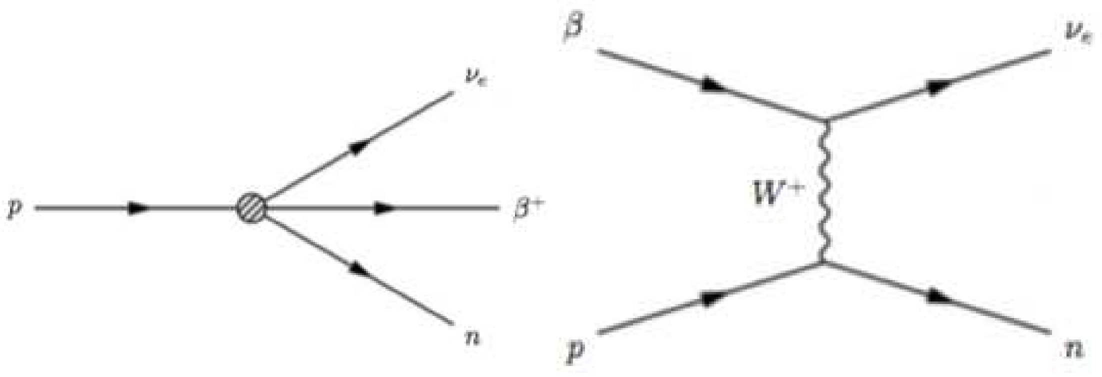

(a) Contact interaction (b) Boson exchange model

Figure 1.1: β^+-decay Feynman diagrams. The original contact interaction gives many useful results, but modern theories describe the interaction through the exchange of a massive, virtual boson.

Table 1.1: Interactions consistent with Lorentz invariance. All linearly independent forms for an interaction consistent with Lorentz invariance. The operators are defined by the Dirac γ-matrices associated with them.

Type	Operator	Parity
Scalar	1	$+$
Pseudo-scalar	γ_5	$-$
Vector	γ_μ	$-$
Axial vector	$\gamma_\mu\gamma_5$	$+$
Tensor	$\gamma_\mu\gamma_\nu - \gamma_\nu\gamma_\mu$	N/A

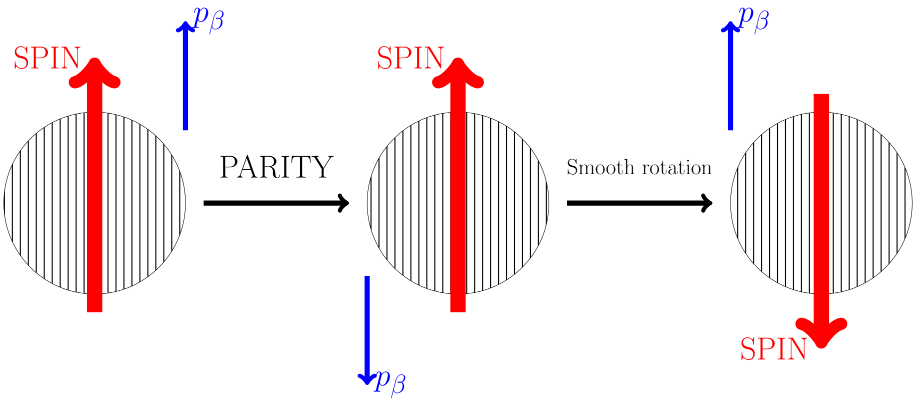

Figure 1.2: Schematic diagram of an experiment to test for parity conservation. The parity operation reverses the momentum of the emitted β particle, but, since it is an axial vector, does not effect the direction of the spin vector. Therefore, if parity is conserved the rate of particles emitted along the spin axis should equal the rate of particles emitted opposite the spin axis. Furthermore, by applying a smooth rotation in space, we reverse the direction of *all* the vectors. In this case, if parity is conserved, the rate of particles emitted along a given axis will remain constant if the spin direction is reversed.

physical laws were, up to 1956, thought to respect parity. However, after a survey by Lee and Yang [6] revealed no evidence for this in the weak interaction, Wu and collaborators set out to test this in the β decay of polarized ^{60}Co [7]. They observed the rate of β^- particles in their detector with an external magnetic field polarizing the atoms towards the detector and away from the detector (see Fig. 1.2 far left and far right panels). If parity were conserved, these two cases, being parity reflections of one another, should yield equal rates. By observing a large asymmetry, they found that parity was *not* conserved.

Although initial experiments suggested that the weak interaction was scalar and tensor in nature [8, 9], it was soon established that the form of the weak interaction is vector − axial vector ($V - A$) or: $\mathscr{O} = \gamma_\mu(1 - \gamma_5)$ where γ_μ, γ_5 are Dirac γ-matrices [10, 11]. Therefore, not only is parity violated in weak interactions, but it is *maximally* violated. This was true not only in β-decay but in all weak interactions including experiments with muons [12] and pions [13].

We now know that, compared to Fermi's contact interaction, a more accurate description of β-decay at the microscopic level is given by the boson exchange model.

This model treats the transformation of an up quark to a down quark as mediated by a virtual W^+ boson or the opposite process, $d \rightarrow u$, as mediated by a virtual W^-. It is the large mass of the $W^\pm$, $m_W = 80.385(15)\,\mathrm{GeV/c^2}$ [5], that gives the weak interaction it short range and explains why Fermi's contact interaction was so successful. This deeper understanding does not change the conclusion that the weak interaction maximally violates parity and is governed by a $V-A$ current. Reframing the statement of parity violation in the language of massive vector bosons, we can say that the SM $W^\pm$ couples only to negative-helicity (left-handed) leptons, i.e. neutrinos having their spin-projection *opposite* to their direction of motion. Although the helicity of a massive particle is not an intrinsic property of that particle[1], the neutrino's low mass means that its helicity is almost equivalent to its chirality, which *is* an intrinsic property.

There is strong experimental evidence that the symmetry structure of the weak interaction is indeed $V-A$. However, exotic interactions beyond the standard model, such as a possible $V+A$ component allowing coupling to right-handed neutrinos, give rise to predictions different from the standard model. The purpose of this experiment is to make a precise measurement of the angular distribution of positrons emitted from polarized ^{37}K atoms. This measurement will be a precision test of the SM with an expected experimental uncertainty of $< 0.5\%$. While providing valuable experimental input on its own, the lessons learned from this experiment will also be used in the design of even-more-precise future experiments with the eventual goal of reaching $\lesssim 0.1\%$ precision. As I will show in Ch. 2, the results will contribute to an independent determination of V_{ud}, the top-left element of the Cabibbo-Kobayashi-Maskawa quark mixing matrix, as well as constrain possible extensions to the SM.

1.2 TRINAT overview

The experiment described here was performed with the TRIUMF Neutral Atom Trap (TRINAT). The apparatus is coupled to ISAC, the radioactive ion beam facility at TRIUMF. Various aspects of the setup as well as details of previous measurements can be found in Refs. [14–25]. In 2014, ISAC delivered 8.10×10^7 ions of ^{37}K per second by bombarding a SiC target with $70-100\,\mu$A of protons. As shown in Figure 1.3, the ions are implanted and neutralized on a hot Zr foil and cooled and confined in a

---

[1] The helicity can reversed by a Lorentz boost as long as $v < c$, i.e. $m > 0$.

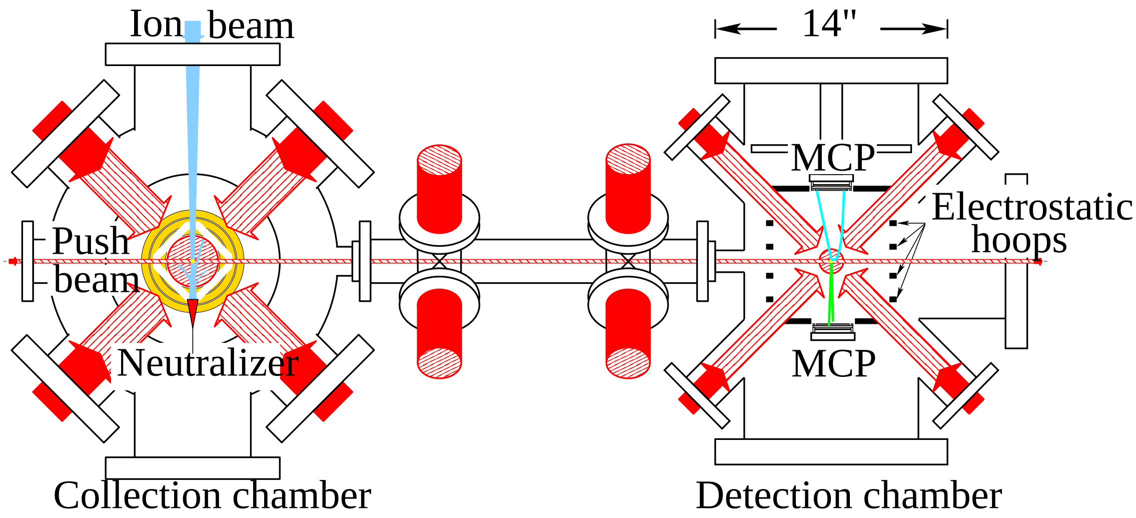

Figure 1.3: The x2 MOT system at TRINAT. Ions delivered by ISAC are neutralized and trapped in the first chamber before being pushed to the second MOT where the precision measurement takes place in order to avoid a background of untrapped atoms. The main nuclear detectors, which are perpendicular to the page, are not shown here. See Fig. 1.4.

cell-vapor magneto-optical trap (MOT) (See Sec. 3.4). Since the trapping efficiency is only 0.1%, there is a large background of untrapped atoms. To avoid this, the atoms are pushed by a pulsed laser beam to a second, open-area region where the precision measurement takes place and re-trapped by an alternating-current MOT (AC-MOT) [26].

Once the atoms are pushed to the second trap, they are cooled and collected by a second MOT. In order to perform the polarized measurement, the MOT is switched off and the atoms are allowed to ballistically expand. During this time, circularly polarized light optically pumps the atoms, achieving an average nuclear polarization of $P = 99.2\%$, measured *in situ*. Both the MOT and optical pumping will be described in more detail in Chapter 3.

Although temporarily untrapped, the polarized cloud of ^{37}K is still well localized in space and, with an average temperature of $\sim 2\,\mathrm{mK}$, the root-mean-square (RMS) velocity is only $\sim 1\,\mathrm{m/s}$, roughly equal to a typical person's walking speed. Clearly, the atoms decay essentially from rest. The effect of gravity produces an exceptionally small perturbation[2] and its effects are safely neglected here. The geometry of the

---

[2] For a K ion with charge $\pm e$, the force of gravity is the same as a the force introduced by

measurement chamber is shown in Figure 1.4. The main nuclear detectors are a pair of β-telescopes along the vertical polarization axis. Each consists of a thin Si-strip detector backed by a thick plastic scintillator. The scintillator fully stops the positrons from the ^{37}K decay ($Q_{EC} = 5.1\,\mathrm{MeV}$) and records their full energy. The Si-strip detector provides position and ΔE information and, due to its low efficiency for detecting γ rays, suppresses the background from 511 keV annihilation radiation. To identify decays that occurred within the region of optical pumping, we detect the low energy shake-off e^- (SOE) by sweeping them with an electric field towards a microchannel plate detector and observing it in coincidence with the β^+. At least one SOE is present for *every* β^+ decay because the nuclear charge undergoes a sudden change from Z to $Z-1$. This combination of detectors has been shown to provide an exceptionally clean signal, almost entirely free from backgrounds [25].

We collect critical information about the size and position of the atom cloud, as well as a sensitive probe of the nuclear polarization, by photoionizing a small fraction of the trapped atoms with a UV light pulse. These photoions, now electrically charged and with no appreciable momentum change compared to their thermal motion, are swept by the uniform electric field onto a microchannel plate (MCP) detector backed by a delay-line anode (DLA) for position sensitivity. Combining the position information with time-of-flight information with respect to the UV pulse, we obtain a 3-D image of the cloud throughout the run. The techniques outlined here allow for an (almost) ideal experiment: polarized atoms decay nearly from rest from a known location, the decay products escape essentially unperturbed by the modest electric and magnetic fields and entirely unperturbed by the trapping potential, there is minimal material near the trapping region that can scatter the outgoing particles, and the decay products are cleanly detected in a pair of symmetric detectors along the polarization axis.

The remainder of this thesis is organized as follows. In chapter 2, I will describe the modern theory of $\beta^\pm$ decay in the context of SM and BSM physics, as well as compare current limits obtained from ^{37}K decay to those from other nuclear systems, muon decay, and collider searches. Chapter 3 will describe the atomic interactions necessary to trap and polarize the atoms, while chapter 4 will describe the experimental apparatus including the data acquisition system and duty cycle. I will present the precision polarization measurement in chapter 5. In chapter 6, I will describe

---

$E = 4 \times 10^{-8}\,\mathrm{V/cm}$.

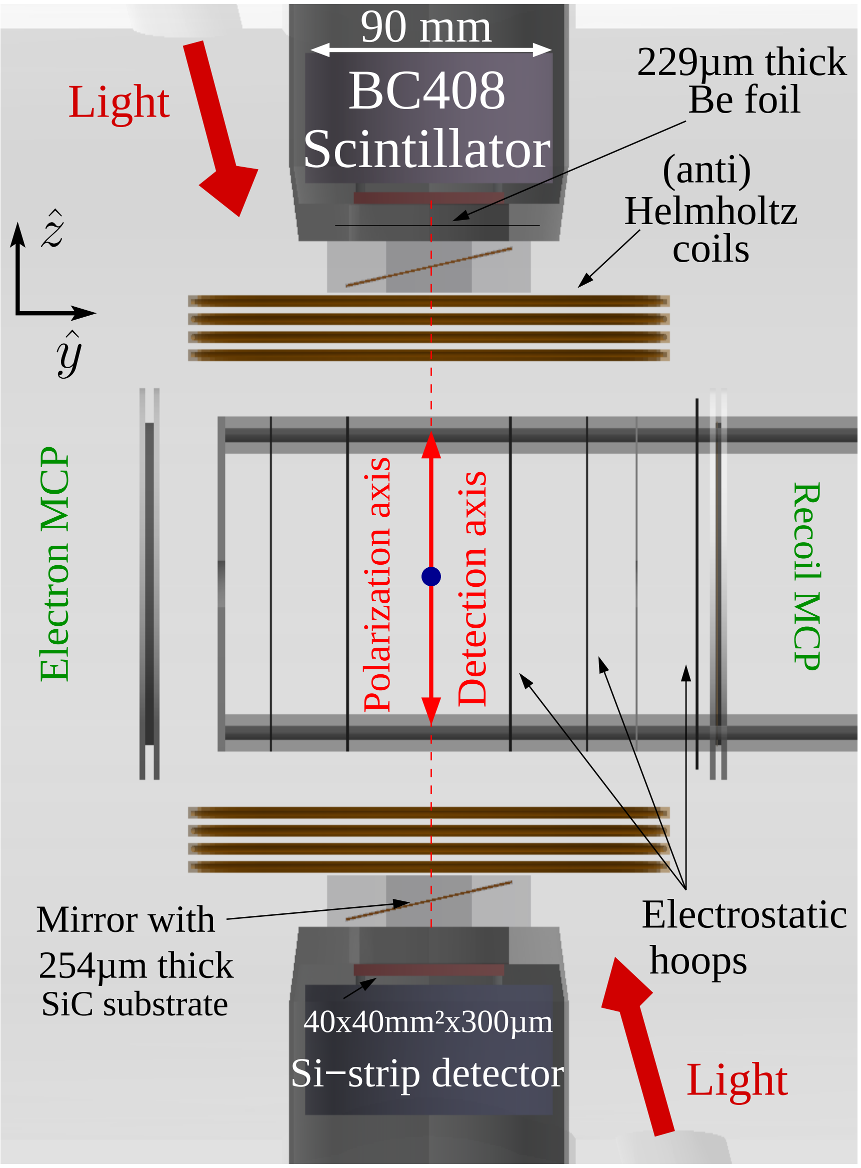

Figure 1.4: The main TRINAT detection chamber. The red lines indicate the direction of incoming light for both the MOT and optical pumping lasers. To polarize the atoms along the axis defined by the scintillator and silicon strip detectors, which are opaque, the light is brought in at a 19° angle with respect to the chamber axis and reflected off of a thin mirror. The detectors are placed along the vertical axis and are housed in a re-entrant flange which is separated from the vacuum by a thin Be foil. Also visible are the water-cooled magnetic field coils which provide the Helmholtz (optical pumping) and anti-Helmholtz (MOT) fields as well as the electrostatic hoops that generate a nearly uniform electric field. The recoil MCP is at negative electric potential, while the electron MCP is at positive potential.

the GEANT4 simulation used in many aspects of the analysis. Chapter 7 contains detector calibration results, and chapter 8 the analysis of the β-asymmetry. Finally, chapter 9 summarizes and interprets the results.

2. THEORY

2.1 β-decay

Here, I extend the picture of β decay developed in the previous section to include the full microscopic treatment as well as effects from the finite size of the nuclear recoil and possible extensions to the standard model. The most general interaction Hamiltonian density, accounting for all the interactions of Table 1.1 is given by [6,27]:

$$\begin{aligned}\mathscr{H}_\beta = &\left(\bar{p}n\right)\left[\bar{e}\left(C_S + C_S'\gamma_5\right)\nu\right] \\ &+ \left(\bar{p}\gamma_\mu n\right)\left[\bar{e}\gamma_\mu\left(C_V + C_V'\gamma_5\right)\nu\right] \\ &+ \frac{1}{2}\left(\bar{p}\sigma_{\lambda\nu}n\right)\left[\bar{e}\sigma_{\lambda\nu}\left(C_T + C_T'\gamma_5\right)\nu\right] \\ &- \left(\bar{p}\gamma_\mu\gamma_5 n\right)\left[\bar{e}\gamma_\mu\gamma_5\left(C_A + C_A'\gamma_5\right)\nu\right] \\ &+ \left(\bar{p}\gamma_5 n\right)\left[\bar{e}\gamma_5\left(C_P + C_P'\gamma_5\right)\nu\right] + \text{H.c.}\end{aligned} \tag{2.1}$$

where $\sigma_{\lambda\nu} = -\frac{i}{2}\left(\gamma_\lambda\gamma_\mu - \gamma_\mu\gamma_\lambda\right)$ is the tensor operator and H.c. means Hermitian conjugate. The coefficients C_i and C_i' with $i = S, V, T, A, P$ for scalar, vector, tensor, axial, and pseudoscalar determine the relative strength of each interaction. The C_i and C_i' coefficients define the parity structure of the interaction. Parity is conserved only if $C_i = 0$ or $C_i\prime = 0$ and is violated otherwise. These coefficients are not fixed *a priori* and are determined via experiment.

Assuming symmetry under time-reversal (T) requires all the C_i and C_i' to be real up to a common phase [28]. Assuming only Lorentz invariance, the combination CPT, with C the charge-conjugation operator and P a parity transformation, must be an exact symmetry of the interaction. Therefore, T violation is inferred from the observation of CP violation [29]. However, time-reversal violation does not contribute to β-decay observables at the current level of precision [30]. Furthermore, the standard electroweak model, which adds maximal parity violation *by hand*, involves only V and A interactions with opposite signs, but equal magnitude. This implies that $C_V/C_V' = C_A/C_A' = 1$, $C_V/C_A = -1$, and all the other coefficients are zero. Any signal that deviates from this prediction, either by restoring parity symmetry or adding a scalar, tensor, or pseudoscalar interaction, would be a clear signal of new physics beyond the SM.

Equation 2.1 is written in terms of nucleon wavefunctions whereas the underlying interaction takes place at the quark level. To translate from the quark interaction, $\bar{u}\gamma_\mu d$, to the nuclear medium, one introduces the hadronic form factor, $g_V(q^2)$, and the Fermi component (F) of the nuclear matrix element $|M_F|$.

$$\langle p| \, \bar{u}\gamma_\mu d \, |n\rangle = g_V(q^2)|M_F|\bar{p}\gamma_\mu n. \tag{2.2}$$

The conserved vector current (CVC) hypothesis asserts that the vector component of the charge-raising ($n \to p$) and charge-lowering ($p \to n$) weak currents along with the entirely vector and charge-conserving electromagnetic current are the three components of an overall isospin current. Therefore, the fact that electric charge is strictly conserved even within the nuclear medium suggests that the vector component of the weak interaction is similarly not renormalized [10]. This implies that $g_V(0) = 1$ independent of the nuclear transition. This key component of the CVC hypothesis has been verified at the level of 1.2×10^{-4} [31]. On the other hand, $|M_F|$ does depend on the specific decay under study. In the limit of strict isospin symmetry, $|M_F|$ is simply the matrix element of the raising or lowering isospin operators. Fermi decays proceeding by the vector current of Eq. 2.2 have the selection rule that the angular momentum change $\Delta J = 0$ between final and initial states. Decays with the spin sequence $0^+ \to 0^+$ are a unique case termed pure-Fermi decays as they are described entirely by the Fermi interaction described in this paragraph.

Similarly, the axial-vector component can be related to the underlying quark interactions via:

$$\langle p| \, \bar{u}\gamma_\mu\gamma_5 d \, |n\rangle = g_A(q^2)|M_{GT}|\bar{p}\gamma_\mu\gamma_5 n. \tag{2.3}$$

The difference from the vector case is the addition of a factor of γ_5, which makes the interaction parity violating, as well as the substitutions $g_V \to g_A$ and $M_F \to M_{GT}$ where M_{GT} is the Gamow-Teller (GT) matrix element. In this case, g_A *is* modified in the nuclear medium. The partially conserved axial current (PCAC) hypothesis estimates $g_A \approx 1.25$ based on strongly interacting pions "dressing" the nucleons within the nucleus [32]. Unlike in the vector case described above, there is not a general expression for M_{GT}. Therefore M_{GT} is experimentally determined for each nucleus. Decays proceeding via the axial-vector current of Eq. 2.3 are termed Gamow-

Teller decays and have the angular momentum selection rule $\Delta J = 0, \pm 1$, except for the case of $0 \rightarrow 0$, which has no GT component.

Nuclear transitions satisfying the spin-selection rules of both a Fermi and a Gamow-Teller decay are called mixed transitions. In these cases, the relative strength of the F and GT amplitudes is defined as

$$\rho = \frac{C_A M_{GT}}{C_V M_F}\left[\frac{1-\delta_C^V}{1-\delta_C^A}\right]^{1/2}\left[\frac{\left(1+\delta_{\text{NS}}^A-\delta_C^A\right)\left(1+\Delta_R^A\right)}{\left(1+\delta_{\text{NS}}^V-\delta_C^V\right)\left(1+\Delta_R^V\right)}\right]^{1/2} \simeq \frac{C_A M_{GT}}{C_V M_F}. \tag{2.4}$$

The terms under the two square roots give small correction terms with details described in Ref. [33]. For all of these terms, the superscript refers to the correction for either the vector (V) or axial-vector (A) component of the decay. The isospin symmetry breaking correction is described by δ_C^i, δ_{NS}^i describes nuclear-structure corrections requiring a detailed calculation, and Δ_R^i gives the nucleus-independent radiative corrections from Ref. [34].

An isobaric analog decay is a special case of nuclear β-decay that proceeds between nuclei with identical wavefunctions in the limit of complete isospin symmetry and under the substitutions $p \leftrightarrow n$. For a mixed transition between isobaric analog states with isospin $T = 1/2$, ρ can be determined by comparing the $\mathscr{F}t$ value for the transition under study to the average $\mathscr{F}t$ value of pure-Fermi $0^+ \rightarrow 0^+$ decays [33]:

$$\rho^2 = \frac{1}{f_A/f_V}\left[2\frac{\mathscr{F}t^{0^+\rightarrow 0^+}}{\mathscr{F}t} - 1\right] \tag{2.5}$$

where

$$\mathscr{F}t = f_V t\left(1+\delta_R'\right)\left(1+\delta_{\text{NS}}^V-\delta_C^V\right) \tag{2.6}$$

is the corrected ft value of the decay under study and is given by the product of the statistical rate function

$$f = \int_{m_e}^{E_0} F(E_e, Z')S(E_e, Z')(E_0 - E_e)^2 p_e E_e \, dE_e \tag{2.7}$$

and the partial half-life

$$t = t_{1/2}\left(\frac{1+P_{\mathrm{EC}}}{\mathrm{BR}}\right). \tag{2.8}$$

The notation in Eq. 2.7 is the same as in Eq. 1.5 and $S(E_e, Z') \approx 1.0$ is the shape-correction function and the approximation holds for allowed decays. The values of f_A and f_V give the statistical rate function for the two components of the decay, $t_{1/2}$ is the half-life, and m_e is the electron's rest mass. Furthermore, BR is the specific branching ratio and P_{EC} is the probability of electron capture. The quantity δ_R' is a nucleus-dependent correction term that does *not* require detailed knowledge of the nuclear wavefunctions [33]. Note that the correction terms in Eq. 2.6 are indeed small corrections: for ^{37}K, their product is 1.0063(7) [33].

The $\mathscr{F}t$ value, Eq. 2.6, is the same within uncertainties for each $0^+ \to 0^+$ decay because these decays proceed entirely by the vector component and the dependence of the decay rate on the Fermi function and the β-decay endpoint have been incorporated into Eq. 2.7. Therefore, any deviation in the $\mathscr{F}t$ value for a mixed transition from the value for $0^+ \to 0^+$ decays, $\mathscr{F}t^{0^+\to 0^+} = 3072.27(72)\,\mathrm{s}$ [31], is a measurement of the axial vector component. Note that with these definitions, the axial-vector correction terms do not need to be calculated to determine a value for ρ. However, interpreting ρ as a measure of C_A or $|M_{GT}|$ does require them to be calculated.

The observed strength of the weak interaction is different when considering interactions involving one quark and one lepton, such as β-decay, and weak interactions involving two quarks (K^0-decay) or two leptons (μ-decay). To resolve this, Cabibbo, Kobayashi, and Maskawa (CKM) postulated that the quark eigenstates participating in the weak interaction are different from the mass eigenstates participating in strong and electromagnetic interactions [35, 36]. These two sets of bases are related through the CKM matrix. Denoting the d quark involved in β-decay as d' and the mass eigenstate by d:

$$d' = V_{ud} d, \tag{2.9}$$

where V_{ud} is one element of the CKM matrix with the experimentally determined value $|V_{ud}| = 0.974\,17(21)$ [31]. This consideration modifies the decay rate (Eq. 1.5) to include a factor of $|V_{ud}|^2$.

2.1.1 Angular correlations

The complete evaluation for an allowed transition of Eq. 2.1 to determine the value of $\mathscr{M}_{fi}$ in Eq. 1.5 was presented in [27]:

$$\begin{aligned}\frac{d^5W}{dE_e d\Omega_e d\Omega_\nu} = 1 &+ a_{\beta\nu}\frac{\vec{p}_e\cdot\vec{p}_\nu}{E_eE_\nu} + b\frac{m_e}{E_e} \\ &+ \frac{\vec{I}}{I}\cdot\left[A_\beta\frac{\vec{p}_e}{E_e} + B_\nu\frac{\vec{p}_\nu}{E_\nu} + D\frac{\vec{p}_e\times\vec{p}_\nu}{E_eE_\nu}\right] \\ &+ c_{\text{align}}\left[\frac{I\left(I+1\right) - 3\langle\left(\vec{I}\cdot\hat{i}\right)^2\rangle}{I\left(2I-1\right)}\right]\left[\frac{1}{3}\frac{\vec{p}_e\cdot\vec{p}_\nu}{E_eE_\nu} - \frac{\left(\vec{p}_e\cdot\hat{i}\right)\left(\vec{p}_\nu\cdot\hat{i}\right)}{E_eE_\nu}\right].\end{aligned} \tag{2.10}$$

The momentum and energy of the leptons are given by $\vec{p}_i$ and E_i with $i = e, \nu$. The spin of the parent nucleus is given by $\vec{I}$ and its magnitude is I. I assume that the spin of daughter leptons is unobserved. The first line gives the terms independent of the nuclear spin, while the second line displays correlations between the momenta of the emitted leptons and the nuclear spin of the parent nucleus. The third line has terms containing the second moment of the nuclear spin $(\vec{I}\cdot\hat{i})^2$. The parameters $a_{\beta\nu}, b, A_\beta, B_\nu, D, c_{\text{align}}$ determine the magnitude of each correlation. Note that as a practical matter, $\vec{p}_\nu$ is inferred from the momentum of the daughter nucleus and $\vec{p}_e$ using momentum conservation. When the the neutrino momentum is unobserved, terms proportional to $a_{\beta\nu}$, c_{align}, B_ν, and D vanish. Each of the correlation coefficients can be written in terms of the C_i's of Eq. 2.1, the Fermi and Gamow-Teller matrix elements (M_F, M_{GT}), and the spin of the parent nucleus (see the Appendix of Ref. [27]). For example, within the standard model, the beta-asymmetry (A_β) is written as:

$$A_\beta = \frac{\mp\rho^2\lambda_{I'I} - 2\delta_{I,I'}\rho\sqrt{\frac{I}{I+1}}}{1+\rho^2}, \tag{2.11}$$

where the upper (lower) sign is for β^- (β^+)-decay, $\delta_{I',I}$ is the Kronecker delta, $\lambda_{I',I}$ is given by

$$\lambda_{I',I} = \begin{cases} 1, & I' = I - 1 \\ \frac{1}{I+1}, & I' = I \\ \frac{-I}{I+1}, & I' = I + 1, \end{cases} \tag{2.12}$$

and I' denotes the spin of the daughter nucleus. It is clear from Eq. 2.11 that in order for a measurement of A_β to be meaningful, ρ must be independently determined from Eqs. 2.4 and 2.5. Therefore, measurements of an isotope's half-life, branching ratio, and Q-value are sufficient to calculate a prediction for A_β, as well as the rest of correlation coefficients, within the assumptions of the standard model.

This presents two general avenues for interpreting a measurement of A_β. First would be to accept the value of ρ, and compare the observed asymmetry to the SM. Deviations from this would potentially be signals of new physics. Alternatively, Eq. 2.4 can be rearranged to use correlation measurements as a measurement of ρ. Then, the $\mathscr{F}t$ value can be calculated independently of the most precise determination using pure Fermi decays and provide a check on these measurements. Before describing these scenarios in more detail, I will describe the specifics of ^{37}K decay including recoil-order corrections to the correlation coefficients.

2.2 ^{37}K decay

The allowed β^+ decay of ^{37}K is a mixed Fermi-Gamow Teller ($I^\pi = \frac{3}{2}^+ \rightarrow \frac{3}{2}^+$) decay primarily to the ground state of ^{37}Ar as shown in Fig. 2.1. The half-life was measured at the Cyclotron Institute: $t_{1/2} = 1.236\,51(94)$ s [37] and I take the Q-value, branching ratio to the ground state, and f_A/f_V from [33]: BR $= 97.99(14)\,\%$, $Q_{\mathrm{EC}} = 6.147\,46(20)\,\mathrm{MeV}$, and $f_A/f_V = 1.00456$. With this information, $\rho = 0.5768(21)$, and this can be used to calculate the values of the correlation coefficients shown in Tab. 2.1.

The most significant branch to an excited state is to the $5/2^-$ state at 2.7961 MeV, which must be pure GT with a value of $A_\beta^{\mathrm{exc}} = -0.6$. This excited state immediately decays to the ground state with 98.5% branching ratio. All other branches to excited states are at the part-per-ten-thousand level and are completely negligible.

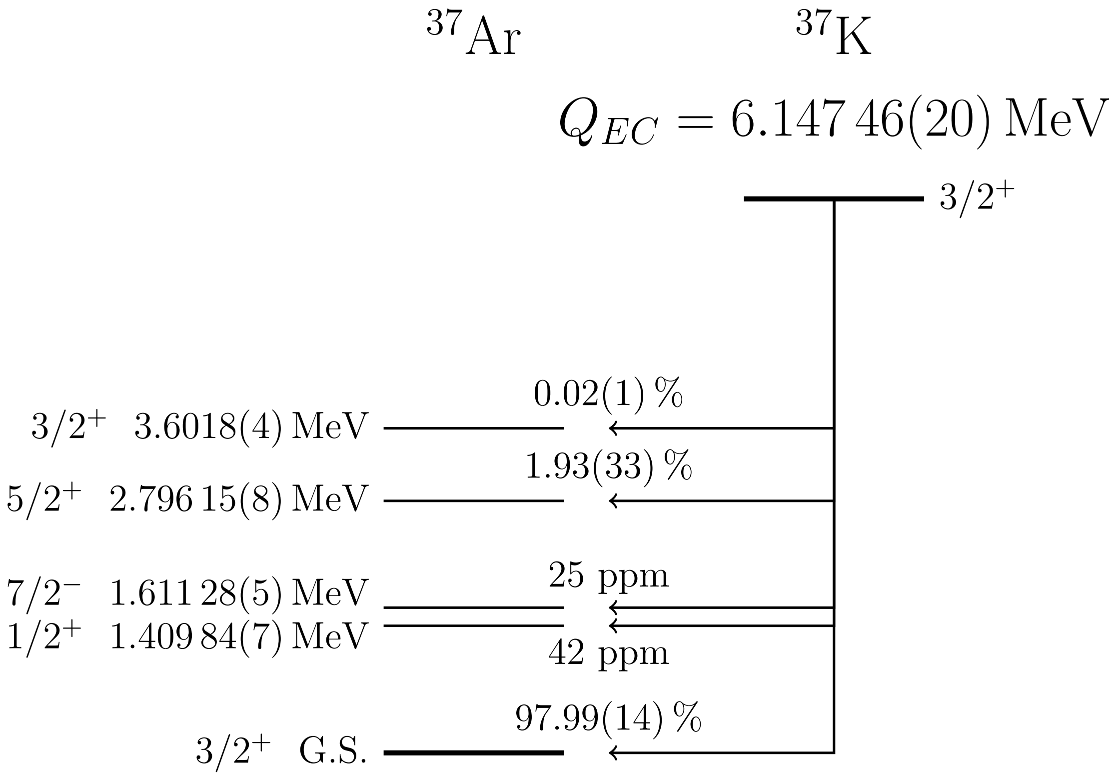

Figure 2.1: Level scheme for the decay of ^{37}K. The main branch is to the isobaric analog ground state of ^{37}Ar. The value for the branching ratio adopted here is taken from the review of [33], which differs by $< 1\sigma$ from the value adopted by the National Nuclear Data Center, which considers only the most precise measurement [38].

Table 2.1: Correlation coefficients values in the SM. Assumes the SM $V - A$ interaction and the validity of the CVC hypothesis. The values shown here ignore recoil-order effects and all physics beyond the SM. The Fierz term (b) requires the existence of either C and V or T and A currents while the D coefficient requires imaginary coupling constants. Therefore, they are *identically* zero in the SM.

Correlation		SM Value ^{37}K
Beta-neutrino	$a_{\beta\nu}$	0.6671(18)
Fierz	b	0
Beta asymmetry	A_β	−0.5706(7)
Neutrino asymmetry	B_ν	−0.7704(18)
Triple correlation	D	0
Alignment term	c_{align}	0.1997(11)

2.2.1 *Recoil-order corrections*

The discussion up to this point has assumed that the nucleus is infinitely heavy. Here, this assumption is relaxed and the values of Tab. 2.1 are modified as well as acquire an energy dependence. The section draws extensively from the work of [39]. Defining q as the momentum transfer, recoil-order corrections are $\sim q/m_N$ and $(qR)^2$ with m_N the nucleon mass and R the nuclear radius. Since q is on the order of MeV, the magnitude of these corrections is $\sim 0.1\%$.

The decay rate is written in terms of ten form factors including the standard vector and axial-vector terms along with form factors for weak magnetism, induced tensor, induced scalar, and induced psuedoscalar terms. In terms of these form factors, the β-asymmetry parameter is

$$A_\beta = \frac{f_4(E) + \frac{1}{3} f_7(E)}{f_1(E)} \tag{2.13}$$

where the spectral functions $f_i(E)$ are given in Appendix B of [39].

Application of the CVC hypothesis allows some of the form factors to be related to magnetic dipole moment (μ) and electric quadrupole moment (Q) of the parent and daughter nuclei while requiring others to be zero. Furthermore, terms that violate G-parity, defined as a rotation in isospin space as $\hat{G} \equiv C \exp(-i\pi T_2)$, are not expected to exist, which further simplifies the expressions. The remaining form factors, which do not benefit from the symmetry arguments presented here, require shell-model calculations of the nuclear matrix elements [40]. The form factors contributing to A_β are listed in Tab. 2.2 along with documentation of how the value was derived.

Inserting these values into Eq. 2.13 produces the SM prediction for A_β as a function of energy as shown in the solid red curve of Fig. 2.2. The magnitude of the predicted asymmetry including recoil-order corrections increases slightly with increasing positron energy.

An advantageous feature of low-energy probes of new physics is that these experiments are sensitive to a wide range of physics beyond the standard model (BSM) without making reference to a specific model of new physics. While direct searches may provide tighter limits on a specific class of new physics, by making a precise comparison to the standard model, low energy experiments could signal the existence of exotic new interactions and help to guide dedicated searches. With this overarching principle in mind, the following section will describe one class of extensions to the

Table 2.2: Recoil-order correction form factors. Adopted values for the form factors defined in [39]. The CVC hypothesis allows b and g to be related to electromagnetic moments of the parent and daughter nucleus. Second-class currents, defined by a violation of G-parity, are not predicted by the SM.

Form factor	Description	Value	Source
a	Vector	M_F	CVC
b	Weak Magnetism	45.03(5)	CVC & [41, 42]
c	Axial	M_A	
d	Induced Tensor	0	G-Parity
e	Induced Scalar	0	CVC
f		0	CVC
g		$-1.4(4) \times 10^5$	CVC & [43, 44]
h	Pseudoscalar	-4.10×10^4	[40]
j_2		0	G-Parity

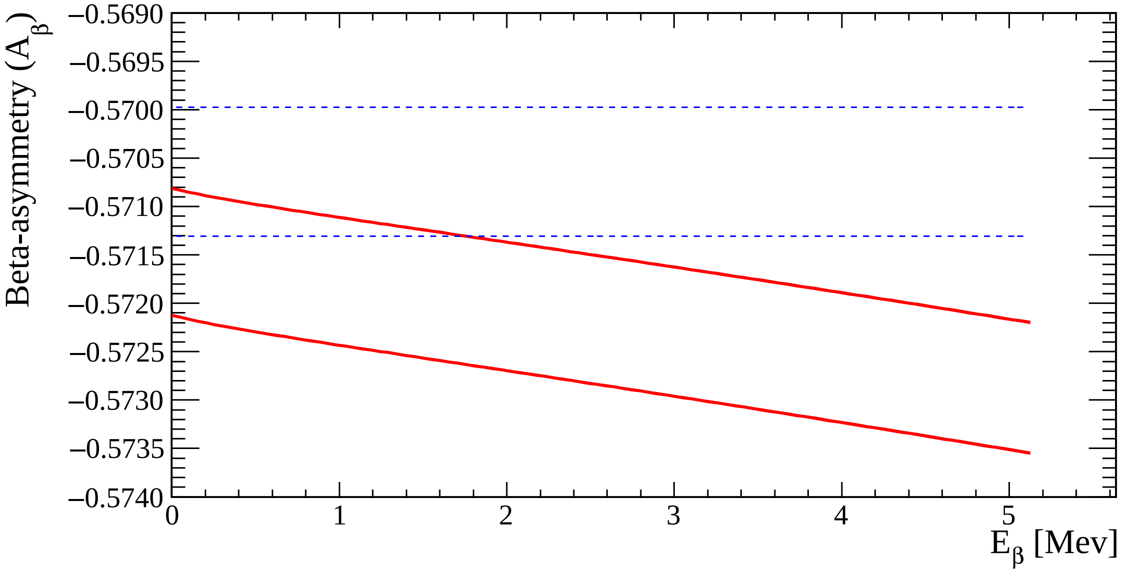

Figure 2.2: Standard model predictions for the β-asymmetry parameter. The blue dashed line gives the 1σ confidence band assuming an infinitely heavy nucleus as in [27] while the region between the solid red lines adopts the recoil-order corrections of [39] and again gives the 1σ confidence band. In both cases, the uncertainty is dominated by the experimental value for ρ, which in turn depends on the experimentally determined values for the branching ratio and half-life.

standard model, and how a measurement of A_β in ^{37}K will contribute to constraining these models.

2.3 Physics beyond the standard model

Having established the conventional prediction for A_β in ^{37}K, I now present how these predictions would be modified with the existence of new physics as well as constraints on these new physics from other experimental efforts. In general these new theories are under-constrained by experiments[1]. Therefore, a single deviating measurement is unlikely to be an unambiguous signal in support of a *specific* new theory. However, elucidating how each measurement fits in with the larger picture is an important task and the focus of this section. The electroweak interaction obeys the symmetry structure

$$SU(2)_R \times U(1)_Y. \tag{2.14}$$

As has been noted previously, this structure displays *maximal* parity violation. A natural extension to this model is to restore parity symmetry through the introduction of a parity-conserving weak sector, adding to Eq. 2.14 a term $SU(2)_R$. This extension necessitates the existence of right-handed analogs $(W_R^\pm, Z_R)$ of the SM bosons $(W_L^\pm, Z_R)$. The right-handed analogs couple only to right-handed, i.e. positive helicity, neutrinos. In terms of the C_i's of Eq. 2.10, this would correspond to $C_i/C_i' \neq 1$ with $i = V, A$ and $C_V/C_A \neq 1$. Additionally, the two gauge-sectors are coupled via a mixing angle ζ, such that the weak eigenstates mediating β-decay are $W_{L,R}$ defined in terms of the mass eigenstates $W_{1,2}$ as [45]:

$$\begin{aligned} W_L &= W_1 \cos\zeta - W_2 \sin\zeta \\ W_R &= \left(W_1 \sin\zeta + W_2 \cos\zeta\right) e^{-i\omega}. \end{aligned} \tag{2.15}$$

Equation 2.15 introduces the CP violating phase ω. This model is consistent with the observed parity violation if both $W_L \approx W_1$ $(\zeta \to 0)$ and $m_R \gg m_L$. In general, the right-handed sector introduced here has an independent CKM matrix $(V_{ij}^R \neq V_{ij}^L)$, as well as a potentially different overall coupling strength $(g_L \neq g_R)$. The

---

[1] Hence, the need for more experiments!

vector and axial-vector parts of the Hamiltonian, making explicit the spin-symmetric structure, are given by [46,47]:

$$\begin{aligned} H_{V,A} =& \bar{e}\left(1+\gamma_5\right)\nu^L\left[a_{LL}\bar{u}\gamma_\mu\left(1+\gamma_5\right)d + a_{LR}\bar{u}\gamma_\mu\left(1-\gamma_5\right)d\right] + \\ & \bar{e}\gamma_\mu\left(1-\gamma_5\right)\nu^R\left[a_{RR}\bar{u}\gamma_\mu\left(1-\gamma_5\right)d + a_{RL}\bar{u}\gamma_\mu\left(1+\gamma_5\right)d\right] + \text{H.c.} \end{aligned} \tag{2.16}$$

where a_{LR} denotes the coupling of a left-handed chirality neutrino to a right-handed chirality d-quark.[2] In the SM, $a_{LL} = G_F V_{ud}/2$ and the rest zero [47]. The C_i of Eq. 2.10 are related to a_{ij} by

$$C_V = g_V\left(a_{LL} + a_{LR} \pm a_{RR} \pm a_{RL}\right) \tag{2.17a}$$

$$C_A = g_A\left(a_{LL} - a_{LR} \pm a_{RR} \mp a_{RL}\right) \tag{2.17b}$$

where the lower sign gives the expression for C_i' and $C_{T,S,P}$ are given in [47]. While the discussion of left-right (L-R) symmetric models has, to this point, been entirely general, the simplest SM extension is the *minimally* L-R symmetric model. This assumes that the CKM matrices and couplings strengths of the left- and right-handed sectors are identical and the CP violating phase is zero: $V_{ud}^R = V_{ud}^L$, $g_R = g_L$ and $\omega = 0$. This leaves only two parameters yet to be determined: the mixing angle ζ and $\delta = (m_1/m_2)^2$. Note that the measured mass of W_L is 80.385(15) GeV [5]. Thus, the new physics discussed in this section has an energy scale $\sim m_L/\sqrt{\delta}$. Expressions for a_{ij} in terms of δ, ζ, are given in [45]. To first order in δ and ζ, $a_{LL} = g^2 V_{ud}/8M_1^2$, and the C_i's of Eq. 2.17 are given by:

$$C_V = g_V a_{LL}(1+\delta-2\zeta) \tag{2.18a}$$

$$C_V' = g_V a_{LL}(1-\delta) \tag{2.18b}$$

$$C_A = g_A a_{LL}(1+\delta+2\zeta) \tag{2.18c}$$

$$C_A' = g_A a_{LL}(1-\delta). \tag{2.18d}$$

Having written the values for C_i as functions of BSM physics parameters, the

---

[2] N.B.: The metric and definitions of the γ-matrices are as in [47], which is different than in [46].

next section presents a survey of results from both nuclear and high-energy physics. Observables in the various systems each have a different dependence on the BSM parameters, such that each class of experiments gives a complementary set of limits.

2.3.1 Limits for pure-Fermi decays

Fundamental to the standard electroweak model is the unitarity of the CKM matrix, and the most stringent test of this unitarity comes from the sum of the squares of the elements in the top row. I have described the first-generation coupling, V_{ud}, which is most precisely determined from the average $\mathscr{F}t$ value of pure-Fermi β-decays. The second-generation coupling, $V_{us} = 0.2253 \pm 0.0008$, is derived from kaon-decay with a 3-flavor lattice QCD calculation, while the final element, $V_{ub} = (4.13 \pm 0.49) \times 10^{-3}$, is derived from the decay of the B meson. Both values cited here are PDG recommended values from [5]. In the minimally L-R symmetric model, the combination of these is sensitive to the mixing angle ζ.

$$\begin{gathered} V_{ud}^2 + V_{us}^2 + V_{ub}^2 = 1 - 2\zeta \\ -0.0003 < \zeta < 0.0006 \qquad 90\% \text{ C.L.} \end{gathered} \tag{2.19}$$

As we will see, this is by far the strictest limit on ζ. However, results from purely leptonic kaon decays are inconsistent with those from semi-leptonic decays when using the latest 4-flavor lattice QCD calculations [31]. In some scenarios, the result is inconsistent with unitarity. Clearly this puzzle is not entirely resolved and deserves further attention both theoretically and experimentally.

2.3.2 Limits for pure-Gamow Teller decays

A measurement of the polarization-asymmetry correlation is sensitive to a combination of correlation coefficients (see Ref. [27], Eq. 6) and is determined by measuring the longitudinal polarization of β particles following the nuclear decay. By taking the ratio of a pure-Fermi to a pure-GT decay, many systematic effects cancel. Combining the most precise measurements from ${}^{26m}\text{Al}/{}^{30}\text{P}$ [48] and ${}^{14}\text{O}/{}^{11}\text{C}$ [49], gives the combined result [50]:

$$\delta\zeta = (1.3 \pm 5.6) \times 10^{-4} \qquad 90\% \text{ C.L.} \tag{2.20}$$

Since only the product $\delta\zeta$ appears here, these measurements lose all sensitivity as either $\delta \to 0$ or $\zeta \to 0$. The sensitivity can be restored by adding a polarization to the parent nuclei. In this case, only one isotope is used and a comparison is made between polarization states of the parent nuclei or between an unpolarized and a polarized parent. The most sensitive measurements are from ^{107}In [51, 52] and ^{12}N [53]. An overview of these experiments is given in [54] where the combined sensitivity is found to be:

$$(\delta + \zeta)^2 = -0.0004 \pm 0.0043 \qquad 90\% \text{ C.L.} \tag{2.21}$$

Finally, a measurement of the β-asymmetry in a pure-GT decay also gives limits on right-handed couplings. The sensitivity is given by

$$\tilde{A} \equiv A_\beta^{\text{exp}} - A_\beta^{\text{SM}} = \pm 2\lambda_{J'J}(\delta + \zeta)^2 \tag{2.22}$$

where the signs refer to $\beta^\pm$ decay and $\lambda_{J'J}$ is given in Eq. 2.12. In ^{60}Co (β^-, $5^+ \to 4^+$), the experiment was performed by polarizing the nuclei in a strong external magnetic field with the result that $\tilde{A} = -0.027 \pm 0.022$ [55]. In the case of ^{114}In (β^-, $1^+ \to 0^+$), the In were polarized by the internal magnetic hyperfine field induced in a host Fe material, resulting in the limit $\tilde{A} = 0.006 \pm 0.014$ [50,56]. The most recent experiment of this type was performed in ^{67}Cu (β^-, $3/2^- \to 5/2^-$) [57], again using the internal hyperfine magnetic field of a host Fe foil. They simultaneously measured the β-asymmetry for ^{68}Cu to serve as a normalization and reduce systematic uncertainties. Their result, $\tilde{A} = -0.012 \pm 0.014$ is consistent with the SM value.

2.3.3 Limits from mixed decays

The sensitivity of mixed Fermi-Gamow Teller decays to admixtures of right-handed currents is a central motivation to this work. However, as the correlation coefficients in these decays depend on the additional parameter ρ, the extraction of limits on ζ and δ is not as straightforward in this case as ρ itself depends on the admixture of right handed currents (see Eq. 2.4).

Therefore, for each combination of δ and ζ, ρ is treated as a free parameter, chosen by minimizing the χ^2 with respect to the experimental data. The experimentally determined $\mathscr{F}t$ is still related to $\mathscr{F}t^{0^+\to 0^+}$ by Eq. 2.5, with ρ modified by the inclusion of right-handed currents [58]. Therefore, the ratio $r \equiv \mathscr{F}t^{0^+\to 0^+}/\mathscr{F}t$ is included in the minimization function. In addition to this value, all measured correlation coefficients are included in the χ^2, with is minimized with respect to ρ:

$$\chi^2\left(\rho;\zeta,\delta\right) = \left(\frac{r(\rho;\zeta,\delta) - r^{exp}}{dr}\right)^2 + \sum_i \left(\frac{X_i(\rho;\zeta,\delta) - X_i^{\mathrm{exp}}}{dX_i}\right)^2 \tag{2.23}$$

where the sum goes over all the measured correlations in a given isotope and X stands for any of the correlation coefficients given in Eq. 2.10. Also note that only the correlations A_β and B_ν, in which the parent nuclei are polarized, are relevant to this discussion as the others have little or no sensitivity to right-handed currents.

Currently, only three mixed transitions have been measured precisely enough to contribute to limits in L-R symmetric models: neutron decay, ^{19}Ne, and ^{37}K. In the case of ^{19}Ne, the β-asymmetry was measured by polarizing the ions to $\approx 100\%$ via a Stern-Gerlach apparatus and detecting the βs with 4π solid angle in a storage cell. The experimental asymmetry was found to vary as a function of β energy, with the extrapolation to $E = 0$ giving $A_\beta = -0.0391 \pm 0.0015$ [59] compared to the SM value -0.04166 ± 0.00095 . I take $\mathscr{F}t = 1720.3(30)\,\mathrm{s}$ from the review of [60] with references to the experimental data given therein.

For ^{37}K, previous work at TRINAT, using many of the same techniques as in this work, has measured the neutrino-asymmetry, $B_\nu = -0.755 \pm 0.024$ [19, 20], and the positron-asymmetry, $A_\beta = -0.563 \pm 0.009$ [25]. The beta-neutrino correlation ($a_{\beta\nu}$) was also measured but does not contribute to limits on right-handed currents [17,21]. The other experimental inputs were discussed in Sec. 2.2.

Neutron decay is the simplest mirror decay as it avoids any dependence on nuclear structure calculations. The Q-value is simply the neutron-proton mass difference and the branching ratio is 1.0. Currently two methods for determining the lifetime have comparable precision. The "beam" approach measures the decay rate from a known density of neutrons as in [61, 62] while the "bottle" method confines ultra-cold neutrons in a material trap and measures the survival fraction as a function of time as in [63]. Multiple experiments have been performed with both the bottle and the beam techniques. The average values of τ_n for each of the experimental methods differ by 3.8σ [64]. Further experiments are planned to hopefully resolve this discrepancy, and I will follow the PDG recommended value of $\tau_n = 880.3(11)\,\mathrm{s}$ found by averaging the seven most precise measurements and scaling the uncertainty by a factor of 1.9 to account for the scatter in the data. Both the β-asymmetry as well as the ν-asymmetry have been measured multiple times in this system with recent reviews in [65, 66]. The recoil asymmetry has also been measured in [67] and all values used here are taken from the 2015 PDG evaluation [5].

The combined limit from the nuclear systems described in this section are shown in Fig. 2.3. At ζ=0, the tightest limits come from measurements of longitudinal polarization of electrons following the β-decay of a polarized nucleus: $\delta < 0.06$. This corresponds to a limit on the mass of W_2 of $m_2 > 320\,\mathrm{GeV/c^2}$. The current limits from ^{37}K on this parameter are $m_2 > 200\,\mathrm{GeV/c^2}$ with both numbers at 90% C.L.

2.3.4 Other limits

The universality of the charged weak interaction suggests that any extension to the standard model seen in nuclear decays should also be observed in other systems where at $W^{\pm}$ is exchanged and vice versa. In this section, I lay out constraints from muon decay as well as from collider experiments of L-R symmetric extensions to the standard model.

Muon decay ($\mu^- \to e^-\bar{\nu}_e + \nu_\mu$) was suggested as a possible probe of parity-symmetric extensions to the SM in Ref. [45]. The electron energy distribution in the decay of a polarized muon is described by a set of four parameters, dubbed the Michel parameters. Each of these parameters takes on a definite value in the SM and can be altered by BSM extensions. The TWIST collaboration has made the most precise measurements of the Michel parameters ρ [68], and δ [69], as well as the combination $P_\mu^\pi \xi$ [70] where ξ is a third Michel parameter and P_μ^π is the polarization of the muon following pion decay, equal to 1 in the SM. The combined results give

$$\begin{gathered} -0.020 < \zeta < 0.017 \qquad 90\%\,\mathrm{C.L.} \\ \delta < 0.0184 \qquad 90\%\,\mathrm{C.L.} \end{gathered} \tag{2.24}$$

corresponding to a mass limit $m_2 > 592\,\mathrm{GeV/c^2}$ [70]. Comparing these limits to those shown in Fig. 2.3, this limit on the mass of W_2 is stronger than that obtained in nuclear decays. However, the limit on the mixing angle ζ is weaker than that obtained from requiring that the CKM matrix be unitary.

All of the searches discussed to this point can be termed “indirect” in the sense that they seek to detect new particles through their subtle influences on naturally

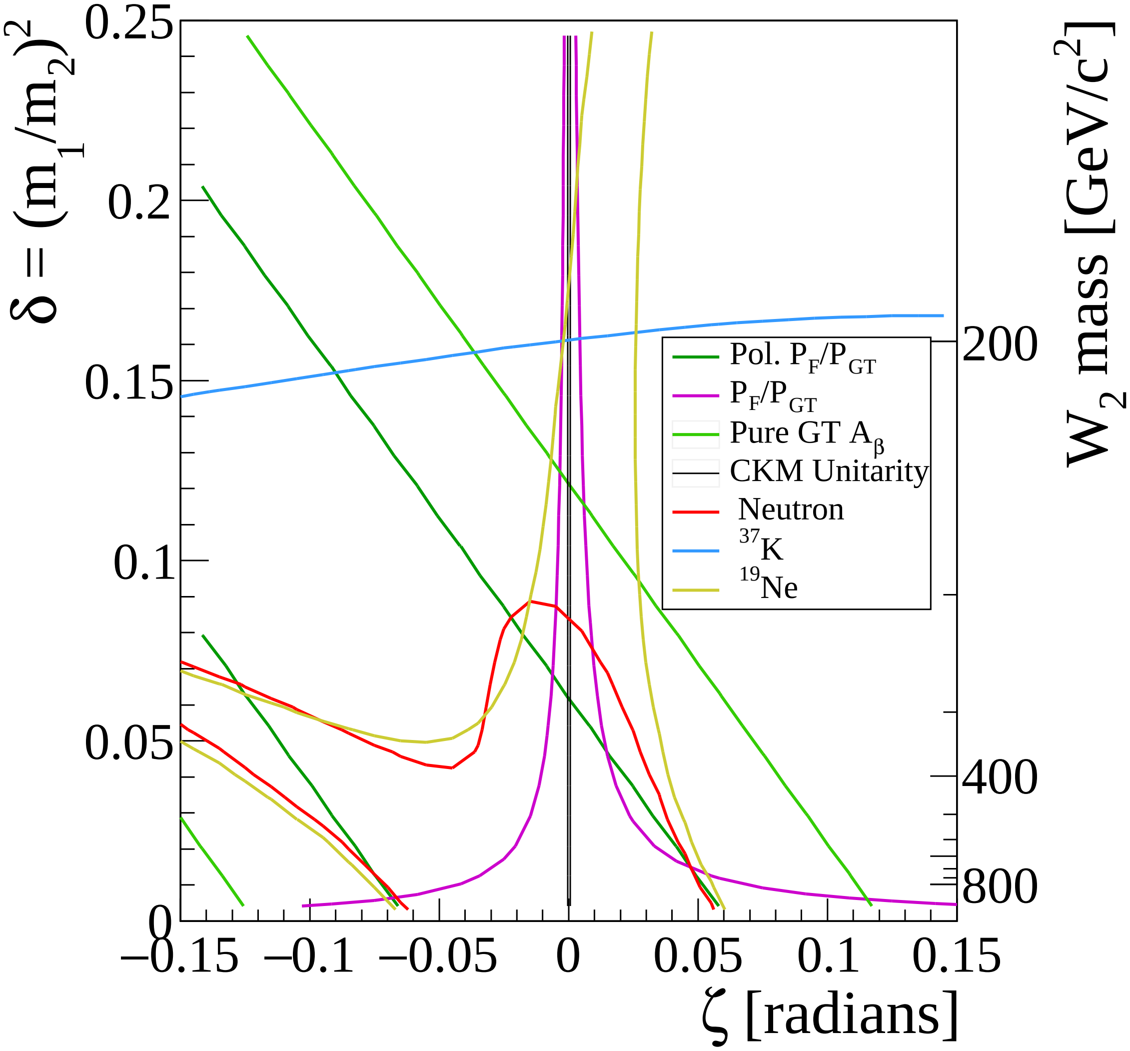

Figure 2.3: Limits on right-handed currents in the weak interaction. The unitarity of the CKM matrix provides very tight constraints on the mixing angle, but is insensitive to the mass of the new W boson. At $\zeta = 0$, the most stringent limit on δ arises from measurements of longitudinal polarization of the $\beta^{\pm}$ in the decay of a polarized nucleus. Measurements in ^{37}K provide complementary constraints to the other experiments. See section 2.3.4 for limits from non-nuclear decays.

occurring radioactive decays[3]. On the other hand, searches at the Large Hadron Collider (LHC) seek to produce the new particles directly in high-energy pp collisions. Ref. [71] describes a search for W_R with the condensed muon solenoid detector (CMS) detector at a center-of-mass energy $\sqrt{s} = 8\,\mathrm{TeV}$ and integrated luminosity of $19.7\,\mathrm{fb}^{-1}$. They report a 2.8σ excess of events in the decay chain $W_R \to ee+$two jets at $2.1\,\mathrm{TeV}$. However, no excess of events was found in any other channel and the observed excess was significantly less than predicted by the minimal L-R symmetric model. Therefore, the authors find insufficient evidence to reject the hypothesis of an excess in a SM background. Furthermore, they report a lower limit on the mass of W_R: $m_R > 3\,\mathrm{TeV}$ at 95% C.L.. This is the highest limit for this parameter.

However, the observed excess of events can be reconciled with the existence of W_R if $g_R/g_L \sim 0.6$ [72], scaling down the predicted number of events by this factor. Intriguingly, this value for g_R/g_L can be predicted by group theoretic arguments [73]. Clearly, the model is no longer minimally symmetric. Future runs of the LHC will be able to lend support to or rule out these scenarios.

While the unitarity requirement of the CKM matrix provides the strongest limit on the L-R mixing angle from any source, the mass of the new boson is most strictly limited by measurements of muon decay parameters and direct high-energy searches. However, in more general models, the constraints are considerably weaker and precision measurements in nuclear decays can make significant contributions to the model parameters. In fact, as an indirect probe of BSM physics, low-energy precision measurements can detect BSM physics in a largely model-independent fashion. Furthermore, these measurements have totally independent systematic uncertainties to muon and high-energy experiments and provide an important cross-check if any new physics that may be discovered is also detectable in nuclear decays.

Relaxing the requirements that $V_{ij}^L = V_{ij}^R$ and $g_L = g_R$, we can relax the model dependence of the limits described here as well as emphasize the complementary nature of the experimental approaches. Collider experiments are typically sensitive to $(g_R/g_L)^2$ and V_{ud}^R/V_{ud}^L. In nuclear and neutron β-decay, the presence of two weak vertices in Fig. 1.1 indicates that the ratio g_R/g_L enters to the fourth power and V_{ud}^R/V_{ud}^L appears squared. If $g_R/g_L \sim 0.6$ as suggested by [72,73], this would suppress limits from nuclear decays by a factor of ~ 0.4 compared to high-energy searches,

---

[3] Of course, short lived isotopes are not naturally *occurring*, but the *decay* proceeds naturally, i.e. without inducement

although if $g_R > g_L$, the β-decay limits are enhanced. In muon decay, the Michel parameters each depend on $(g_R/g_L)^2$ and $(g_R/g_L)^4$, while the muon polarization appearing in $P_\mu^\pi \xi$ adds a dependence on (V_{ud}^R/V_{ud}^L) and $(V_{ud}^R/V_{ud}^L)^2$. Clearly, the experimental approaches are complementary to one another, and taken together can cover a large region of the potential parameter space.

2.4 CVC and V_{ud} in mirror decays

As an alternative to interpreting a measurement of A_β as a probe of BSM physics, this measurement can be used, in conjunction with other measurements in mirror nuclear decays, to test the CVC hypothesis and to determine a value for V_{ud}. Both these approaches are in complete analogy with the most precise determination from $0^+ \to 0^+$ pure-Fermi decays. According to the CVC hypothesis, the Fermi component of nuclear decays should be independent of the specific nuclear transition. Pure-Fermi decays are an ideal system to test this in, because they *have no* Gamow-Teller component. In nuclear mirror decays, isolating the Fermi component to compare it across isotopes requires a precise measurement of ρ. In this interpretation, measurements of correlation parameters are combined with a measurement of the $\mathscr{F}t$ value to form a nucleus-independent quantity that can be compared across nuclear transitions.

This approach is described in detail in [60] with the primary results summarized here. For mixed decays, Eq. 2.4 can be recast and related to fundamental constants with the result

$$\mathscr{F}t = \frac{K}{G_F^2 V_{ud}^2} \frac{1}{C_V^2 |M_F|^2 \left(1+\Delta_R^V\right)\left[1+\left(f_A/f_V\right)\rho^2\right]} \tag{2.25a}$$

$$= \frac{\mathscr{F}t_0}{C_V^2 |M_F|^2 \left[1+\left(f_A/f_V\right)\rho^2\right]} \tag{2.25b}$$

where $K/(\hbar c)^6$ has the value $8120.278(4) \times 10^{-10}$ GeV^{-4} s, and $\Delta_R^V = 2.361 \pm 0.038\%$ is again the radiative corrections [34]. Examination of Eq. 2.25 shows that $\mathscr{F}t_0$ contains only fundamental constants and should be independent of the nuclear transition. Therefore, measuring this value in as many nuclear decays as possible provides an independent test of the CVC hypothesis.

Fig. 2.4 shows the value obtained for $\mathscr{F}t_0$ among all relevant transitions with

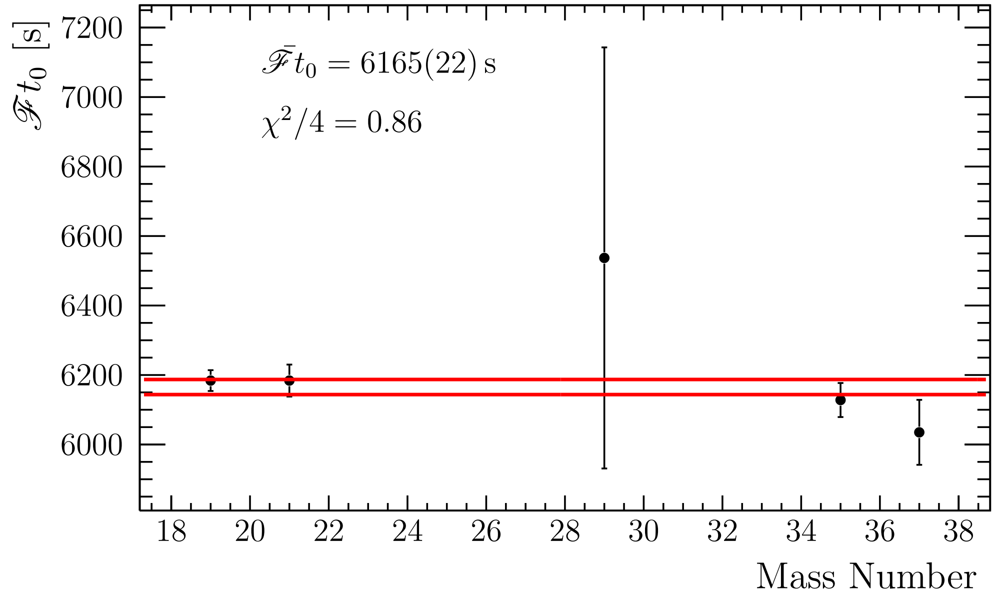

Figure 2.4: Current status of CVC test with mirror transitions. Values are adapted from Refs. [25, 60, 74].

values adopted from [60]. The isotopes included are: ^{19}Ne, ^{21}Na, ^{29}P, ^{35}Ar, and ^{37}K. The value shown for ^{21}Na includes the updated $t_{1/2}$ measurement of Ref. [74] and the status of ^{37}K includes the updated $t_{1/2}$ and A_β measurements [25,37]. The isotope ^{17}F has also been measured, but the values of the correlation coefficients are insensitive to ρ and it does not contribute to this determination. Other mirror nuclei have no correlation coefficient measured to-date, so that $\mathscr{F}t_0$ cannot be calculated. The consistency of $\mathscr{F}t_0$ across these systems provides a test of CVC at the 0.35% level. In ^{37}K, the uncertainty is dominated by the uncertainty in the measured correlation coefficients and the present work will reduce this uncertainty.

Having verified the CVC hypothesis in mirror nuclei, and proceeding in analogy to superallowed pure-Fermi decays, the value of V_{ud} can be extracted from

$$V_{ud}^2 = \frac{K}{\bar{\mathscr{F}}t_0 G_F^2} \frac{1}{1+\Delta_R^V} \tag{2.26}$$

giving the result

$$V_{ud}^{\mathrm{mirror}} = 0.9725 \pm 0.0017. \tag{2.27}$$

For the sake of comparison, the value of V_{ud} can be extracted for each nuclear transition independently. For ^{37}K *alone*, the result turns out to be

$$V_{ud}^{\mathrm{K}} = 0.9830 \pm 0.0076 \tag{2.28}$$

where the uncertainties from [25] have been symmeterized. Although less precise than the value obtained from pure-Fermi decays, V_{ud}^{mirror} is comparable in precision to the value obtained from neutron decay and is more precise than the value measured in pion decay.

This chapter has laid out the theoretical framework within which the measurement of A_β will be interpreted. The measurement can be used to search for possible extensions to the standard model and is complementary to other searches in nuclear decays, muon decay and high-energy physics. Alternatively, the result can be interpreted as a test of the CVC hypothesis in mirror nuclei. Having established the validity of CVC, mirror decays such as ^{37}K can independently or as a group provide a value for V_{ud} independent of other determinations.

3. ATOMIC INTERACTIONS

Using the techniques described in this chapter, we confine, cool, and polarize the ^{37}K atoms using a magneto-optical trap (MOT) for confinement and cooling and optical pumping for spin-polarization. These techniques use a combination of laser and magnetic fields to manipulate the momentum and internal quantum numbers of the atoms in order to get the desired effect. This chapter will first describe the electronic structure of alkali atoms such as potassium before describing the physics of an alternating-current magneto-optical trap (AC-MOT) and optical pumping.

3.1 Electronic structure of alkali atoms

The electronic configuration of potassium in the ground state is denoted as [Ar]$4s_{1/2}$ where [Ar] denotes the closed-shell core of Ar and $4s_{1/2}$ is specified in the nL_J notation where n is the principal quantum number, L is the orbital angular momentum of the electron and J is the is the total atomic angular momentum $\vec{J} = \vec{L} + \vec{S}$ where $S = 1/2$ is the electron's spin.

The first two excited states representing the fine structure are written in the same notation as $4p_{1/2}$ and $4p_{3/2}$, each having $L = 1$. As a result of the relative orientation of the electron spin and orbital angular momentum, these states are separated in energy from each other by $E_{fine}/h = 1.6\,\text{THz}$, which is large enough that all other interactions, which have energies on the order of MHz, can be safely treated as perturbations and, therefore, independently for the $4p_{1/2}$ and $4p_{3/2}$ states respectively.

3.1.1 Hyperfine structure

The dominant correction to the fine structure described above is the hyperfine interaction coupling the atomic spin $\vec{J}$ to the nuclear spin $\vec{I}$ into the total spin $\vec{F} = \vec{I} + \vec{J}$. Since in our application the hyperfine structure is small compared with the fine structure, its Hamiltonian can be written as

$$\mathscr{H}_{HF} = A_{HF}\vec{I} \cdot \vec{J} \tag{3.1}$$

where A_{HF} is determined from experiment for each hyperfine level. For the case of ^{37}K, $A_{s_{1/2}} = 120.1336(4)\,\mathrm{MHz}$ [41], $A_{p_{1/2}} = 14.4\,\mathrm{MHz}$ [75], and $A_{p_{3/2}} = 4.03\,\mathrm{MHz}$ [75]. As a result of this effect, states with $\vec{I}$ anti-parallel to $\vec{J}$ are shifted down in energy while states with $\vec{I}$ parallel to $\vec{J}$ lie at higher energy.

The atomic states can be expressed in a basis defined by the quantum numbers $|I, J, M_I, M_J\rangle$ or equivalently in a basis defined by $|I, J, F, M_F\rangle$. Since the hyperfine interaction can be treated as a perturbation, the I, J quantum numbers are unaffected and will no longer be written except where necessary. Although the choice of basis is in principle arbitrary, it will be convenient to perform calculations in both sets of bases. The $|F, M_F\rangle$ basis states are the eigenstates of the system, making it the most convenient basis for performing calculations. On the other hand, the nuclear polarization in the β-decay rate (Eq. 2.10) is expressed most simply in the $|M_I, M_J\rangle$ basis as

$$P = \frac{\langle\psi|\, I_z \,|\psi\rangle}{I} \tag{3.2a}$$

$$T = \frac{I(I+1) - 3\,\langle\psi|\, I_z^2 \,|\psi\rangle}{I(2I-1)}. \tag{3.2b}$$

where the I_z and I_z^2 operators are given by

$$I_z\,|M_I, M_J\rangle = M_I\,|M_I, M_J\rangle \tag{3.3a}$$

$$I_z^2\,|M_I, M_J\rangle = M_I^2\,|M_I, M_J\rangle\,. \tag{3.3b}$$

Therefore, we must develop both the connection between the two bases as well as derive an expression for $\mathscr{H}_{HF}$ in both bases. First, we can express the Hamiltonian in the $|F, M_F\rangle$ basis. To do this, we simply rearrange equation 3.1, expressing $\mathscr{H}_{HF}$ as

$$\mathscr{H}_{HF} = \frac{1}{2}A_{HF}(\vec{F}^2 - \vec{I}^2 - \vec{J}^2). \tag{3.4}$$

The angular momentum operators in Equation 3.4 have matrix elements given by:

$$\vec{F}^2\,|I, J, F, M_F\rangle = F(F+1)\,|I, J, F, M_F\rangle \tag{3.5}$$

and similarly for $\vec{I}$ and $\vec{J}$. Therefore, in this choice of basis, the Hamiltonian is diagonal, proving the assertion above that these basis states are the eigenstates of the system with energy given by

$$E_{HF} = \frac{1}{2} A_{HF} [F(F+1) - I(I+1) - J(J+1)]. \tag{3.6}$$

On the other hand, the hyperfine interaction can be expressed in the $|M_I, M_J\rangle$ basis making use of the ladder operators:

$$\mathscr{H}_{HF} = A_{HF}[I_z J_z + \frac{1}{2}(J_+ I_- + J_- I_+)] \tag{3.7}$$

$$\begin{aligned} J_+ &= J_x + iJ_y \qquad & I_+ &= I_x + iI_y \\ J_- &= J_x - iJ_y \qquad & I_- &= I_x - iI_y. \end{aligned} \tag{3.8}$$

In this basis, the operators have matrix elements and selection rules given by

$$J_\pm |M_I, M_J\rangle = \sqrt{J(J+1) - M_J(M_J \pm 1)}\, |M_I, M_J \pm 1\rangle \tag{3.9a}$$

$$I_\pm |M_I, M_J\rangle = \sqrt{I(I+1) - M_I(M_I \pm 1)}\, |M_I \pm 1, M_J\rangle \tag{3.9b}$$

$$J_z |M_I, M_J\rangle = M_J |M_I, M_J\rangle . \tag{3.9c}$$

$$\tag{3.9d}$$

The first term in equation 3.7 contains diagonal elements while the second term, containing the ladder operators, gives rise to off-diagonal terms in $\mathscr{H}_{HF}$. Now, we must determine the connection between the two possible basis states, defined by the Clebsch-Gordon coefficients, c_k:

$$|I, J, F, M_F\rangle = \sum_k c_k |I, J, M_I, M_J\rangle_k . \tag{3.10}$$

Since I have already shown the the $|F, M_F\rangle$ states are the eigenstates of the system, calculating the Clebsch-Gordon coefficients is equivalent to diagonalizing the Hamiltonian written in the $|M_I, M_J\rangle$ basis. In fact, with no magnetic field, this can be done analytically and the results are tabulated. However, in the next section I will introduce a magnetic field and so the problem must be solved numerically. A variety of software packages provide methods to accomplish this including the GNU Scientific Library [76].

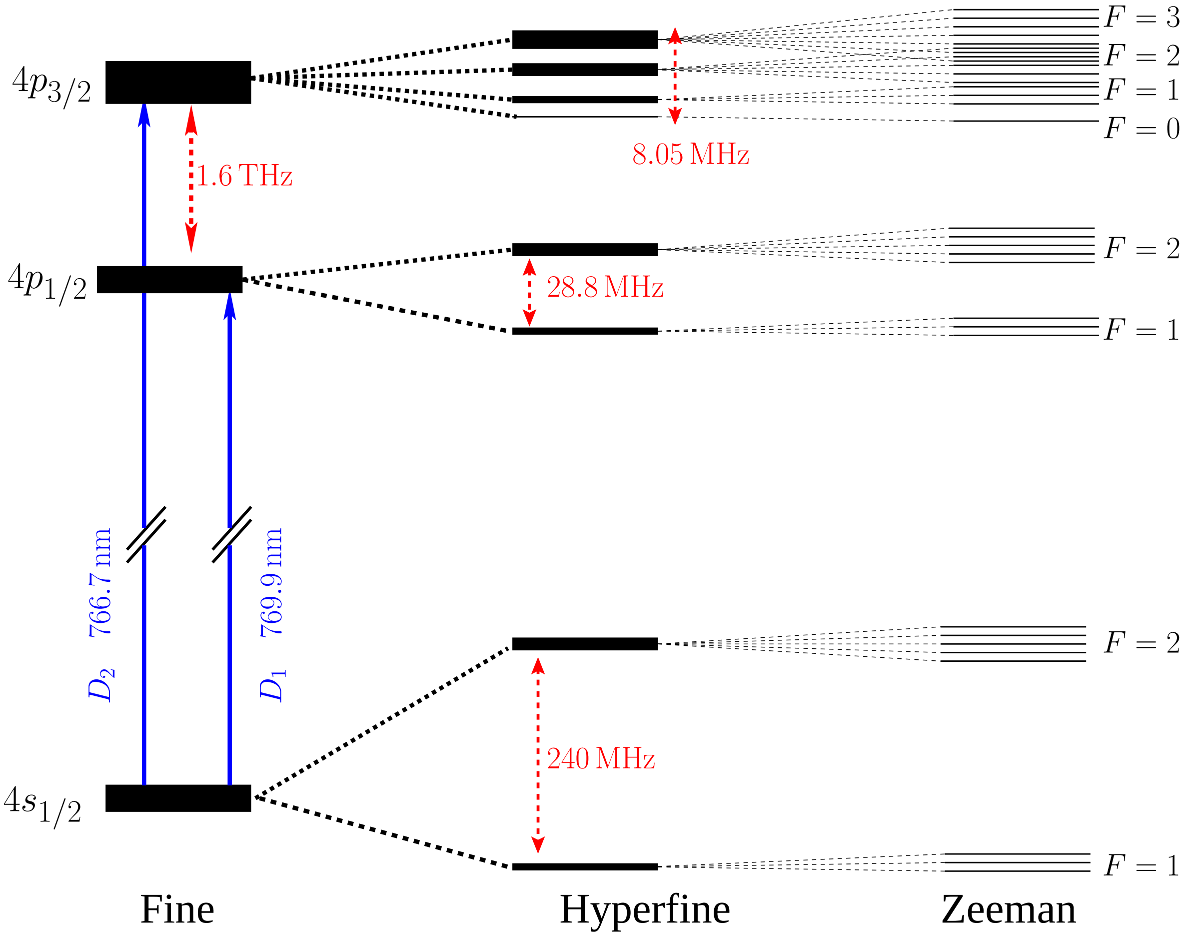

Figure 3.1: Atomic energy level diagram of ^{37}K. The fine structure results from the interaction with the orbital angular momentum L with the electron's spin, S. In the 4s state, with $L = 0$, there is no fine structure, however the $L = 1$ (4p) states have an energy difference of 1.6 THz. The hyperfine interaction results from the coupling of the atomic and nuclear angular momenta and has a much smaller energy difference, on the order of MHz. Lastly, a non-zero magnetic field introduces a further perturbation, with magnitude roughly determined by the Bohr magneton. Note that due to the vastly different scales of these interactions, the diagram is *not* drawn to scale.

Figure 3.1 summarizes the level scheme. The hyperfine interaction acts as a perturbation with the magnitude within each fine level determined by the F quantum number and the hyperfine strength A_{HF}. The $|F, M_F\rangle$ states are the eigenstates of the system and can be related to a representation using the $|M_I, M_J\rangle$ quantum numbers through the Clebsch-Gordon coefficients which are found by diagonalizing the Hamiltonian.

3.2 Magnetic field effects

The presence of a magnetic field introduces a term coupling the magnetic moment of the atom with the external magnetic field. This is often called the Zeeman effect and for weak magnetic fields can be written in terms of the magnetic dipole moment, $\vec{\mu}$ of the atom as:

$$\mathscr{H}_B = -\vec{\mu} \cdot \vec{B}_{\text{ext}}. \tag{3.11}$$

A rough estimate for the scale of this interaction can be found by using the Bohr magneton $\mu_B = 1.4\,\text{MHz/G}$ and a typical magnetic field in our experiment $B_{\text{ext}} \sim 2\,\text{G}$. This leads to an energy scale of $E_B/h \sim 2.8\,\text{MHz}$. Since this is smaller than the scale of the hyperfine interaction, F and M_F will continue to be used as good quantum numbers and each hyperfine manifold, defined by a constant F, will be treated independently.

3.2.1 Aligned field

If the applied magnetic field is restricted to lie entirely along one axis, defined as $\hat{z}$, equation 3.11 reduces to

$$\mathscr{H}_{B_z} = -\mu_z B_z. \tag{3.12}$$

An atom or particle's magnetic moment is related to its angular momentum quantum numbers through its g-factor. In the case of the electron's spin, $\vec{\mu}_S = -g_s \mu_B \vec{S}$ where $g_S = 2.002319$ and in the case of its orbital motion: $\vec{\mu}_L = -g_L \mu_B \vec{L}$ with $g_L = 1$. Since $g_L \neq g_S$, the combined magnetic moment will not lie in the direction of $\vec{J}$, but will precess around it. However, the components of $\vec{\mu}_J$ perpendicular to $\vec{J}$ will average to zero and therefore, effectively $\vec{\mu}_J \parallel \vec{J}$. Therefore, we can write

$$\vec{\mu} = -\mu_B(g_L\vec{L} + g_S\vec{S}) \overset{ave}{=} -g_J\mu_B\vec{J} \tag{3.13}$$

where the last equality requires averaging over the perpendicular components. A straightforward derivation of g_J, the Landé g-factor, is given in Chapter 4 of [77] and the result is

$$g_J = g_L\frac{J(J+1) + L(L+1) - S(S+1)}{2J(J+1)} + g_S\frac{J(J+1) + S(S+1) - L(L+1)}{2J(J+1)}. \tag{3.14}$$

Additionally, the nuclear spin contributes to the magnetic moment with $\vec{\mu}_I = +g_I\mu_N\vec{I}$ where the g-factor has been measured as $g_I = 0.2029$ in ^{37}K [41]. Also note that the sign is opposite to that in $\vec{\mu}_L$ and $\vec{\mu}_S$. Furthermore, the Bohr magneton has been replaced by the nuclear magneton which is smaller by a factor of $m_e/m_N = 1/1846$. Therefore, this effect on the overall g-factor is quite small, although I will include it for completeness. Including this effect, the magnetic moment of the atoms is

$$\vec{\mu} = -g_F\mu_B\vec{F} \tag{3.15}$$

where g_F is given by the same formula as equation 3.14 with the substitutions $J \to F$, $L \to J$, $S \to I$, $g_L \to g_J$, and $g_S \to -g_I$. Therefore, the Hamiltonian arising from an aligned magnetic field is

$$\mathscr{H}_{B_Z} = g_F\mu_B B_z F_z. \tag{3.16}$$

This demonstrates that the $|F, M_F\rangle$ basis states remain eigenstates of the system with Zeeman energy levels given by

$$E_B = g_F\mu_B B_z M_F. \tag{3.17}$$

In addition to lifting the degeneracy of the $|F, M_F\rangle$ states, an external magnetic field modifies the Clebsch-Gordon coefficients connecting the $|F, M_F\rangle$ and $|M_I, M_J\rangle$ basis in Equation 3.10. However, the $|F, M_F\rangle$ states remain eigenstates of the atomic Hamiltonian. In the following, a transverse magnetic field will be considered which has the effect of mixing $|F, M_F\rangle$ states.

3.2.2 Transverse magnetic field

In the previous section, I assumed that the $\hat{z}$ axis was arbitrary and oriented it to align with the total magnetic field. While this is an acceptable approach, it will be more convenient when calculating P and T to fix the $\hat{z}$ axis along the direction of propagation of the laser light. In this case, an arbitrary external magnetic field can be represented as the sum of an aligned component ($\hat{z}$) and a transverse component defined to lie along the $\hat{x}$ axis:

$$\vec{B}_{\text{ext}} = B_z\hat{z} + B_x\hat{x}. \tag{3.18}$$

Note that I do not need to consider a $\hat{y}$ component because, although the $\hat{z}$ direction is fixed, the $\hat{x}$ direction is still arbitrary. Classically, a transverse magnetic field will cause the total magnetic moment $\vec{\mu}$ to precess around the total magnetic field $\vec{B}_{\text{ext}}$ at the Larmor frequency. Quantum mechanically, we must consider an additional term in the atomic Hamiltonian, following closely the work in Ref. [78].

$$\mathscr{H}_{\mathscr{B}} = g_F\mu_B B_x F_x. \tag{3.19}$$

The constants have been defined in the previous section and in analogy with Eqs. 3.8 and 3.9a for the $\vec{I}$ and $\vec{J}$ spins, the F_x operator is defined as $\frac{1}{2}(F_+ + F_-)$. Since the raising and lowering operators have off-diagonal matrix elements in the $|F, M_F\rangle$ basis, these states are no longer true eigenstates of the system, but instead the exact eigenstates are linear superpositions of the $|F, M_F\rangle$ states. In the experiment, $B_x \ll B_z$ and each superposition is dominated by a particular $|F, M_F\rangle$ sublevel. Therefore, these states remain *approximately* eigenstates. The full effect of B_x on the Clebsch-Gordon coefficients is considered when calculating the nuclear polarization and alignment terms. However, when calculating the transition rates in Sec. 3.5, I ignore this effect and treat the $|F, M_F\rangle$ as the good eigenstates. This approach is justified considering that the c_k in Eq. 3.10 change by at most 9×10^{-4} in the presence of the small transverse magnetic fields used here. This demonstrates that the true eigenstates are very nearly equivalent to the $|F, M_F\rangle$ levels, and that any correction to this, which depends on the *square* of the c_k coefficients, is completely negligible.

3.3 Interaction with a radiation field

The quantum nature of the atomic structure implies that an atom will only absorb a photon if the energy of the photon, $\hbar\omega_L$, equals the energy difference between the discrete atomic levels, $\hbar\omega_0$. In practice, the laser light is not entirely monochromatic. Furthermore, excited levels in the atom have a natural linewidth given by $\hbar/\tau$ with τ the lifetime of the excited state. Therefore, qualitatively the energy of the γ need not exactly equal $\hbar\omega_0$, but an atom will have a higher probability of absorbing a photon as $\delta = \omega_L - \omega_0 \to 0$. Furthermore, when absorbing a photon, the atom also absorbs its angular momentum. Since the photon has spin $\hbar$, the projection of this angular momentum along the photon's direction of travel must be $0, \pm\hbar$. In order to absorb a photon, the atom must have an excited state with the appropriate spin quantum numbers to satisfy angular momentum conservation.

Upon absorption, the momentum of the photon, $h\nu/c$ is transferred to the atom. With typical wavelengths, this momentum, $p_\gamma \approx 2\,\mathrm{eV/c}$, is small compared to the momentum of a K atom in our magneto-optical trap: $p_{\mathrm{K}} \approx 114\,\mathrm{eV/c}$. Although the absorption of a photon produces only a small change in the atom's momentum, the absorption of *many* photons can be used to control the momentum of the atom. This is the principle of the magneto-optical trap described in the next section: the repeated absorption of laser light leads to an observable, and useful, change in the atom's momentum, allowing it to be cooled an trapped.

3.4 Magneto-optical traps

The Nobel Prize was awarded in 1997 to Steven Chu, Claude Cohen-Tannoudji, and William D. Phillips "for development of methods to cool and trap atoms with laser light." [79]. Today, magneto-optical traps are used in a variety of applications including ultra-precise atomic clocks, quantum information processing, and β-decay correlation studies. Using six pairs of counter-propagating laser beams and a quadrupole magnetic field, MOTs can effectively confine and cool neutral atoms. Since these techniques were not a focus of this work, I will only give a general description of the main features of a MOT. A more thorough description is given, for example, in Ref. [80].

A neutral atom in a radiation field will feel a radiation pressure due to the scattering of photons. As described in the previous section, this requires the absorption of a large number of photons. To trap *and* cool the atoms requires both a position dependent force (for trapping) and a velocity dependent force (for cooling). In order to arrange for a large number of transitions, the atoms are pumped on the D_2 cycling ($s_{1/2} \rightarrow p_{3/2}$) transition from $F = 2 \rightarrow F' = 3$ (see Fig. 3.1). From the $F' = 3$ excited state, angular momentum selection rules require that they decay back to the $F = 2$ ground state, allowing the atom to absorb another photon, completing the cycle. Here I will describe first the velocity dependent drag force and then the position-dependent trapping force.

3.4.1 Drag potential - Doppler cooling

The scattering rate grows as ω_L is tuned closer to the atomic resonance frequency ω_0 or equivalently when the detuning $\delta = \omega_L - \omega_0$ is small. Consider a laser that is detuned to the red (longer wavelength) compared to the resonance frequency of the atoms. Atoms that are moving *towards* the laser will experience a light of frequency *closer* to resonance due to the Doppler effect whereas atoms moving away from the laser see the light as being further from resonance. Therefore, atoms moving towards the laser will experience a larger radiation pressure than atoms moving away from it. Arranging three sets of intersecting, counter-propagating beams creates a damping force in all directions, acting as an optical molasses. Assuming that the light intensity is low enough that stimulated emission can be safely ignored, the total force acting on the atoms is given by [80]:

$$\vec{F}_{OM} \approxeq \frac{8\hbar k^2 \delta (I/I_s)\vec{v}}{\gamma(1 + (I/I_s) + (2\delta/\gamma)^2)^2} \tag{3.20}$$

where k is the wave number of the laser, I is the intensity, $I_s = \frac{\pi h c \gamma}{3\lambda^3}$ is the saturation intensity, $\vec{v}$ is the velocity of the atom and γ is the transition linewidth. For a simple model of ^{37}K, the lowest temperature that can be reached (the “Doppler limit”) is $T_D = 150\,\mu\text{K}$, corresponding to a mean velocity of 32 cm/s. At this speed, the atoms escape the $\sim 3\,\text{mm}^3$ trapping region in 3 ms, demonstrating that the atoms still require a *position* dependent force in order to be considered trapped.

3.4.2 Trapping potential

To establish a position dependent force, the magneto-optical trap uses a linearly inhomogeneous magnetic field: $B = B(z) = Az$ such as that formed by flowing current in *opposite* directions through a pair of Helmholtz coils. For simplicity, I will describe the one dimensional case. In order to generalize to three dimensions, the following arguments apply individually in all three directions. Since the magnetic field grows linearly with position and changes sign at the origin, so does the magnitude of the Zeeman shift of the atomic sublevels.

In order to further simplify the description, I will describe the case of an atom with $I = 0$ such that the cycling transition goes $J_g = F_g = 1/2 \to J_e = F_e = 3/2$. This case is shown in Fig. 3.2. For $z > 0$, the $M'_J = -1/2$ and $M'_J = -3/2$ states are shifted lower in energy by the inhomogeneous magnetic field. Since $\omega_L < \omega_0$ in order to produce the optical molasses, the two states with $M_J < 0$ are moved *closer* to the transition frequency. Since at $z > 0$, these transitions require $\Delta M_J = -1$, the light incident from the right is circularly polarized with σ^- polarization. An atom located at $z < 0$, which has its $M_J = +1/2$ and $M_J = +3/2$ states shifted closer to the laser frequency, will not absorb photons incident from the right because there is no transition near resonance satisfying angular momentum conservation. Instead, light incident from the left is polarized σ^+ and drives transitions with $\Delta M_J = +1$. Therefore, an atom will always preferentially absorb a photon that pushes it back towards the center.

The case of ^{37}K with $I = 3/2$ involves two complications. First, the addition of more excited sublevels as well as multiple ground states ($M_F = -2, -1, 0, 1, 2$) complicates the simple picture described above but does not change the conclusion that for $z > 0$, σ^- transitions are preferred whereas the opposite is true for $z < 0$. Second, in addition to the $F' = 3$ sublevel used to trap the atoms, the finite linewidths of both the laser and atomic levels means that the $F' = 0, 1, 2$ levels can also be populated by the trapping laser and decay back to the $F = 1$ ground state, removing them from the cycling transition. Therefore, a second "repump" laser is put on resonance with the $F = 1 \to F' = 2$ transition to avoid losses due to this mechanism. For K isotopes in particular, the excited state hyperfine splitting is rather small and this repump laser is especially important. The trapping of K isotopes is described in Ref. [81] while the initial experiments trapping ^{37}K in particular are described in Ref. [14].

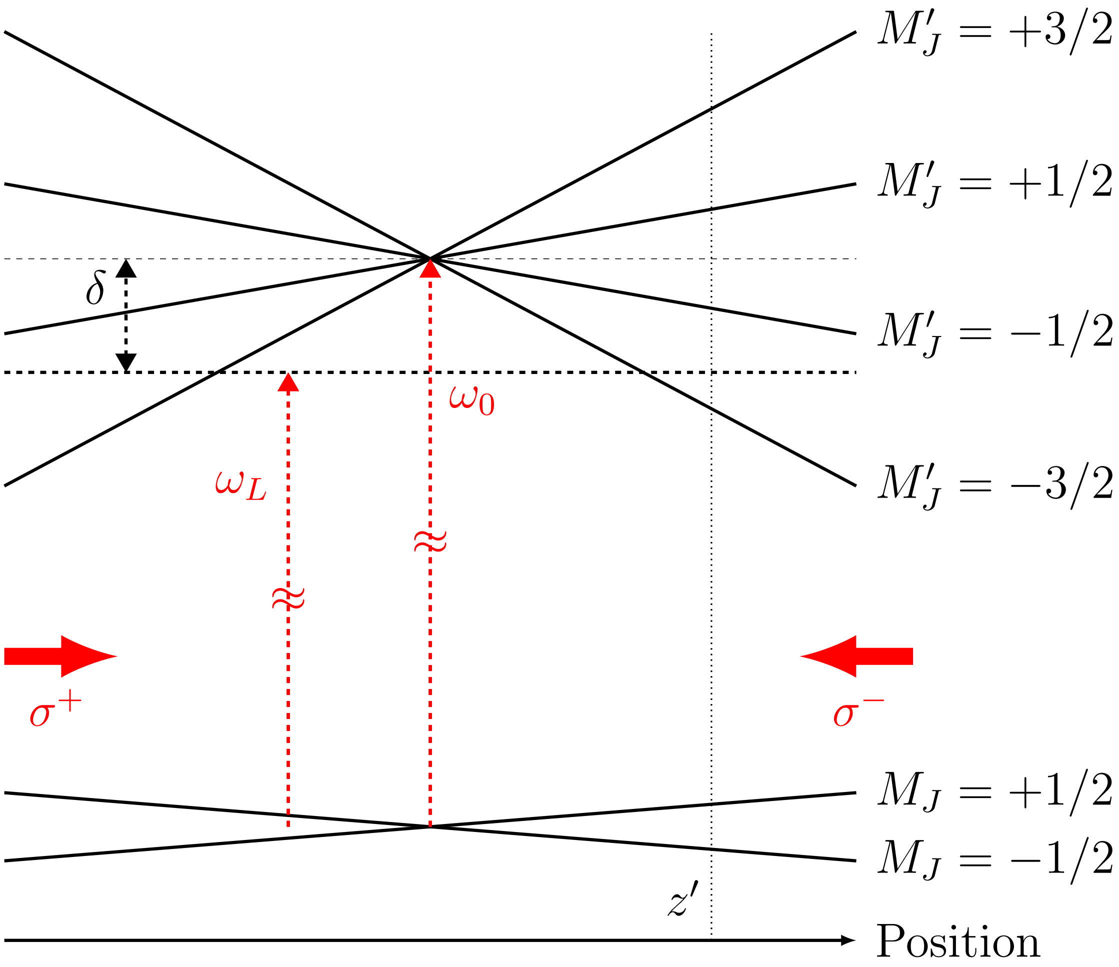

Figure 3.2: A simplified diagram showing the principle of MOT operation. With a linearly inhomogeneous magnetic field creating position-dependent Zeeman shifts, an atom with $z > 0$ will have its $M_J < 0$ levels shifted closer to resonance with the laser light with the $M_J > 0$ levels shifted further away. If σ^- light is incident as shown in the diagram, an atom will preferentially absorb light from this laser and be pushed back towards the center. For atoms with $z < 0$, the situation is reversed.

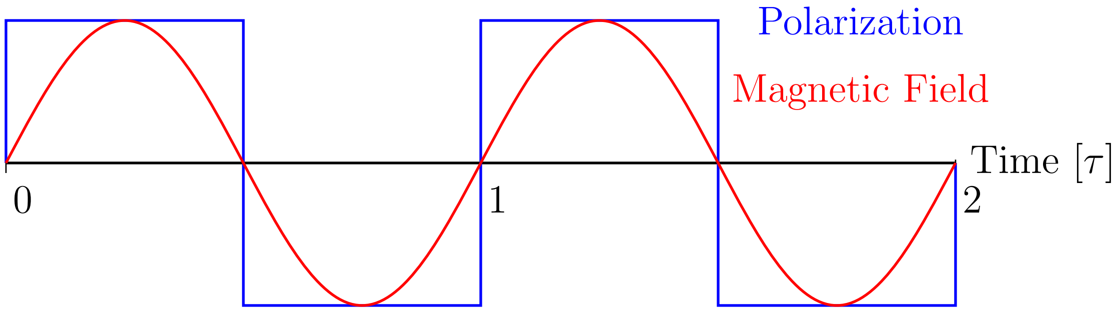

Figure 3.3: Principle of AC-MOT operation. In order to maintain a trapping force at all times in an AC-MOT, the laser polarization (blue) and magnetic field (blue) are kept in phase with one another. The transition to a uniform field for optical pumping is done when the magnetic field is close to off, which minimizes eddy currents.

3.4.3 The alternating-current MOT

To perform measurement with polarized atoms, the MOT must be switched off in order to allow for efficient optical pumping (see Sec. 3.5). While the MOT light is rapidly extinguished, we must also switch the magnetic field configuration from an anti-Helmholtz (quadrupole) arrangement to a Helmholtz (dipole) arrangement for a uniform magnetic field. In order to accomplish this switching as quickly as possible, we use an *alternating current* MOT (AC-MOT), named after the electrical current in the magnetic field coils [26].

In an AC-MOT, the quadrupole magnetic field varies sinusoidally as shown in Figure 3.3. In order to maintain a trapping force on the atoms at all times, the polarization of the light must be simultaneously varied with the same frequency as the magnetic field, which in our application was 699.3 Hz. Then, in order to minimize the residual magnetic field after shutting off the MOT, the current through the coils is shut off when the combined magnetic field is zero. The optimal shutoff phase is a function of chamber geometry and material, as well as the frequency of the AC current [26]. The demonstration of an AC-MOT in ^{41}K, which has a similar hyperfine structure as ^{37}K, is reported in Ref. [82].

3.5 Optical pumping

I now turn to a discussion of optical pumping (OP), which provides a method to selectively populate a desired Zeeman sublevel by illuminating the atomic cloud with polarized light. In this experiment, we have used circularly polarized light on the D_1 ($s_{1/2} \to p_{1/2}$) transition to select the $|F = 2, M_F = +2\rangle = |M_I = +3/2, M_J = +1/2\rangle$ or $|F = 2, M_F = -2\rangle = |M_I = -3/2, M_J = -1/2\rangle$ states. These sublevels, with $|M_F|$ at its maximum value, have a definite value for the $\hat{z}$-projection of the nuclear spin with $M_I = \pm I$ and therefore represent complete nuclear polarization with $P = +1$ and $P = -1$ (see Eq. 3.2).

The process of optical pumping can be visualized as a biased random walk along Zeeman sublevels. To take a concrete example, consider a ^{37}K atom with $M_F = 0$. When this atom absorbs a photon on resonance with a transition to the $p_{1/2}$ state with circular polarization and therefore angular momentum $+\hbar$, it must transition to an excited state with $M_F = +1$. Once there, the atom is free to decay by stimulated emission back to its original $M_F = 0$ state or to spontaneously decay. This spontaneous decay can occur with the emission of a photon of *any* polarization leaving the atom with $M_F = 0$, $+1$, or $+2$. In the experiment, the laser powers used were such that the rate of stimulated emission was much less than that of spontaneous emission. The process of excitation by a polarized photon followed by de-excitation primarily by spontaneous emission is repeated until the atom is in the ground state with $M_F = +2$. At this point, there is no excited state near resonance with $M_F = +3$ and the atom can no longer absorb the light. Therefore, once in this extreme or "stretched" state, the atom remains there.

To determine the nuclear polarization to the required precision, we monitor the total $p_{1/2}$ population of the atoms by photoionizing atoms in this state using UV light at 355 nm from a pulsed laser at 10 kHz repetition rate. These photons do not have the energy necessary to photoionize atoms in the ground state. We apply a uniform electric field which sweeps the photoions onto a microchannel plate where they are observed in coincidence with the UV light.

As atoms accumulate in the fully polarized, stretched state, they can no longer absorb the optical pumping light and the population of atoms in the $p_{1/2}$ manifold decreases as does the rate of photoionization as seen in Fig. 3.4. Therefore, the photoionization rate is a direct probe of the net *unpolarized* population of the atoms.

However, the photoionization rate has no sensitivity to the sublevel distribution of the unpolarized population among the various $s_{1/2}$ ground states. Although the total unpolarized population can be made quite small, the precision measurement described here requires knowledge of its distribution. There have been methods developed to probe this directly [83–85], but the specific constraints of our experiment make these impractical. The number of trapped atoms is limited to $< 10^4$ primarily by the flux of ^{37}K delivered by ISAC and the collection efficiency in the first MOT (0.1%). Additionally, the polarization measurement must be non-destructive, preserving the polarization of the atoms in order to observe the β-asymmetry in the nuclear decay.

To satisfy these requirements, we adopt the method of monitoring the $p_{1/2}$ population with photoionization as described above and modeling the sublevel distribution of the partially polarized atoms. The $p_{1/2}$ population, inferred from the photoionization measurement, is directly proportional to the total partially polarized population, and the theoretical model must only determine the sublevel distribution of this relatively small population. To describe this numerical model, I first describe the rate equation approach, which gives a simple intuitive picture before turning to the density matrix description.

3.5.1 The rate equations - an intuitive picture

The sublevel populations can be modeled phenomenologically by using and quantifying the picture described above. The population change for each state is the sum of changes from three physical processes: stimulated absorption, stimulated emission, and spontaneous decay. Although this model is not used in the analysis, it provides an intuitive picture of the process, gives similar results to the more accurate density matrix model described below, and introduces much of the terminology.

The rate of spontaneous decay from an excited $|F', M'_F\rangle$ state to a ground state $|F, M_F\rangle$ is proportional to the spontaneous emission rate: $\gamma = 1/\tau$ and the matrix element connecting them via the emission of a photon [86]:

$$a_{F,m_F \to F',m'_F} = e \langle f | \, \hat{\epsilon}_q \cdot \vec{d} \, | i \rangle \, . \tag{3.21}$$

Here, $\vec{\hat{\epsilon}}_q$ is the polarization of the emitted or absorbed photon and I use the convention that $q = -1, 0, 1$ is the angular momentum of the photon in units of $\hbar$. In the case

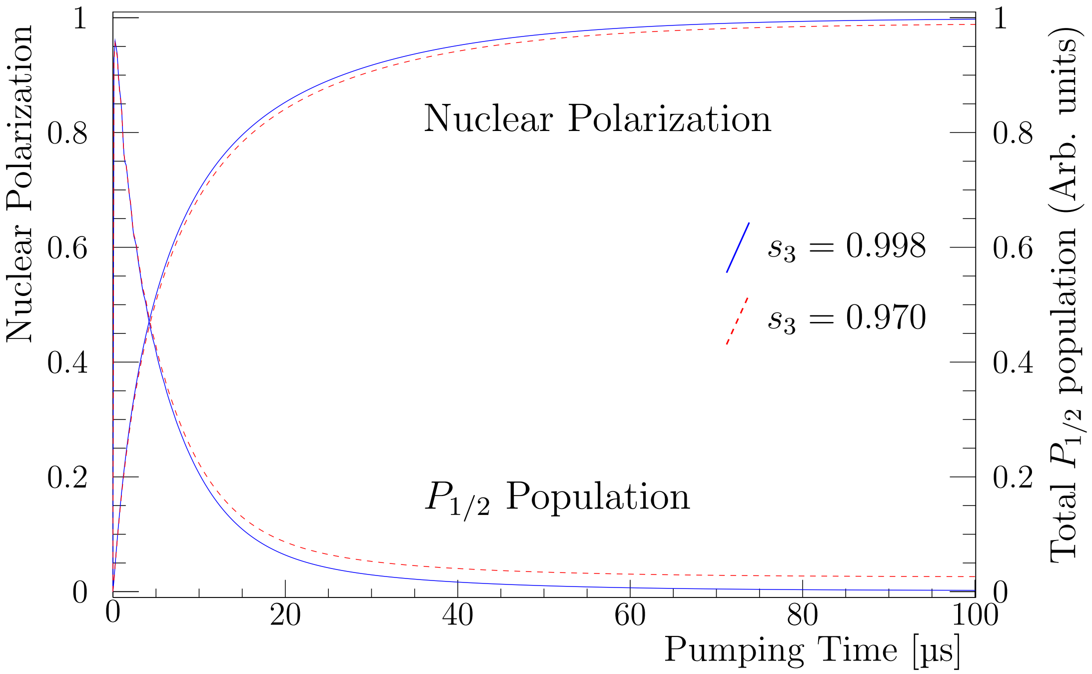

Figure 3.4: Principle of optical pumping measurement. Simulated time evolution of optical pumping with $\sigma^{\pm}$ light on the D_1 transition. The photoionization is observed and used to infer the nuclear polarization by comparing to a numerical simulation of optical pumping. As the rate of photoionization in the region $t \to \infty$ decreases, the degree of polarization increases towards unity. The atoms are considered fully polarized after the optical pumping light has been on for 100 µs (see Ch. 5). The parameter s_3 gives the degree of circular polarization of the OP light. The nuclear alignment term follows the same measurement strategy.

of spontaneous decay, q can take on any of these values as the polarization of the emitted photon is arbitrary. The quantity $\vec{d}$ gives the electric dipole moment of the atom whereas $\langle f|$ and $|i\rangle$ give the final and initial atomic wavefunctions. This term is evaluated by considering the atomic ($\vec{J}$), electron ($\vec{S}$), and nuclear ($\vec{I}$) angular momenta as well as the polarization of the photon, and the result is [18, 80]

$$
\begin{aligned}
a_{F,m_F\rightarrow F',m'_F} &= e(-1)^{1+L'+S+J+J'+I-M'_F} \times \sqrt{(2J+1)(2J'+1)(2F+1)(2F'+1)} \\
&\times \begin{Bmatrix} L' & J' & S \\ J & L & 1 \end{Bmatrix} \times \begin{Bmatrix} J' & F' & I \\ F & J & 1 \end{Bmatrix} \times \begin{pmatrix} F & 1 & F' \\ M_F & q & -M'_F \end{pmatrix} \times \langle f|\,|d|\,|i\rangle\,. \qquad (3.22)
\end{aligned}
$$

The terms in curly braces are known as Wigner 6-j symbols and the term in parentheses is the Wigner 3-j symbol; both are described in detail in Ref. [87] and can be calculated using numerical libraries such as Ref. [76]. Primed quantum numbers refer to the excited state while unprimed quantum numbers to the ground state. The reduced matrix element $\langle f|\,|d|\,|i\rangle$ arises from the radial part of the dipole matrix element, and, because it only depends on the principal quantum number n, only enters as a normalization constant. Note that the selection rules for the 3-j and 6-j symbols given in [87] imply that $M_F + q = M'_F$, conserving angular momentum, and $F - 1 \leq F' \leq F + 1$, as expected from any coupling of angular momenta.

Now considering the case of stimulated emission and absorption, I first note that the decay constant for these processes is the same for a given pair of sublevels.

$$
W_{F,m_F\rightarrow F',m'_F} = W_{F',m'_F\rightarrow F,m_F} = \frac{3\lambda^3\mathcal{I}_L}{8\pi hc} A_{F,m_F\rightarrow F',m'_F} \times \int_{-\infty}^{+\infty} g_{F,m_F\rightarrow F',m'_F}(\nu)\rho_L(\nu)d\nu. \qquad (3.23)
$$

Here, λ is the laser wavelength, $\mathcal{I}_L$ the laser intensity, and $A_{F,m_F\rightarrow F',m'_F} = a^2_{F,m_F\rightarrow F',m'_F}/\tau$ is the *spontaneous* transition rate calculated in Eqs. 3.21 and 3.22. The integral on the right side represents the overlap of the atomic lineshape, $g(\nu)$, and the laser lineshape, $\rho_L(\nu)$. Taking both of these to be Lorentzians with FWHM of 2γ and $2\gamma_L$, the result of the integral is [88]

$$
\frac{1}{\pi}\frac{\gamma + \gamma_L}{(\nu_L - \nu_{F,m_F\rightarrow F',m'_F})^2 + (\gamma + \gamma_L)^2}. \qquad (3.24)
$$

The laser frequency is defined as ν_L and $\nu_{F,m_F \to F',m'_F}$ is the frequency difference between the two atomic levels.

For the stimulated processes the polarization of the photon is derived from the electric field $\vec{E}$ of the (circularly polarized) laser light. For light that has perfect right-handed circular polarization, $q = +1$, while left-handed circular polarization has $q = -1$. Although the light in this experiment is highly polarized, it does contain a small component of the "wrong" polarization. I quantify the polarization using the parametrization in terms of the normalized Stokes parameters as defined in [89]. In the circular basis, with unit vectors $\vec{\epsilon}_\pm$, the relevant parameter is s_3 quantifying the degree of circular polarization:

$$s_3 = \frac{\mathcal{I}_+ - \mathcal{I}_-}{\mathcal{I}_+ + \mathcal{I}_-} = \frac{|\hat{\epsilon}^*_+ \cdot \vec{E}|^2 - |\hat{\epsilon}^*_- \cdot \vec{E}|}{|\hat{\epsilon}^*_+ \cdot \vec{E}|^2 + |\hat{\epsilon}^*_- \cdot \vec{E}|}. \tag{3.25}$$

We measure s_3 independently for each polarization state to determine $\mathcal{I}_+$ and $\mathcal{I}_-$, the laser intensity in the σ^+ and σ^- states, separately. Therefore I calculate the contribution separately for Eq. 3.23 with $q = +1$ and $q = -1$ weighted by the respective powers.

Combining the simulated and spontaneous processes, I obtain the rate equations for the population of each sublevel:

$$\frac{dN_{F',m'_F}}{dt} = -\gamma N_{F',m'_F} + \sum_{F,m_F,q} W_{F,m_F \to F',m'_F} \left(N_{F,m_F} - N_{F',m'_F}\right) \tag{3.26a}$$

$$\frac{dN_{F,m_F}}{dt} = +\gamma \sum_{F',m'_F,q} a^2_{F,m_F \to F',m'_F} N_{F',m'_F} - \sum_{F',m'_F,q} W_{F,m_F \to F',m'_F} \left(N_{F,m_F} - N_{F',m'_F}\right). \tag{3.26b}$$

The population of the $|F, M_F\rangle$ is given by N_{F,m_F} where the primes indicate an excited ($p_{1/2}$) state. The first term represents spontaneous emission, with the rate defined by $\gamma = 1/\tau$, and the second term combines stimulated and spontaneous emission. Although formally, the sum in the stimulated emission and absorption terms goes over $q = -1, 0, +1$. Each term must use the power in the corresponding polarization state: $\mathcal{I}_+$ for $q = 1$ and $\mathcal{I}_-$ for $q = -1$, and we assume there is no light with $q = 0$.

3.5.2 Density matrix

The above rate equation picture of optical pumping is entirely phenomenological in nature and essentially classical. Although it does a remarkably good job of reproducing experimental data, I present here a more accurate model treating the atoms as a statistical ensemble. The dynamics of the laser-atom system, for a statistically large ensemble of atoms, can be described by the density matrix formalism, which will only be briefly sketched here. These results are found in many textbooks including [90]. Consider an ensemble of $\mathscr{N}$ identical systems. The wavefunction of the kth system can be written in terms of the Φ_n eigenstates as

$$\Psi^k(t) = \sum_n a_n^k(t)\Phi_n. \tag{3.27}$$

In this way, the time evolution of the system is contained in the time evolution of the coefficients $a_n^k(t)$. Physically, $|a_n^k(t)|^2$ represents the probability of finding system k in state Φ_n at time t. I define the density operator $\hat{\rho}$ through its matrix elements:

$$\rho_{mn}(t) = \frac{1}{\mathscr{N}} \sum_{k=1}^{\mathscr{N}} a_m^k(t) a_n^{k*}(t). \tag{3.28}$$

The matrix element represents the quantum mechanical and statistical average of the quantity $a_m^k(t)a_n^{k*}(t)$ over the sample. In particular, the diagonal elements $\rho_{nn}(t)$ represents the probability of finding a randomly chosen sample in state Φ_n at time t. Similarly, the off-diagonal element $\rho_{mn}(t)$ represents the quantum mechanical coherence between states Φ_m and Φ_n at time t. The expectation value of an operator $\hat{\mathcal{O}}$ is given by:

$$\langle \mathcal{O} \rangle = \mathrm{Trace}(\hat{\rho}\hat{\mathcal{O}}). \tag{3.29}$$

This equation is used to calculate the nuclear polarization and alignment, equation 3.2, once the density matrix is evaluated. The time evolution of the density matrix describing optical pumping is evaluated using the quantum analog of Liouville's equation with the addition of spontaneous emission described phenomenologically by $R(t)$:

$$i\hbar\dot{\hat{\rho}} = [\hat{\mathscr{H}}, \hat{\rho}] + R(t). \tag{3.30}$$

The Hamiltonian, including the fine, hyperfine, and Zeeman terms, has been described beginning in Sec. 3.1, and we use the expressions for the interactions with two finite-linewidth laser fields from Tremblay and Jacques [91]. We extend their expressions to include the effects of two counter-propagating beams. Because both of our frequencies, one driving $F = 1 \rightarrow F' = 2$ and the other driving $F = 2 \rightarrow F' = 2$, come from one laser, then are frequency shifted by an independent RF source into two frequencies, we assume as in [92] that the contribution of the laser linewidth to the ground-state relaxation rate vanishes. We observed short timescale jitter of several hundred hertz in the RF sources and have, therefore, included a 500 Hz linewidth from RF sources in the ground-state relaxation rate (see [91], equation 2.37). The external B field is included in Zeeman shifts of the magnetic sublevels. Primarily, we consider an isotropic initial ground-state distribution, but also consider an initial anisotropy as a systematic uncertainty. The calculation was carried out by numerically solving the density matrix equations, i.e., the 128 complex coupled differential equations of the 16-level system of Fig 3.1 with the result compared to the experimental data in Sec. 5.4.5. Additionally, an arbitrary transverse magnetic field B_x, which can drive transitions with $\Delta F = 0$, $\Delta m_F = \pm 1$, is included using the expressions in [78].

By treating the atoms quantum mechanically, the density matrix approach includes purely quantum effects not included in the classical rate equations. Most importantly, this approach accounts for the possible existence of coherently trapped populations. This effect has been studied for many years [93] and is present when two correlated laser beams have an energy difference equal to the energy difference between two atomic levels: $\Delta E = h(\nu_1 - \nu_2)$ where ν_i is the frequency of the ith optical pumping frequency. Atoms can be put into a superposition of the two atomic levels that does not absorb the laser light. By not absorbing the optical pumping light, this exactly mimics our experimental signature (decrease in photoionization rate) without polarizing the atoms. The approach here describes them naturally as the off-diagonal elements of the density matrix.

In summary, the process of optical pumping can be visualized as a biased random walk towards the Zeeman sublevel with maximum projection of total momentum and described rigorously through the density matrix. This model accounts for the electron's orbital and intrinsic angular momentum, interactions with an arbitrary magnetic field, the coupling of atomic and nuclear angular momentum, the interaction with a laser field, and includes spontaneous decay phenomenologically. This section has described optical pumping as well the numerical model I have used to simulate this process; in Ch. 5 I will apply this model to extract the nuclear polarization and alignment from the experimental data.

4. EXPERIMENTAL OVERVIEW

4.1 Apparatus

The experiment described in this thesis took place between May 22 and June 14, 2014. However, due to instabilities in the detector systems, the data presented here was collected starting on June 9. As described in Ch. 1, ^{37}K atoms were confined in an AC-MOT near the center of the the measurement chamber. The center of the chamber defines the origin of the coordinate axes. The detector geometry in the $\hat{y}$-$\hat{z}$ plane is shown in Fig. 1.4 and in 3-D in Fig. 4.1.

When interacting with the atoms, the optical pumping light propagates along the $\hat{z}$-axis, and this defines the polarization axis. Since the β-detectors are opaque and placed along the polarization axis, the light is brought in at a 19° angle with respect to the $\hat{z}$-axis and reflected off of a thin mirror. The mirror is a 275(5) µm thick SiC substrate coated with a commercial dielectric stack. The mirror is fixed to the vacuum chamber by a stainless steel collimator/mirror mount. The collimator is a total of 13.2 mm thick with a $31 \times 31\text{mm}^2$ center opening. The β-detectors are separated from the vacuum ($\lesssim 10^{-8}$ torr) by a 229 µm ± 10% thick Be window.

Behind this thin window, and placed at both $\pm z$, are the main nuclear detectors. Along each axis, a Si-strip detector provides ΔE and position information while a plastic scintillator fully stops the β^+ and records the full energy. The silicon detectors are manufactured by Micron Semiconductors Ltd. and are model number BB1. Each detector has an active are of $40 \times 40\,\text{mm}^2$ and is nominally 300 µm thick. These double-sided silicon-strip detectors (DSSSD) are segmented on each side into 40 strips, each 1 mm wide. The charge is collected on both faces of the detector with strips arranged in perpendicular directions on the two faces allowing for a measurement of the $\hat{x} - \hat{y}$ position event-by-event.

Each plastic scintillator is made of BC408 ($\rho = 1.032\,\text{g/cm}^3$, H/C=1.11) and is 35 mm thick as shown in Fig. 4.2. The light output is collected in a ET Enterprises 9823B photo-multiplier tube (PMT) with entrance-window ⌀130 mm where the scintillation light is converted into an electric current and recorded by pulse-processing electronics. Since the PMT is sensitive to the AC magnetic fields of the MOT, which are significant at the scintillator's location, a 200 mm light-guide transports the light

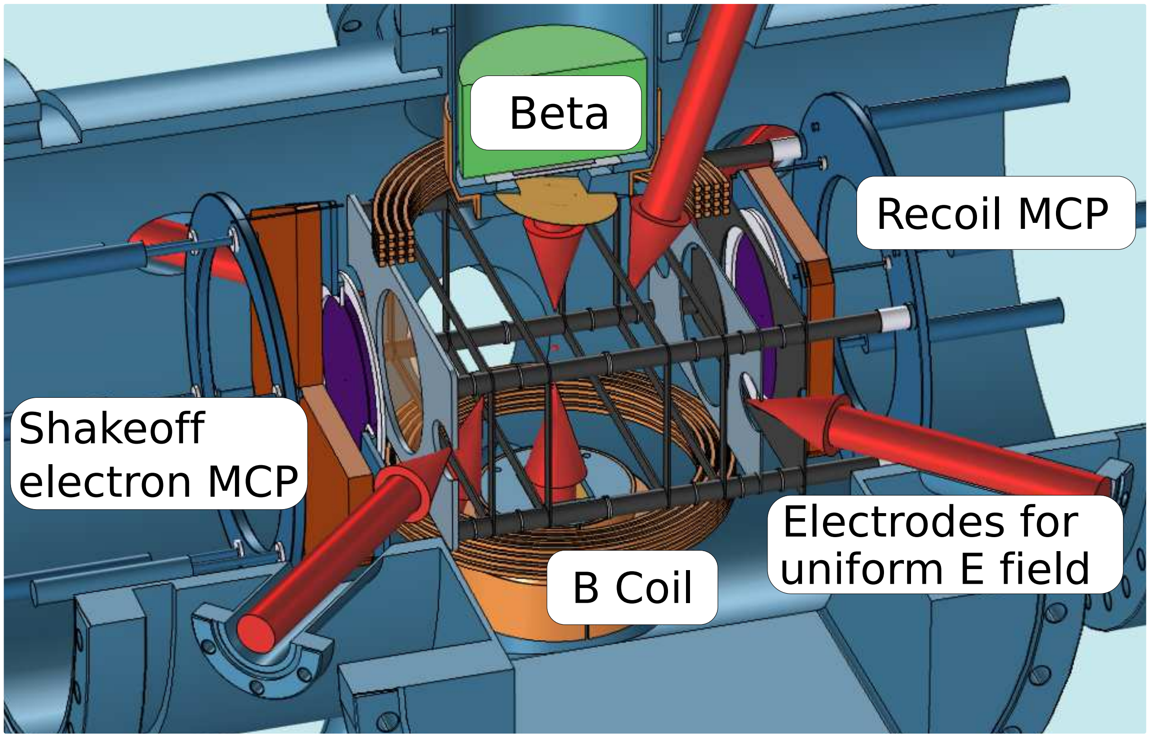

Figure 4.1: Trinat detector layout in measurement chamber. The β-detectors lie along the polarization axis, while the uniform electric field sweeps the charged low-energy products (photoions, photoelectrons, shakeoff electrons, and nuclear recoils) onto a pair of microchannel plate detectors.

.

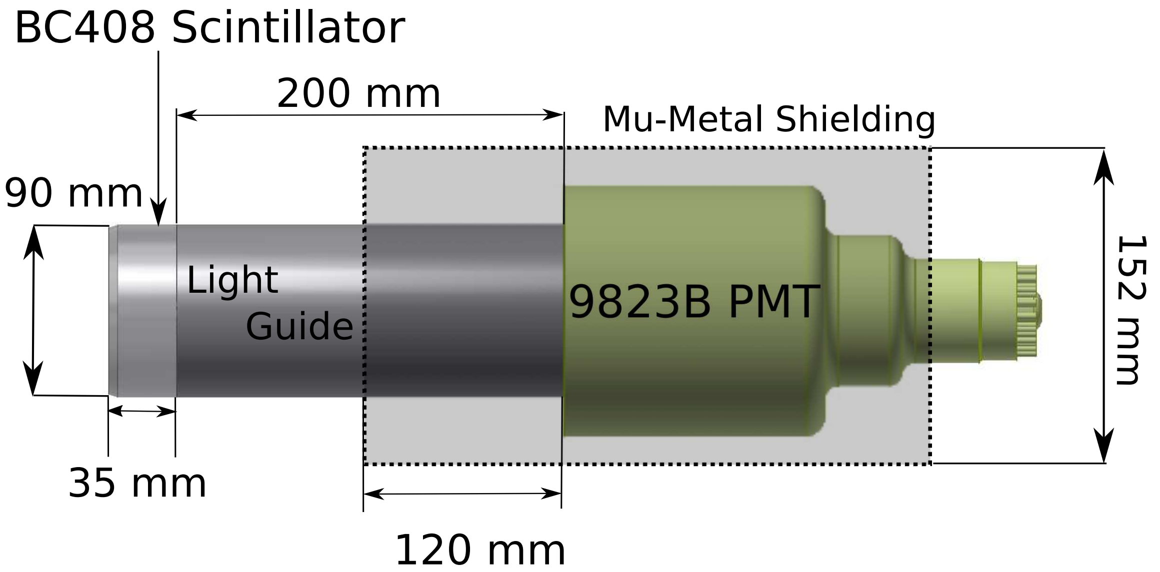

Figure 4.2: Diagram of plastic scintillator, light-guide and PMT readout. The light-guide and mu-metal shielding mitigate the effects of the AC-MOT on the gain of the PMT. The scintillator is thick enough to completely stop the 5.1 MeV β^+s from ^{37}K decay.

to the PMT and allows the PMT to be placed further back from the magnetic field region. Additionally, the PMT is surrounded by mu-metal shielding to further reduce the effects of the AC magnetic field. To prevent losses from the light-guide, it and the scintillator are wrapped in a 3M-ESR reflective sheet. The "front-face" of the scintillator, on the left in Fig. 4.2, is covered in one layer of commercial Teflon tape. This wrapping is thinner than the wrapping on the side, minimizing the energy loss of the β^+, while maintaining good reflective properties. The gain of each plastic scintillator is continuously monitored with a gain-stabilized LED emitting pulses at a repetition rate of 70 Hz. The amplitude of these pulses are well separated from the β-decay spectrum and the LED pulses are tagged in the data acquisition so that they can be completely excluded from the physics analysis.

Along the $\hat{y}$-axis, there are a series of electrostatic hoops that generate a uniform electric field. These hoops are the same as used in our 2012 experiment [25]. Note that, of the seven total hoops, five are made of glassy carbon ($\rho = 1.5\,\mathrm{g/cm^3}$) while the remaining two are made from Grade 5 Ti ($\rho = 4.45\,\mathrm{g/cm^3}$).

At the negative end of the eclectic field, we place a microchannel plate designed to detect primarily electrons from the photoionization of ^{37}K or following a β-decay. Hence, this detector is termed the electron MCP (eMCP). The eMCP has a diameter of 86.6 mm, an active area diameter 75 mm, and is 1 mm thick and made of nickel-coated lead glass ($\rho = 6.62\,\mathrm{g/cm^3}$). It is placed 100 mm from the center of the chamber. An array of 27.5 µm diameter channels, with a center-to-center spacing of 31 µm is etched through the plate at an angle of 20°. When an electric field of 1000 V is applied between the two sides of the MCP, each channel acts as an electron multiplier with a gain of $> 8 \times 10^3$. In order to achieve higher gain, a series of three MCP are arranged in the Z-stack configuration, with each plate's channels opposed to the previous plate such that the channels form a "Z" when viewed from the side. A small gap in between each plate allows the charge to spread out and activate multiple channels on the following plate, therefore reducing gain saturation effects. In this configuration, the MCP assembly achieves a gain of $10^{10} - 10^{12}$.

In order to obtain position information, we use a three-layer delay-line anode (hexanode). This consists of three wires wound at 60° to one another around an insulating ceramic core as shown in Figure 4.3. As the charged particle cloud exits the final MCP stage and passes through this array, it induces a signal in each wire. This current travels in both directions along the wires and is amplified and detected at both ends. The relative timing of the two ends of a single delay-line encodes the position information perpendicular to the direction of winding. The position can be determined from any two delay-lines. The addition of the third layer allows us to distinguish the position of multi-hit events or alternatively to reconstruct an event with incomplete position information [94, 95], the details of which will be given in Ch. 7.

On the positive end of the electric field, placed 104.1 mm from the center of the chamber, is the recoil MCP stack (rMCP). In this work, its role is to detect photoions originating from the trapping region and accelerated by the electric field. This is used to both to image the trap as well as to measure the polarization. The operation of this detector is identical to the eMCP detector. However, it is operated in the chevron configuration, with only two plates in the stack. The first plate is 0.6 mm while the second plate is 1.5 mm thick. This detector is backed by a two-layer delay-line anode for position sensitivity with the two wires wound at 90° to one another. Therefore, both the eMCP and rMCP provide precise timing and position information event-by-event.

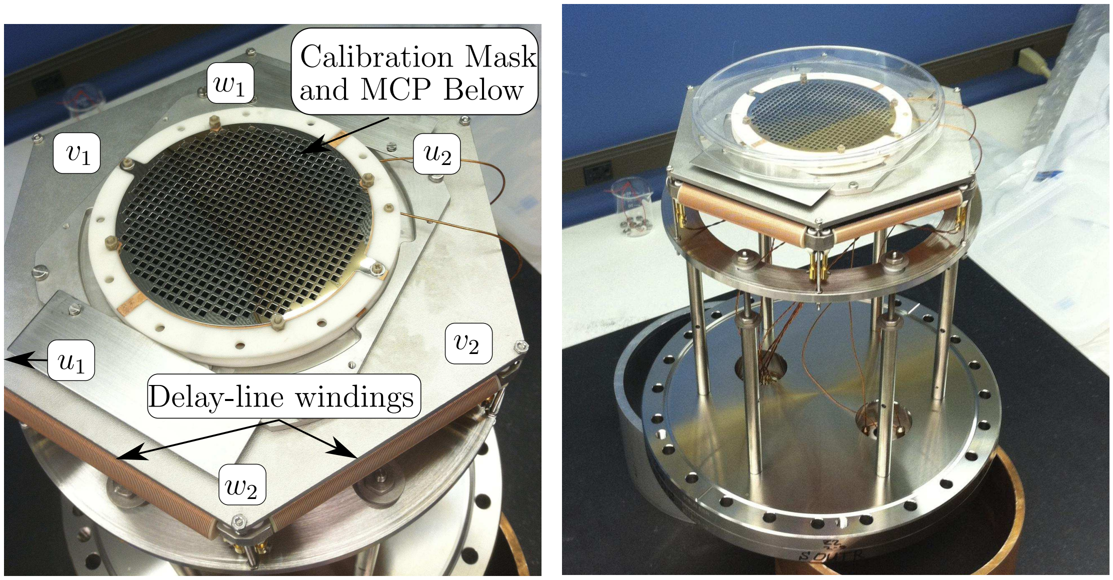

(a) HEX75 layout (b) Full assembly

Figure 4.3: HEX75 delay-line anode layout. The eMCP detector uses a hexanode configuration with three pairs of delay-lines (labeled u, v, and w) to determine the position of an event. The mask is used for position calibration and is removed before collecting data with ^{37}K.

4.2 Duty cycle

Recalling from Sec. 3.4 that a MOT requires a quadrupole magnetic field as well as $\sigma^+ - \sigma^-$ lasers tuned to the D_2 transition and from Sec. 3.5 that optical pumping requires a dipole magnetic field with $\sigma^+ - \sigma^+$ lasers on the D_1 transition, it is clear that we cannot trap and polarize the atoms simultaneously. This section will describe and motivate the duty cycle we have used to accommodate both a MOT and optical pumping.

First, note that both the ion beam as well as the collection MOT (See Fig. 1.3) operate continuously. Schematically, the sequence in the main detection chamber goes as follows:

1. With the MOT in direct current (DC) mode and ready to receive atoms, the pulsed "push beam" laser moves atoms from the collection to the measurement MOT

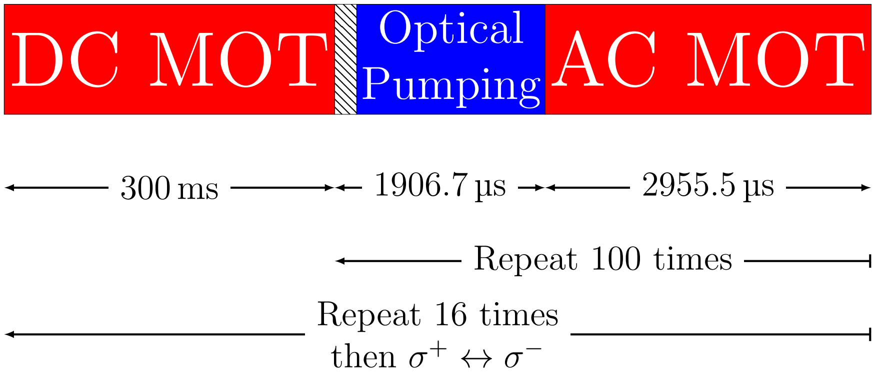

Figure 4.4: The atomic duty cycle for the TRINAT experiment. During the portion of time labeled DC MOT, the atoms are pushed from the first trap by a pulsed laser beam. During the cross-hatched region there is neither optical pumping nor MOT light entering the chamber while. This is done to allow the magnetic field, which must be switched from the quadrupole to a dipole configuration during this time, to stabilize for better optical pumping.

2. The measurement MOT operates in DC mode for better collection efficiency and cooling
3. Complete 100 cycles of:
    (a) Turn off the measurement MOT and optically pump the atoms. Make polarized measurements during this time.
    (b) Turn off the optical pumping and switch the measurement MOT on in AC mode to recollect the atoms.
4. Return to Step 1 and switch the polarization state from $\sigma^+ \leftrightarrow \sigma^-$ every sixteen cycles.

This is shown graphically including the times spent in each region in Figure 4.4. Not shown are pre-programmed delays in the duty cycle in order to take a camera picture of the atoms' fluorescence for diagnostic purposes. This is done every sixteenth cycle during the period while the DC MOT is on. Also, it should be noted that, during the DC phase of the measurement MOT, we use a sub-Doppler MOT cooling scheme specific to K atoms in order to achieve lower trap temperatures [96].

As discussed in Sec. 3.4.3, we employ the AC MOT in order to minimize eddy currents in the chamber. This allows for a well-defined and uniform dipole magnetic field to be established quickly, which is necessary for efficient optical pumping. Even so, this does not entirely eliminate the effect of the residual MOT magnetic field and so we must wait for several hundred microseconds for the magnetic field to stabilize before beginning optical pumping. This is shown as the cross-hatched region in Fig. 4.4. During the run, we adjusted the width of this cross-hatched region, using the values of 332, 432 and 732 µs.

Although we collect data throughout the duty cycle, the atoms are only polarized during the region in Fig. 4.4 labeled "Optical Pumping." Data from other regions of the duty cycle gives useful information about the trap position as well aids in calibration, but the measurement of polarized observables, such as A_β, are done exclusively after the atoms have been optically pumped, making up roughly 24% of the total time. Furthermore, the eddy currents created when turning off the DC-MOT have a negative impact on the optical pumping. Therefore, the first four iterations after the measurement MOT operates in DC mode are excluded from all analyses. Finally, note that we switch the polarization many times within every run, approximately every second, and therefore within each run we have many cycles in both polarization states, which significantly reduces many systematic and environmental effects.

4.3 Run conditions

During the data collection, we were unable to operate both the eMCP and the rMCP simultaneously. When this was tried, we observed a large ($\sim$ 1 kHz) background in one or both of these detectors. Although not entirely understood, the most likely explanation for this problem is a small electrical discharge being produced near the rMCP with the electrons being accelerated by the applied electric field onto the eMCP. When the eMCP was turned off, there was still a large background on this detector although it was typically small compared to when both detectors were on. Measuring the nuclear polarization requires a coincidence with the the eMCP detector while measuring the polarization requires detecting photoions with the rMCP. Therefore, to collect both sets of data, we operated the two MCPs one-at-a-time in an alternating fashion.

Throughout this thesis, the consistency of the results indicates both that they are

Table 4.1: Run conditions for the June 2014 experiment. Due to the problems encountered when the eMCP and rMCP simultaneously, for each experimental run, only was turned on at a time. The labels group sets of runs under identical conditions with the first letter shorthand for which detector was in operation. Groups of runs taken under the same conditions, but which are not sequential, are labeled with a number in the last digit. See Sec. 4.4 for a description of Trigger A. For eMCP runs, only $1/n$ Trigger A events are written to disk with n the number given in the table.

Runs	Mode	Label	Run time hour	$\vec{E}$-field V/cm	t_{OP} µs	TRIG A Scaledown	Polarized β-singles
362-363	eMCP	EA1	2.0	66.7	332	6	436 179
368-378	rMCP	RA1	3.7	395	332	-	1 138 720
383-393	eMCP	EA2	4.5	66.7	332	10	716 077
394-402	rMCP	RA2	4.7	395	332	-	1 652 734
409-419	rMCP	RB1	6.7	535	332	-	3 880 678
420	eMCP	EA3	0.7	66.7	332	6	235 757
421-426	rMCP	RB2	6.0	535	332	-	3 677 524
428-435	eMCP	EB	12.6	150	432	6	3 538 687
446-449	rMCP	RB3	2.5	535	332	-	1 484 987
450-455	rMCP	RC	2.8	395	732	-	1 178 741
460-474	rMCP	RD	7.6	415	732	-	3 164 906
476-477	eMCP	EC	1.8	150	732	6	456 418
478-489	eMCP	ED1	8.4	150	432	6	2 135 203
491-499	rMCP	RE1	1.1	415	432	-	836 571
502-505	eMCP	ED2	3.9	150	432	6	1 769 540
509	rMCP	RE2	0.5	415	432	-	357 246
510	eMCP	ED3	1.6	150	432	6	718 660
513	eMCP	ED4	0.4	150	432	6	97 956

independent of the chosen experimental conditions and that the results are reproducible. For example, when data is collected in the sequence eMCP-rMCP-eMCP, the results are the same, within uncertainties, for the two eMCP data sets. We also operated under different conditions by changing the applied electric field as well as changing the amount of time between turning off the AC-MOT and turning on the optical pumping. A summary of the experimental conditions is presented in Tab. 4.1.

4.4 Data acquisition

To control this experiment, we developed a data acquisition application based on the Maximum Integrated Data Acquisition System (MIDAS) [97]. This system coordinates the collection and storage of data among the hardware modules. The two PMTs, each coupled to a plastic scintillator, produce two outputs apiece, one from each of the last two stages of electron multiplication. The timing of the pulse is taken from the second-to-last stage, processed by a Tennelec Model 455 constant-fraction discriminator (CFD) and digitized by a CAEN V1190B time-to-digital converter (TDC), set to operate with a timing resolution of 98 ps. The signal from the final stage of the PMT is sent to a CAEN V792 charge-integrating charge-to-digital converter (QDC) and recorded with 12-bit resolution.

Each Si-strip detector, segmented into 40 perpendicular strip on each side, produces 80 independent signals. All of the strips' signals, totaling 160 channels between the two detectors, are processed independently. The signals are pre-amplified with custom-designed differential output amplifiers. The amplified signals are then fed into four VF48 Waveform Digitizers [98]. These modules digitize the entire waveform at a rate of 60 Msps (mega-samples per second), equivalent to a timing resolution of 16.7 ns. The VF48 implements a simple "pre-selection" of waveforms such that waveforms are saved only if they satisfy

$$\mathrm{ADC}[n] - \mathrm{ADC}[n-3] \geq 2 \tag{4.1}$$

where ADC[n] is the ADC reading at a time n. If this condition is satisfied for any n, the waveform is saved for further analysis. The threshold was set conservatively at 2 in order to obtain the lowest threshold possible for this detector. In the future, it should be possible to improve the VF48 operation by a more aggressive or sophisticated pre-selection algorithm.

Table 4.2: Trigger menu for the June 2014 experiment. For each classification of run, only the marked triggers were turned on. The scintillator singles trigger was scaled-down by a fixed value. Note that, since the eMCP and rMCP were never turned on simultaneously, Trigger F was not used.

Label	Description	eMCP	rMCP
A	Scintillator singles	✓	✓
B	Scintillator pulser	✓	✓
C	Scintillator-eMCP coincidence	✓	
D	eMCP-UV laser coincidence	✓	
E	rMCP-delayed UV laser coincidence		✓
F	rMCP-delayed eMCP coincidence		

To the determine the position event-by-event, the eMCP detector produces a total of seven output channels: two from each of the delay-lines and one from the MCP itself. Similarly, the rMCP produces 5 timing signals. Each timing signal from the two microchannel plate detectors are amplified and fed into a CFD. The $6 + 1$ signals from the eMCP use a Roentdek CFD8c while the $4 + 1$ rMCP signals use Tennelec Model 455 CFDs. The logic signal from either CFD is sent to the same CAEN V1190b module as the scintillator's timing signals.

Critical information about the status of the atomic duty cycle is recorded by a pair of VME-NIMIO32 modules. These are general purpose VME field-programmable gate array (FPGA) boards capable of receiving input and producing output consistent with NIM and TTL logic standards. This module records information such as the current sign of the polarization (σ^+/σ^-) and time elapsed since the most recent cycle of optical pumping began. A second purpose of the NIMIO32 modules is to accept input pulses from the various detectors and, if the pulses satisfy a set of conditions, to generate an event trigger. Once an event is triggered, data from all the modules are written to disk. Although not all were used in the June 2014 run, Table 4.2 lists the trigger "menu" available as well as whether or not each trigger was selected when operating in eMCP mode and rMCP mode.

Note from Table 4.2 that the BB1 detectors are not included in the trigger logic and that Trigger F was not used. Multiple trigger conditions can be true at once, but the overall event trigger only requires one of the active triggers to be present. Trigger A, the scintillator-singles trigger, is scaled down by a fixed value such that only $1/n$ of the scintillator singles are recorded. On the other hand, if the scintillator is in coincidence with the gain-stabilization LED (Trigger B) or with the eMCP (Trigger C), no scaledown factor is applied. That is, we only apply a scaledown factor if *only* Trigger A is active. We apply no scaledown to Trigger B because its rate is low enough that there is no advantage to this and, in the case of Trigger C, no scaledown is applied because Trigger C provides a loose trigger on β-asymmetry events, which are exactly the most important events to keep! Trigger D is used to select photoelectron events in eMCP mode and Trigger E selects photoion events in rMCP mode. Note that in this case, the signal from the UV laser must be delayed by the photoion time-of-flight. Both of these triggers allow us to image the trap using these low-energy charged products.

When an event is triggered, the ADC modules fed by the PMTs open a 50 ns gate and record the total charge of each signal for each detector. Due to the relatively slow decay time of the gain-stabilization LED pulser, when Trigger B is active, the gate sent to these ADCs is 250 ns long in order to capture the whole pulse. Therefore, the LED signal is on a different scale as the other scintillator signals and only provides a *relative* measurement of the detector's stability. The readout time of the VF48 waveform digitizers are slow compared to the rest of the DAQ system. Therefore, these modules are only written to disk when Triggers A or C are active. The other triggers are unlikely to be the result of β-decays are therefore the BB1 detectors are unlikely to contain useful information for these events. The event information from the QDC and TDC modules are written to disk for every triggered event.

This chapter has given a general description of the experimental apparatus including the detector layout, atomic duty cycle, and data acquisition. The remainder of the thesis consists of the analysis of the TRINAT June 2014 data set to determine the β-asymmetry parameter in ^{37}K. Further technical details of the experimental methods not presented in this chapter will be discussed as they become relevant to the analysis.

5. ATOMIC MEASUREMENTS

In this section, I will describe the nuclear polarization measurement using the distribution of the photoionization events throughout the duty cycle as well as the optical pumping model of Section 3.5.2. First, I will describe measurements of the atom-cloud position and width within the vacuum chamber. This will serve to both select events for the polarization measurement as well define the input parameters for the GEANT4 simulation. The polarization measurement described here has been published as Ref. [99], and much of the discussion of this chapter is also presented in this reference.

5.1 Data selection

We observe photoions with the recoil MCP detector *on* and the electron MCP detector *off* as described in Ch. 4. Photoions are created with an initial kinetic energy of $< 1\,\mathrm{eV}$; compared to an applied electric field of $\geq 395\,\mathrm{V/cm}$, this can be considered as at rest. Therefore, the photoions arrive at the rMCP detector localized spatially as well as in time-of-flight with respect to the UV laser pulse. In order to obtain the time spectra of photoionization events, from which I will determine the polarization, it is important to develop reliable selection cuts for these events.

Although we are interested in photoion events during the optical pumping portion of the duty cycle, there are (intentionally) very few of these events as a result of most of the atoms quickly being pumped to the fully polarized dark state. Therefore, in order to have sufficient statistics for an accurate measurement, we create the photoion position and time-of-flight spectra from data throughout the duty cycle, including times when the MOT is on. The time-of-flight spectra are shown in the top row of Figure 5.1 for sets RB and RD (see Tab. 4.1). We measure the time-of-flight by comparing the arrival time of the signal on the rMCP with the timing of the UV laser pulse. The pulse-processing electronics introduce an arbitrary time-delay between the rMCP signals and the signal from the UV light. Subsequently, we determined the magnitude of this delay to be 44.6(1) ns using an off-line measurement as shown in Fig. 5.2. To do this, we arranged the UV laser to hit the MCP detector directly and observed the time spectrum shown. Combining this with a known difference in

---

Portions of this section are reprinted under a Creative Commons 3.0 Attribution Unported License from Fenker, B. *et al.* *New J. Phys.*, 18(7), 2016:073028 © 2016 IOP Publishing Ltd and Deutsche Physikalische Gesellschaft the path length of the UV light during the offline measurement, we obtain the value $t_0 = 39.9(3)\,\mathrm{ns}$.

Once we have the photoion time-of-flight information in Figure 5.1, we can re-sort the data with a loose cut on the photoion's time-of-flight and observe the $\hat{x}$-$\hat{z}$ position of events on the rMCP using the information from the delay-line anode. These position spectra for representative datasets are shown in the second and third rows of Fig. 5.1. These figures anticipate the calibration results presented in Ch. 7. In the $\hat{z}$ direction, the position spectra are approximately Gaussian in shape while in the $\hat{x}$ direction, for sets RA, RB, and RC, we observe a position spectrum with two prominent peaks, while for the later runs in sets RD and RE only one peak is observed. This is a result of increased efficiency (gain) along one line across the rMCP face where the second peak is. This pattern of high-efficiency stripes is repeated along the $\hat{x}$ direction throughout the face of the MCP. It is likely caused by localized damage to the MCP face causing certain regions to have higher or lower gain than average. Unfortunately, we have not been able to determine the root cause of this damage.[1] Between sets RC and RD, we adjusted the threshold settings for the MCP detector, which mostly eliminates the double-peaked pattern seen in the $\hat{x}$-position spectrum. While this issue may impact the absolute trap position, for the purpose of selecting photoion events, I will treat events in *either* peak as true photoion events.

Once the position spectrum are generated, we can fit each histogram to determine a set of position cuts that can be used to filter the data and generate a cleaner time-of-flight spectrum. Empirically, I fit a Gaussian plus background to the $\hat{z}$-position spectrum and the sum of two Gaussians and background the the $\hat{x}$-position spectrum:

$$N_z = N_1 \exp\left(\frac{z - z_0}{2\sigma_z^2}\right) + b_z \tag{5.1a}$$

$$N_x = N_2 \exp\left(\frac{x - x_0}{2\sigma_x^2}\right) + N_3 \exp\left(\frac{x - x_0'}{2\sigma_x'^2}\right) + b_x \tag{5.1b}$$

where N_1 and N_2 are are normalization factors, z_0 and x_0 are the centers of the

---

[1] Although we do not know the cause, we eliminated a number of possible causes. The pattern is not correlated with any previous mask used in previous experiments and is present even when the electrostatic hoops are removed. That the pattern is seen almost entirely along one axis of the delay-line anode implies that the problem is related to this device. However, the delay-line anode assembly was held at a modest electric potential $< 250\,\mathrm{V}$ difference compared to the back MCP.

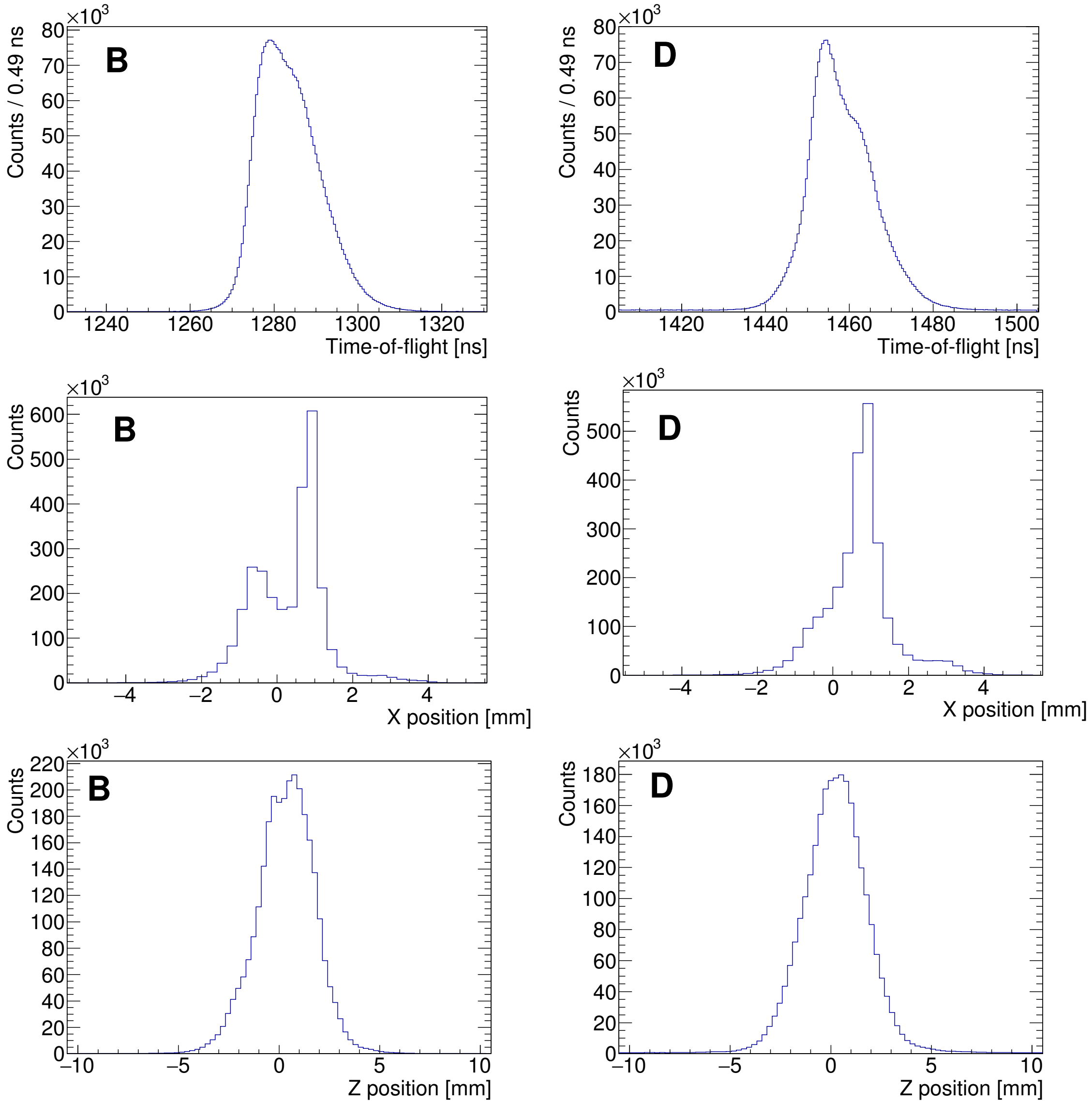

Figure 5.1: Photoion time-of-flight and position spectra. There is very little background in all of these spectra making this an exceptionally clean probe of the polarization. The $\hat{x}$ spectrum labeled "B" has two prominent peaks that are a result of varying gain across the rMCP detector. The corresponding spectrum labeled "D" was taken after the constant-fraction discriminator thresholds were adjusted to reduce this effect. Both the $\hat{x}$ and $\hat{z}$ spectra have been shifted such that the center of the spectra is defined to be at $x = z = 0$.

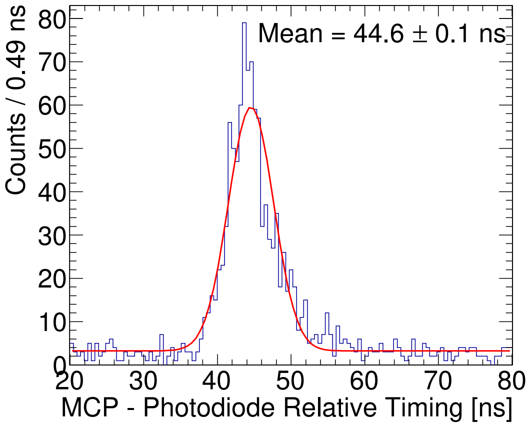

Figure 5.2: Relative timing of the rMCP and UV light signal. In this figure, the UV hits the rMCP directly and the measurement gives the arbitrary timing offset introduced by the data acquisition.

distributions, σ_z and σ_x are the the standard deviations, and b_z, b_x are the number of background counts per bin. Using the results of these fits, we can define an area on the MCP corresponding to photoion events:

$$R^2 = \left(\frac{z - z_0}{\sigma_z}\right)^2 + \min\left[\left(\frac{x - x_0}{\sigma_x}\right)^2, \left(\frac{x - x_0'}{\sigma_x'}\right)^2\right]. \tag{5.2}$$

The data was again re-sorted to generate time-of-flight spectrum with the condition that $R < 3$, equivalent to a three sigma cut in position. This time-of-flight spectrum was then also fit to a Gaussian plus background to obtain a centroid t_0 and width σ_t. The data were then sorted once again, this time requiring no cut on position but that $|t - t_0| < 3\sigma_t$. The new, cleaner position spectrum was again fit to the functions shown in Eq. 5.1 and we obtained new centroids and widths. This processes was repeated until successive iterations resulted in a change in the fit parameters that was less than their uncertainties. The result is a set of clean and unbiased spectra for the time-of-flight and position of photoion events. The final fit parameters are used to select photoion events for the analysis in the following sections. While each fit in the iterative process described above generated position *or* time-of-flight spectra by applying cuts *only* on the opposite information, the final analysis is done using spectrum generated with satisfying $R < 3$ *and* $|t - t_0| < 3\sigma_t$

Table 5.1: Position and time-of-flight results for each dataset. To fit the polarization, I consider events with $R < 3$ and $|t - t_0| < 3\sigma_t$. The variations in t_0 and σ_t are due to changing the electric field between data sets.

Set	x_0[mm]	σ_x[mm]	z_0[mm]	σ_z[mm]	t_0[ns]	σ_t[ns]
A	2.41(10) 1.24(5)	0.237(20) 0.49(5)	−0.236(25)	1.251(31)	1500.7(3)	8.3(3)
B	2.430(20) 1.22(5)	0.227(20) 0.45(5)	−0.363(31)	1.30(4)	1292.5(3)	7.0(3)
C	2.471(20) 1.24(5)	0.226(20) 0.45(5)	−0.119(20)	1.378(25)	1497.7(2)	7.4(3)
D	2.420(35) 1.44(15)	0.312(35) 0.40(10)	−0.221(10)	1.414(10)	1468.4(2)	7.0(2)
E	2.50(5) 1.34(35)	0.50(5) 0.40(20)	−0.44(4)	1.54(5)	1461.8(2)	6.9(3)

according the the values shown for each set in Table 5.1.

5.2 Cloud characterization

In addition to selecting photoionization events for the polarization measurement, the time-of-flight and delay-line anode position information is also used to define the overall trap position, width, sail velocity, and temperature, which are inputs for the GEANT4 simulation described in Ch. 6. In this case, rather than averaging over the whole duty cycle, I plot the position of the photoion as well as the photoion's time-of-flight throughout the duty cycle as shown in Fig. 5.3. At $t = 0$, the AC-MOT is turned off in order to begin optical pumping. With no confining force, the atoms ballistically expand. While optical pumping, there are few atoms available for photoionization so that there are not enough events during this time to measure the cloud distribution reliably. Once the atoms are re-trapped by the AC-MOT at $t = 1906\,\mu\text{s}$, we observe that the trap distribution's standard deviation has expanded by $\lesssim 1\,\text{mm}$. The dashed line in Fig. 5.3 is an interpolation described below. In addition to the expansion of the trap, we also observe that the center of the distribution drifts slightly during optical pumping times. Once the AC-MOT is turned back on, we observe that the cloud's width gradually shrinks as expected now that the confining forces are active.

To quantify the information contained in Fig. 5.3, each bin along the time axis is fit to a Gaussian function. The center of this distribution where at least 50 events occured with the 100 µs time bin is shown as the red points overlayed on the color-plot while the standard deviation is plotted on the panel below. The center of the atom cloud as the MOT is turned off is defined as $\vec{r}_0 = (x_0, y_0, z_0)$. The value of $\vec{r}_0$ is calculated by taking the weighted average of the center of the distribution along each coordinate axis during the final 300 µs that the AC-MOT was on. Note the left-most point in each panel is not used in this calculation because the AC-MOT is already off at this point. In the case of the $\hat{y}$-axis, we do not have the position information directly, but must calculate it from the time-of-flight information. The photoion starts from rest and I assume that the electric field is uniform. With this:

$$y(t) = \frac{qEt^2}{2M} \tag{5.3}$$

where q is the charge of the electron, t is the time-of-flight, and M is the mass of ^{37}K. The width of the Gaussian distribution in each dimension is calculated in the same manner: by comparing the width of the distribution as the atoms are released to when the atoms are re-trapped. For the time-of-flight axis, the time-of-flight width, σ_t is converted to the actual trap with via

$$\sigma_y(t, \sigma_t) = \frac{1}{2}\left[y(t+\sigma_t) - y(t-\sigma_t)\right] = \frac{qE\sigma_t t}{M}. \tag{5.4}$$

As the atoms are optically pumped, we consider both the atom's thermal velocity as well as a sail velocity representing the bulk motion of the center of the distribution. We determine the sail velocity with a linear interpolation between $\vec{r}_0$ described above and $\vec{r}_f$, the position of the cloud at $t_f = 1900$ µs when the MOT is turned back on and the atoms are re-trapped. The atoms' sail velocity is interpolated via

$$\vec{v}_{\text{sail}} = \frac{\vec{r}_f - \vec{r}_0}{t_f} \tag{5.5}$$

and is shown as the dashed line in Fig. 5.3. Following the arguments presented in Ref. [19], the trap width is expected to expand according to

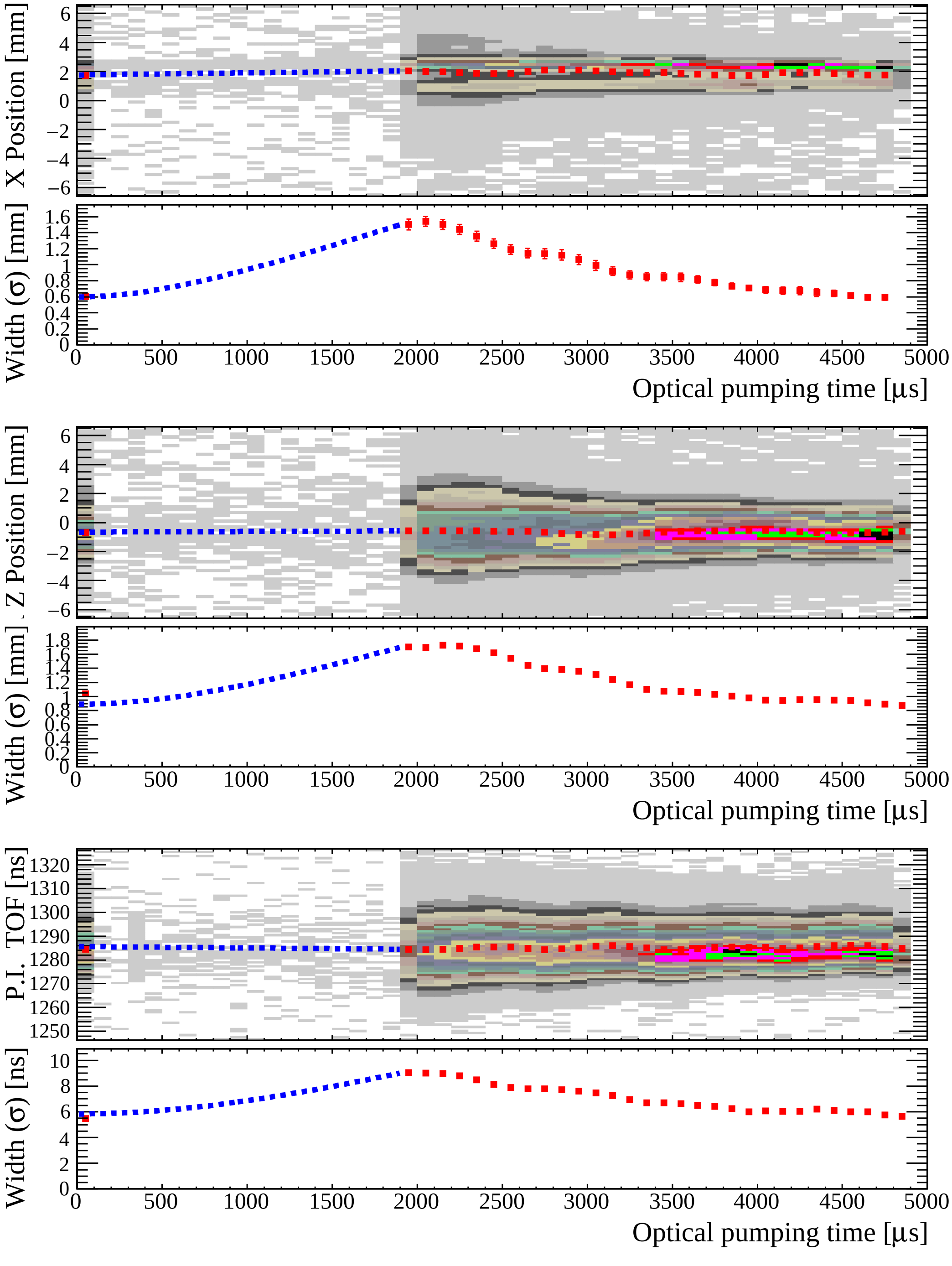

Figure 5.3: Trap position as a function of duty cycle. The top two panels, measuring the $\hat{x}$ and $\hat{z}$ directions, are measured using the delay-line anode while the bottom panels shows the photoion's time-of-flight. This can be used to calculate the position of the trapped atoms by assuming that the electric field is constant.

$$\vec{\sigma}^2(t) = \vec{\sigma}^2(0) + \frac{1}{2}\vec{v}^2 t^2 \tag{5.6}$$

where $\vec{v}$ is the thermal velocity of the atoms in each dimension and the vector signs are to be interpreted to mean that the equation holds for each axis independently (i.e. $\vec{v}^2 \neq \vec{v} \cdot \vec{v}$). To determine $\vec{v}$ in each dimension, I solve Eq. 5.6 for it and interpolate based on the width of the atoms' distribution using the same points for the case of the sail velocity described above. In order to understand the result, the thermal velocity calculated in Eq. 5.6 is taken to be the mean velocity of a Maxwell-Boltzmann distribution with temperature given by

$$\vec{T} = M\frac{[\vec{\sigma}^2(t_f) - \vec{\sigma}^2(0)]}{k_B t_f^2} = \frac{M\vec{v}^2}{2k_B} \tag{5.7}$$

where again, the vector signs indicate that each dimension is calculated independently, and k_B is the Boltzmann constant. These results are shown in Tables 5.2, 5.3, and 5.4 for each coordinate axis. The results are broken down by dataset (see Tab. 4.1) as well as by polarization state. Between polarization states, there is no significant difference in the trap parameters. This directly limits a source of false asymmetry that would be would potentially bias the β-asymmetry results. However, the variation in the trap parameters between sets is larger than the quoted statistical uncertainties. Keeping in mind that these variations are still only $\approx 0.1\,\text{mm}$, I take the average over the sets to determine the final trap position. When propagating the uncertainty in trap parameters to the final uncertainty on A_β, I will take the spread of the values as the uncertainty rather than the smaller statistical uncertainty.

The shift in $\hat{x}$-position and width between sets RB and RC is an exception to this statement. In this case, the trap shifts from a consistent value to another value where it also remains constant. We observed a shift at this same time with a CCD camera taking pictures of the atoms during DC-MOT phase of the duty cycle and can attribute this change to a drift in power of a MOT beam that was corrected at this time. Therefore, the $\hat{y}$- and $\hat{z}$-positions are taken to be constant throughout the data taking while the $\hat{x}$-position takes on two discrete values before and after this change.

Table 5.2: Trap parameters in the $\hat{x}$-direction. The shift in position observed between sets B and C is simulated seperately for the relevant data sets.

		x_0 mm	v_{sail} µm/ms	σ_0 mm	Temp mK
A	σ^+	1.93(5)	111(63)	1.17(4)	0.99(31)
	σ^-	1.97(5)	58(67)	1.00(4)	1.64(34)
B	σ^+	1.76(4)	144(59)	0.598(19)	2.33(25)
	σ^-	1.77(4)	157(57)	0.603(19)	2.34(24)
C	σ^+	2.19(6)	66(80)	1.16(5)	1.3(4)
	σ^-	2.24(7)	46(73)	1.19(5)	1.1(4)
D	σ^+	2.317(18)	94(44)	0.385(23)	2.17(22)
	σ^-	2.320(17)	100(43)	0.387(22)	2.16(20)
E	σ^+	2.511(13)	130(43)	0.453(16)	2.00(20)
	σ^-	2.494(13)	122(46)	0.430(17)	2.15(24)
A-B	σ^+	1.83(3)	130(40)	0.70(2)	1.8(2)
	σ^-	1.85(3)	120(40)	0.68(2)	2.1(2)
C-E	σ^+	2.437(10)	106(29)	0.478(13)	1.98(14)
	σ^-	2.426(10)	100(29)	0.466(13)	2.02(14)

Table 5.3: Trap parameters in the $\hat{z}$-direction

		z_0 mm	v_{sail} µm/ms	σ_0 mm	Temp mK
A	σ^+	−0.525(8)	51(22)	0.893(6)	2.48(12)
	σ^-	−0.535(9)	17(19)	0.887(6)	2.45(11)
B	σ^+	−0.658(6)	42(15)	0.891(5)	2.58(8)
	σ^-	−0.663(7)	74(15)	0.891(5)	2.63(8)
C	σ^+	−0.432(14)	34(26)	0.929(10)	2.70(15)
	σ^-	−0.442(12)	62(27)	0.924(9)	3.13(16)
D	σ^+	−0.585(6)	44(13)	0.966(4)	3.09(8)
	σ^-	−0.589(6)	67(13)	0.971(4)	3.12(8)
E	σ^+	−0.837(12)	65(24)	1.024(9)	3.43(15)
	σ^-	−0.811(12)	54(27)	1.030(9)	3.09(18)
avg	σ^+	−0.610(4)	46(8)	0.935(3)	2.83(5)
	σ^-	−0.607(4)	59(8)	0.936(3)	2.84(5)

Table 5.4: Trap parameters in the $\hat{y}$-direction. This is derived from the photoion time-of-flight data.

		y_0 mm	v_{sail} µm/ms	σ_0 mm	Temp mK
A	σ^+	−4.10(5)	75(24)	1.037(16)	1.68(11)
	σ^-	−4.02(5)	74(24)	1.040(18)	1.51(11)
B	σ^+	−3.51(6)	100(21)	1.011(18)	1.74(8)
	σ^-	−3.50(6)	94(21)	1.007(18)	1.68(7)
C	σ^+	−3.67(5)	160(26)	0.968(18)	1.44(12)
	σ^-	−3.69(5)	225(33)	0.961(17)	1.52(18)
D	σ^+	−4.54(5)	144(13)	0.986(11)	1.60(6)
	σ^-	−4.54(5)	131(13)	0.986(12)	1.56(6)
E	σ^+	−3.68(5)	229(23)	0.943(16)	1.39(10)
	σ^-	−3.68(5)	260(24)	0.947(16)	1.31(11)
avg	σ^+	−3.93(2)	141(9)	0.988(7)	1.59(4)
	σ^-	−3.91(2)	141(9)	0.986(7)	1.56(4)

5.3 Shakeoff-electron measurements

The paucity of photoion events while the atoms are being optically pumped requires that the trap position during this time be interpolated between between turning the MOT off and the MOT on. However, for runs in eMCP mode, the shakeoff electrons following β^+-decay arrive uniformly throughout the duty cycle and allow us to check that the interpolation presented above is indeed valid. Similar to the rMCP, the eMCP gives directly the position in the $\hat{x}-\hat{z}$ plane, while the $\hat{y}$-direction requires time-of-flight information.

In this application, the shakeoff electrons are deflected by the magnetic field. While optical pumping, this takes the constant value of 2.339 G, but while the AC-MOT is on the field is oscillating at 699 Hz. The field lies along the $\hat{z}$-axis and the amount of deflection in the $\hat{x}$-direction can be calculated assuming constant electric and magnetic fields and that the shakeoff starts from rest:

$$\Delta x = \frac{B_z}{3}\sqrt{\frac{2qy^3}{m_e E}} \tag{5.8}$$

where B_z and E are the fields, m_e is the electron's mass, and $y = 100\,\mathrm{mm}$ is the position of the front plate of the eMCP. While the optical pumping magnetic field is in place, with $E = 66.7\,\mathrm{V/cm}$, $\Delta x = 18\,\mathrm{mm}$, and with $E = 150\,\mathrm{V/cm}$, $\Delta x = 12\,\mathrm{mm}$. The exact magnitude of these shifts depends on the details of the E and B fields including possible inhomogeneities. Along the $z = 0$ plane, we expect the magnetic field to be well defined and uniform with the non-uniformities growing as $|z| > 0$. Therefore, this measurement does not give a precise measurement of the trap position in the $\hat{x}$-direction. In the $\hat{y}$-direction, the expected shakeoff electron (SOE) time-of-flight is $\approx 10\,\mathrm{ns}$. With typical cloud widths $\approx 1\,\mathrm{mm}$, the time-of-flight between opposite sides of the atom cloud changes $< 100\,\mathrm{ps}$. Therefore, the width of the distribution in time-of-flight is not sensitive to the size of the distribution.

Despite the caveats described in the preceding paragraph, Fig. 5.4 shows the $\hat{z}$ and $\hat{x}$ projections of shakeoff electrons as observed on the eMCP throughout the duty cycle. While the AC-MOT magnetic field is on, its AC quadrupole field distorts the observed position spectra. The fluctuations in the SOE distribution's position and size shown Fig. 5.4 have the same period as the AC magnetic field. I emphasize that this is *not* related to a distortion of the trap location and size but instead the distortions are the result of the magnetic field's effects on the SOE trajectory. During OP times, the observed position in the $\hat{x}$-direction is offset $\sim 10\,\mathrm{mm}$ from the center of the detector as a result of the magnetic field deflecting the electron trajectories. While the uniform DC optical pumping magnetic field is on, the position is observed to vary approximately linearly while the width grows in proportion to t^2 as expected from Eq. 5.6. These two observations validate the interpolations of the last section and lend confidence to the assertion that the atoms continue to be well-localized throughout the duty cycle.

5.4 Polarization

Section 5.1 described the analysis cuts used to define photoion events. With these in place, this distribution in time of these events throughout the duty cycle is used to probe the total unpolarized and partially polarized population. Referring to Fig. 3.4, the degree to which the photoionization rate is extinguished is directly related to this population. With the high polarization we achieve, this method has

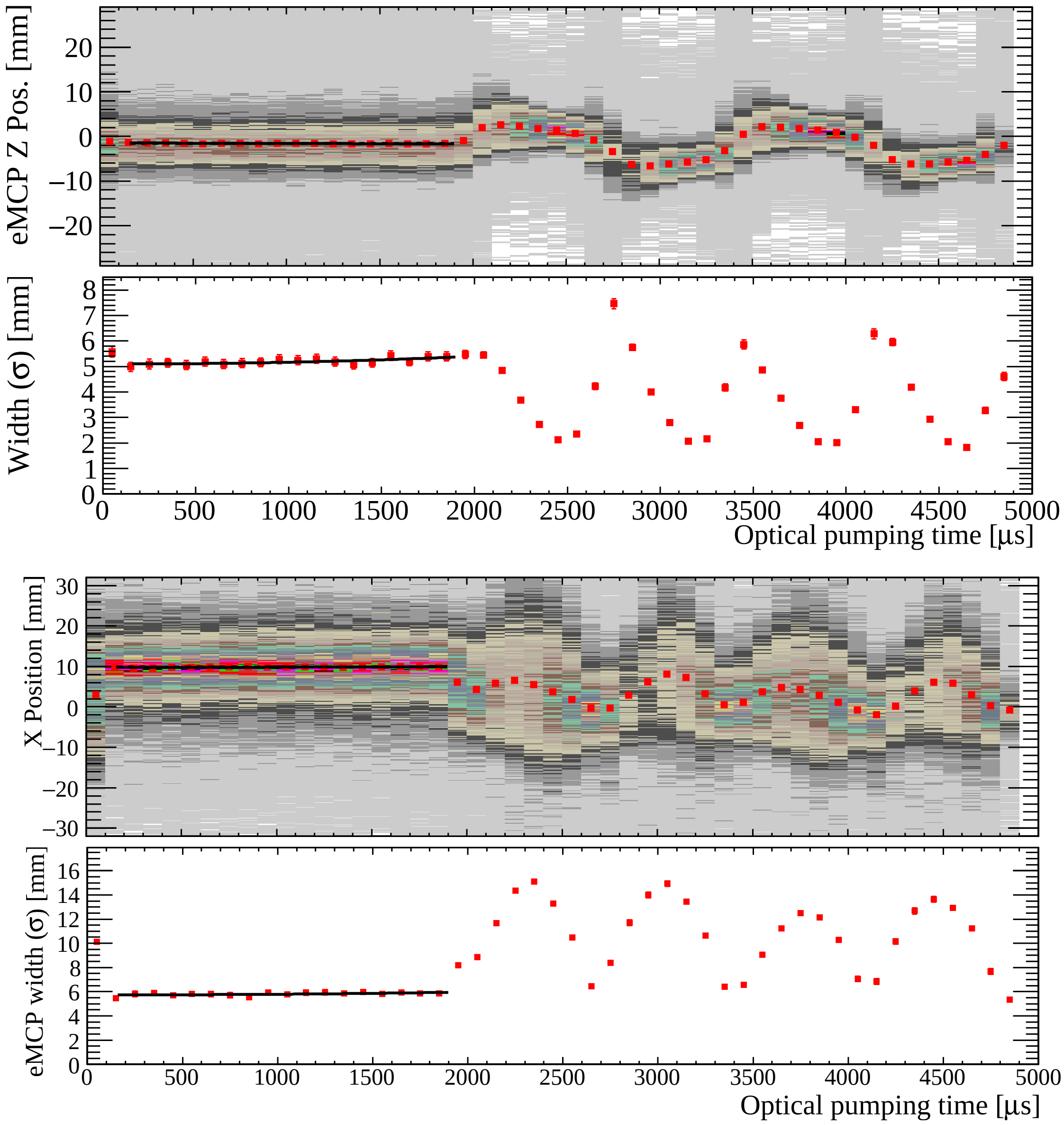

Figure 5.4: Shakeoff electron position spectrum. The smoothly varying values up to t = 1900 µs validate the simple interpolations used for the rMCP data. The oscillations beyond this are caused by the AC magnetic field distorting the observed SOE position. Note that this is *not* the result of the atom cloud moving. The $\hat{x}$-position is offset from $x = 0$ during OP times due to the magnetic field deflecting the trajectories of the SOE.

the advantage of measuring $\approx 1 - P$ with P the nuclear polarization. For example, if $1 - P$ is measured to 10%, reaching a polarization of $P = 0.99$ implies that $\Delta P = 0.001$, a 0.1% measurement of the polarization. The nuclear alignment, T, is measured with the same method. However, the term in the nuclear decay rate proportional to T contains the neutrino momentum. Since in this work the neutrino is unobserved, T does not influence the observed decay rate. However, future analyses of the same dataset plan to deduce the neutrino momentum by reconstructing the recoiling daughter's momentum. Therefore, the results presented here also include a determination of the nuclear alignment term for inclusion in this work.

The idea behind optical pumping as well as how it is measured via photoionization is described in Sec. 3.5. In brief, once the AC-MOT is shut off circularly polarized σ^+ or σ^- light near resonance with $F' = 2$ excited state interacts with the atoms propagating along the $\hat{z}$-axis. This drives atoms on a biased random walk to a state of 100% nuclear polarization. Simultaneously, a magnetic field is applied to break the degeneracy of the Zeeman sublevels. As atoms accumulated in the fully polarized state, they are no long available to be photoionized, and the rate of photoionization decreases, proving a direct probe of partially polarized population fraction. To measure the relatively small but still significant contribution of the partially polarized atoms to the nuclear polarization, we model their sublevel distribution by simulating the time evolution of the system using the density matrix approach described in Sec. 3.5.2. Before presenting the polarization results, I will first give a series of additional experimental details about the optical pumping setup that are critical to the precision polarization measurement.

5.4.1 Optics details

To correctly model the optical pumping process, we must ensure that no other light is present in the chamber during this time. The laser that pushes atoms from the first, collection MOT to the measurement MOT is controlled by a double-pass acousto-optic modulator (AOM) setup, is turned on only briefly during atom transfers, and misses the second trap by aiming the beam 1 cm above the measurement trap's height except during atom transfers. The magneto-optical trapping beams themselves are switched off to less than 10^{-4} of their maximum value by turning off the first-order diffracted beam from an AOM. Any remaining trap light is from the tail of the zeroth-order beam, 90 MHz (15 linewidths) off-resonance. The resulting excitation is less than 2×10^{-4} of the optical pumping light.

To minimize systematic effects, the polarization state is reversed every 16 s and simultaneously a frequency shift of $\Delta(\sigma^+) - \Delta(\sigma^-) = 4\,\mathrm{MHz}$ is applied. Figure 5.5 shows the atomic levels and transitions relevant to optical pumping and defines these parameters. Shifting the laser frequency is done in order to move closer to the desired $m_F = \pm1 \to m_{F'} = \pm2$ transition frequency while moving the laser frequency further from the unwanted $m_F = \pm2 \to m_{F'} = \pm1$ transition, which can be excited by a component of the optical pumping light circularly polarized with the "wrong" sign. Note that the sign of B_z is not changed throughout the experiment.

To obtain the highest polarization, both the $F = 1$ and $F = 2$ ground states must be optically pumped. The two frequencies needed to accomplish this are created by RF power injected directly into the diode laser with the frequency close to the ground state hyperfine splitting. We apply this standard technique [100] at relatively low RF power levels that produce light at about 1/2 the power of the carrier frequency and split from the carrier frequency by the RF frequency. This frequency is easily adjusted from the hyperfine splitting of ^{41}K ($A_{s_{1/2}} = 127\,\mathrm{MHz}$) to ^{37}K ($A_{s_{1/2}} = 120\,\mathrm{MHz}$) without changing the alignment or beam spatial quality. The optical sideband strength is monitored with a Fabry-Perot cavity and is stable in power to about 10%.

The saturation spectroscopy and double-pass AOM setup shown in Fig. 5.6 allows frequency locking for either ^{41}K or ^{37}K. The light is also detuned 1 MHz with respect to the ground-state hyperfine splitting to completely destroy dark state coherences [92] (see section 5.4.4). Following this, the light is divided into two beams and injected into polarization-maintaining optical fibers. The remainder of the optical path after exiting these optical fibers is shown in figure 5.7.

After exiting the optical fiber, the OP light passes through a polarizing beamsplitter and contrast 5×10^4, 25 mm diameter suspended silver nanoparticle linear polarizer (CODIXX ColorPol VIS 700 BC4). This is shown in Fig. 5.7. Next, the polarization state is determined by the voltage applied to a liquid crystal variable retarder which either maintains the linear polarization or rotates it 90°.

Since the OP and MOT light must travel the same path through the vacuum chamber, they are combined by an angle-tuned laser line filter. This Semrock LL01-780 nominally transmits 98% of 766.49 nm OP light while reflecting 98% of the 769.9 nm MOT light at 20° incidence. The transmission of OP light changes by 4%

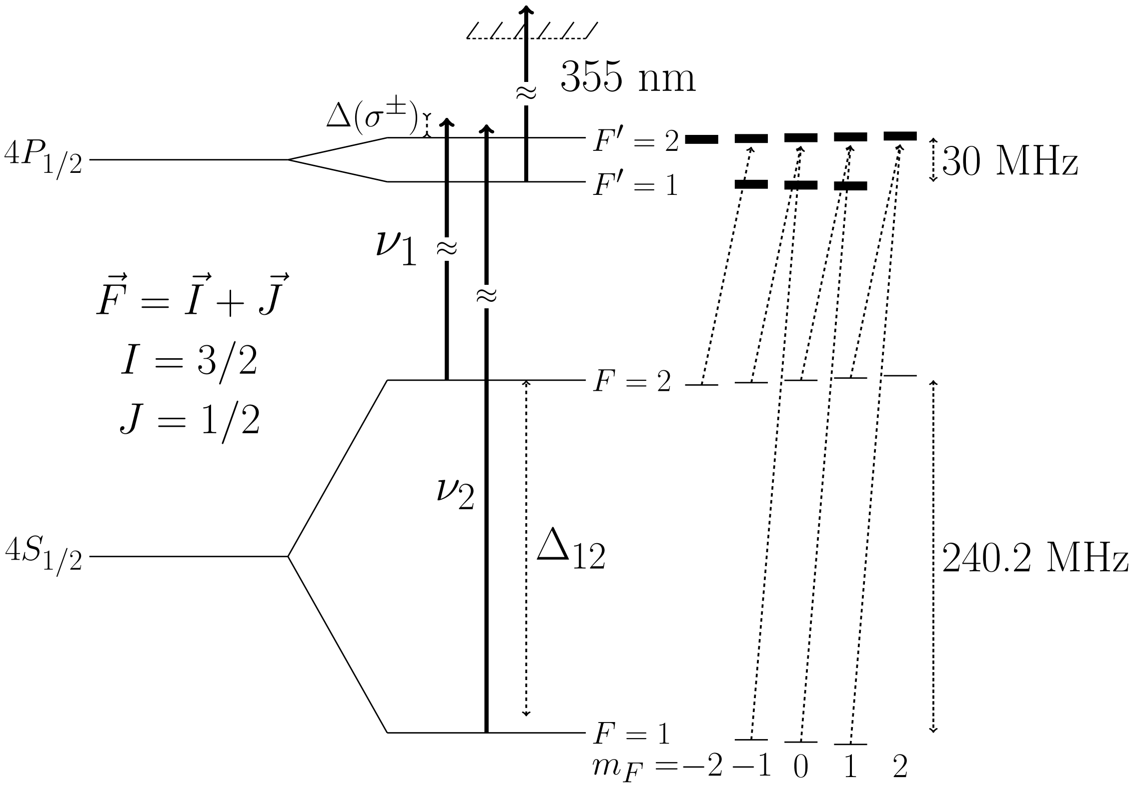

Figure 5.5: Optical pumping level diagram. The fine and hyperfine structure of ^{37}K showing the laser transitions relevant to optical pumping. The natural linewidth of the $4p_{1/2}$ state is 6 MHz. Circularly polarized light brought in along the vertical axis (see figure 1.4) and tuned to the D_1 transition pumps atoms into the $F = 2$, $m_F = \pm 2$ state, resulting in a very high cloud polarization. The parameter Δ gives the detuning from the $F = 2 \to F' = 2$ resonance and is different for the σ^+/σ^- polarization states. The second frequency is detuned a fixed amount, Δ_{12}, from this frequency and optically pumps atoms which occupy $F = 1$ ground states. Neither Δ nor Δ_{12} are shown to scale. The 355 nm light continually probes the excited state population by photoionizing atoms from the excited P states, which are subsequently detected by the recoil MCP. Reprinted from [99].

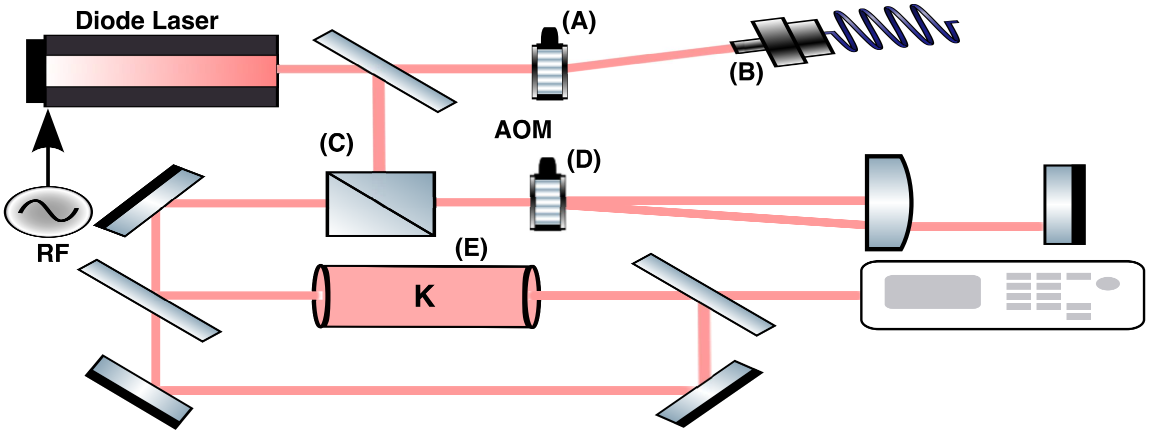

Figure 5.6: Optical pumping frequency locking scheme. The $F = 2 \rightarrow F' = 2$ and $F = 1 \rightarrow F' = 1$ frequencies are generated by RF modulation of the diode laser current. The OP light is turned on and off by changing the RF input frequency of an AOM (A), whose first-order diffraction is steered on and off an optical fiber (B). That scheme, unlike turning the RF power on and off, keeps the AOM at near-constant temperature, avoiding steering and light profile distortion as the light is injected into the optical fiber; thus the light power is switched well from zero to full value without transients. 10% of the light is diverted to lock the laser frequency (C). The light is shifted in frequency by a tunable double-pass AOM (D) before going to a vapor cell of potassium (E), allowing frequency locking either for naturally occurring ^{41}K, or for accelerator-produced ^{37}K, by referencing to Doppler-free Zeeman-dithered saturation absorption peaks of stable isotopes [101]. Reprinted from [99].

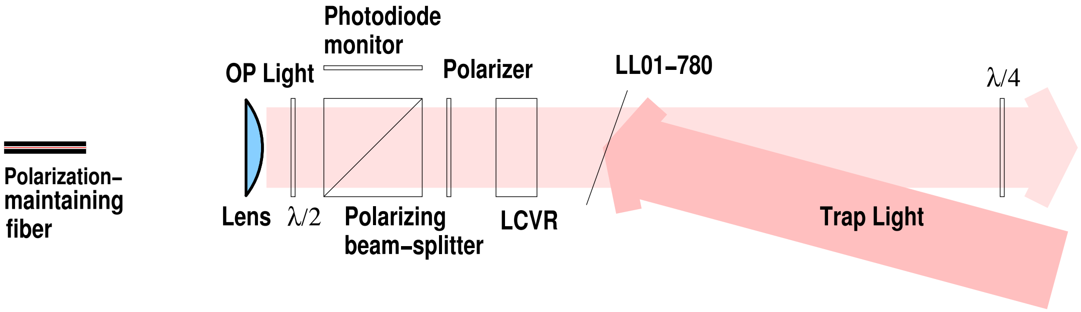

Figure 5.7: Optical elements creating the circularly polarized light. This arrangement is repeated for both OP arms. The liquid crystal variable retarder (LCVR) is used to control the sign of the circular polarization of the OP light and the LL01-780 laser line filter is used to combine the OP and MOT light along the same optical path. Reprinted from [99].

between the linear polarization states. The output of this feeds a high-quality 1/4-wave plate before being injected into the vacuum chamber. Note that there are no lenses in the path after the polarizer, avoiding position-dependent birefringence.

The quality of circular polarization is critical to the final nuclear polarization achieved. Any component of the light with the "wrong" polarization removes atoms from the fully polarized state and drives $|P| < 1$. We parametrize the quality of circular polarization with the normalized Stokes parameter (also see Eq. 3.25):

$$s_3 = \frac{\mathcal{I}_+ - \mathcal{I}_-}{\mathcal{I}_+ + \mathcal{I}_-} \tag{5.9}$$

where $\mathcal{I}_+$ ($\mathcal{I}_-$) is the laser intensity in the σ^+ (σ^-) state.

The degree of linear polarization is measured in each polarization state along both OP arms immediately before passing through the atom-trap viewports and s_3 is determined for each case. However, stress-induced birefringence in the viewport glass can change the light ellipticity. We characterize this birefringence by its effect on s_3 as the light passes through the viewport. If the s_3 parameter of the incoming light is denoted s_3^{in}, then this same parameter for the light after it has passed through the viewport is given by [102]:

$$s_3^{\mathrm{out}} = \sin(\arcsin(s_3^{\mathrm{in}}) + \Delta n\, kL) \tag{5.10}$$

where Δn parametrizes the effect of the viewport, k is the wave number of the light and L is the thickness of the viewport glass.

Viewports to minimize Δn have been developed, replacing the elastomer in a commercial viewport with polychlorotrifluoroethylene (PCTFE, sold commercially as Neoflon), which is compatible with UHV [102]. We obtain $\Delta n = (-6 \pm 2) \times 10^{-6}$ and $(-2 \pm 1) \times 10^{-6}$ for the two arms respectively. Although this measurement is done with the viewports in air, we have measured the cumulative effect of both viewports on s_3 both in air as well as with the viewports under vacuum and observe no difference. This is consistent with the pressure on the viewports having no effect on Δn. The measured values for s_3 both before and after the viewport are shown in Tab. 5.5.

To polarize the atoms along the $\hat{z}$-axis, the optical pumping light must be propagating in this direction when it interacts with the atoms. Since the BB1 detector and PMT are opaque, the light is brought in at a 19° with respect to the vacuum

Table 5.5: Results of the measurement of the OP light polarization.The direct measurement of s_3^{in} is done before the viewport, and the value after the viewport (s_3^{out}) includes a calculation of the effect of the birefringence in each viewport. Reprinted from [99].

	Laser port	s_3^{in}	s_3^{out}
σ^-	Upper	$-0.9980(4)$	$-0.9958(8)$
	Lower	$-0.9990(10)$	$-0.9984(13)$
σ^+	Upper	$0.9931(9)$	$0.9893(14)$
	Lower	$0.9997(3)$	$0.9994(5)$

chamber and reflected once. The mirror used for this purpose is coated with a commercial dielectric stack with 99.5% reflectivity. We observe a change in the outgoing light's ellipticity $|s_3' - s_3| < 10^{-4}$ at this 9.5° incidence angle. The angle of this mirror is fixed with mechanical precision to the vacuum chamber and aligned to within $\Delta\theta = 1\,\text{mrad}$. Since the β-asymmetry is proportional to $\cos(\theta)$, this produces a negligible error of 5×10^{-7}.

5.4.2 Magnetic fields

A second mechanism that can drive $|P| < 1$ is a magnetic field transverse to the optical pumping axis (B_x) that causes Larmor precession out of the stretched state. We have carefully designed the apparatus to minimize eddy currents once the AC-MOT is turned off, which in turn produce a magnetic field. Non-magnetic materials such as 316L and 316LN grade stainless steel and titanium were used wherever possible and the chamber welds were kept thin to minimize their magnetic permeability. We measured the relative permeability of the welds to be < 1.25. The vacuum chamber has a large (12 in) diameter to place potentially magnetic materials as far away from the trapped atoms as reasonably possible. The nearest material to the atoms is the set of electrostatic hoops which direct the photoions onto the MCP. These are made from SIGRADUR G grade glassy carbon, a semiconductor with resistivity $4500\,\mu\Omega\,\text{cm}$, two orders of magnitude better than stainless steel.

In order to cancel out magnetic fields that are constant on the time scale of optical pumping, we arranged two pairs of magnetic trim coils exterior to the vacuum chamber. By varying the DC current in these coils, we were able to apply a transverse magnetic field to cancel stray fields at the location of the trapped atoms. To optimize these settings, we optically pumped ^{41}K, which can be trapped in large numbers and has a similar hyperfine structure to ^{37}K. We used the same system described in this section except that we monitored the fluorescence directly rather than the photoionization. Keeping all the laser parameters fixed, we scanned the trim-coil current and observed the residual fluorescence after optical pumping. The minimum residual fluorescence corresponds to the optimal current setting which was also used for the ^{37}K experiment.

Additionally, the AC quadrupole magnetic field is switched off before the optical pumping begins but induces eddy currents in the surrounding material, which in turn produce a magnetic field. Although the purpose of using an AC-MOT is to reduce these eddy currents by turning off the magnetic field when it is nearly zero, we used a Hall probe to measure an initial residual field gradient of $\sim 103\,\mathrm{mG/cm}$, which decays to a final value of $\sim 22\,\mathrm{mG/cm}$ with a time constant of $\sim 130\,\mu\mathrm{s}$. Although this measurement was done with one vacuum flange removed, it demonstrates both the approximate size of this effect as well as the need, described in section 5.4.5, to wait until this field has completely decayed away before starting optical pumping.

5.4.3 Photoionization light

The 355 nm UV light that photoionizes the excited atoms is circularly polarized and has a near-TEM$_{00}$ mode with a $1/e^2$ diameter of 12 mm. It comes from a commercial diode-pumped solid-state pulsed laser making 0.5 ns pulses at 10 kHz repetition rate. The light propagates at 35° with respect to the optical pumping axis. After interacting with the atoms, the UV light is reflected along the same path in order to provide a second opportunity to interact with the atoms with $\sim 90\%$ of the original intensity. Next the sign of the polarization is reversed, and the light again interacts with the atoms twice, although with the third pass now at 41% of the original intensity. In total, the UV light photoionizes about $1/10^6$ atoms per pulse.

In order to correctly interpret the photoionization signal as a probe of the total $p_{1/2}$ population, we must consider the relative photoionization cross-sections of the magnetic sublevels. Photoionization from the $p_{1/2}$ state populates outgoing s- and d-wave photoelectrons with the cross-section proportional to the square of radial ($\mathcal{R}$) and angular portions of the matrix element connecting a pair of final and initial states. Since the angular part does not depend on the details of the central potential, it is well known. Using a single-electron model with a parametric central potential, Aymar, Luc-Koenig, and Combet Farnoux calculate the total cross-section for s- and d- wave photoelectrons and their results are $\mathcal{R}_d/\mathcal{R}_s \approx 1.7$ at $E_e = 760\,\mathrm{meV}$ [103].

Considering the off-axis propagation as well as the multiple passes of the UV light (see section 5.4.3), the total photoionization cross-section changes by no more than 4% in our setup compared to the assumption that all states have an equal probability to be photoionized. The polarization results change by $< 10^{-5}$ assuming a 50% uncertainty on the ratio $\mathcal{R}_d/\mathcal{R}_s$.

Note that the cross-section of photoionization is on the order of 1 Mb, while Rayleigh scattering has a cross-section 10^6 lower. Therefore, the 355 nm light is effectively a passive probe that does not disturb the system. It either photoionizes the atom, removing it from the population so its subsequent less-polarized β-decay is not observed, or has negligible probability of disturbing the polarization.

5.4.4 Coherent population trapping

The multi-level system of Fig 5.5 can support coherent population trapping (CPT) states on three distinct sets of λ-atomic systems ($m_F = -1, 0, 1$)[2]. A λ-atomic system is defined by two ground states driven by two laser frequencies to the same excited state. CPT are especially problematic for this measurement as atoms in these states are not available to be photoionized and detected, exactly mimicking our experimental signature for good polarization, while simultaneously having $|P| < 1$. Although CPT states are adequately described by the model of section 3.5.2, we describe both how their formation is eliminated in our setup as well as the steps that we have taken to verify this.

First, the OP light is retroreflected such that it interacts with the atomic cloud twice: first propagating along $+\hat{z}$ and second along $-\hat{z}$. Since these relative velocities are different for the two passes, the relative Doppler shift of the light frequency between the first and second pass greatly reduces the CPT effect in all but the coldest atoms.

To verify that CPT states are not created, we performed measurements with ^{41}K.

---

[2] Although coherent population trapping and the combination charge-conjugation, parity, time-reversal both share the abbreviation CPT, they are in no other way related. In cases where the context makes the abbreviation clear, I will continue to use CPT to refer to both concepts.

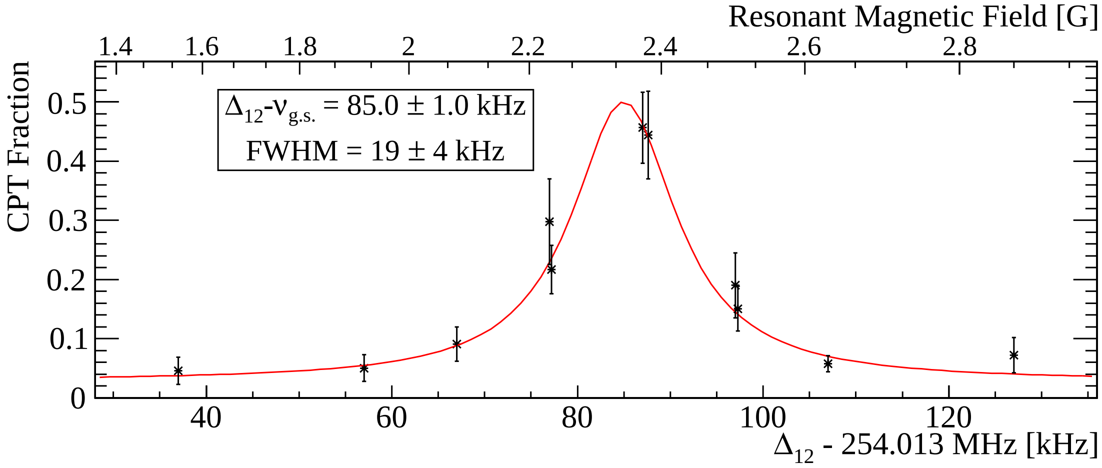

Figure 5.8: Coherent population trapping measurement. The difference between the two OP frequencies, Δ_{12}, is scanned near the ground state hyperfine resonance. The resonant frequency is 85 kHz from the ground-state hyperfine splitting, providing a clean measurement of the aligned $(\hat{z})$ magnetic field. The width of this resonance is only 19 kHz and, along with the $m_F = \pm 1$ resonances, is carefully avoided during the ^{37}K experiment. Reprinted from [99].

We measure the magnitude of the CPT state similarly to [92] by optically pumping the atoms with Δ_{12} set to intentionally create CPT states (see Fig 5.5). After the atoms are optically pumped, we switch the frequency of the $F = 1 \rightarrow F' = 2$ laser away from this resonance, allowing the atoms that had been trapped in this state to be optically pumped to the $m_F = \pm F$ state, creating a second burst of photoionization. The relative size of the two photoionization bursts is a measurement of the CPT fraction.

We scan the OP frequency around the $m_F = 0$ ground-state hyperfine resonance as shown in Fig 5.8 and observe that the CPT resonance in our system has a FWHM of only 19(4) kHz. We avoid this narrow resonance, as well as the $m_F = \pm 1$ resonances, during the polarization measurement by setting Δ_{12} to be 1.1 MHz from the ground-state hyperfine splitting. Simultaneously, since the resonant CPT frequency is equal to the energy difference between the two $m_F = 0$ ground states, we use this to determine the aligned magnetic field from the second-order Zeeman shift: $B_z = 2.339(10)$ G.

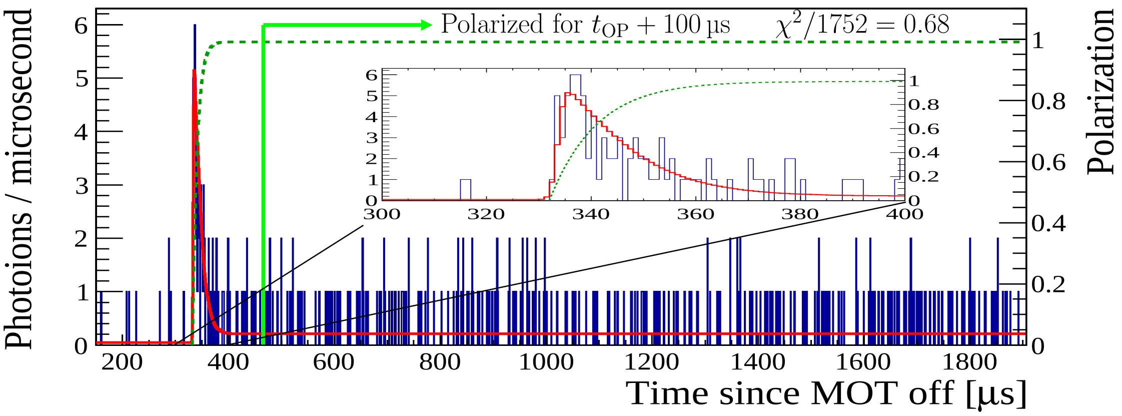

Figure 5.9: Typical polarization fit. Result of the fit to the σ^- polarization state with $t_{OP} = 332$ µs and $E = 535$ V/cm. The data is shown as the blue histogram and overlaid with the fit result in red. The nuclear polarization is shown in dark green and quickly approaches one as atoms accumulate in the stretched state. Reprinted from [99].

5.4.5 Polarization results

Fig 5.9 shows a typical photoionization curve recorded during the experiment. The MOT magnetic field and lasers are switched off at $t = 0$. There was no MOT or OP light interacting with the atoms until the OP light was turned on at $t = t_{OP} = 332$ µs. This was done in order for the MOT magnetic field to die away as it would spoil the final polarization as well as to give a long enough light-free region that we use to measure backgrounds.

The atoms are fully polarized after 100 µs and are re-trapped by the MOT at $t = 1906$ µs after expansion from 2.0 mm to 4.5 mm FWHM. Separate photoionization curves were recorded for the two polarization states. This histogram is fit to the optical pumping calculation, and the best-fit values are used to calculate the nuclear polarization and alignment according to Eq. 3.2.

We include a constant background rate in the fitting function. In order to separate this background from the residual photoionization that results from unpolarized atoms, we extend the fitting region to begin at $t = 150$ µs, before the optical pumping has begun. At this point, there is no light, either from the MOT or the OP light, illuminating the atoms. Therefore, all events between this point and t_{OP}, when the optical pumping is turned on, are considered background. The primary source of background events are random coincidences between the UV pulse and the β-decay of a ^{37}K atom, delayed by the photoion time-of-flight. Also at this point, the MOT magnetic field has mostly decayed away while still leaving enough time before the OP light is turned on to achieve a good statistical sensitivity on the background level.

We also observed a defect in the event timing system which caused the recorded time to be distributed around the actual event time with a resolution of 1.0 µs. Figure 5.10 shows this effect by displaying the photoion time spectra as the MOT light is turned on after an optical pumping cycle. In this figure, before $t = 1944\,\mu\text{s}$, optical pumping is occuring and there are very few photoionization events because the atoms have been optically pumped. At this time, the AC-MOT light turns on with a rise-time $\lesssim 100\,\text{ns}$ which should increase the photoionization rate on the same time scale. However, the photoionization rates takes $\sim 5\,\mu\text{s}$ to reach its maximum value as a result of the timing defect in the apparatus. I fit this rise to a step-function distorted by a Gaussian timing jitter. The result was a jitter of $\sigma = 1.00(5)\,\mu\text{s}$.

This slower-than-expected rise time is also seen, although less clearly due to the lower statistics, as the optical pumping light turns on at t_{OP} in Figure 5.9, indicating that this jitter is universal to the apparatus and must be associated with the data acquisition electronics. Fitting the width of the timing jitter directly to the optical pumping data results in a less-precise but entirely consistent result of $\sigma = 0.9(3)\,\mu\text{s}$. However, I adopt the more precise value determined from the MOT rise-time and treat this timing resolution as a fixed parameter.

The variable fitting parameters were a constant background rate described above, which is parametrized by the average signal-to-noise ratio (S/N) and the OP laser intensity in each polarization state ($\mathcal{I}^{\pm}$). Additionally, the constant transverse magnetic field (B_x) and one parameter describing the laser frequencies were used as free fitting parameters. Of these, the nuclear polarization depends strongly only on B_x. The light ellipticity also strongly influences P, but this is not a free fitting parameter; it is fixed to the values of s_3^{out} shown in Tab. 5.5. Although the transverse magnetic field is minimized in the experiment by a pair of orthogonal magnetic field coils, its absolute value at the atoms' position has a complicated dependence on eddy currents in the vacuum chamber and is difficult to determine reliably. Therefore, it is best fit directly to the experimental data as is done here.

Other parameters, including the laser frequencies, were held constant during the

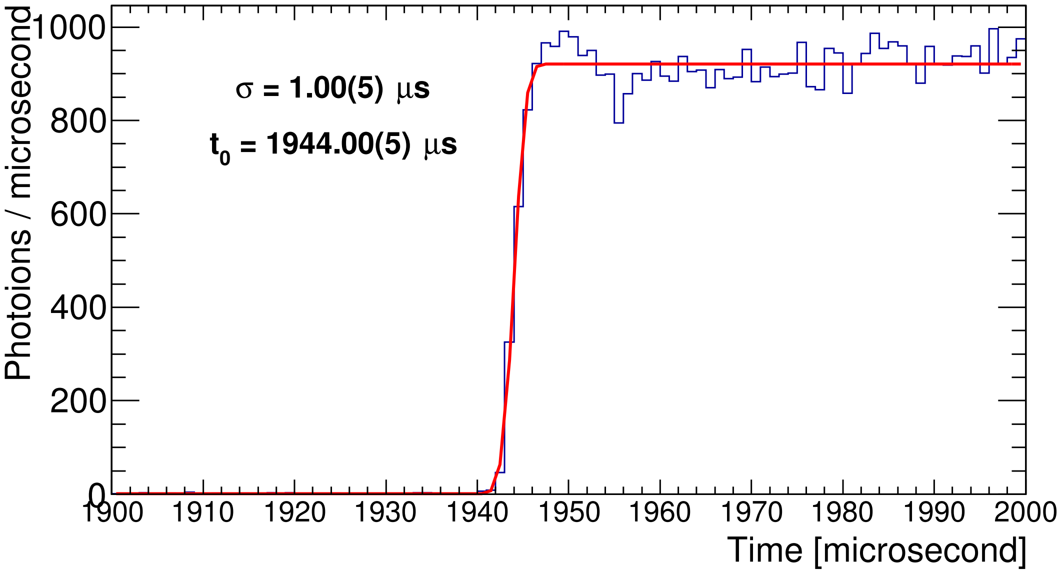

Figure 5.10: Timing jitter in optical pumping signal. Photoionization spectrum as the MOT is switched on. The left side of this figure, showing almost no counts, is the tail of the optical pumping time where there are few atoms available to be photoionized. At t_0, the MOT light with a rise-time of $\lesssim 100\,\mathrm{ns}$ is switched on. Due to an electronic timing jitter, this rise time is distorted, and is fit with the resolution shown. This resolution is used in the optical pumping fit.

Table 5.6: Parameter values following global polarization fit. The uncertainties listed here are purely statistical; the result of propagating the systematic uncertainties are discussed in the text. Reprinted from [99].

Parameter	σ^-	σ^+
Misaligned field, B_x [mG]	124(8)	
Average S/N	4.7(6)	
Laser intensity [W/m^2]	2.33(19)	2.26(13)
Nuclear polarization	$-0.9912(7)$	$+0.9913(6)$
Nuclear alignment	$-0.9761(21)$	$+0.9770(17)$

fit. Note that both $\Delta(\sigma^-) - \Delta(\sigma^+) = 4.0\,\text{MHz}$ and $\Delta_{12} = 239.2\,\text{MHz}$ are well defined experimentally and the laser linewidth is 0.2 MHz. Therefore, only one overall parameter is required to describe the laser frequencies. We determine this overall frequency by fixing the laser intensity in the two polarization states such that $\mathcal{I}^+ = \mathcal{I}^-$ and fitting the photoionization data to obtain the best-fit value of $\Delta(\sigma^-) = -2.8(2)\,\text{MHz}$, which is consistent with the direct resonance measurement [14, 104]. Finally, the magnetic field (B_z) is taken from the CPT resonance measurement described in section 5.4.4.

Throughout the data collection, we varied the time at which we turned on the OP light as well as the strength of the uniform electric field to collect photoions (see Tab. 4.1). Each dataset was independently fit with the binned maximum likelihood method, this time *not* requiring that $\mathcal{I}^+ = \mathcal{I}^-$, and the results for the nuclear polarization calculated using the best-fit parameters are shown in Fig 5.11. The differences in statistical sensitivity are a result of spending different amounts of time collecting data at the various conditions. Since there is no significant difference among datasets, we conclude that the polarization remained constant throughout the data taking.

Taking this into account, we performed the final analysis by fitting each dataset simultaneously to one set of optical pumping parameters. Since the gain of the rMCP detector fluctuated throughout the run, each set was fit with an independent signal-to-noise ratio representing a constant background in the detector for a total of eight free fitting parameters ($\mathcal{I}^\pm$, B_x, and $(S/N)_{A-E}$). The results are shown graphically in Fig 5.12 and summarized in Tab. 5.6.

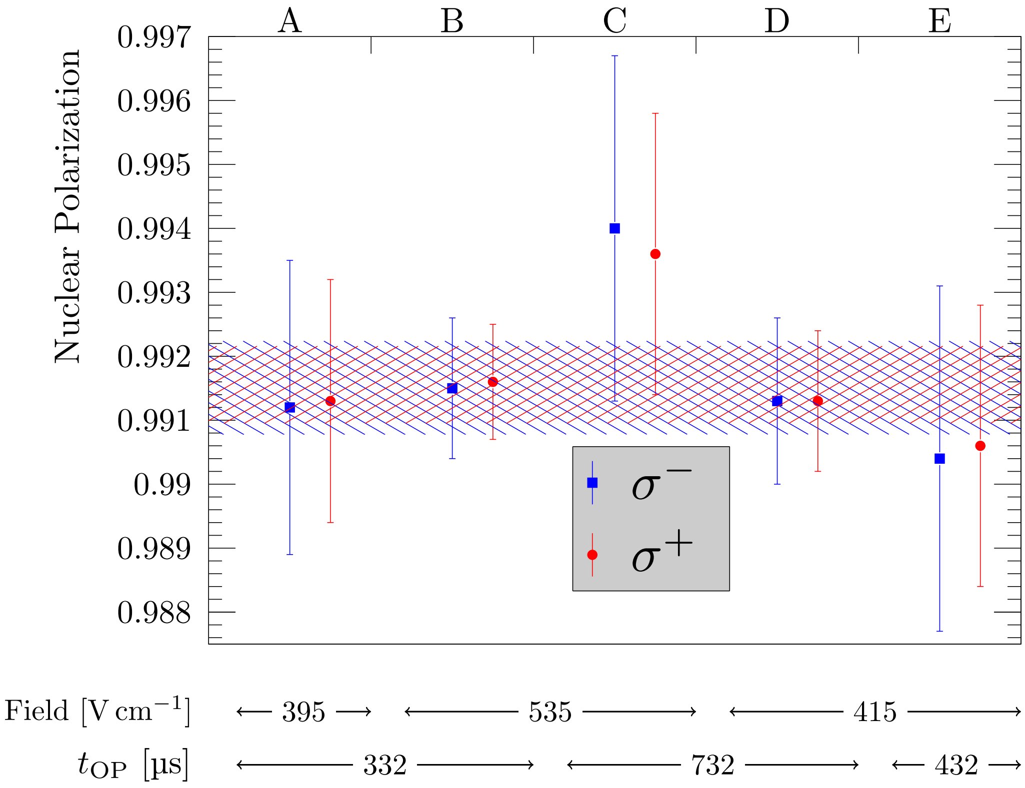

Figure 5.11: Polarization results - each dataset. The polarization we find as a result of fitting each set of data independently. The cross-hatched region shows the 1σ uncertainty on the polarization when combining the results of fitting each dataset this way. Note that the two polarization states are not independent as the transverse magnetic field is the same in both cases. Since there is no difference between sets, the final result is fit to all datasets simultaneously. Reprinted from [99].

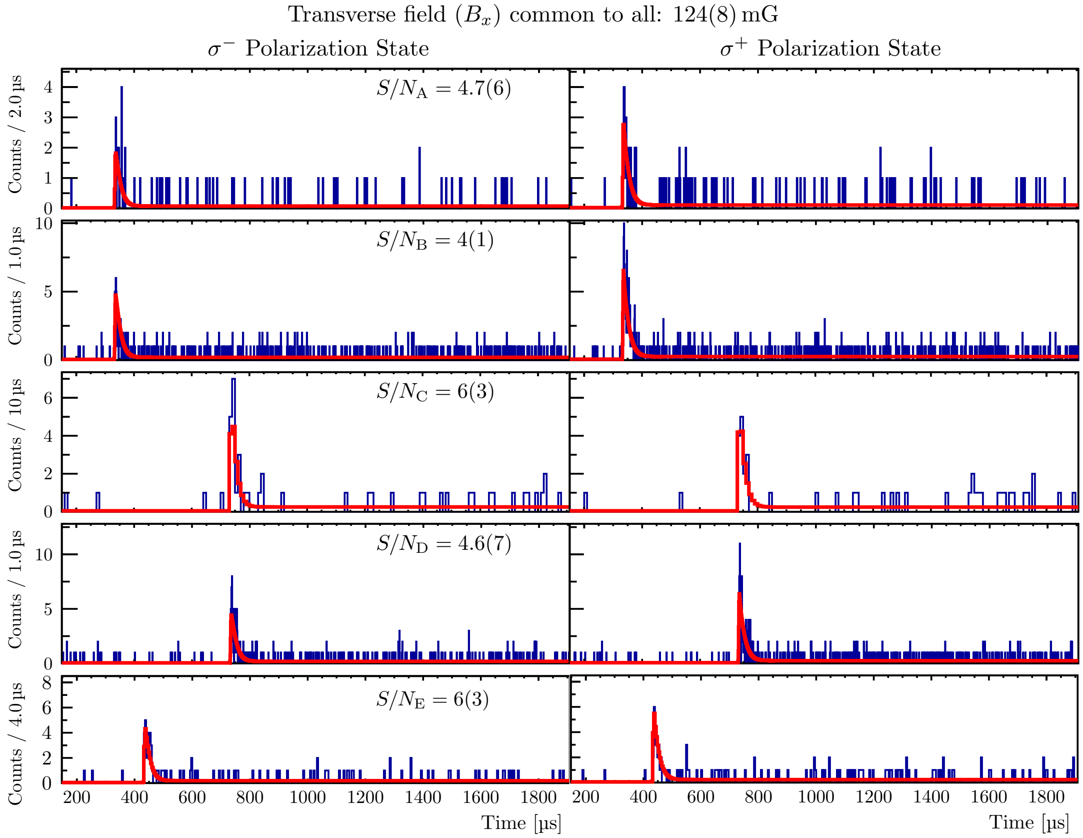

Figure 5.12: Polarization results - global fit. Global fit result including a consistent set of parameters. The Stokes parameter, s_3, was fixed at its experimentally determined value. A single transverse magnetic field, B_x, and separate laser intensities for each polarization state were fit to the entire dataset. The signal-to-noise ratios ($S/N_{\mathrm{A-E}}$) were allowed to vary independently for each of the five datasets. Other parameters were fixed as indicated in the text. The binning for each dataset was chosen to be as fine as possible while producing roughly equal peak bin contents in each set. The effects of using a uniform binning are discussed in section 5.4.6. The datasets shown here from top to bottom correspond to the conditions shown in figure 5.11 from left to right. Reprinted from [99].

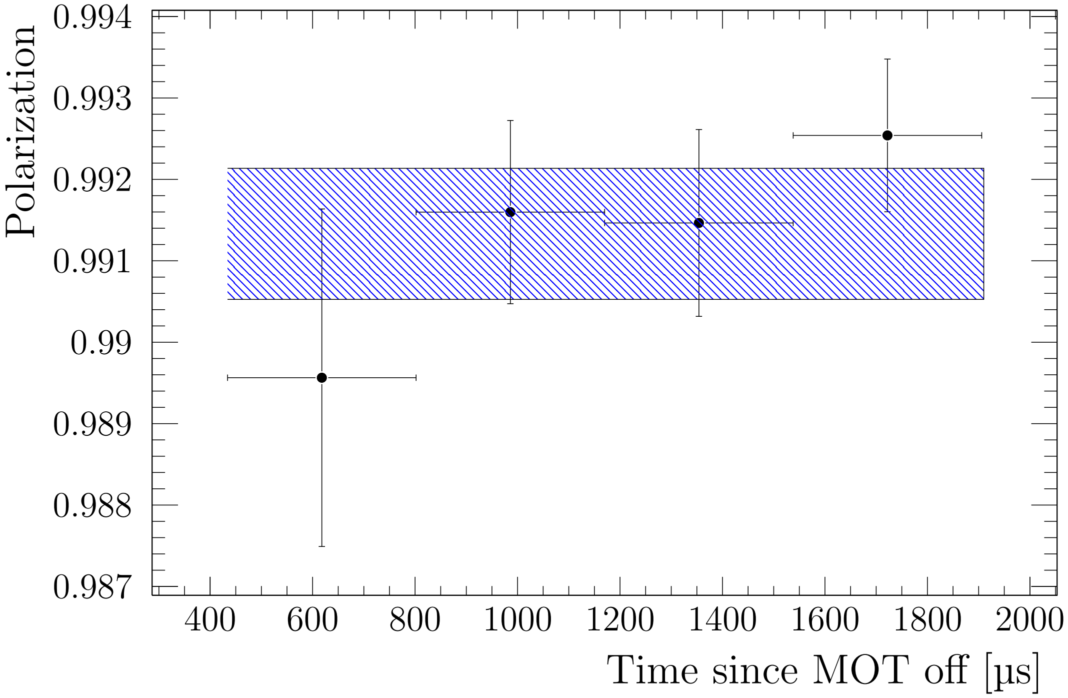

Figure 5.13: Time dependence of the nuclear polarization. The shaded region shows the result with all the data considered while each point considers only the data in the indicated range in addition to the initial OP peak. The polarization seems to improve slightly with time, indicating a gradual decrease in B_x. Reprinted from [99].

The photoion spectra of Fig 5.12 indicate a slight decrease in the partially polarized population even after the atoms are considered fully polarized. This is a result of the AC-MOT quadrupole field, and the eddy currents it creates, slowly decreasing with time. The polarization results dividing the time when the atoms are fully polarized into quadrants are shown in Fig 5.13. All of the data collected with $t_{\mathrm{OP}} = 332\,\mu\mathrm{s}$ is shown as this has the most sensitivity to this effect. This figure suggests that the polarization may be improving even after 100 µs of optical pumping, although the magnitude of this effect is only $\sim 1\sigma$. Keeping this in mind, we reiterate that the results shown represent the average polarization from $t_{\mathrm{OP}} + 100\,\mu\mathrm{s} \rightarrow 1906\,\mu\mathrm{s}$.

5.4.6 Systematic uncertainties

In this section, I discuss the systematic uncertainties in the fitting routine and lay out the procedure I used to quantify them. The final results are determined by performing a global fit to all datasets at once. However, it is also possible to find the weighted average of results in Fig 5.11 where each dataset is fit independently. The difference between these two analysis choices gives a systematic uncertainty of 2×10^{-4}. Note that if we fit each dataset independently, there are a total of twenty fitting parameters: $\mathcal{I}^{\pm}$, B_x, and a (S/N) for each of the five datasets. Therefore, the global fit is preferred simply because it captures the same physics with fewer fitting parameters.

The uncertainty on the s_3 parameter is propagated to the final result by varying the input s_3^{out} value by $\pm 1\sigma$ and comparing the results. Although we do not expect the light's polarization to be correlated in the two polarization states, we conservatively treat them as though they are. This procedure gives the most variation in the relative strengths of the two depolarizing mechanisms, resulting in the largest difference in average nuclear polarization. Even with this conservative approach, the systematic uncertainty is at most 2×10^{-4} and does not limit the measurement.

Next, the dependence of the results on the binning of the data is studied by fitting the data with bins of width 1, 2, 5, 10 and 20 µs. The central value is taken from the fit with varying bin widths shown in Fig 5.12 and we take the largest difference between any choice of binning and this value as the systematic uncertainty.

As described in section 5.4.5, we determine one overall frequency by fitting the photoionization data with the requirement that $\mathcal{I}^{+} = \mathcal{I}^{-}$. Since this requirement is only approximately true, we relax this requirement when determining the final results. However, we conservatively treat this condition as a systematic uncertainty.

The magnetic field (B_z) has been measured by two independent methods: the Hall probe technique described in section 5.4.2 and the CPT field measurement described in section 5.4.4. Because the Hall probe measurement was performed in air with one vacuum flange removed and without the presence of the electrostatic hoops or MCP assembly, it is expected to be less reliable than the CPT measurement. The results of these two measurements differ by 180(20) mG, which is significantly larger than the uncertainty of the CPT measurement itself. Conservatively, this difference is treated as a systematic uncertainty rather than propagating the smaller uncertainty on the CPT measurement.

Finally, we allow a possible anisotropy in the initial ground-state sublevel distribution of the atoms and characterize this by an initial polarization P_0 and alignment T_0. We measure P_0 by observing the β-asymmetry of the positrons emitted in the ^{37}K decay before the optical pumping light is turned on. Comparing this to the expected asymmetry ($A_\beta = -0.5706$), we conservatively measure an initial polarization $|P_0| < 0.022$. Including an initial population distribution with this distribution produces a systematic uncertainty of 1×10^{-5}. Since the asymmetry of polarized atoms is significantly different from 0, and the asymmetry expected when observing unpolarized atoms is 0, any new physics contributions to A_β are certainly small enough to make a negligible impact on this result. In other words, the precision to which this experiment measures A_β is much higher than required for this determination of $|P_0|$, making this systematic uncertainty independent of the final result.

However, T_0 does not produce a signal in the nuclear decay that we can measure with the current setup. In order to constrain this possibility, we model the sublevel distribution of the MOT on the D_2 ($F = 2 \rightarrow F' = 3$) transition. The vertically ($\hat{z}$) propagating beams combine to produce a linearly polarized standing wave in the $\hat{x}$-$\hat{y}$ plane, while the orthogonal arms produce linearly polarized standing waves in the $\hat{x}$-$\hat{z}$ and $\hat{y}$-$\hat{z}$ planes, which represent a combination of linearly and circularly polarized light along the $\hat{z}$ axis. Since the atom velocities are Doppler limited, their motion averages over the polarization gradients of the resultant electric field. Each pair of $\sigma^\pm$ beams have equal power and the ratio of total power propagating along $x : y : z$ is $2 : 2 : 1$ so that the effective ratio of linearly to circularly polarized light is $3 : 2$. Since the AC-MOT is deliberately turned off with B_z close to zero, we adopt the value of $B_z = 100\,\mathrm{mG}$. Since a transverse magnetic field would only serve to decrease the anisotropy, we assume that it is zero for this calculation. The resulting population distribution has $T_0 = 0.03$. Adopting a conservative uncertainty, we constrain the maximum initial alignment to $T_0 < 0.06$ and compare the results. These systematic uncertainties are summarized in Tab. 5.7.

At the current level of precision, the total systematic uncertainty is of similar, but slightly smaller, magnitude as the statistical uncertainty. Since the model that is fit to the experimental data only needs to account for the small contribution to the average polarization from the unpolarized population, all of the uncertainties as well as the statistical uncertainty can be reduced by improving both the light polarization and further minimizing the transverse magnetic field to reduce the unpolarized

Table 5.7: Uncertainty budget for the nuclear polarization measurement. The largest systematic uncertainty arises from the potentially non-zero initial alignment (T_0) of the atoms, which we modeled as described in the text. Also significant is the choice to perform a global fit rather than average the result of each dataset after a series of individual fits. The choice to prefer the global fit is justified by considering the lower number of fit parameters using this method. Reprinted from [99].

Source	ΔP [$\times 10^{-4}$]		ΔT [$\times 10^{-4}$]	
	σ^-	σ^+	σ^-	σ^+
Systematics				
Initial alignment	3	3	10	8
Global fit vs. average	2	2	7	6
Uncertainty on s_3^{out}	1	2	11	5
Cloud temperature	2	0.5	3	2
Binning	1	1	4	3
Uncertainty in B_z	0.5	3	2	7
Initial polarization	0.1	0.1	0.4	0.4
Require $\mathcal{I}_+ = \mathcal{I}_-$	0.1	0.1	0.1	0.2
Total systematic	5	5	17	14
Statistics	7	6	21	17
Total uncertainty	9	8	27	22

population that must be modeled. The final results are:

$$\begin{aligned} P(\sigma^+) &= +0.9913(8) \qquad & T(\sigma^+) &= -0.9770(22) \\ P(\sigma^-) &= -0.9912(9) \qquad & T(\sigma^-) &= -0.9761(27) \end{aligned} \tag{5.11}$$

which represent an order of magnitude improvement compared to previous work [20, 25].

6. SIMULATIONS

This chapter describes the detailed Monte Carlo simulation used to make a quantitative comparison between the experimental data and expectations. Also, a comparison of backscattered events will be given which serves to both validate the simulation and constrain the various simulation parameters.

We have developed an application using the GEANT4 package for the simulation of the passage of particles through matter [105]. This application includes a complete representation of the geometry as well as the material of each volume. The starting point for each event is to randomly choose a decay position based on the known trap parameters given in Tabs. 5.2,5.3, and 5.4. An initial position, $\vec{r}_0$ is chosen from a Gaussian distribution for each dimension with the center and width given in these tables. The time at which the atom decays, t_{decay}, is chosen randomly between 0 and 1906 µs, at which point the atoms are re-trapped by the AC-MOT and are no longer polarized. The atom's thermal velocity is also randomly chosen in each dimension according to the temperature in each dimension. The overall "sail" velocity is added to the thermal velocity to obtain the total velocity, $\vec{v}_{tot}$ of the atom. The position of the atom is then evolved by an amount $\vec{v}_{tot} t_{\text{decay}}$ to obtain the decay position where the event begins: $\vec{r}_{\text{decay}} = \vec{r}_0 + \vec{v}_{tot} t_{\text{decay}}$.

Once the position has been chosen, the momenta of the β^+ and ^{37}Ar are generated according to well-known acceptance-rejection methods, described in general in Ref. [106] and for this experiment in particular in Ref. [25]. In brief, uniform random variables for the momenta of the decay products are chosen, and if they are allowed kinematically, the decay rate, dW_{test} is calculated according to Eq. 2.10. Next, a uniform random variable, R, is chosen up to the maximum of the decay rate and the event is accepted if $dW_{\text{test}} > R$. Recoil-order effects describing the finite mass of the daughter nucleus are included as described in Sec. 2.2.1. The most significant branch to the excited state at 2.8 MeV is also included in the event generator, although recoil-order corrections are not included for this branch as they are at the level of 2×10^{-5} of the total decay rate.

We use the traditional Fermi-Function in the evaluation of the decay rate as described in [25, 107]. There is a negligible difference compared to a more detailed calculation including the screening by the atomic electrons and a non-spherical daughter nucleus (see Fig 3.4b of [25]).

Once the event "begins," the β^+ is tracked through the geometry. Although the application is built to optionally track the recoiling daughter as well, to reduce the CPU time required and because it is not relevant to a measurement of A_β, the recoil was not considered. Note that to include accurately the effects of β-scattering off of surrounding material, even βs that were emitted *not* in the direction of a β-detector were tracked. The energy deposited in each scintillator and BB1 detector were recorded for each event, and the hit-position on the BB1 detector was converted to a "strip" number to match the experimental data. The simulated data is output in the same format as the TRINAT data, allowing for the same analysis code to be used on both simulated and real-world data without modification.

Simulations were performed with GEANT4 version 4.9.6.p04. The physics input of the particle tracking is controlled by the selection of a particular physics list, and by a multiple scattering model. Since energetic electrons experience a large number of Coulomb scatters, the CPU time required is greatly reduced by approximating a large number of individual scatters with a multiple scattering model (MSC) [108]. Separate from this, the physics list controls the other interactions: bremsstrahlung, ionization, and, for β^+, annihilation. Finally, the simulation can be further fine-tuned by adjustment of the "cut-for-secondaries" parameter, the "range factor," the "geometry factor," and the "skin." parameter [109, 110]. The geometry factor determines the minimum number of steps a particle will take in a given volume while the skin parameter defines a thin region near the edge of each volume where each individual Coulomb scatter will be simulated. Changing these parameters has been found to not have a significant influence on the simulation results [109]. This reference also gives a detailed study of the dependence of the simulation on the other parameters as well. Therefore, I will typically follow the recommendations of these authors while varying the simulation parameters as a systematic uncertainty.

The physics lists appropriate for the relatively low energy of this experiment are `emstandard_opt3`, `empenelope`, and `emlivermore`. The `emstandard_opt3` model uses the standard physics models intended for Large Hadron Collider applications, but extends their applicability to lower energies and provides higher accuracy for tracking of electrons and positrons [110]. The `emlivermore` package includes atomic effects and makes direct use of cross-section data [111] while the `empenelope` package makes use of the `PENELOPE` simulation package [112], but does not include the

`PENELOPE`-specific MSC model. Note that the choice of physics list and the choice of MSC model are *completely independent.*

There are two MSC models to choose from for $e^{\pm}$ scattering at the energies relevant to this thesis: the Urban MSC model based on Ref. [113] and the Goudsmit-Saunderson model based on Ref. [114]. However, when measuring the fraction of backscattered $e^{\pm}$ with incident energy $< 1\,\mathrm{MeV}$ using the Goudsmit-Saunderson model, the backscattering fraction exhibits an unphysical staggering as a function of energy. This behavior is shown in Fig. 3 of Ref. [109], and I have verified the results by reproducing them. Therefore, the Urban MSC model is preferred and used throughout this work.

The cut-for-secondaries (CFS) parameter describes the minimum range a secondary particle must have in a given material in order for it to be tracked by GEANT4. This prevents very-low energy particles that would have no impact on the simulation from being generated and reduces CPU time. By defining this parameter in terms of the particle range, one parameter can be used throughout the simulation and provide consistent results regardless of a material's atomic number and density. The default value in GEANT4 is 1 mm. However, with detectors of thickness 0.3 mm and an even-thinner Be window with thickness 0.229 mm, a CFS parameter of 1 µm is more appropriate for this work. The range factor, which limits the step length to a fraction of the mean-free path, takes the default value 0.04. Based on the evaluation of [109], a more accurate value for energies below 1 MeV and for thin detectors is 0.002. Therefore, I will use this value and treat the differences when changing this value as a systematic uncertainty. Table 6.1 shows a summary of simulation parameters used.

Although not included in the GEANT4 simulation, the detector resolution is included separately when comparing to experimental data. This is done for the two scintillators and all 160 strips of the BB1 detector. For each event, a Gaussian random number is thrown with mean equal to the true energy deposited and with width given by the resolution of the detector or BB1 strip under consideration. For the five BB1 strips that were not working (see Tables 7.3 and 7.4), the analyzed energy was set to 0 regardless of the actually-deposited energy.

Since the noise present in the BB1 strips showed significant variation (see Sec. 7.2), the result of the fit described in Sec. 7.2.2 was used to define an individual empirical noise function for each strip. As described in the aforementioned section, the empir-

Table 6.1: Parameters used in the GEANT4 Monte Carlo simulation. Discussion of these choice is given in the text.

	Value	Notes
	`emstandard_opt3`	Ref. [110]
Physics list	`emlivermore`	Ref. [111]
	`empenelope`	Ref. [112]
Multiple scattering model	Urban	Ref. [113]
Cut-for-secondaries	$1\,\mu\text{m}$	
Range factor	0.002	
Geometry factor	2.5	Default
Skin	3	Default

ical noise is dominated (for most strips) by a distribution obtained by simulating a large number of waveforms with 0 energy with the width of this distribution fit to the experimental data. For events with $E < 5\,\text{keV}$, the empirical noise function was used and otherwise the detector's resolution was used as described in the preceding paragraph.

6.1 Backscattering coefficient

Here, I present a direct comparison of the measured backscattering fraction obtained from GEANT4 simulations to the experimental data. As I will show, the data and Monte Carlo are in good agreement with appropriate choices of simulation parameters. That there is good agreement when examining the case described below increases confidence that the backscattering is simulated correctly *throughout the simulation*, even in situations where we have no experimental data with which to verify the simulation.

Knowledge of the backscattering fraction is critical to a measurement of A_β. Since the plastic scintillator serves as the event trigger, a β^+ that initially travels in the $\hat{z}$ direction, but does not reach the scintillator due to scattering off of the intervening mirror, window, Si-detector, or other material will not trigger an event. Clearly, this can bias an asymmetry measurement. Even worse are events initially traveling along $+\hat{z}$, but eventually detected in the detectors at $-\hat{z}$! Therefore, the accurate simulation of β^+-scattering in the geometry is important. With this in mind, the comparisons shown here not only validate the GEANT4 simulation, but also are used as a systematic check on the final result given in Ch. 8. This section makes use of the detector calibrations presented in Ch. 7, but note that these calibrations and analysis choices were fixed prior to the backscattering analysis.

In order to verify the simulation, the fraction of events that backscatter off of the plastic scintillators and into the nearby BB1 detector is compared to the experimental data. These events have the unique signature of energy deposited in the scintillator along with energy in *two* different pixels of the BB1 detector. Due to limitations in the analysis of the BB1 detector, the two pixels must have no BB1 strips in common. As described in Sec. 7.2, the energy detected in each pixel must agree to within $n_{\mathrm{cut}}\sigma$ where $n_{\mathrm{cut}} = 3$ and σ is the combined resolution of the $\hat{x}$ and $\hat{y}$-strips. Furthermore, requiring a coincidence with the eMCP ensures that the decay originated from the trapping region. In all cases, the simulated data was analyzed identically to the TRINAT data.

I define the backscattered fraction, f_{BS}, in terms of the number of events triggering *two* BB1 pixels, N_{multi}, divided by the number of events triggering *one* BB1 pixel, N_{single}. Note that I define N_{single} to specifically exclude events triggering two BB1 pixels, i.e. there are no events counting towards both N_{multi} and N_{single}. Alegbraically,

$$f_{\mathrm{BS}} = \frac{N_{\mathrm{multi}}}{N_{\mathrm{single}}}. \tag{6.1}$$

Note that the specific BB1 hit-detecting algorithm developed (Fig. 7.12), does not detect multi-hit where the two hits share a BB1 strip. That is, the second event must trigger a BB1 pixel displaced by at least 1 mm in both $\hat{x}$ and $\hat{y}$ from the first hit. Fig. 6.1 displays the comparison of the results for both the data and Monte Carlo simulation. Especially above 1 MeV, the data and GEANT4 agree rather well. Also shown in the top panel is the 1σ error band from an empirical fit to backscattering data off of targets ranging from Li to U with energies from $0.01 - 20\,\mathrm{MeV}$ [115]. This empirical curve contains 8 constants fit to the data, but does not include effects of detector resolution, dead strips, etc. Therefore, although the data does not follow the curve precisely, this is not considered a problem.

How the backscattering coefficient depends on the simulation parameters is shown in Fig. 6.2. The three panels each show the evolution of the backscattering coefficient as one simulation parameter is adjusted. The other parameters are fixed to the values

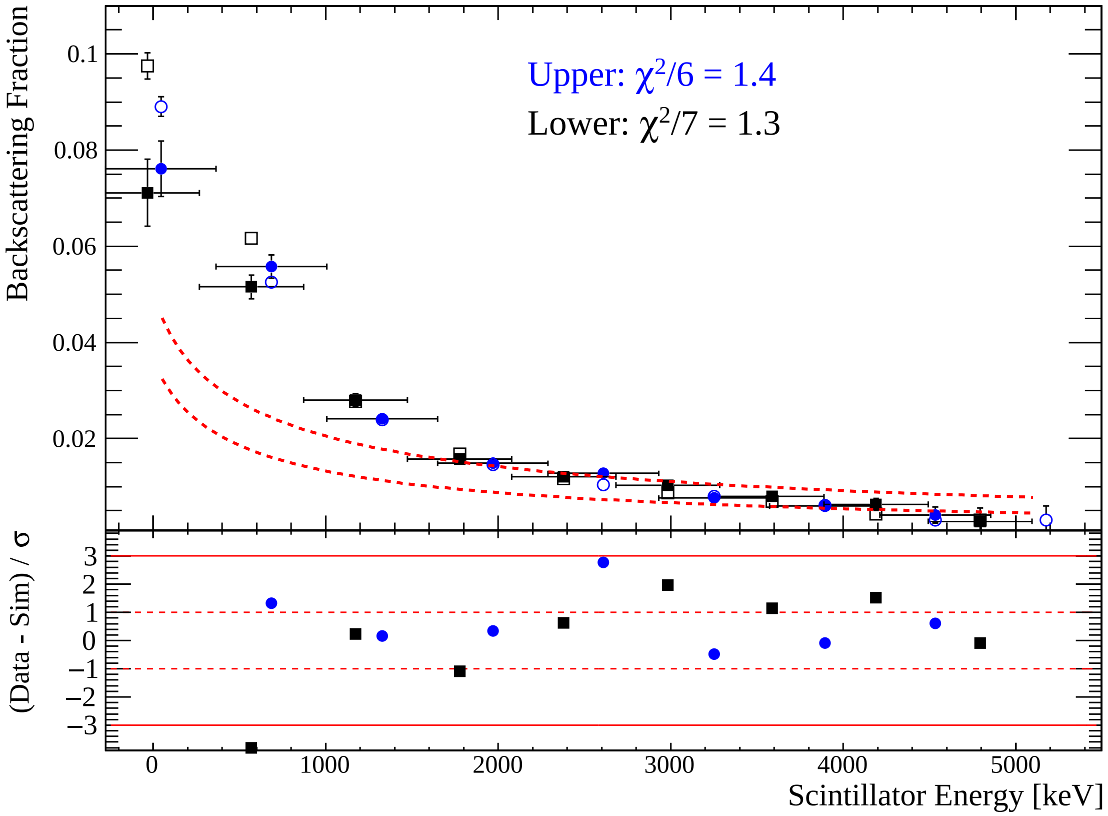

Figure 6.1: Comparison of backscattering between simulation and experiment. Data shown is for Set B. Data is shown in the filled markers with simulation in the open markers. The marker color denotes the detector: upper or lower and the bottom panel gives the residuals. There is good agreement between simulation agreement above 1 MeV. The dashed red lines in the top panel show the 1σ error band from [115]. Although the data does not follow the band very closely, this is not altogether unexpected due to the detector-related effects discussed in the text.

given in Tab. 6.1. The simulation underestimates the backscattering coefficient by 4% in the best case. This level of agreement is sufficient for this work as the effects of backscattering are suppressed by the relatively large distance separating the two detectors. As viewed from one detector, the symmetric β-detector subtends a solid angle of $\approx 1.6\%$ of 2π. Therefore, the underestimate of the backscattering coefficient produces a negligible error of 6×10^{-4}. Future work could investigate this difference more thoroughly by independently simulating the β^+ in our geometry with other packages including `PENELOPE` and `EGSnrc`. The backscattering coefficient does not appear to depend on either the range parameter or the chosen physics list. However, the CFS parameter has a strong impact on the backscattering fraction. As noted above, choosing the value 1 µm is necessary to reproduce the experimental data.

This chapter has described the GEANT4 simulation and shown that it can reproduce the observed fraction of events backscattering from the plastic scintillators. This lends confidence to the assertion that the simulation is able to correctly account for the scattering of β particles *throughout* the experimental geometry. The next chapter will detail detector calibrations, many of which make extensive use of the simulations presented here.

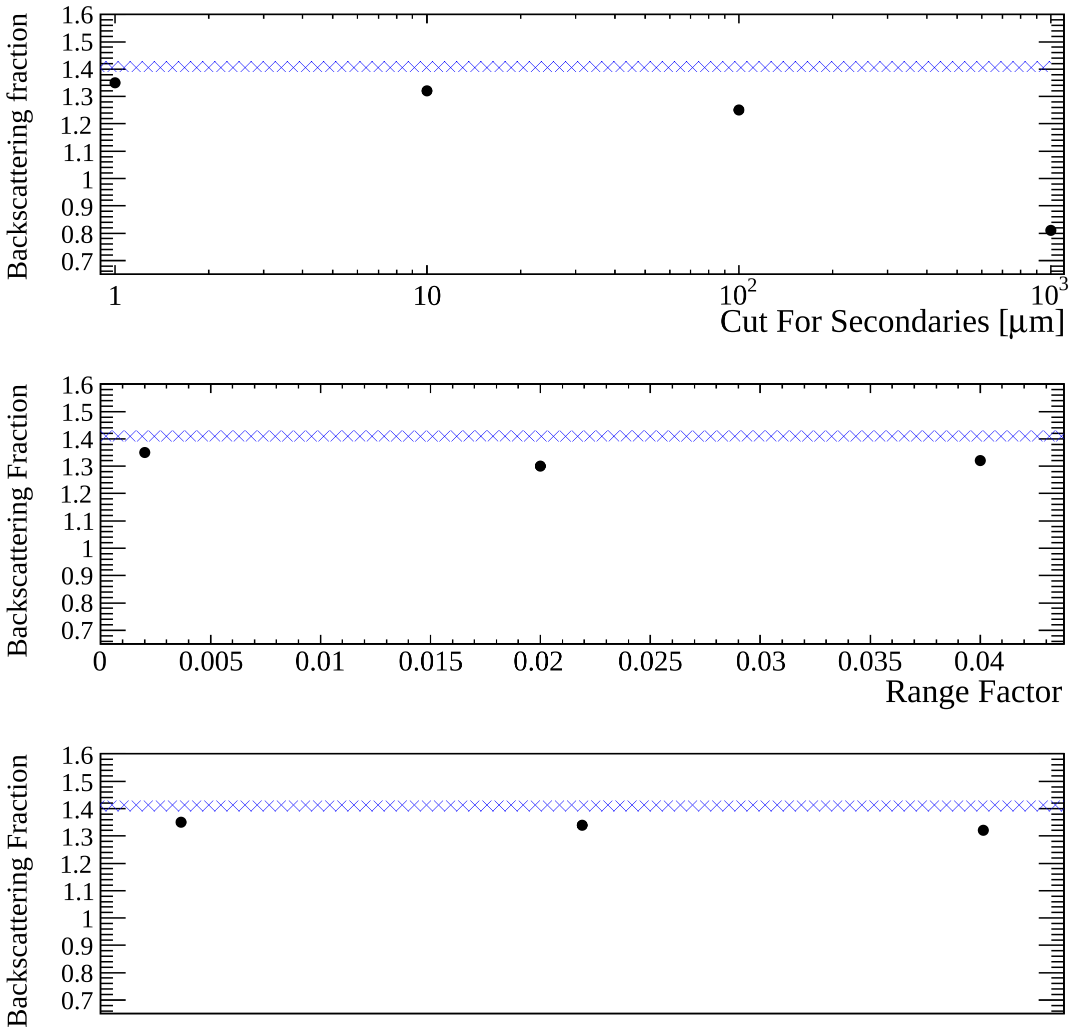

Figure 6.2: Comparison of the backscattering coefficient simulation parameters. The solid band shows experimentally determined 1σ error band for $> 1\,\mathrm{MeV}$ energy deposited in the plastic scintillator. The top panel indicates that the CFS parameter must be to $\sim 1\,\mu\mathrm{m}$ to reproduce the data in our geometry. The range factor and physics list do not appear to have a significant influence on the backscattering coefficient.

7. DETECTOR CALIBRATIONS

7.1 Electron microchannel plate and delay-line anode

The microchannel plate (MCP) detector in our apparatus positioned at negative potential is designed to detect photoelectrons and shakeoff electrons, and is dubbed the eMCP. In addition to a precise timing signal, we have used a three-layer delay-line anode (hexanode or HEX75) to record the hit position on an event-by-event basis.

7.1.1 Position calibration

This detector was calibrated offline using a stainless steel mask of known dimensions and a bright ^{241}Am α-source. Figure 7.1 shows the $\hat{x}-\hat{y}$ position constructed from one pair of delay lines. Labeling the wire planes as u, v, w, and the relative timing between the two ends of the delay line as $u' = u_2 - u_1$ and similarly for v, w (see Fig. 4.3), the Cartesian $\hat{x}-\hat{z}$ coordinates are given by [95]:

$$x = \frac{1}{\sqrt{3}}(2u' + v') \qquad z = \quad u' - v' \tag{7.1a}$$

$$x = -\frac{1}{\sqrt{3}}(w' - 2v') \qquad z = \quad -w' \tag{7.1b}$$

$$x = -\frac{1}{\sqrt{3}}(w' - 2v') \qquad z = \; -w'. \tag{7.1c}$$

The center of each open square, indicated by the red star, is at a known position and used to calibrate the detector. Since high-precision position information on this detector is not critical to the experiment, the calibration is assumed to be linear. The procedure is repeated for each combination of delay lines and an independent calibration is fit to each set of positions. We conservatively take the uncertainty in the position to be twice the maximum difference in the calculated center-position and the true center-position to account for possible non-linear effects outside of the twenty-five most central open-areas used in the fit. The results of this process for each set of planes is given in Table 7.1. The average uncertainty in the HEX75 position is 0.48 mm, which is sufficient for this experiment.

Table 7.1: Calibration results for the HEX75 detector. The linear calibration is applied after orthogonalizing the coordinates with Equation 7.1.

	X Slope mm/ns	X Offset mm	Z Slope mm/ns	Z Offset mm	Δmm
UV	0.36	4.0	0.35	-0.63	0.28
VW	0.35	3.8	0.34	-0.35	0.60
UW	0.35	3.6	0.35	-0.63	0.56

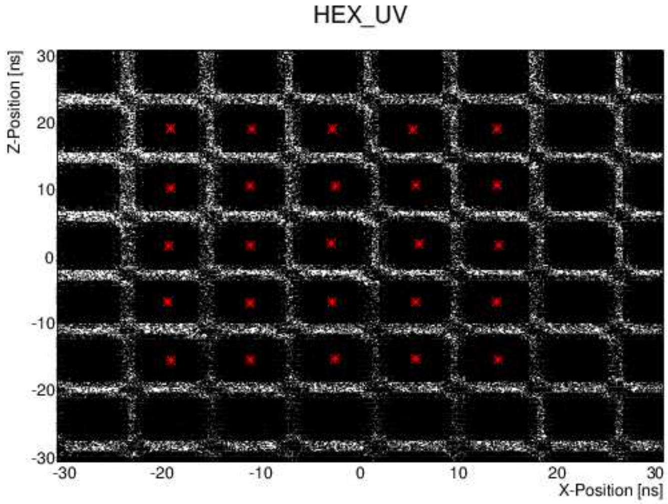

Figure 7.1: HEX75 off-line calibration procedure. The position is reconstructed from two of the three wire planes. The dense regions are areas where the mask is open and the red stars represent the known position of the center of each open area. These points are used to derive the HEX75 calibration.

With three delay-lines present and only two needed for position information, the hexanode configuration allows the calculation of the position information from any two of the three pairs of delay lines. In this case, the positions u', v', w' are calculated and the coordinate with the largest absolute value is discarded and the Cartesian $\hat{x}$, $\hat{z}$ coordinates are calculated using the remaining two. This corresponds to discarding the delay line where one signal traveled the longest distance and is therefore more dispersed and less precise than any other signal. This procedure calculates the Cartesian coordinates using the two delay-lines with the most precise position information for each event.

In the case where one or more delay-line signals were not above threshold, the position information is often able to be reconstructed by making use of the timing signal taken directly from the MCP itself (t_{mcp}). For each delay line, the time sum, $T_{\text{sum}} = u_1 + u_2 - 2t_{\text{mcp}}$ is just the total pulse propagation time along the entire length of the delay line and therefore should be constant. In reality this is a peaked distribution with width giving roughly the resolution of the detector. Using this information, the hexanode coordinates can be calculated according to

$$u' = u_2 - u_1 = 2(u_2 - t_{\text{mcp}}) - T_{\text{sum}} = 2(t_{\text{mcp}} - u_1) + T_{\text{sum}} \tag{7.2}$$

where t_{mcp} is the timing signal directly from the MCP and a similar expression holds for v, w. From here, the Cartesian coordinates are again calculated using Equation 7.1 and the same calibrations given in Table 7.1; no extra calibration is needed. This procedure allows the position to be calculated for events where otherwise this information would be lost without compromising the resolution of the detector.

7.1.2 Timing information and shakeoff electrons

The eMCP is used to tag decays as occurring within the region of optical pumping. After the ^{37}K undergoes β^+-decay, the outermost atomic electron is no longer bound to the daughter Ar nucleus. Starting essentially from rest, this shakeoff electron (SOE) is accelerated by the nearly uniform electric field and detected with the eMCP detector described in this section. If a ^{37}K escapes the region of trapping and optical pumping before decaying, its SOE will not be detected by the eMCP. These decays must be excluded from the analysis because the parent nucleus will not be polarized by optical pumping.

The eMCP allows us to associate βs detected in the DSSSD and scintillator (see Sec. 7.2) both in time-of-flight with respect to the scintillator as well as in position on the hexanode. The relativistic β^+ takes $\approx 0.3\,\mathrm{ns}$ to travel from the center of the vacuum chamber to the front of the scintillator while the SOE is expected to take $\approx 11.5\,\mathrm{ns}$ to reach the eMCP in an electric field of $66\,\mathrm{V/cm}$ and $8.0\,\mathrm{ns}$ in a field of $150\,\mathrm{V/cm}$, although all of these values depend on the exact location of the trap and the details of the electric field.

The pulse-processing electronics introduce an arbitrary time-delay between the two detectors. To measure this offset, I consider events where the β^+ triggers the eMCP *directly*, and a resulting γ is detected in the scintillator. Since all particles are relativistic, the time between these two events does not depend on the details of electric field or trap position: it is expected to equal $t_{\mathrm{delay}} = 0.5\,\mathrm{ns}$. In order to select these events for analysis, I require $E_{\mathrm{scint}} < 340\,\mathrm{keV}$, below the Compton edge from annihilation radiation, in order to bias the spectrum towards selecting γ-events. I also require that the DSSSD described in Sec. 7.2 has *not* been triggered. This intentionally excludes βs that trigger the scintillator directly, while allowing γs, including those generated on the surface of the eMCP, to be included in the analysis.

Fig. 7.2 shows the time-difference spectra of these two detectors with the red dashed curve showing the cuts selecting γs described above. The left (right) panel shows the spectrum for the top (bottom) detector. The large peak (B) comes from events where a β^+ from the decay of ^{37}K was emitted *not* in the direction of one of the scintillators, but instead annihilated on surrounding material and the resulting γ triggered the scintillator. These are in coincidence with the eMCP because the decay occurred from within the trap and the SOE was detected. The smaller peak (A) represents the scattering events described in the last paragraph and are used to determine the timing offset between the two detectors. The horizontal axes on the top of Fig. 7.2 gives the timing of the eMCP detector after this offset has been applied.

Again referring to Fig. 7.2, the solid black curve gives the timing spectrum requiring $E_{\mathrm{scint}} > 340\,\mathrm{keV}$ and that the DSSSD detected a particle. Opposite to the dashed red curve, this selects β-events and excludes γ-events. The two peaks (C) and (D) represent β-SOE coincidences for the two electric field states where the decay occurred from the region of optical pumping (more data was taken at $150\,\mathrm{V/cm}$,

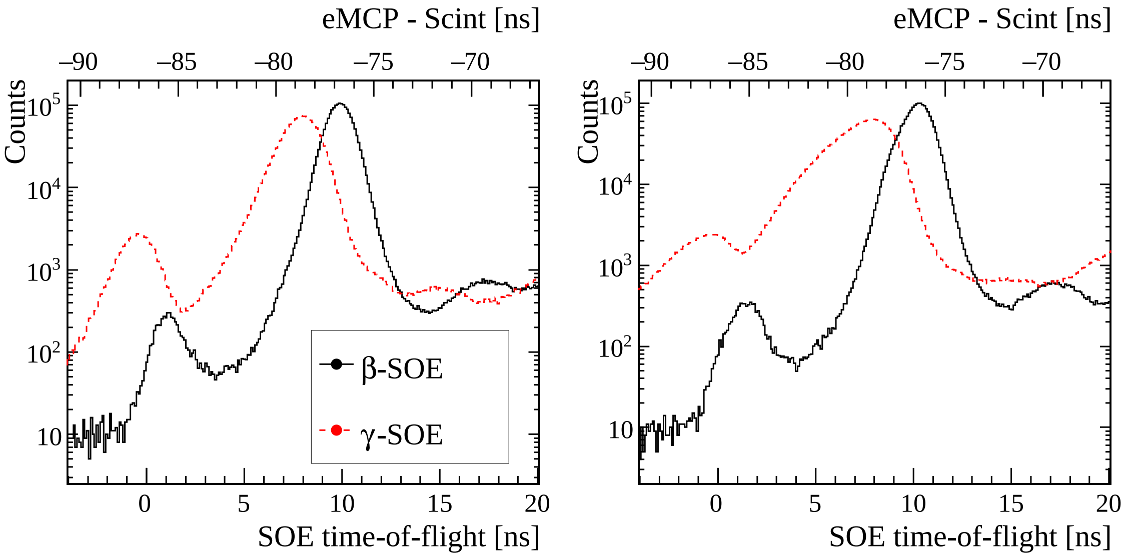

Figure 7.2: Electron MCP timing spectrum with respect to the plastic scintillator. The red dashed curve primarily selects γs entering the scintillator after a β^+ annihilates while the black solid curve shows βs that trigger the scintillator directly. The left (right) panel shows the timing spectrum of the top (bottom) detector.

Table 7.2: Shakeoff electron time-of-flight and position spectra. These values will be used when requiring that decays occurred from within the region of optical pumping.

	$\hat{x}$ [mm]		$\hat{z}$ [mm]		$\hat{y}$ (t) [ns]	
	x_0	σ_x	z_0	σ_z	t_0	σ_t
66.7 V/cm	14.8(1)	6.4(2)	0.4(1)	5.7(1)	14.20(3)	1.10(3)
150 V/cm	9.6(1)	4.5(1)	−1.6(1)	4.5(1)	9.981(9)	0.800(8)

which accounts for the difference in size). These peaks are offset from the γ-SOE peak described above because the initial β^+ in γ-SOE events must annihilate to create the γ, increasing the distance traveled before being detected. The center and width of these distributions are shown in Tab. 7.2. These results are used to select which events are used for the β-asymmetry analysis in Ch. 8.

Finally, the eMCP position information is used as a further condition to define decays occurring from the region of optical pumping. Note that the applied magnetic field, either for the AC-MOT or the optical pumping, effects the trajectory of the SOE. Therefore, the position spectra observed depends on the magnetic field. The position spectra during optical pumping times for the two electric field states are shown in Fig. 7.3. They are also fit to Gaussian functions to measure the center and width of the distributions, with the results shown in Tab. 7.2.

7.2 Double-sided silicon-strip detectors

7.2.1 Waveforms

A pair of silicon-strip detectors are placed along the polarization axis directly in front of the thick scintillator detectors. The primary roles of these detectors are to 1) provide a clean tag that the detected particle is a β^+, 2) provide position information about the β^+, allowing for a complete momentum reconstruction of the event, and 3) record the energy deposited in this detector which can then be added to the energy deposited in the scintillator resulting in a more reliable energy reading of the β^+.

As described in Ch. 4, the entire waveform from these detectors is digitized and recorded in a VF48 waveform digitizer. The entire set of waveforms for a single event from one detector plane (all the $\hat{x}$- strips e.g.) is shown in Fig. 7.4.

During the run, we observed that storing 160 waveforms per event was severely

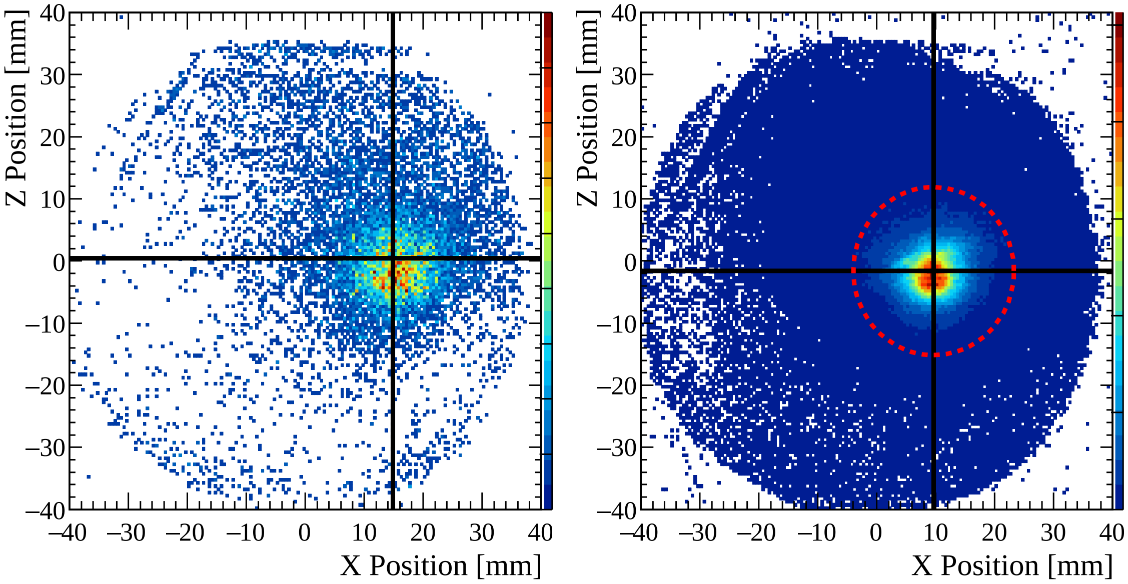

Figure 7.3: Shakeoff electron position while optical pumping. The uniform magnetic field deflects the low-energy electrons as they travel to the detector as shown by the non-zero value of the centroid in the $\hat{x}$-direction. The cross-hairs show the center of the distribution as reported in Tab. 7.2.

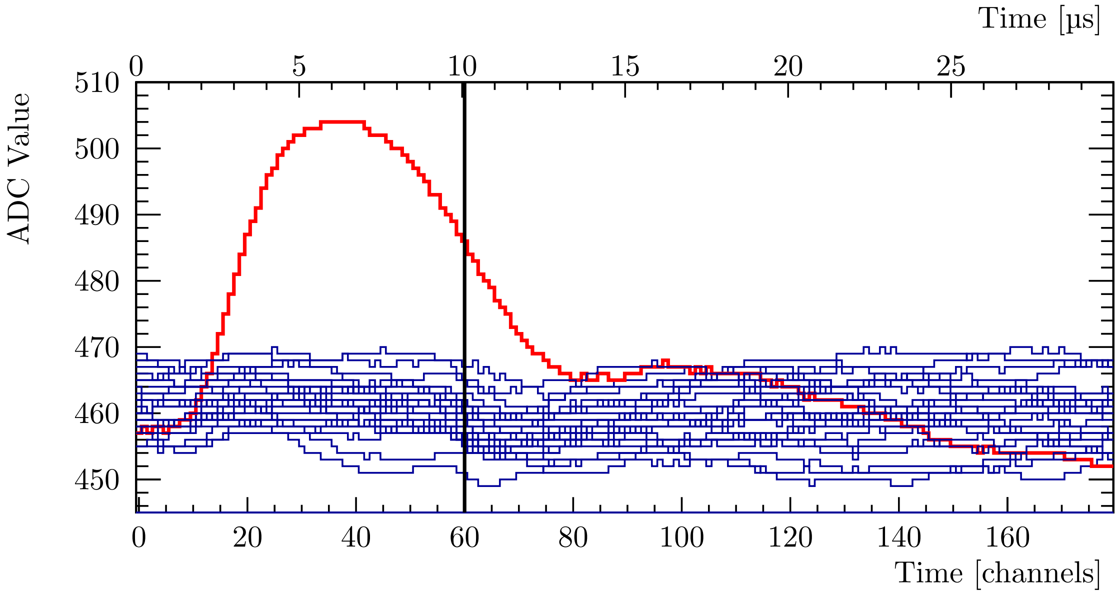

Figure 7.4: Sample BB1 waveforms. Waveforms for one event on the $\hat{x}$-plane of the lower DSSSD. The strip corresponding to the highlighted waveform represents the location the particle entered the detector while the rest of the strips simply record noise. The vertical line represents the portion of the waveform that remained after truncation.

limiting our maximum event rate. To improve this situation, we decreased the number of samples that were stored per waveform from 180 to 60 as indicated by the vertical line in Fig. 7.4. This change was implemented for Run 410 and all following runs (see Tab. 4.1). This allowed us to increase the maximum event rate from 550 Hz to 950 Hz, greatly reducing our dead-time. Since much of the tail of each waveform was not saved, we must use the peak-height rather than the integral of the waveform to represent the energy of the incident particle. With this truncation, we observed no waveforms where the peak appeared likely to occur outside of the truncated region.

Similar to previous work in our group (see Ref. [25], Figure 6.5), the VF48s introduce a DC offset that must be calculated event-by-event. Therefore, the first five samples of each waveform are averaged, and this value is subtracted from the peak height, i.e. the maximum ADC reading recorded for a given event, to obtain the final energy reading for each waveform, defined as Q_{ADC}. In addition to this data, the time corresponding to the peak value described above, t_{peak}, is stored. Using the highlighted wave in Fig. 7.4 as an example, the maximum ADC value is channel 504, occurring at $t_{\mathrm{peak}} = 35$. The average of the first 5 bins is 457.6, giving $Q_{\mathrm{ADC}} = 46.4$.

7.2.2 Energy calibration

The energy spectra of the BB1 detectors are simulated with the GEANT4 simulation described in Sec. 6. This simulation includes the initial energy distribution of outgoing βs as well as the energy loss of the βs as they travel through a thin mirror and Be window before entering the silicon detector. Figure 7.5 shows the simulated energy spectra in these detectors. The black line represents the detector taken as a single piece, while the other curves give the spectrum expected for a single $1\times40\,\mathrm{mm}^2$ strip. The outermost strips have a longer path length through the detector as well as more probability for scattering on surrounding materials or adjacent strips. The effects lead to the differences in the simulated spectra shown in Figure 7.5.

Each BB1 strip is independently calibrated. For each strip, an initial uncalibrated spectrum is generated requiring $E_{\mathrm{scint}} > 500\,\mathrm{keV}$ and $25 < t_{\mathrm{peak}} < 40$ with t_{peak} measured in number of ADC samples. These arbitrary cuts are used only to generate the initial spectra; the final BB1 energy cuts based on $\hat{x} - \hat{y}$ energy agreement are described in Sec. 7.2.3. We observed larger-than-expected variations in the noise on the BB1 strips and traced this variation to differences in noise associated with what preamplifier module each strip used. Some preamplifier modules performed better

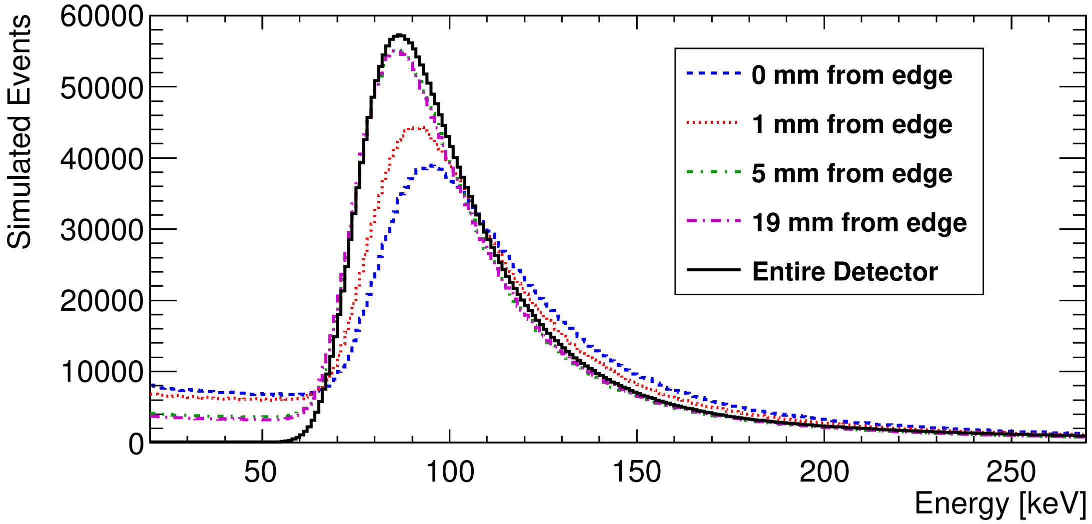

Figure 7.5: Simulated BB1 energy spectra. Comparison of simulated energy spectra for different regions of the detector. Events near the edge show more differences compared to the total energy spectrum.

(introduced less noise) than others. A representative sample of uncalibrated spectra, meant to highlight the varying noise levels, is shown in Figure 7.6.

Examination of Fig. 7.6 reveals three distinct features. To calibrate the detector using the GEANT4 simulation, each of these features should be modeled as accurately as possible. In the next paragraphs, I describe these features and how they were modeled before discussing the result of confronting these models with experimental data.

First, each spectrum in Fig. 7.6 contains a large peak at low-energy ($Q_{\mathrm{ADC}} \approx 10$). This corresponds to events where the incident particle deposited its energy in a *different* strip than the one plotted. Since each strip is only 1/40 of the total detector, this peak is large compared to events where the β entered the strip of interest. Although the peak is roughly Gaussian in shape, the specific peak-height algorithm used to analyze the waveforms biases the distribution to higher channels. This distribution was modeled by generating a series of random numbers to represent a waveform containing only noise. Then, the waveform was processed with the same peak-height algorithm and Q_{ADC} was calculated. Repeating this many time generates a simulated noise spectrum. This simulated distribution is parametrized by its width,

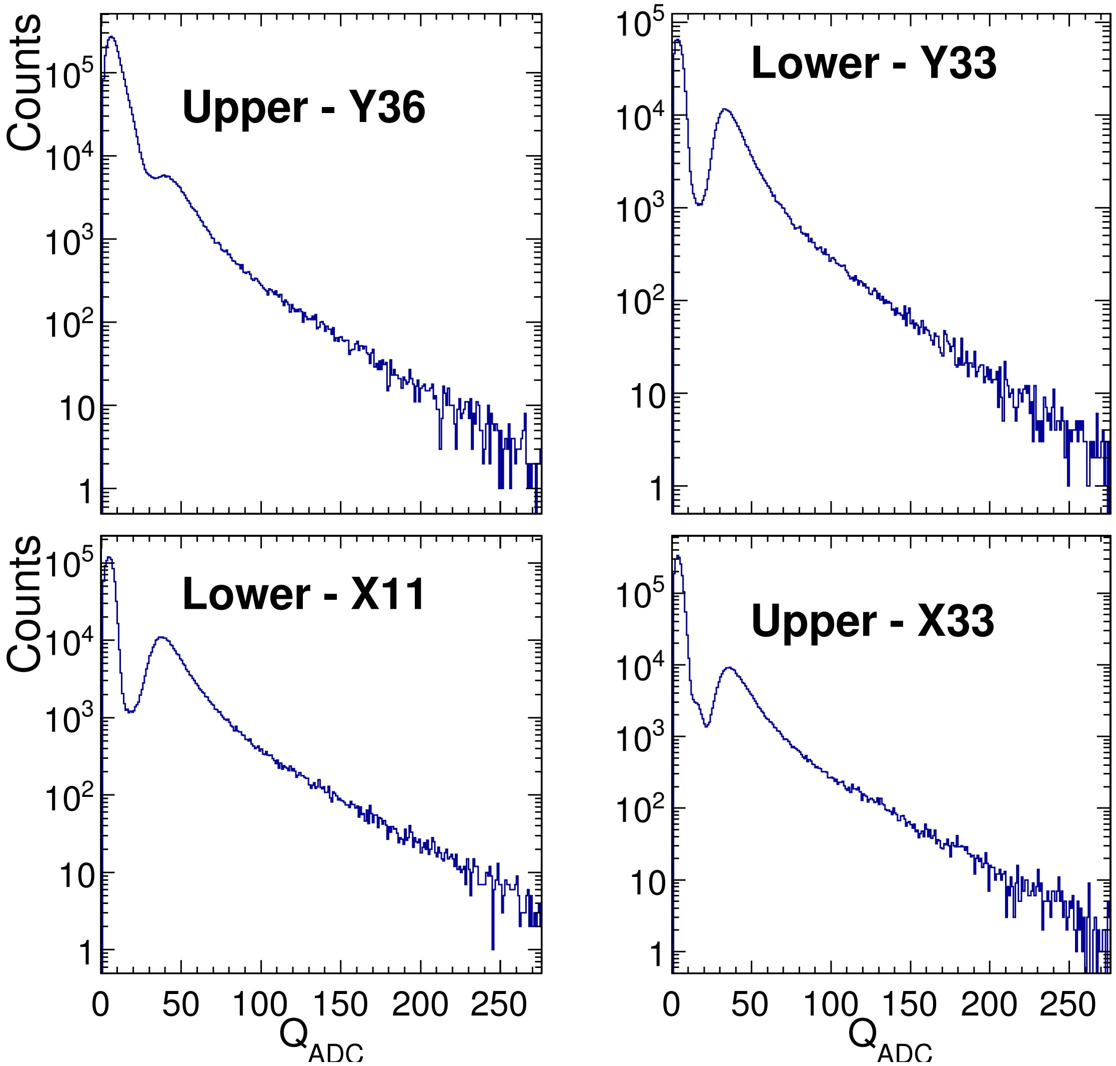

Figure 7.6: Samples of uncalibrated BB1 spectrum. The peak of the Landau distribution is seen to be typically around $Q_{\mathrm{ADC}} \sim 40$ with a long high-energy tail. The text indicates the detector, plane, and strip number corresponding to the displayed spectrum. The “Lower - Y33” and “Lower - X11” spectra both are representative of the commonest spectra with no outstanding features and good resolution. The “Upper - Y36” spectrum demonstrates a strip with larger noise and lower resolution than is typical while the “Upper - X33” spectra has an extra bump in the low-energy noise. In all cases, the noise at low energy corresponds to events where the particle entered a different strip than the one shown.

centroid, and relative amplitude, which are each fit to the experimental data.

The energy distribution from βs entering the *same* strip as shown is roughly a Landau distribution peaked at $Q_{\mathrm{ADC}} \approx 40$. This distribution is simulated in Fig. 7.5. The peak of the distribution provides a known energy with which to calibrate these detectors. The long high-energy tail is characteristic of minimally ionizing βs interacting with thin silicon detectors. Since all particle detectors have an associated noise, I convolute the spectra of Fig. 7.5 with Gaussian noise, assumed to be independent of energy. This reflects an assumption that the noise is electronic in nature and not related to the number of particle-hole pairs produced. Furthermore, the final resolution used in the analysis is calculated from the average difference in the energy deposited in the two detector planes.

Finally, some strips, for example the "Upper-X33" spectrum of Fig. 7.6, show a bump in the spectrum between the noise and Landau peaks ($Q_{\mathrm{ADC}} \approx 13$). This bump, although small compared to the other components of the distribution, influences the fit significantly: it tends to produce Landau peaks at higher-than-simulated energies as well as worse resolution compared to fits with this bump excluded. Although not entirely understood, it is believed that its origin is an extra source of noise coming from only some of the preamplifier modules. This aspect of the data is modeled phenomenologically with a Gaussian function.

Each strip's calibration is fit to the appropriate simulated spectra of Fig. 7.5. It is important to note that all of these spectra have the DC-offset subtracted event-by-event so that $Q_{\mathrm{ADC}} = 0$ corresponds exactly to $E_{\mathrm{DSSSD}} = 0.0\,\mathrm{keV}$. Therefore, there is no calibration offset necessary and the energy is calculated simply as:

$$E_{\mathrm{DSSSD}} = Q_{\mathrm{ADC}}/\lambda \tag{7.3}$$

where $1/\lambda$ is the calibration slope. In addition to the calibration, a detector resolution, σ_{res}, is also included in fitting the simulated spectra to the data. The detector resolution is assumed to be independent of particle energy.

Since the simulated noise spectrum described above is nearly Gaussian in shape, it and the phenomenological Gaussian component are highly correlated with one another for most strips where there is no noticeable need for the extra Gaussian function. However, for the subset of spectra where this extra bump is seen, this correlation is greatly reduced. Therefore, in these cases, I fit the data with both the simulated noise and phenomenological Gaussian functions completely variable. This resulted in an average centroid for the Gaussian of $Q_{\mathrm{ADC}} = 12.9$ and width $\sigma = 4.13$. I then obtained the final results with these values fixed for *all* strips; in the final calibrations only the relative amplitude of this Gaussian function is free to vary.

In summary, the *entire* uncalibrated BB1 spectra, down to $Q_{\mathrm{ADC}} = 0$, is fit to a model containing three components. First is a simulated spectrum produced by GEANT4 and containing a variable slope and resolution. Next is the simulated noise spectrum. The width, center, and relative amplitude compared to β-spectrum are free parameters. Finally, a Gaussian function is included to account for the extra bump in some of the spectra. The centroid and width of this distribution are fixed, but its normalization is free. In order to correctly account for the events in the high-energy tail with very few (< 10) counts per bin, Poisson statistics were used.

Typical fits to the BB1 spectra are shown in Fig. 7.7. The spectrum is overlaid with the fit result with the colors noted in the caption. Note that the top panel demonstrates a strip requiring the extra Gaussian component while in the bottom component this component is entirely negligible. Below each is plotted the difference between simulation and data. There are noticeable differences between the two. However, the differences lie mostly in the region of the spectrum dominated by noise. Clearly, the details of the low-energy noise model do not provide a complete description of the data. However, these problems are not very significant because these noise events are well below the minimum energy threshold and not saved for further analysis.

However, by examining the residuals, it is also true that the data is not completely reproduced by the model even for the portions of the spectrum that is dominated by βs ($E_{\mathrm{DSSSD}} \gtrsim 70\,\mathrm{keV}$). With only one calibration point available (in addition to $E_{\mathrm{DSSSD}} = 0$) at the peak of the Landau distribution at $E_{\mathrm{DSSSD}} \approx 100\,\mathrm{keV}$, the calibration at higher energies is essentially an extrapolation. Therefore, small errors in the calibration at 100 keV can produce larger errors for the βs leaving the most energy in the strip detector.

Before discussing possible explanations for this, I will first put this measurement in context of the entire experiment. This will demonstrate that the calibrations presented here are sufficient to produce a reliable measurement of A_β. The energy deposited in the strip detectors, show in Fig. 7.7, are on the order of a few hundred keV. This is a small energy compared to the total energy of the β, which is recorded in the plastic scintillators. Since the strip detector energy is a small fraction of the

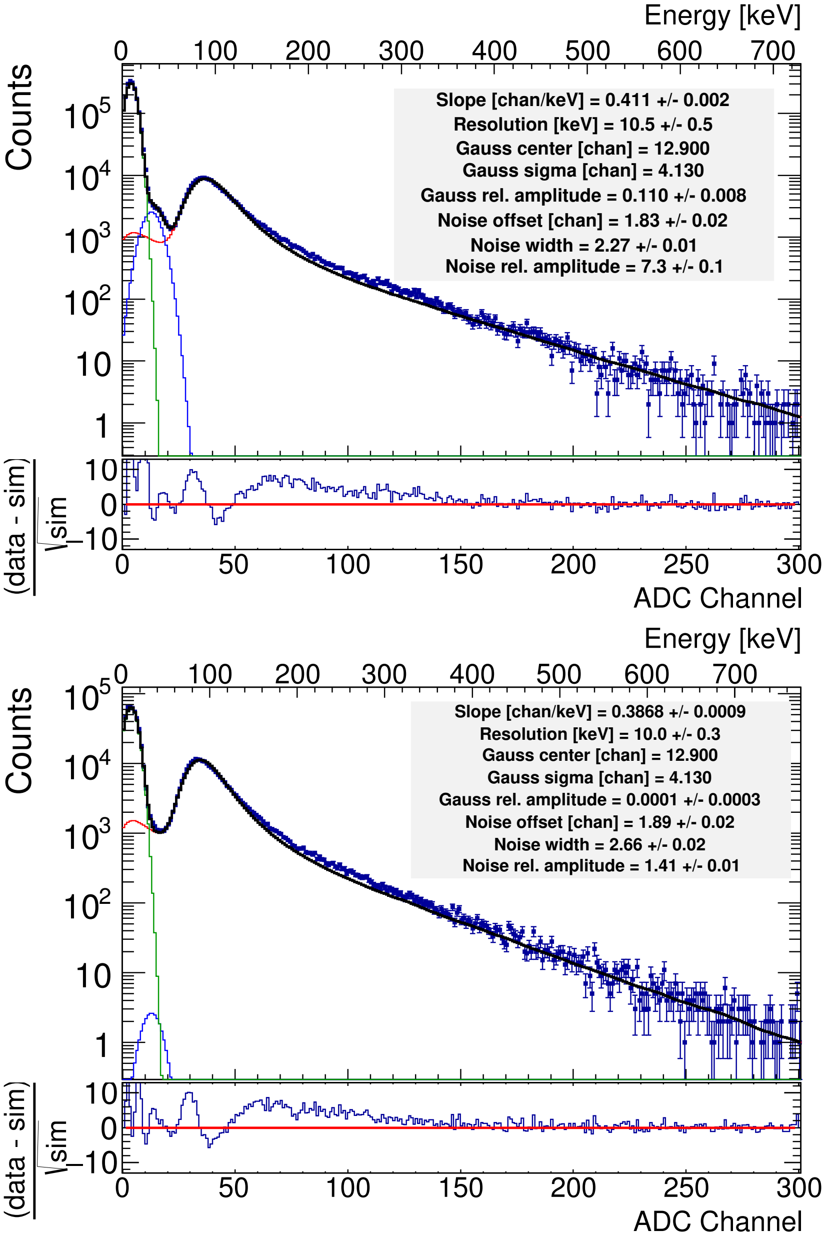

Figure 7.7: Typical fits to the BB1 energy spectra. The three components to the fit are described in the text. The Monte-Carlo simulation is shown in red, the simulated waveform noise in green, and the phenomenological "extra" noise is shown in blue. The sum of the components is shown in black. In the upper panel (upper detector X33), the extra Gaussian function dominates the spectra between the Landau peak and the simulated noise peak. It must be included in order to give the most accurate calibration. In the lower panel (lower detector Y33), this component contributes negligibly. The errors shown have been scaled by $\sqrt{\chi^2/292}$ to account for the disagreement between data and model shown in the residuals below each fit. Discussion of these differences is reserved for the text.

total energy, a small error in the DSSSD energy calibration will not significantly effect the total β energy detected by the combination of scintillator and DSSSD. Nevertheless, the uncertainties in the calibration presented here will be discussed as a systematic uncertainty in Sec. 8.4.

Even considering Fig. 7.7, the calibration of these detectors is still correct. Recall that the calibration is done to essentially one point: the peak of the Landau distribution. In this case, we can test the accuracy of the calibration by comparing the location of this peak in the experimental data after calibration to the simulated data. This result is shown in Fig. 7.8.

Although the most probable (energy) value (MPV) is susceptible to random fluctuations, the simulated and experimental values agree to within 5.1 keV for the strips shown. The mean of the distribution, considering only energy bins dominated by βs, shows even closer agreement. This provides evidence that, although the shape of the distribution at high-energies is not reproduced perfectly, the calibration is correct.

Higher moments of the distribution are sensitive to both the accuracy of the calibration and to the resolution obtained. Again, by comparing the representative values shown in Fig 7.8, there is good agreement between simulation and experiment. All of this points to the conclusion that the calibration is correct and the discrepancies between data and simulation are a result of some other factor.

These possible explanations are associated with limitations in the Geant4 simulation. Geant4 uses a multiple-scattering algorithm to approximate the scattering of high-energy particles, including βs as they pass through thin detectors. These models are known to perform with reduced accuracy below incident energies ≈ 1 MeV [108,109]. Although Geant4 is capable of simulating individual scatters in a single-scattering model, the simulation time required is prohibitive. Furthermore, variations in detector thickness and dead layer can effect the deposited energy. These effects and not included in the simulation. With this in mind, I conclude that there is sufficient uncertainty in the Geant4 simulation to account for the discrepancies seen in Figs. 7.7 and 7.8 without implying an error in the calibration.

7.2.3 Energy agreement and resolution

One important consideration when analyzing the DSSSD spectra is to ensure that the two planes of each detector record the same energy. For these events, we expect $E_x = E_y$ where E_x and E_y are the energy recorded in the $\hat{x}-$ and $\hat{y}$-planes of the

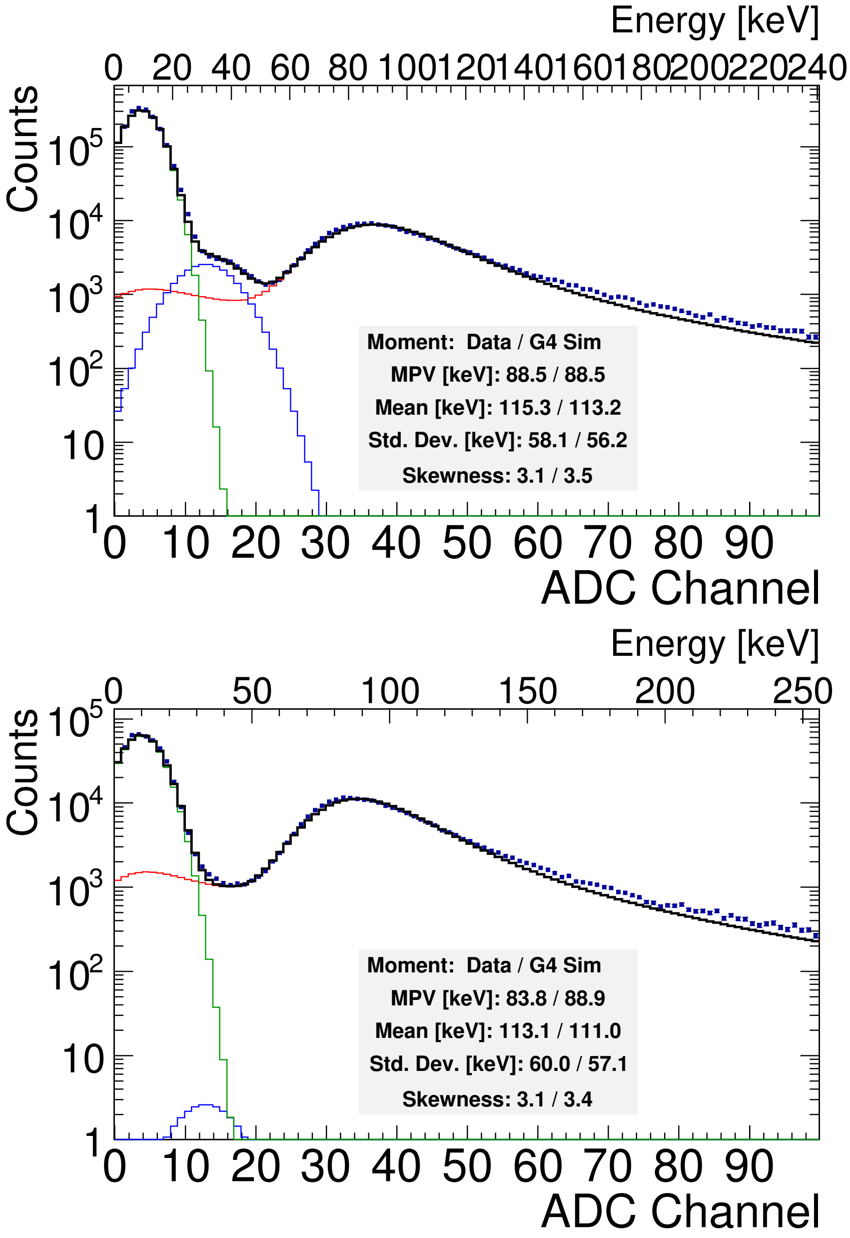

Figure 7.8: BB1 fit results, zoomed in. These are as in Fig. 7.7 highlighting the fit to the Landau peak. Although the data consistently has more counts for the high-energy tail shown here, the peak of the distribution is generally in agreement between simulation and data. This can be seen by noting that the first three moments of the β energy distribution are consistent with simulation. The legend for these figures is the same as in Fig. 7.7 and is described there.

DSSSD. This amounts to a requirement that the energy spectrum for each strip lines up with all the others. Although a common systematic error on the energy deposited in the DSSSD is still possible, the DSSSD will still effectively provide a β-tag as well as position information. While requiring energy agreement also provides a useful way to filter out good events (see Sec. 7.2.4), here I use this both as a consistency check for the detector calibrations as well as a way to quantify the resolution of each detector strip.

Figure 7.9 shows the energy of a specific $\hat{x}$-strip plotted along the horizontal axis with the corresponding energy in the $\hat{y}$-plane along the vertical axis. In each event, the $\hat{y}$-strip with the highest energy reading is plotted while the rest are not shown. The result is that, if enough events are recorded, all of the $\hat{y}$-strips are included along the vertical axis. Since the energy reading in the $\hat{x}$- and $\hat{y}$-directions are expected to be the same, most ("good") events fall roughly along a line with slope equal to 1.0. In effect, Fig. 7.9 compares the *average* calibration of the strips in the $\hat{y}$-plane with calibration of *just one* strip in the $\hat{x}$-plane.

To obtain the red points in Fig. 7.9, the 2D spectrum is projected along the vertical axis for a specific bin in the horizontal direction. This projection is fit to a Gaussian function. The red points are shown at x equal to the center of the bin in the horizontal direction and y equal to the centroid of the Gaussian fit. After repeating this for all the points shown in Fig. 7.9, the data points are fit to a straight line to determine its slope.

Ideally, this slope would be exactly 1.0. A large deviation from 1.0 implies that the calibration of the specific $\hat{x}$-strip plotted on the horizontal axis does not agree with the *average* calibration of the $\hat{y}$-strips. Therefore, the slope of this line is used to correct the calibrations in order to force this slope to be exactly 1.0:

$$\lambda \to \lambda/m. \tag{7.4}$$

In this way, the calibration of the various strips are "aligned" with one-another. Although this does not guarantee that the absolute calibration is correct, it does permit requiring $E_x \approx E_y$ as a condition for accepting an event.

After correcting all the $\hat{x}$-strips, the process is repeated: specific $\hat{y}$-strips are plotted along the horizontal axis against the energy recorded in the various $\hat{x}$-strips. Then, the $\hat{y}$-calibration is corrected to agree with the average (corrected) $\hat{x}$-calibration. The average size of this correction was 1.4%, with only 4/155 func-

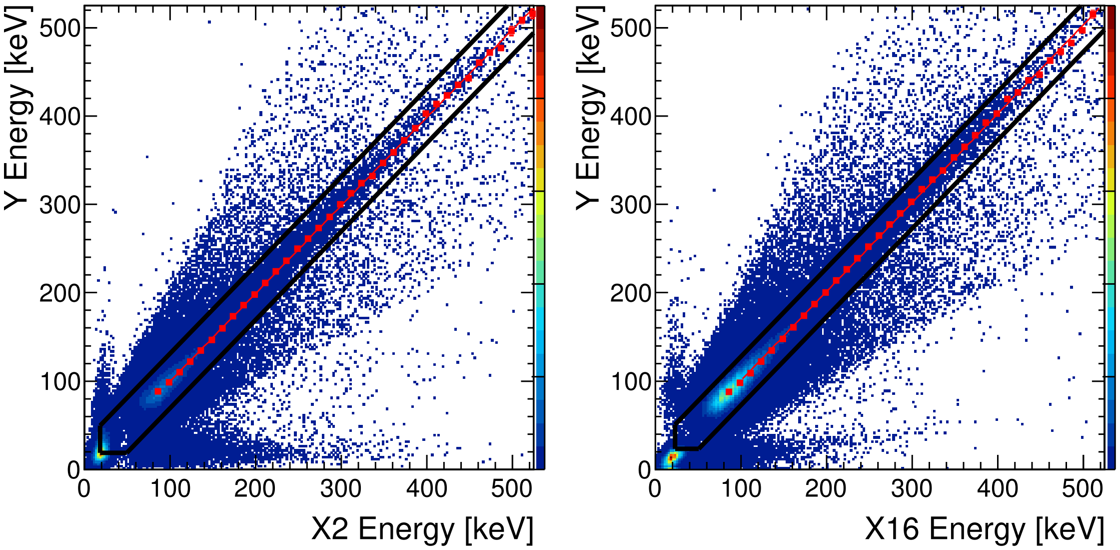

Figure 7.9: BB1 energy linearity and x-y comparison. Demonstration of the linearity requirement between the two faces of the silicon-strip detectors. Good events should have the same energy recorded in the two planes. The red points show the center of a Gaussian fit for the $\hat{y}$-energy at a fixed $\hat{x}$-energy bin while the line is a fit to these points. The fit is used to correct the calibration of the strips in order to align them with average of the perpendicular strips. Note that the calibration has been corrected as shown in this figure so that the slope of the line is very nearly 1.0. The black lines show the energy and energy-agreement conditions imposed on the detector that define a single-pixel event. The left panel shows the upper detector, while the right panel shows the lower detector.

tioning strips having corrections $> 5\%$.

Once the calibrations, including the corrections described above, are complete the resulting energy agreement can be checked by displaying the average *difference* between the energy recorded in an $\hat{x}$-strip and the corresponding $\hat{y}$-strip. Figure 7.10 gives typical examples of these spectra requiring that exactly one strip has been triggered in both the $\hat{x}$- and $\hat{y}$-planes. This reduces the tails of the distributions where energy is shared between adjacent strips. That these distributions are centered near $E_x = E_y$ demonstrates that the energy calibration is in agreement between the two planes. Furthermore, the widths of these distributions quantify the resolution of the detector: the average resolution of a functioning strip via this method is $\sigma = 11.5\,\text{keV}$ (27.1 keV FWHM). The strip-by-strip data for the calibration and resolution, as well as the single-strip threshold described in Sec. 7.2.4 are shown in Tab. 7.3 and 7.4.

The distributions shown in Fig. 7.9 appear to deviate more from the best-fit line as the energy deposited in the BB1 detector increases. This is likely the result of decreasing resolution at higher values of the deposited energy. The analysis described below requires energy agreement within a range that is independent of deposited energy. This may introduce a small bias towards wrongly rejecting events that deposit the most energy in the BB1 detector. However, varying the level of agreement required provides an approximate way to account for this and is considered as a systematic uncertainty in Sec. 8.4 and found to *not* be a dominant uncertainty.

Table 7.3: Energy calibration and resolution of upper DSSSD. Energy calibration includes the small corrections used to align the $\hat{x}$- and $\hat{y}$-energies. Also shown is the individual threshold energy for each strip. This is calculated from the fits to the GEANT4 simulation (Figs. 7.7, 7.8) and is included to demonstrate the amount of variability in the strip detector / preamplifier performance. Strips with no values listed were not functioning and are excluded from the analysis.

Strip #	$\hat{x}$-strips			$\hat{y}$-strips		
	Calib. chan/keV	Resolution keV	E^i_{min} keV	Calib. chan/keV	Resolution keV	E^i_{min} keV
0	0.395(2)	10.6(2)	29.0		-	
1	0.380(3)	10.9(2)	31.0	0.437(2)	11.0(3)	21.5
2	0.407(2)	10.3(1)	27.6	0.427(5)	11.7(1)	45.7
3	0.402(2)	10.7(1)	28.6	0.424(1)	10.4(1)	19.7

Table 7.3: (continued)

Strip #	$\hat{x}$-strips			$\hat{y}$-strips		
	Calib. chan/keV	Resolution keV	E^i_{min} keV	Calib. chan/keV	Resolution keV	E^i_{min} keV
4	0.394(1)	10.3(1)	28.9	0.435(3)	11.2(1)	44.8
5	0.413(2)	10.5(2)	27.8	0.430(1)	10.2(1)	19.7
6	0.403(1)	10.5(1)	28.4	0.434(3)	12.0(1)	48.0
7	0.417(2)	10.6(1)	27.6	0.424(1)	10.4(2)	20.0
8	0.400(1)	10.3(1)	28.6		-	
9	0.396(2)	10.9(1)	28.8	0.444(1)	10.4(2)	19.0
10	0.406(1)	10.4(1)	28.2		-	
11	0.384(2)	10.8(1)	27.4	0.446(1)	10.2(2)	19.0
12	0.402(1)	10.4(1)	28.5	0.437(3)	12.1(1)	45.6
13	0.417(2)	12.3(2)	32.5	0.436(1)	10.1(1)	19.4
14	0.396(1)	10.5(1)	29.1	0.436(3)	11.4(1)	45.1
15	0.404(2)	10.7(1)	28.6	0.439(1)	10.2(1)	19.2
16	0.408(1)	10.4(1)	28.3	0.443(2)	11.0(1)	42.9
17	0.408(2)	10.8(1)	28.4	0.460(1)	10.1(1)	18.3
18	0.414(1)	10.3(1)	27.9	0.445(2)	10.7(1)	43.2
19	0.412(2)	10.9(1)	28.2	0.439(1)	10.0(1)	19.4
20	0.395(1)	13.1(1)	34.3	0.467(2)	10.4(1)	41.0
21	0.427(2)	10.7(1)	27.2	0.424(1)	10.1(1)	20.1
22	0.417(1)	10.4(1)	27.7	0.440(2)	10.5(1)	40.8
23	0.414(2)	10.7(1)	28.0	0.438(1)	10.2(1)	19.5
24	0.393(1)	10.4(1)	29.3	0.435(2)	10.5(1)	41.7
25	0.422(2)	10.8(1)	27.6	0.425(1)	9.9(1)	19.8
26	0.406(1)	10.4(1)	28.5	0.420(2)	10.5(1)	43.1
27	0.405(2)	10.7(1)	28.8	0.425(1)	9.9(1)	20.1
28	0.411(1)	10.4(1)	28.1	0.430(2)	10.4(1)	42.2
29	0.428(2)	10.6(1)	27.4	0.434(1)	10.0(1)	19.7
30	0.395(1)	10.5(1)	29.3	0.443(2)	10.5(1)	43.2
31	0.397(2)	10.8(1)	29.3	0.436(1)	10.0(1)	19.6

Table 7.3: (continued)

Strip #	$\hat{x}$-strips			$\hat{y}$-strips		
	Calib. chan/keV	Resolution keV	E^i_{min} keV	Calib. chan/keV	Resolution keV	E^i_{min} keV
32	0.400(1)	10.2(1)	29.1	0.417(2)	11.5(1)	47.7
33	0.419(2)	10.4(1)	27.7	0.443(1)	10.0(1)	19.2
34	0.402(1)	10.2(1)	28.8	0.417(2)	12.8(1)	54.3
35	0.395(2)	10.6(1)	29.3	0.439(1)	10.0(1)	21.7
36	0.386(1)	10.3(1)	29.6	0.428(2)	13.7(1)	53.8
37	0.401(3)	10.7(1)	28.1	0.422(1)	10.2(1)	22.4
38	0.396(2)	10.4(1)	28.8	0.426(2)	13.8(1)	56.2
39	0.411(4)	11.3(2)	29.5	0.408(2)	10.7(2)	22.6

Table 7.4: Energy calibration and resolution of lower DSSSD. See caption for Tab. 7.3 for explanation.

Strip #	$\hat{x}$-strips			$\hat{y}$-strips		
	Calib. chan/keV	Resolution keV	E^i_{min} keV	Calib. chan/keV	Resolution keV	E^i_{min} keV
0	0.429(2)	9.5(1)	36.2		-	
1	0.422(2)	9.3(1)	27.1	0.413(2)	9.9(1)	24.5
2	0.421(2)	9.3(1)	34.1	0.408(2)	9.4(1)	21.8
3	0.436(1)	9.2(1)	26.1	0.414(2)	9.5()	24.9
4	0.409(1)	9.2(1)	32.7	0.412(1)	9.4()	20.9
5	0.419(1)	9.1(1)	27.4	0.413(1)	9.3(1)	22.9
6	0.411(1)	9.2(1)	32.6	0.429(1)	9.4(1)	22.2
7	0.430(1)	9.3(1)	26.7	0.410(1)	9.4()	22.9
8	0.425(1)	9.3(1)	34.1	0.416(1)	9.3(1)	20.4
9	0.431(1)	9.3(1)	26.7	0.393(1)	9.3(1)	24.0
10	0.430(1)	9.3(1)	33.8	0.421(1)	9.5(1)	22.6
11	0.440(1)	9.4(1)	26.3	0.395(1)	9.4()	23.9
12	0.429(1)	9.4(1)	33.9	0.434(1)	9.2(1)	19.5

Table 7.4: (continued)

Strip #	$\hat{x}$-strips			$\hat{y}$-strips		
	Calib. chan/keV	Resolution keV	$E^i_{\min}$ keV	Calib. chan/keV	Resolution keV	$E^i_{\min}$ keV
13	0.409(1)	9.6(1)	28.2	0.431(1)	9.2()	21.9
14	0.410(1)	9.4(1)	33.0	0.413(1)	9.3()	20.5
15	0.426(1)	9.5(1)	27.1	0.425(1)	9.2()	22.2
16	0.450(1)	9.2(1)	32.3	0.411(1)	9.3()	20.6
17	0.444(1)	9.2(1)	26.1	0.404(1)	9.4()	23.5
18	0.433(1)	9.4(1)	33.6	0.443(1)	9.2(1)	21.1
19	0.435(1)	9.3(1)	26.6	0.407(1)	9.4(1)	23.4
20	0.429(1)	9.5(1)	33.9	0.418(1)	9.2(1)	20.2
21	0.429(1)	9.5(1)	27.0	0.440(1)	9.3()	21.6
22	0.423(1)	9.4(1)	34.4	0.418(1)	9.4()	20.1
23	0.427(1)	9.3(1)	27.2	0.430(1)	9.2(1)	21.8
24	0.442(1)	9.3(1)	33.1	0.402(1)	9.3(1)	21.1
25	0.439(1)	9.3(1)	26.4	0.419(1)	9.4()	22.5
26	0.431(1)	9.4(1)	33.8	0.448(1)	9.2()	20.9
27	0.435(1)	9.4(1)	26.8	0.430(1)	9.4(1)	22.0
28	0.438(1)	9.5(1)	33.3	0.434(1)	9.3()	21.8
29	0.415(1)	9.5(1)	28.0	0.409(1)	9.3(1)	23.2
30	0.437(1)	9.4(1)	33.4	0.406(1)	9.3(1)	21.0
31	0.413(1)	9.4(1)	28.0	0.430(1)	9.4()	24.4
32	0.444(1)	9.3(1)	32.9	0.401(1)	9.4()	21.2
33	0.422(1)	9.3(1)	27.5	0.389(1)	10.1(1)	26.9
34	0.441(1)	9.2(1)	35.3		-	
35	0.437(1)	9.2(1)	26.4	0.398(1)	10.5(3)	26.3
36	0.411(2)	9.3(1)	34.9	0.437(1)	9.3(1)	21.1
37	0.403(1)	9.5(1)	28.2	0.408(2)	9.4(1)	22.8
38	0.417(2)	9.5(1)	36.6	0.400(3)	9.7(1)	21.8
39	0.407(2)	9.8(2)	30.6	0.431(3)	10.8(3)	26.7

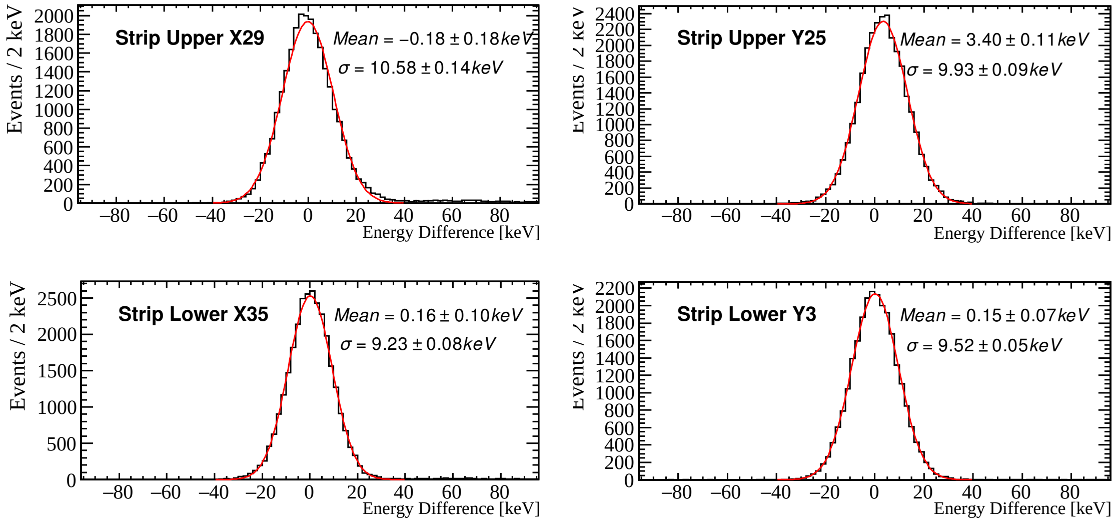

Figure 7.10: BB1 energy resolution. Energy agreement between the two planes of the silicon-strip detector requiring exactly one strip above threshold in both detector planes. That the distributions are centered near 0 is evidence that the calibrations $\hat{x}$- and $\hat{y}$-planes are in agreement. The widths of these distributions is used to quantify the detector resolution.

7.2.4 Event selection and position information

Once the resolution and calibration of the strips are known, the information is used to make decisions about which events to save for further analysis and the position of these events within the detector. In general, two requirements must be satisfied for a "good" event: the energy recorded by the two detector planes should be consistent and the position of the hit should correspond to a single pixel within the detector. The simplest events to analyze are those where only one strip recorded an energy above threshold in both the $\hat{x}$- and $\hat{y}$-directions with energies E_x and E_y. Note that due to the variation in preamplifier performance, each strip is compared to its individual threshold shown in Tables 7.3 and 7.4. The motivation for this will be described in the next paragraphs. The energy recorded is considered consistent if

$$|E_x - E_y| \leq n_{\text{cut}}\sqrt{\sigma_x^2 + \sigma_y^2} \tag{7.5}$$

where n_{cut} is an adjustable parameter and σ_x (σ_y) is the resolution of the relevant $\hat{x}$-strip ($\hat{y}$-strip). If this condition is satisfied, the final energy reading is taken as the average of E_x and E_y, weighted by the respective resolutions of the corresponding strips. Furthermore, the position of the hit is taken to be the intersection of the centers of the two strips above threshold. Numbering the strips $s = \{0 - 39\}$, the position corresponding to the center of each strip is given by:

$$r = 19.5 - s \text{ mm} \qquad \text{Upper det. Y-plane} \tag{7.6a}$$

$$r = s - 19.5 \text{ mm} \qquad \text{All others} \tag{7.6b}$$

where r can stand for x or y as appropriate.

In addition to the energy agreement condition, I also require that the peak of the waveforms occur simultaneously. Although the energy agreement condition is more stringent, this additional cut further reduces the number of noisy events. The distribution in Fig. 7.11 shows $t^x_{\text{peak}} - t^y_{\text{peak}}$ for the two detectors. That the distribution is centered around zero is encouraging. The widths shown in the figure are used to define the time-agreement condition:

$$|t^x_{\text{peak}} - t^y_{\text{peak}}| \leq n_{\text{cut}}\sigma_t \tag{7.7}$$

where n_{cut} is the same adjustable parameter as in Eq. 7.5. For an event to be considered "good", it must satisfy both Eq. 7.5 and Eq. 7.7.

Having described the condition for energy agreement, the remainder of the subsection describes two special classes of events and how they are analyzed in the strip-detector data. First, there are back-scattered events that pass through the DSSSD twice. These events are characterized by having two hits on the detector that each satisfy the energy and time agreement conditions. One situation which produces such a "multi-hit" event is when a β^+ passes through the DSSSD before scattering off of the scintillator and back through the DSSSD, although scattering off of other sources is, of course, possible. These fraction of multi-hit events compared to single-hit events was compared to GEANT4 simulations in Sec. 6.1. Second, I will describe events that leave energy in two adjacent strips as they pass through the detector. These "inter-strip" events are *not* multi-hit events, and are most commonly the result of a β^+ simply passing through the detector once, but near the intersection of two strips. The logic flow used to analyze these events is shown in Fig. 7.12 and described in the next paragraphs.

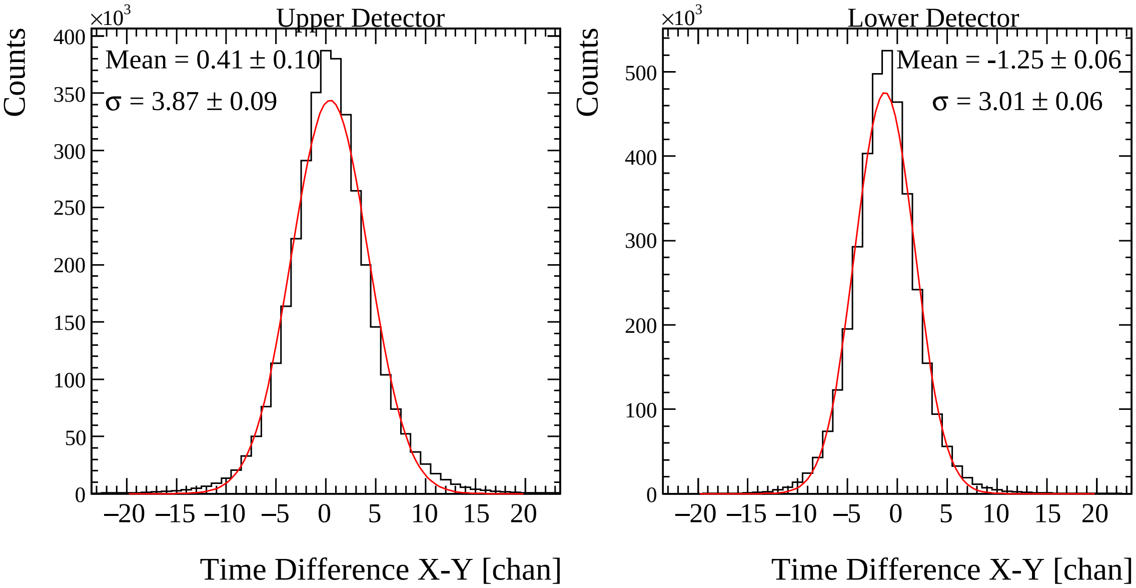

Figure 7.11: BB1 waveform peak amplitude time spectra. Distribution of the peak time of each of the strip-detector waveforms. Agreement in time between the two signals is used, along with energy agreement, to select events for further analysis.

Since both multi-hit and inter-strip events are quite rare, neglecting multi-hit events that leave energy in adjacent strips introduces negligible error but simplifies the analysis enormously. Note that the 16.7 ns timing resolution of the VF48s does not allow multi-hit events to be distinguished based on arrival time. Therefore, multi-hit events satisfy a strict, but simple, set of criteria: a pair of hits in both the $\hat{x}$- and $\hat{y}$- detector planes with each pair satisfying the energy and time agreement criteria.

In inter-strip events, a single particle passing through the detector deposits energy into two adjacent strips, resulting in two strips recording an energy above the threshold. This can occur in none, one, or both detector planes in a given event. In all cases, each plane is analyzed independently as described here to arrive at E_x and E_y (as well as σ_x and σ_y). Once this is complete, the two energy readings are checked for consistency using Eq. 7.5 regardless of the number of strips above threshold in each plane.

Denoting the energy in the two adjacent strips as E_i and E_{i+1}, the analysis should

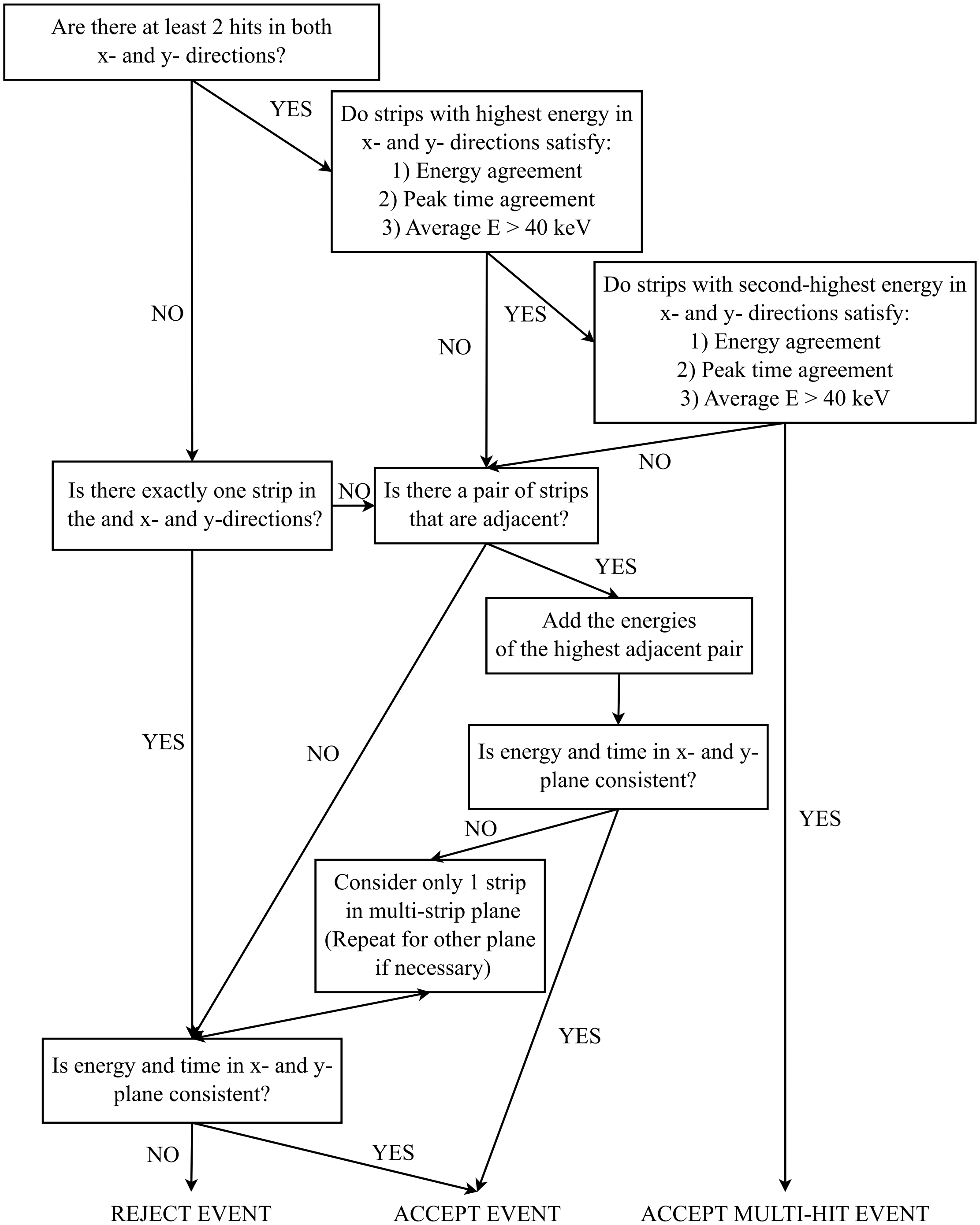

Figure 7.12: BB1 detector energy agreement algorithm. Multi-hit events are searched for first and require energy agreement as well as a comparison to an overall detector threshold. Next, the algorithm searches for adjacent pairs of strips that are each above individual strip thresholds and requires energy agreement between the two detector planes. Finally, there is a check for energy agreement considering only one strip per plane.

accept events where the minimum energy deposited in the detector by any β event (e.g. $E_{\text{min}} = 60\,\text{keV}$) is distributed over the two strips. These events satisfy:

$$E_i + E_{i+1} \gtrsim E_{\text{min}} = 60\,\text{keV}. \tag{7.8}$$

Therefore, the individual strip thresholds, E^i_{min} (see Tables 7.3, 7.4), must be set significantly *lower* than E_{min}. In order to accomplish this, as well as to account for the varying noise level between strips and preamplifier modules, E^i_{min} is set at a different energy for each strip such that the signal-to-noise (S/N) ratio at the threshold energy is uniform across the detector. Said another way, I set a uniform S/N threshold by imposing an uneven energy threshold. The values shown in Tables 7.3 and 7.4 correspond to a S/N threshold of 0.17, or an average energy threshold of $\bar{E}_{\text{min}} = 28\,\text{keV}$. Although it is desirable to set this threshold still lower, this is not possible at the current level of noise seen by the detectors. In future experiments a more sophisticated analysis that takes into account the pulse shape as well as simply the peak height may allow us to achieve a lower threshold with this detector.

Many events that are the result of electronic noise pass this low threshold. In order to allow for inter-strip events in the face of this noise, I select events *only* where the above-threshold strips are immediately adjacent. If more than one set of strips is adjacent, the pair of strips with the highest total energy is used. Although this algorithm does not accept events leaving energy in three adjacent strips (unless the event passes as a two-strip event), these events are extremely rare and can be safely excluded from the analysis. Finally, if no pair of above-threshold events is adjacent, the event is analyzed considering only the strip with maximum energy.

Once each plane is analyzed for inter-strip events, the energy agreement condition for the two detector planes is checked and events passing this requirement are saved for further analysis. The energy of each plane is simply equal to the sum of the energies deposited in the two strips:

$$E_x = E_i + E_{i+1} \tag{7.9}$$

where the same is true in the $\hat{y}$-direction. The resolution of each plane is the average resolution of the two relevant strips. Defining the position of the two strips as r_i and r_{i+1} by using Eq. 7.6, each hit coordinate is calculated as:

$$r = \frac{r_i E_i + r_{i+1} E_{i+1}}{E_i + E_{i+1}}. \tag{7.10}$$

The very low thresholds (E^i_{min}) tend to assign too many events to the inter-strip category. For example, if a particle leaves energy in strip i, while strip $i+1$ records noise above E^{i+1}_{min}, the calculated energy of this event would be incorrect and the event may be rejected because of poor energy agreement between the two planes. Therefore, if a inter-strip event fails to satisfy the energy and time agreement conditions, it is re-checked considering only the strip with the highest energy reading. If there is now energy agreement, the event is saved for further analysis.

The position distribution of detected events on the DSSSD, shown in Fig. 7.13, provides a sensitive test of the analysis presented here. The distribution is strongly peaked at the locations of the strip-centers because most events leave energy in only one strip. That this distribution is flat near the center of the detector implies that the uneven energy thresholds have correctly accounted for the varying amount of noise in each strip of the detector. There are fewer events near the edges of the detector. This is a result of the stainless steel mirror mount also functioning as a collimator. The opening of the collimator is a square with sides 31 mm and the decrease in events is consistent with both this dimension as well as GEANT4 simulations of the detector and collimator.

The bottom panel is zoomed in to show inter-strip events. The position of these events appears to be peaked 1/2 of the way between adjacent strips. Events that occur very near one strip deposit most of the energy in that strip and only a small fraction of their total energy in the adjacent strip. Therefore, the energy in the adjacent strip is often below even the low thresholds used here. As a result, multi-strip events near the edge of one strip are possibly misassigned as single-strip events, and an event satisfying the multi-strip criteria is most likely to deposit roughly equal energy in the two adjacent strips, leading to the position distribution shown.

Finally, Fig. 7.14 shows the energy distribution of events satisfying the conditions described here. It is overlaid with a GEANT4 spectrum and shows good agreement between simulation and experiment for both the upper and lower detector. The mean of the spectra for the data and simulation differ by < 6 keV. As described on an individual strip basis in Sec. 7.2.3, the differences shown here can be accounted for considering the variation in detector thickness, and the limitations of GEANT4.

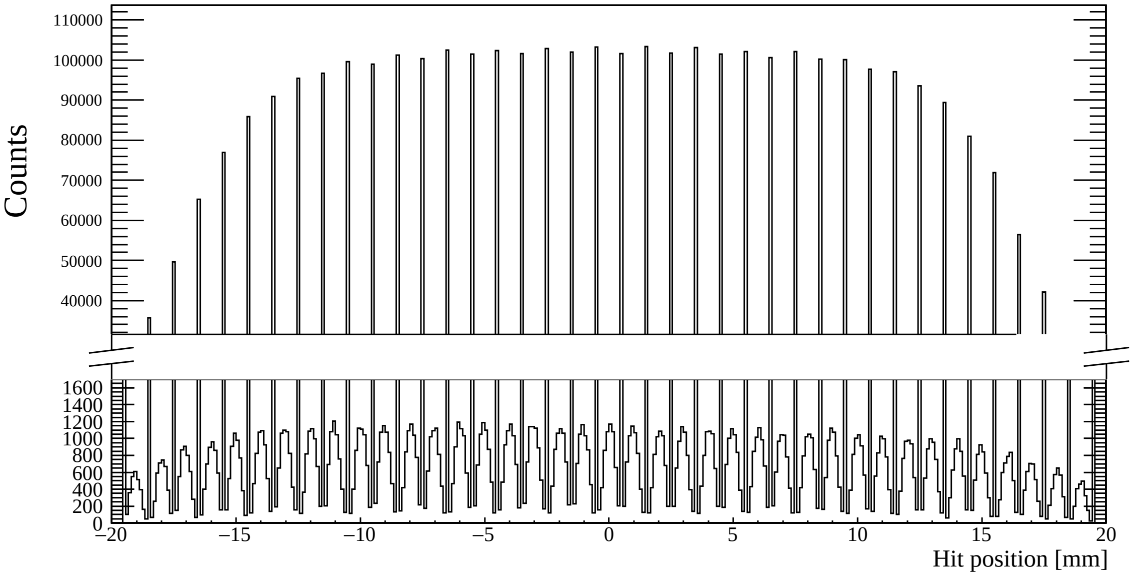

Figure 7.13: BB1 detector position spectrum. Distribution of the hit position on the $\hat{x}$-plane of the lower detector. The inter-strip events appear peaked 1/2 of the way between adjacent strips because events that are very close to one strip often do not leave enough energy in the adjacent strip to register above threshold. The rolling off of the events near the edges is consistent with the collimator opening of $31 \times 31\,\mathrm{mm}^2$.

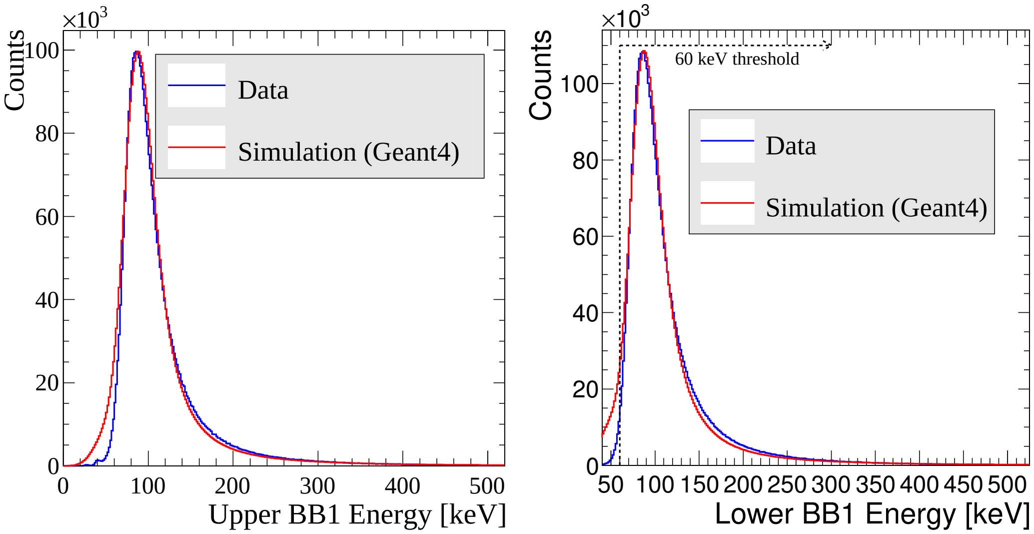

Figure 7.14: Energy spectra of BB1 detector compared to Geant4. The agreement between simulation and experiment demonstrates the validity of the analysis described in this section.

7.3 Plastic scintillators

The pair of plastic scintillators, one placed immediately behind each BB1 detector, are thick enough to fully stop the 5.1 MeV βs from ^{37}K and produce a light output proportional to the amount of energy deposited. The calibration is performed on-line with two calibration points: the Compton-edge from the 511 keV γs and the end-point of the β-spectrum. As I will show, the experiment is sufficiently free from backgrounds that the ^{37}K end-point is a good calibration point.

Despite the steps outlined in Ch. 4 to shield the PMT from the AC magnetic field, the gain of these detectors has been found to oscillate with the magnetic field strength. A gain-stabilized LED was mounted adjacent to the light guide and was present throughout the run. It emitted light pulses of constant amplitude at 70 Hz and was not synchronized with any other element of the experiment. Therefore, the LED pulses arrived uniformly distributed throughout the duty cycle. Fig. 7.15 shows the mean LED pulse height throughout the duty cycle. While the AC MOT is in operation, the scintillator gain oscillates by $\sim 0.5\%$ of its value. While the MOT is off, the gain is more stable: varying by only $\sim 0.2\%$.

Since the measurement of the β-asymmetry requires the MOT be off in order for the atoms to be polarized, the calibrations shown here are performed using *polarized data only*. This eliminates the time dependence shown in Fig. 7.15. Note that the polarized events used in the calibration are the same events used in the final β-asymmetry analysis: the events while the MOT is on are decays from unpolarized atoms, and are not relevant to the β-asymmetry analysis. A possible improvement in future experiments making use of these system would be to develop more effective magnetic shielding at the AC-MOT frequency or use detector technology that is insensitive to magnetic fields.

A number of basic analysis cuts are necessary to eliminate unwanted events types from affecting the calibration. Although the UV light pulse triggers DAQ, these events are not related to β-decay and therefore are excluded from this analysis, as are events in coincidence with an LED pulse. Note that there are no events in Fig. 7.16a occuring near the position of the LED spectra shown in Fig. 7.15. From this, it is clear that the rejection of LED events from the calibration analysis is essentially perfect. Finally, in order to keep the analysis independent from the β-asymmetry, the calibration will include data from only one polarization state. Since $A_\beta < 0$,

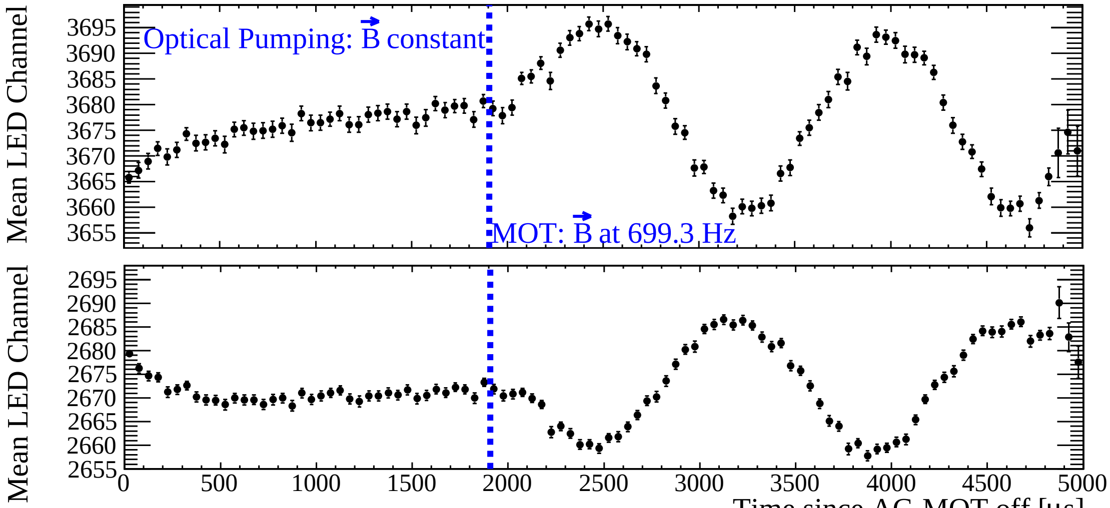

Figure 7.15: Mean LED pulse height throughout duty cycle. The upper and lower panels correspond to the upper and lower detectors. The error bars displayed represent the standard error on the mean, i.e. RMS/$\sqrt{N}$ where N is the number of entries. At $t = 0$, the MOT is switched off and the AC-MOT magnetic field dies away. As it does so, the scintillator gain changes in response. Throughout the optical pumping period, the gain is relatively stable, although the upper detector demonstrates some residual drift. Once the AC-MOT starts again at $t = 1906\,\mu s$, the gain of the scintillators oscillates in response to the varying magnetic field at the same frequency at which the magnetic field oscillates. In both detectors, the magnitude is $\sim 0.5\%$ of the average value. That the two curves have different scales on the y-axes reflects different calibrations and LED light transmission. That the two curves appear to oscillate in opposite phases is likely due to the different orientation of first PMT electrode with respect to the magnetic field direction.

each detector will use data only from when the polarization vector was opposite to the detector under consideration.

The starting point for the energy calibration of the scintillators is to examine the scintillator spectrum shown in Fig. 7.16a. The spectrum is generated requiring that the eMCP timing signal was above threshold. Clearly visible are both the sharp Compton edge from 511 keV γ-rays as well as the broad β-decay energy spectrum.

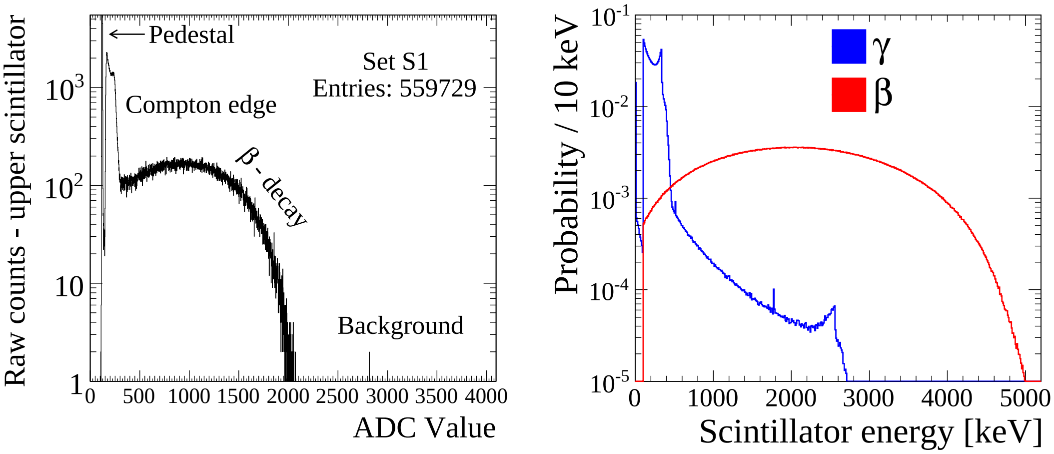

(a) Data - Raw spectrum

(b) Simulated

Figure 7.16: (Left) Raw scintillator spectrum. Generated requiring that the eMCP was triggered in the same event, but not requiring the SOE time-of-flight cuts described in Sec. 7.1.2. The steep order-of-magnitude drop at the 341 keV Compton edge is well defined. Since the spectrum is essentially free from background above the ^{37}K endpoint energy, this too is a well-defined point for calibration. (Right) Scintillator spectrum simulated with Geant4. The two curves show the two components of the spectrum: the scintillator response to an incident β^+ and the response to a secondary γ. The curves shown here do *not* include the resolution of the detectors as in Eq. 7.12, but do include elements of the detector response simulated by Geant4.

I apply a linear calibration to the data. In comparison to the BB1 detectors, there is no reason to set the calibration offset, b, to zero *a priori*. Therefore, the calibration contains two fitting parameters:

$$E_{\text{Scint}} = (Q_{\text{QDC}} - b)/m. \tag{7.11}$$

Additionally, the resolution of the detector arises from photon-counting statistics, and therefore depends on the detected energy. Since $E \propto N_{\mathrm{phot}}$, the energy resolution must be

$$\sigma_{\mathrm{Scint}} = \sqrt{\lambda E} \tag{7.12}$$

where λ is a fitting parameter defining the detector resolution and is unrelated to the λ appearing in Eq. 7.3. Most of the information about λ is contained in the comparison of the "steepness" of the Compton edge in Fig. 7.16a to that in Fig. 7.16b. Since the broad β-decay spectrum is a smoothly varying function, it is less sensitive to the value of λ.

The calibration is performed by comparing to the Geant4 simulation of the detectors and decay scheme described in Ch. 6. Separate spectra are generated for events where a β^+ triggered the scintillator and for when a γ was responsible for the event. These two spectra, each normalized to unit area, are shown in Fig. 7.16b. In both cases, the full experimental setup is included to obtain the most realistic distribution of energy loss in the surrounding material and angle of incidence upon the detector. Although the eMCP coincidence provides an excellent tag for decays occuring withing the trapping region, the low trapping efficiency of the first MOT leads to a large background of annihilation radiation that is not entirely suppressed by the eMCP coincidence. Therefore, the relative abundance of γs and βs in the spectrum is left as a free fitting parameter.

During the experimental run, the scintillator calibration changed abruptly, most likely the result of changing QDC modules after one failed. Except for this single shift, the calibration shows no evidence of changing. Therefore, for each detector, two separate calibrations were determined, and I label the two data sets S1 for runs up through Run 449 and S2 for runs beginning with 450 (see Tab. 4.1).

The fit is performed with the four variable parameters described in this section: m and b defining the calibration, λ defining the energy-dependent resolution, and N_{norm} defining the relative weight of the individual γ and β Monte Carlo spectra. Since defining the β-decay endpoint is critical to the calibration, bins at energies *higher* than this must be included in the fit in order for the lack of events in these bins to influence the fit result. Therefore, Poisson statistics were used.

For the set S1, the result of this fit to the upper and lower detectors are shown in Fig. 7.17 and 7.18. The Geant4 simulation is able to reproduce the data well over the energy region of interest. The residuals, shown in the bottom panel of each figure, demonstrate that the agreement is worst at the lowest energies, below the 511 keV Compton edge. This is in line with expectations as these events are the most difficult to simulate accurately. However, both the Compton edge and the β-decay endpoint are both well reproduced by the simulation, leading to a good calibration.

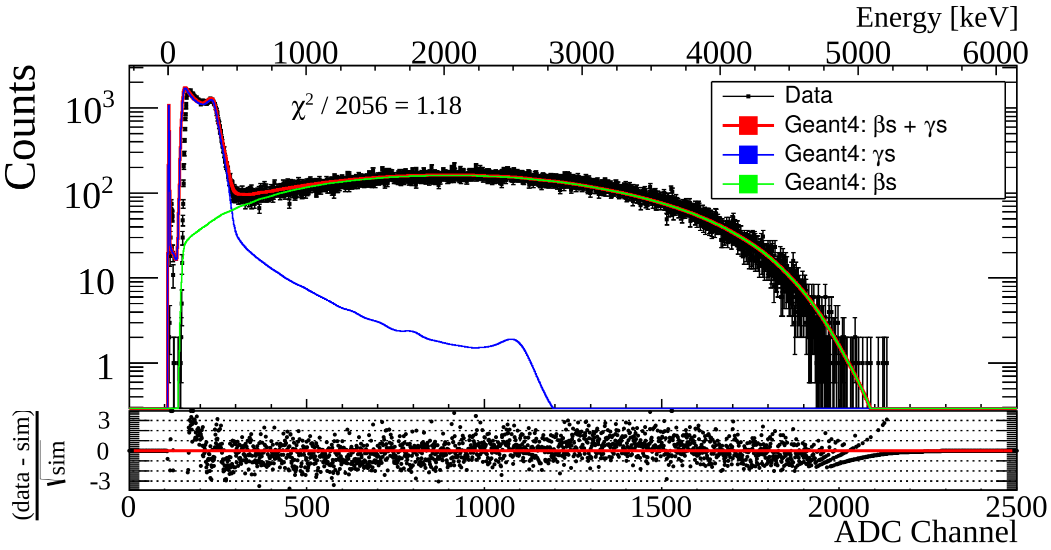

Figure 7.17: Result of calibration fit for set S2, upper scintillator. The data is fit to the sum of two simulated spectra: a spectrum generated by primary βs and a spectrum generated by secondary γs. The relative normalization of these two spectra is fit to the data as discussed in the text. The bottom panel shows the residuals of the fit. The largest difference between simulation and experiment takes place at low energy.

As discussed above, the resolution of the detectors is mostly dependent on the "steepness" of the Compton edge. Since the β-spectrum is a smoothly varying function, the resolution at higher energies contains a good deal of extrapolation from the single point where the resolution is well defined. An improvement in future iterations would be a detailed off-line calibration with multiple sources in order to more thoroughly define the detector's resolution and response.

The calibration results for the spectra shown in Fig. 7.17 and 7.18, as well as the corresponding results for set S1 are shown in Table 7.5. The largest correlation

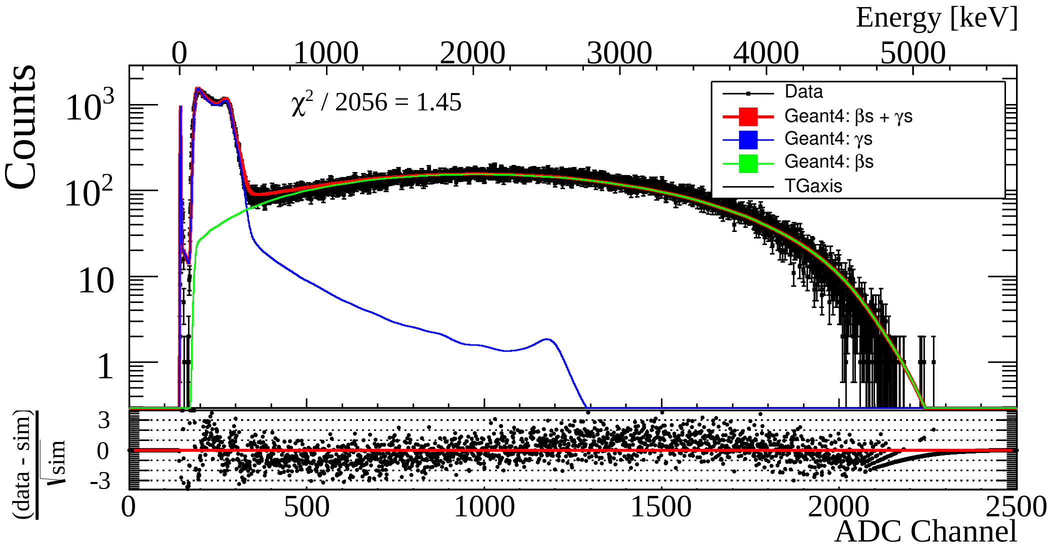

Figure 7.18: Result of calibration fit for set S2, lower scintillator. See caption for Fig. 7.17.

Table 7.5: Calibration results for the scintillators. The abrupt, one-time change in calibration is attributed to a change in QDC modules.

		b [ch]	m [ch/keV]	λ [keV]	N_{norm}	χ^2/NDF
Upper	S1	110.0(3)	0.3985(4)	1.55(9)	0.490(3)	2341 / 2110
	S2	110.7(2)	0.3883(4)	1.42(8)	0.502(3)	2412 / 2056
Lower	S1	142.0(3)	0.4234(4)	1.28(8)	0.467(3)	2776 / 2241
	S2	143.0(3)	0.4132(4)	1.32(8)	0.454(2)	2972 / 2187

in the fitting parameters is between the calibration slope and offset, with a correlation coefficient of 71% averaged over the detectors. All correlations between fitted parameters are included in the final uncertainties.

Once the detectors are calibrated, the final scintillator spectrum, including a coincidence with both the eMCP and BB1 detectors ($E_{\text{BB1}} = 60\,\text{keV}$), is created. The final spectrum includes the SOE time-of-flight cuts described in Sec. 7.1.2 as well as a valid hit on the BB1 detector, including $\hat{x}$-$\hat{y}$ energy agreement as described in Sec. 7.2.3. These spectra as well as the simulated spectra undergoing the same event-selection are displayed for set S2 in Figs. 7.19 and 7.20 for the case of $n_{\text{cut}}^{\text{BB1}} = 3$ and $n_{\text{cut}}^{\text{TOF}} = 5$ (see Eqs 7.5 and 7.7). Additionally, these two figures require that the position of the event on the BB1 detector falls with a 10 mm radius surrounding the center of the detector. Restricting events to this region on the BB1 detector minimizes the effects of scattering off of the surrounding material, and in particular minimizes scattering off of the stainless steel collimator/mirror mount shown in Fig. 1.4. By reducing the amount of β-scattering in the data, the difficulty of the Geant4 simulation reproducing the simulation is reduced.

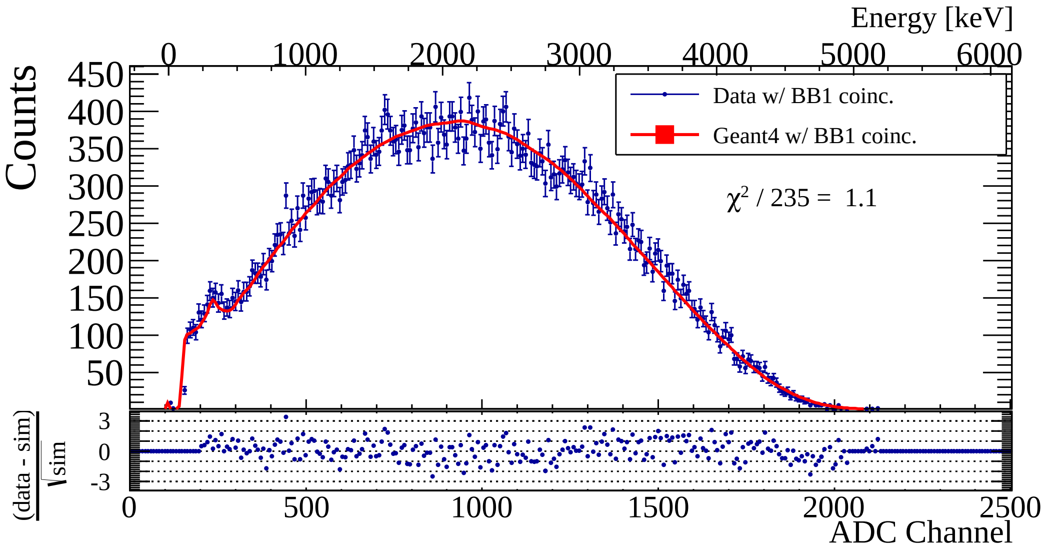

Figure 7.19: Scintillator spectrum in coincidence with BB1 - upper. After calibrating the scintillator, a spectrum is generated in coincidence with the BB1 detector. This, combined with the eMCP coincidence already in place, provides a very clean selection of β-decay events originating from the trapping region. The same analysis is performed with the Geant4 simulation and the results are overlayed. Since there is no evidence for a background in this spectrum, the β-asymmetry measurement is exceptionally clean. Figures shows upper detector, Set S2.

Although the χ^2/N shown in Fig. 7.20 is 1.4, it is important to note that *there is no background included in the simulation.* The only source of events included in Geant4 is the β^+-decay of ^{37}K from the trapping region. Furthermore, no simulated spectra is consistent with the observed spectra. Cosmic rays, which can leave energy

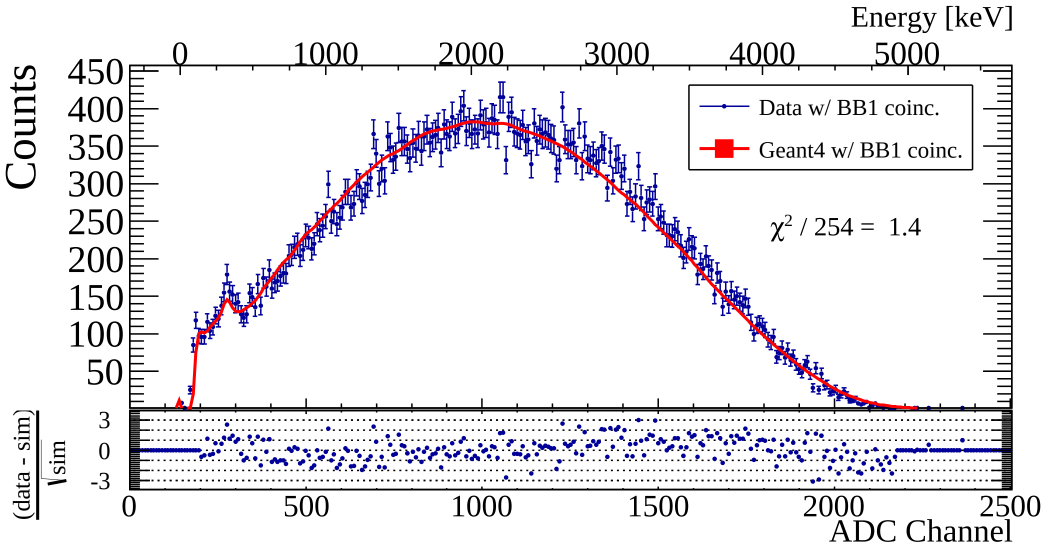

Figure 7.20: Scintillator spectrum in coincidence with BB1 - lower. See caption for Fig. 7.19. Figure shows lower detector, Set S2.

in both the scintillator and BB1 detectors, are not likely to be in coincidence with the eMCP. Even then, their mean energy loss is 6.7 MeV, which is above the β-decay endpoint, as discussed in Sec. 7.3.1. Beam-line contaminants, including isotopes of K other than ^{37}K are not trapped by the MOT due to their different atomic structure. Atoms of ^{37}K that escape the trap before decaying are excluded by the coincidence with the eMCP detector. That the GEANT4 simulation reproduces the observed scintillator spectrum at the level it does validates the assertion that the triple coincidence between scintillator, BB1 detector, and eMCP eliminates essentially all sources of background radiation.

The observed discrepancy between data and simulation is instead attributed to an uncertainty in the detector response. Although the two calibration points used in this section cover the energy region of interest, additionally calibration points would be useful to firmly establish, or at the very least, check the calibration. Additionally, the resolution of the detector is determined almost entirely at a single energy, 341 keV, and the resolution at higher energies is essentially extrapolated from this. Finally, the agreement between data and simulation depends critically on the accuracy of the simulation of the β^+ energy loss through the $\approx$ 800 µm of material separating the trapping region from the scintillator[1]. The average total energy loss through these materials is 330 keV. Although the fraction of backscattered events, discussed in Ch. 6, validates the GEANT4 simulation, discrepancies at the few percent level are still possible.

7.3.1 Cosmic rays

At the surface of the Earth, cosmic rays are mostly muons, with a mean energy $\approx 4\,\mathrm{GeV}$ and an expected rate of $1/(\mathrm{cm}^2\,\mathrm{min})$ [5]. The distribution of polar angles is $\approx \cos^2(\theta)$, meaning that many muons are propagating vertically down. Therefore, these particles can trigger both scintillators simultaneously. At these energies, muons are minimally ionizing, with the most probable energy loss 6.3 MeV in each of the two plastic scintillators. For these reasons, selecting events with energy greater than the ^{37}K endpoint energy in *both* scintillators is a clean tag of cosmic-ray events. Following this, the scintillator energy spectrum can be compared to GEANT4 simulations as a higher energy check of the calibration described above.

Figure 7.21a shows a scatter plot of the two scintillator energies for the same event. The vast majority of events have one detector with $< 1\,\mathrm{MeV}$ of deposited energy as shown by the thick black bands along both axes. These represent a typical β or γ event where only one detector is expected to record any energy. There are few events with both detectors having $> 1\,\mathrm{MeV}$. The dashed red lines show the events selected requiring the energy in *both* scintillators be $> 5.5\,\mathrm{MeV}$. There is clearly a high concentration of events with $E_{\mathrm{top}} \approx E_{\mathrm{bottom}} \approx 6.5\,\mathrm{MeV}$, which is consistent with the spectrum for minimally ionizing muons described above.

Furthermore, there is a band of events with energy in one detector $E \approx 6.5\,\mathrm{MeV}$, with the other detector having less energy than this value. These events are the result of muons passing through both detectors, but leaving more energy in one detector than the other. By examining simulated events satisfying these criteria, many of these events are a result of the muon having a longer path length through one detector than the other, i.e. the path is a “glancing hit” in one detector. Other events in this class are the result of delta-ray production, where the e^- produced has a continuous energy distribution.

The projection of Fig. 7.21a onto the $\hat{y}$-axis requiring $E_{\mathrm{top}} > 5.5\,\mathrm{MeV}$ is shown in Fig. 7.21b as the square points with uncertainties. Note that because neither the

---

[1] SiC: 275(5) µm, Be: 229(23) µm, Si: 295(5) µm

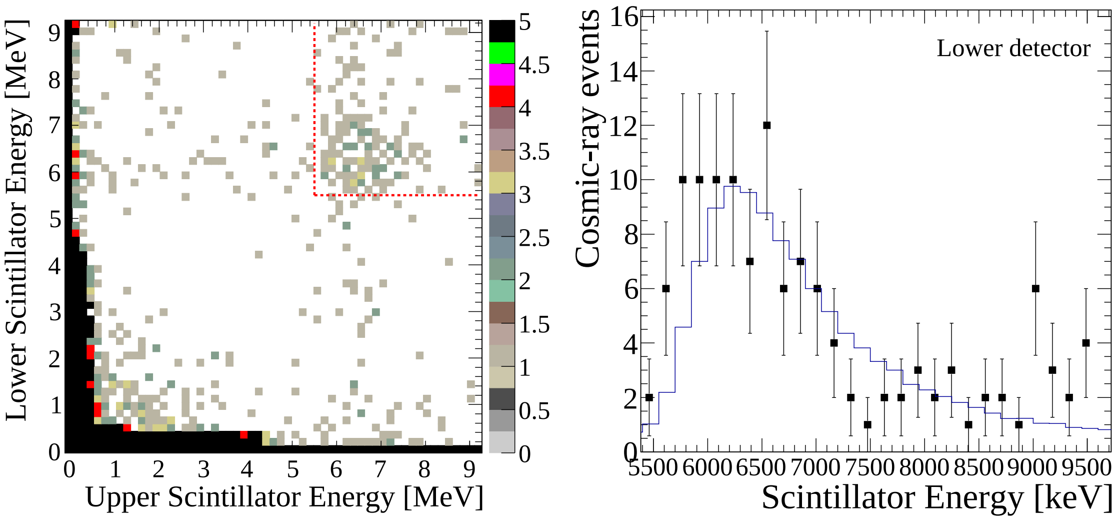

(a) Selection of cosmic ray events

(b) Cosmic ray energy distribution

Figure 7.21: Cosmic ray events. Left: Energy distribution of events with energy deposited in both scintillators. The thick black bands have significant energy in only one detector, corresponding to β-decay events. Cosmic-ray muons can be selected with high-confidence with the cut shown by the red dashed line. Right: Energy of cosmic-ray events as recorded by the lower detector. In this case, each event is required to have $E > 5.5\,\text{MeV}$ in the upper scintillator as well.

rMCP nor the eMCP is required for these events, data from both sets of runs are combined. Also shown in this figure is a GEANT4 simulation of cosmic-ray events. The simulation is performed with the identical geometry to that described in Ch. 6, with only modification being the event generator. Cosmic ray muons are simulated making use of the `G4GeneralParticleSource` class. This pre-defined event generator allows the user to define the source of events using only an initialization file and supplies many commonly used energy and angle distributions. The initial position of these events was defined to be a $15 \times 15\,\mathrm{cm}^2$ planar region above the upper scintillator and the initial energy chosen from a uniform distribution from $0.1 - 10\,\mathrm{GeV}$. The simulated spectrum is overlayed with the data in Fig. 7.21b. There is good agreement between model and experimented, indicating that the scintillator calibration derived in the previous section is correct.

The agreement of the scintillator data with the spectrum predicted by minimally ionizing muons supports the validity of the scintillators' calibration at energies beyond the ^{37}K endpoint. The cosmic ray spectrum can also be included in the original fits to the scintillator spectrum. However including this additional data has a negligible impact on the calibration and resolution of the detectors due to the relatively low statistics of these events.

8. POSITRON ASYMMETRY

The nuclear measurement of the β-asymmetry makes use of all of the analysis and discussion up to this point. Schematically, the coincidence requirements described in Ch. 7 are used to select events representing a β^+ depositing energy in one of two plastic scintillators along the polarization axis. The coincidence with the eMCP selects events where the ^{37}K decayed from within in the trapping region, although as discussed in Sec. 8.3, decays from other regions within the detection chamber account for 0.3 % of events and introduce a non-negligible background.[1] Furthermore, appropriate timing within the experimental duty cycle ensures that the atoms are polarized with the degree of polarization precisely measured in Ch. 5.

Starting from Eq. 2.10, I first note that the only daughter particle whose momentum is observed in this analysis is the β^+. Therefore, I integrate Eq. 2.10 over the neutrino momentum with the simplified result that

$$\frac{d^3W}{dE_e d\Omega_e} = 1 + b\frac{m_e}{E_e} + \frac{\vec{J}}{J} \cdot \left[A_\beta \frac{\vec{p_e}}{E_e} \right]. \tag{8.1}$$

The Fierz interference term (b) is sensitive to scalar (S) and tensor (T) currents, and takes the value $b = 0$ in the SM. A recent survey of β-decay results limits the amplitude of the these coupling constants relative to the dominant vector (V) and axial-vector (A) terms [54]:

$$|C_S^{(\prime)}/C_V| < 0.07 \qquad |C_T^{(\prime)}/C_A| < 0.09. \tag{8.2}$$

With no experimental evidence of scalar or tensor currents in nuclear β-decay, I adopt $b = 0$ for this analysis. Defining r_1 (r_2) as the rate of detected events with $\vec{J}\cdot\vec{p_e} = +1$ ($\vec{J}\cdot\vec{p_e} = -1$), we can construct the simple ratio and define the experimental asymmetry:

$$A_{\text{obs}}\left(E_e\right) = \frac{r_1(E_e) - r_2(E_e)}{r_1(E_e) + r_2(E_e)} = PA_\beta \frac{p_e}{E_e} \tag{8.3}$$

where P is the magnitude of the nuclear spin projected along the observation axis.

---

[1] The double-MOT system is isotopically selective, meaning that there are no contaminants in the trapping region.

Although this discussion assumes point-like detectors, it is relevant as it describes the method and how it minimizes many sources of systematic uncertainties as well as how it facilitates blinding the analysis.

Although Eq. 8.3 demonstrates the principle of the measurement of A_β, it does not make use all the information. In addition to having the two detectors along the polarization axis, we periodically reverse the sign of the polarization state. This allows us to cancel many systematic effects. Defining the rate r_1^+ as the rate of events in detector 1 (or 2) while the polarization has the sign + (or −), I define the super-ratio as [116, 117]

$$A_{\mathrm{obs}}^{\mathrm{SR}}\left(E_e\right) = \frac{1 - s\left(E_e\right)}{1 + s\left(E_e\right)} = A_{\mathrm{obs}} \qquad s\left(E_e\right) = \sqrt{\frac{r_1^-\left(E_e\right) r_2^+\left(E_e\right)}{r_1^+\left(E_e\right) r_2^-\left(E_e\right)}}. \tag{8.4}$$

In order to see how this ratio cancels systematic effects, I introduce ϵ_1 and ϵ_2 for the efficiencies of the two detectors and n^+ and n^- for the number of trapped atoms in the polarization states, i.e. the luminosity of each polarization state. To use in the discussion further on, I also introduce two blinding factors, f_1 and f_2. However, for the present discussion, $f_1 = f_2 = 1$. Note that there is no assumption that $\epsilon_1 = \epsilon_2$ or $n^+ = n^-$. Furthermore, the rate of detected events is converted to the *number* of detected events by enforcing that equal time be spent in the two polarization states. Defining the number of counts $N_{1,2}^{\pm}$ equivalently to $r_{1,2}^{\pm}$ and including the efficiency and luminosity of each state, the result assuming $b = 0.0$ is:

$$\begin{aligned}
N_1^+\left(E_e\right) &= f_1 n^+ \epsilon_1 \left(1 + |P| \frac{p_e}{E_e} A_\beta\right) \\
N_1^-\left(E_e\right) &= f_2 n^- \epsilon_1 \left(1 - |P| \frac{p_e}{E_e} A_\beta\right) \\
N_2^+\left(E_e\right) &= f_2 n^+ \epsilon_2 \left(1 - |P| \frac{p_e}{E_e} A_\beta\right) \\
N_2^-\left(E_e\right) &= f_1 n^- \epsilon_2 \left(1 + |P| \frac{p_e}{E_e} A_\beta\right).
\end{aligned} \tag{8.5}$$

Here the magnitude of the two polarization states is assumed equal: $P^+ = -P^- = |P|$. This assumption is entirely consistent with the results presented in Ch. 5. Substituting the expressions into Eq. 8.4 under the substitutions $r_{1,2}^{\pm} \rightarrow N_{1,2}^{\pm}$, we can see in this simplified picture that a difference in detector efficiencies or luminosity does not enter in the final result when using the super-ratio:

$$A_{\text{obs}}^{\text{SR}} = \frac{f_1 - f_2 + |P|\frac{p_e}{E_e}A_\beta\left(f_1 + f_2\right)}{f_1 + f_2 + |P|\frac{p_e}{E_e}A_\beta\left(f_1 - f_2\right)} \xrightarrow{f_1=f_2=1} |P|\frac{p_e}{E_e}A_\beta. \tag{8.6}$$

As I will discuss below, f_1 and f_2 are blinding factors and are set to 1 in the final analysis. This provides the motivation for utilizing the super-ratio method. False asymmetries introduced by a difference in detector efficiencies or a difference in number of trapped atoms in the two polarization states do not impact the final result. Note also that the detector efficiencies include the effective solid angle seen by the two detectors. Therefore, the position of the trap also does not impact the result. The final analysis will compare the data to a Monte Carlo simulation and the cancellation of $\epsilon_{1,2}$ and $n^{\pm}$ does not hold exactly due to the effects of β-scattering. However, the principle result shown here remains that the super-ratio technique significantly reduces systematic uncertainties.

Furthermore, a rearrangement of the terms in Eq. 8.4 allows us to eliminate *any two* of the asymmetry-producing factors: the physics (A_β), different detector efficiencies ($\epsilon_{1,2}$), and different luminosities ($n^{\pm}$). Eq. 8.4 has eliminated $\epsilon_{1,2}$ and $n^{\pm}$ leaving the physics. Alternatively, we can eliminate the physics asymmetry and leave only the asymmetry produced by detector efficiencies or the asymmetry produced by a luminosity asymmetry. Therefore, these asymmetries, which are already accounted for by the super-ratio can also be measured by the same method.

$$A_{\text{det}}\left(E_e\right) = \frac{\sqrt{N_1^+\left(E_e\right)N_1^-\left(E_e\right)} - \sqrt{N_2^+\left(E_e\right)N_2^-\left(E_e\right)}}{\sqrt{N_1^+\left(E_e\right)N_1^-\left(E_e\right)} + \sqrt{N_2^+\left(E_e\right)N_2^-\left(E_e\right)}} = \frac{\epsilon_1 - \epsilon_2}{\epsilon_1 + \epsilon_2} \tag{8.7}$$

$$A_{\text{lum}}\left(E_e\right) = \frac{\sqrt{N_1^+\left(E_e\right)N_2^+\left(E_e\right)} - \sqrt{N_1^-\left(E_e\right)N_2^-\left(E_e\right)}}{\sqrt{N_1^+\left(E_e\right)N_2^+\left(E_e\right)} + \sqrt{N_1^-\left(E_e\right)N_2^-\left(E_e\right)}} = \frac{n^+ - n^-}{n^+ + n^-} \tag{8.8}$$

These equations are functionally the same as Eq. 8.4. By rearranging terms in the super-ratio we can isolate the asymmetries from other sources than the physics of interest. Note also that the blinding factors, $f_{1,2}$, have also been eliminated in the result. In the following section, I will describe how the data were blinded in order to prevent human bias influencing the final result before detailing the analysis of A_β in Sec. 8.2.

8.1 Blinding

As measurements become more and more precise, it has become necessary to obfuscate the final result of an experiment from those performing the analysis until the analysis is complete. This process, known as blinding, prevents the experimenter's bias from impacting the final result. As every experiment is unique, there is no universal method to accomplish this, although there are some typical ways in which this is done. For example, in the discovery of the Higgs Boson, all of the analysis optimizations were finalized *before* analyzing the kinematic region where the new particle was searched for [118]. In the analysis of the Michel parameters, the TWIST collaboration generated simulated spectra with unknown parameters in order to fit the experimental data. The difference in the best-fit parameter compared to this unknown value was finalized and only then was the actual value for the unknown parameter revealed [68,69]. Furthermore, the UCNA collaboration performed a blind analysis by artificially adjusting the clock frequency that keeps track of how much time their experiment collected data in the two spin-polarization states [117, 119].

Our blinding scheme, most similar to that used by the UCNA collaboration, was alluded to in the introduction to this chapter. Two unknown blinding factors were chosen and a fraction of events equal to $(1 - f_{1,2})$ were temporarily culled from the data stream. As shown in Eq. 8.6, this biases $A_{\mathrm{obs}}^{\mathrm{SR}}$ in an unknown way. All of the analysis decisions were finalized on the blinded data and only then were the culled events restored and the full data set reanalyzed in a predefined way. This analysis flow is shown graphically in Fig. 8.1. The degree to which the data is blinded should be similar to the expected uncertainty in the final result. In order to obtain a uniform distribution for the degree that A_{obs} is shifted by the blinding procedure, we randomly chose f_1 or f_2 to equal exactly 1. The other factor was chosen on the interval $[0.99, 1.00)$, corresponding to a maximum bias in A_{obs} of $\pm 0.7\,\%$, slightly larger than the expected uncertainty for this experiment.

In order to bias *only* the asymmetry analysis, not all events were subject to this culling. Only a fraction of events triggered by either scintillator were subject to the blinding. This means that the polarization analysis and the other atomic measurements described in Ch. 3 were *not* performed blind. Furthermore scintillator-triggered events were culled independently of the deposited energy, which means that the detector calibrations are not affected by the blinding procedure. Therefore, the

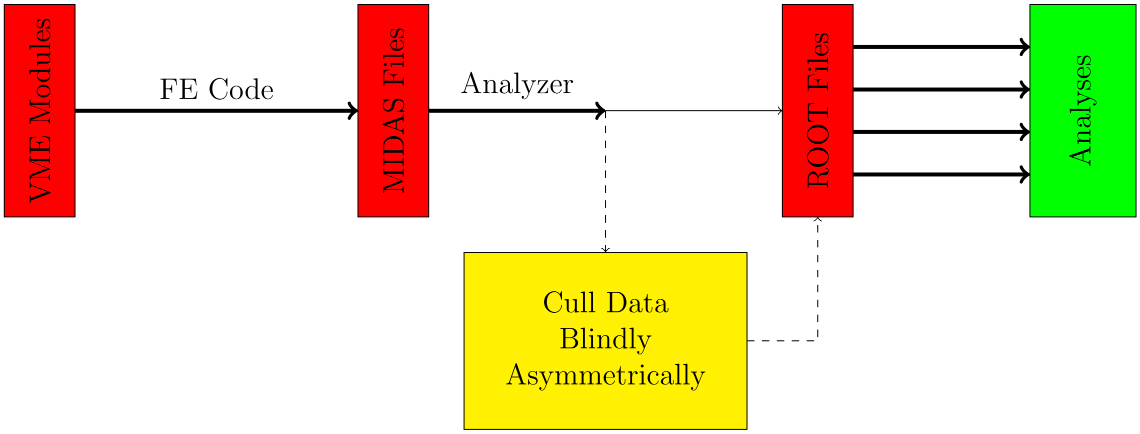

Figure 8.1: Implementation of the blinding scheme. The thick solid lines represent the portions of the analyses that are unchanged before and after blinding. The dashed line indicates the analysis path to create blinded data while the thin solid line shows the path taken in the final analysis after the blinding is removed. MIDAS and ROOT files denote the format of the data at the various stages of analysis. “FE Code” and “Analyzer” are program names to translate the data from one format to another.

calibrations performed on blinded data are carried forward to the final analysis. Similarly, the backscattering analysis presented in Ch. 6 also does not depends on the blinding procedure and those results are also carried forward. In this chapter, all analysis choices were finalized on blinded data. Only after this was complete was the blinding removed and the analysis repeated. All figures, tables, and results shown in this chapter therefore show data with no blinding applied.

8.2 Asymmetry analysis

Although discussed individually in the preceding pages, I will start by collecting together all of the experimental signatures of an event that should be used in the asymmetry analysis. Of course, neither the UV laser making photoions nor the LED pulser monitoring the gain of the plastic scintillators should be in coincidence with a β-decay event. Furthermore, we kept an electronic log of time intervals where one aspect of the experiment was not functioning properly and exclude events during these times from the analysis. These time intervals were identified in real-time and quickly corrected. They were typically the result of either the MOT or OP laser frequency drifting or the ion beam from ISAC being temporarily off. The average duration of one of these intervals was 6 min with the total amount of time excluded for these reasons is 74 min. To ensure that equal amounts of data were collected in the $\sigma^{\pm}$ states, and because the atomic duty cycle is not synchronized with the data acquisition, one complete cycle at the beginning and at the end of each run is discarded. This is described in more detail in Ref. [25].

We require a beta-decay event to have a coincidence between three detectors:

1. Energy deposited in the plastic scintillator. Energy threshold of 400 keV excludes the Compton edge from annihilation radiation.
2. Silicon strip detector
    (a) Energy threshold 60 keV.
    (b) Agreement in detected energy between the two detector planes within 3× the average resolution of the strips.
    (c) Hit position within 15.5 mm of the detector's center. This radius is chosen to match the the dimensions of stainless steel mirror mount placed in front of each β-detector and also serving as a collimator.
3. eMCP detects shakeoff electrons and ensures that the decay occured from the region of optical pumping. We require a time-of-flight coincidence but impose no position cut. Many signals on the HEX75 detector were below the hardware threshold. Therefore, a large fraction of events did not have enough information to calculate a valid position and any position cut would unnecessarily discard good events.

The specific selection cuts described above will each be considered as a systematic uncertainty. As described in Sec. 7.1.2, the observed shakeoff electron time-of-flight for the 150 V/cm data was 9.981 ns with the distribution approximated by a Gaussian function with 1σ width of 0.800 ns. During the course of the analysis, it was found that the result was sensitive to the specific time-of-flight cut chosen. Figure 8.2 illustrates the possible choices. It displays the relative timing of the scintillator and eMCP detector versus the scintillator amplitude. For events with $\lesssim$ 700 keV deposited in the scintillator, the observed time difference decreases by 1 to 2 ns as a result of the "walk" effect in the constant-fraction discriminator where results from

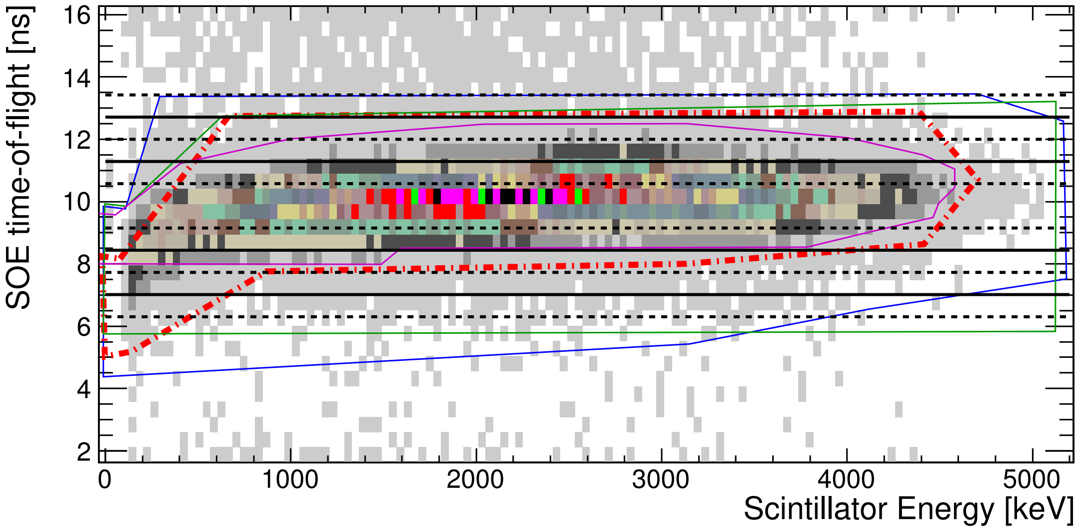

Figure 8.2: Shakeoff electron timing and scintillator energy cuts. The horizontal regions defined by solid and dashed black lines represent cuts only on the time-of-flight. Since they do not account for the observed timing walk at low scintillator energy, the other regions offer more consistent results. The diagram pictures a series of four possible regions in this plane that could be used, although it will be shown later on that the final result depend only weakly on the region chosen.

lower amplitude pulses are recorded at later times relative to high-amplitude pulses despite efforts to avoid this effect. Because of this, selecting events solely based on the shakeoff electrons' time-of-flight, shown by the dashed and solid black lines, can introduce an unwanted bias in the observed asymmetry at low energy if made too narrow. To avoid this, the colored lines in Fig. 8.2 display cuts in the two dimensional plane shown. By allowing the shakeoff electron timing cut to vary as a function of scintillator energy, the constant-fraction walk can be accounted for.

Fig. 8.3 shows the time-of-flight spectrum for events with $E_{\text{scint}} > 400\,\text{keV}$ on a logarithmic scale. The large peak at 10 ns corresponds to the region-of-interest shown on the left-hand side. The regular spacing of the peaks at 10, 24, 39 and 53 ns suggests that they represent not a new class of events but are instead ringing in the detector electronics. This period of ringing is not inconsistent with the observed pulse shape of the signals from the eMCP. Furthermore, the peaks at 0.8 and 14 ns are from prompt coincidence events described in Sec. 7.1.2 and from the detector ringing after this peak. All of these features lie on top of a broad time-of-flight background extending

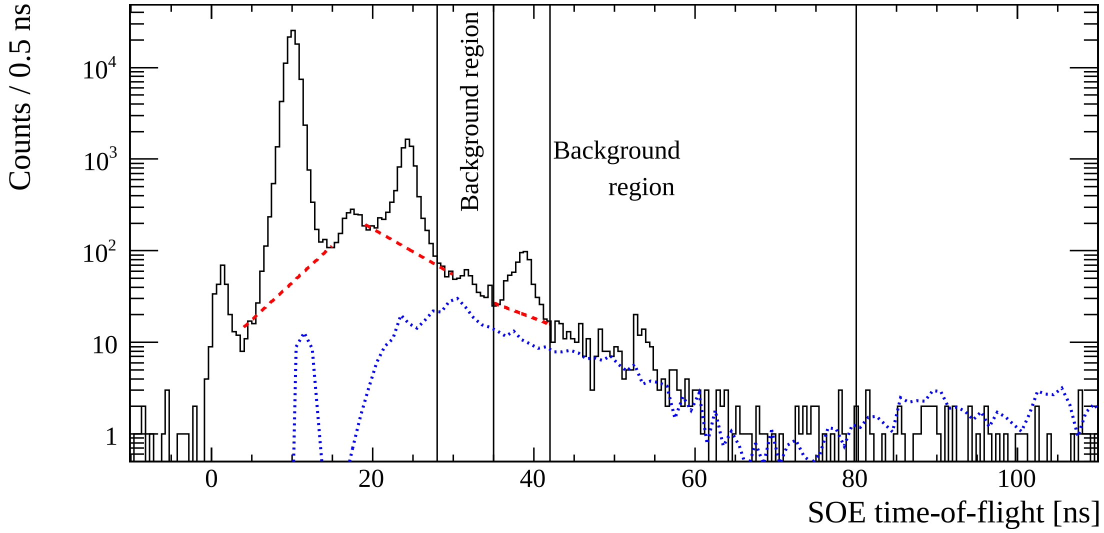

Figure 8.3: Shakeoff electron time-of-flight spectrum. The histogram in black is Set EB. The features of this spectrum are discussed in the text. The red dashed lines are exponential fits to the background spectrum and used to determine the signal-to-noise ratio. The dotted blue lines are a simulated time-of-flight spectrum for atoms that decay from the SiC mirrors and from the electrostatic hoops on the rMCP side of the setup. The background from decays from the mirrors appears to be a significant fraction of the background beginning at 15 ns although it does not account for the background underneath the main peak at 10 ns. The vertical lines define "background-only" regions where the asymmetry of this background can be measured.

from -5 to 70 ns. The blue dashed line to the right in Fig. 8.3 represents the simulated time-of-flight background from atoms that leave the trapping region and implant on the SiC mirrors before decaying [120]. While this background reproduces the broad spectrum well for $t > 15$ ns, the background at shorter time-of-flight is still not understood. The second blue dashed line at 12 ns is a similar simulation of times-of-flight from atoms decaying from an electrostatic hoop. Unfortunately, estimates of the relative number of these events suggest that these events cannot account for the size of the observed background. Therefore, this background and its effect on the measurement will be discussed in more detail in Sec. 8.3.

If all the conditions described above are satisfied, the event is likely be the result of a β-decaying ^{37}K originating from the optical pumping region. For the parent nucleus to be polarized, the atoms must be optically pumped. As described in Ch. 5, we consider the atoms to be fully polarized after 100 µs of optical pumping and until the MOT is turned on to re-trap the atoms (see Fig. 5.9 and Tab. 4.1). To illustrate this point, Fig. 8.4 displays the observed physics asymmetry as a function of time within the duty cycle for the EB dataset. Clearly, starting at ~ 450 µs since the MOT was turned off, equivalent to 118 µs since the OP began, the nuclei have acquired a substantial polarization leading to the observed asymmetry. The atoms remain polarized for the duration of the optical pumping before the asymmetry and the polarization drops to 0 once the MOT is turned on at 1900 µs along the $\hat{x}$-axis. Figure 8.4 also displays the asymmetry requiring a coincidence with the eMCP and BB1 separately to demonstrate the better selection of the full asymmetry as the selection cuts are layered on.

Figure 8.5 shows the deposited energy in each detector in each polarization state and represents the data from which the subsequent analysis begins. Before describing the measurement of A_{obs}, I will first present the measurement of the luminosity and detector asymmetries described in Eq. 8.8. Figure 8.6 shows the super-ratio comparing the number of events between polarization states as a function of scintillator energy. There is no observed energy dependence, but the data suggests a slight preference for atoms in the σ^- polarization state, although this 0.22 % effect is only at the 1.2σ level. As the collection and trapping of the atoms are completely independent of polarization state, there is little possibility for an asymmetric number of atoms being loaded into the trap. Any possible difference must be the result of the OP light pushing more atoms out of the trap in one state than the other. However,

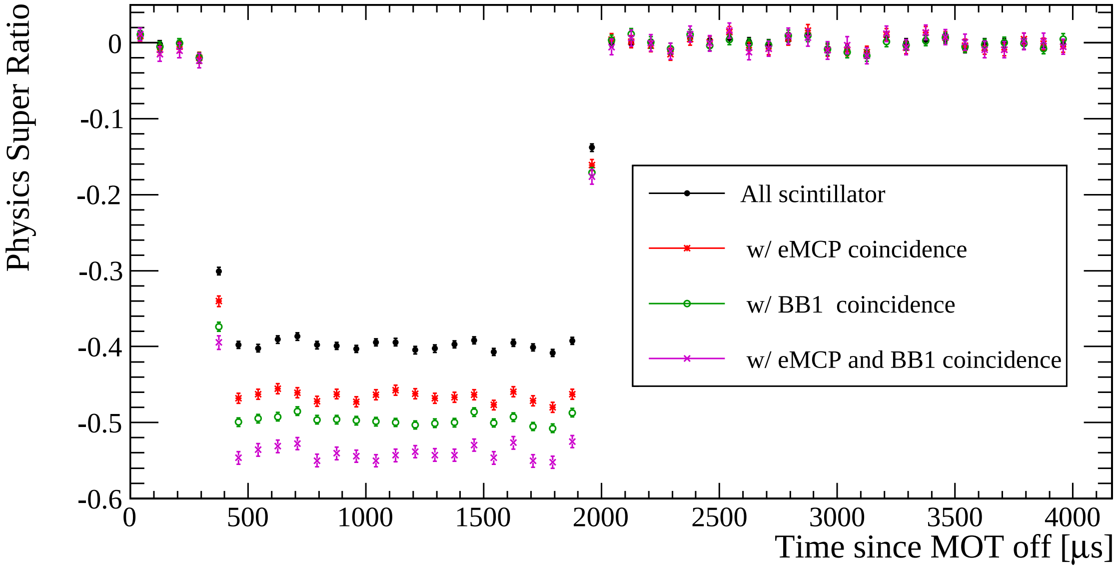

Figure 8.4: Asymmetry throughout the duty cycle. Physics super ratio asymmetry as a function of time since the MOT was turned off. The OP light is turned on at $t = 332\,\mu s$ and the nuclei are considered polarized $100\,\mu s$ after this. While polarized, there is a large asymmetry in the β-decay, but for the rest of the duty cycle the asymmetry is essentially 0 as a result of the nuclei being unpolarized during these times.

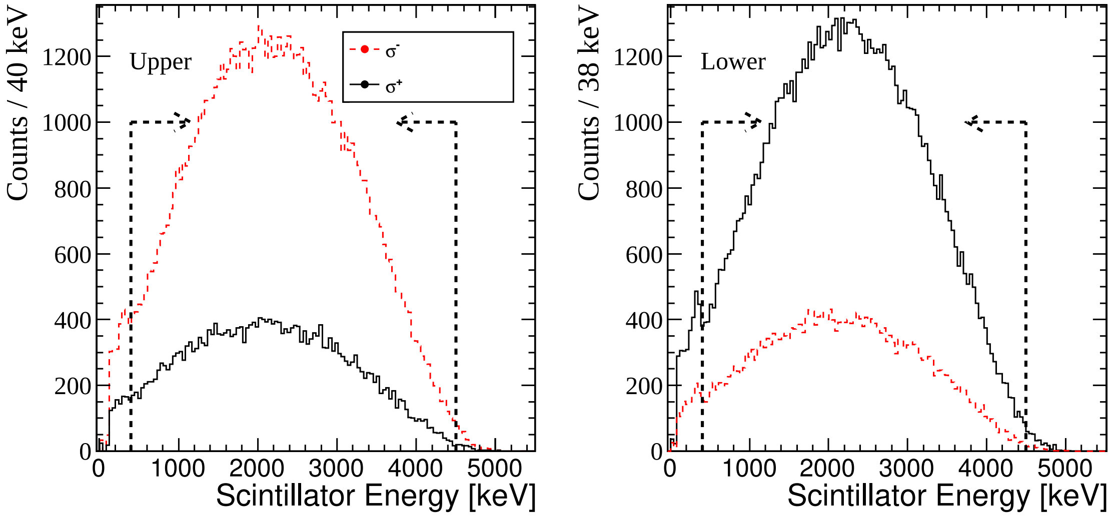

Figure 8.5: Scintillator energy spectrum: detector/polarization state. Energy spectrum of scintillator hits broken up by detector and polarization state. A clear asymmetry is observed. The β-asymmetry is a comparison of these spectra. Data shown is Set EB.

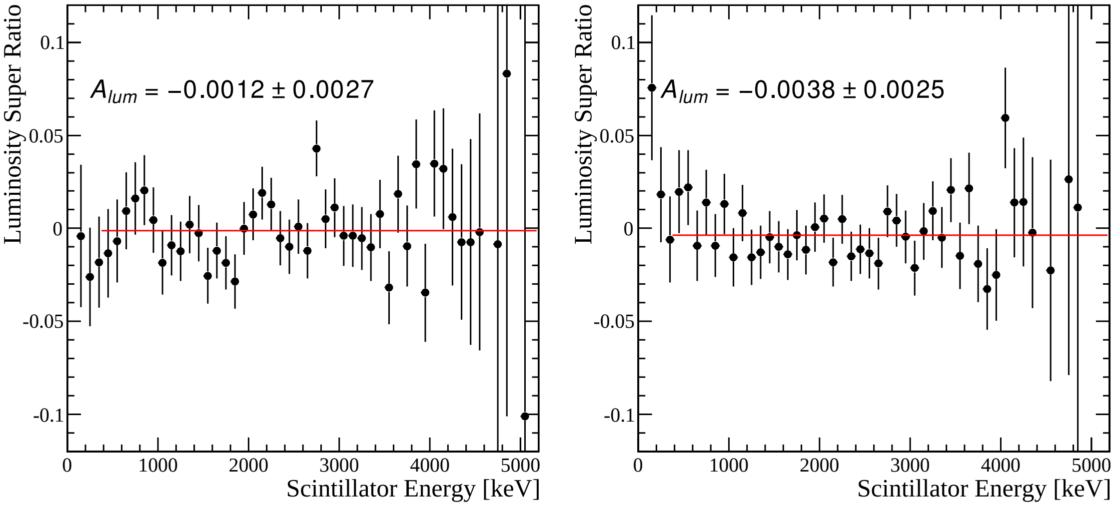

Figure 8.6: Luminosity super ratio. Shows the difference in number of trapped atoms between the two polarization states. Sets EB and ED, making up 90 % of the data collected, are shown in the left- and right-panels respectively. The best-fit values shown indicate the possibility of more atoms trapped in the σ^- polarization state, although the magnitude of this effect is only 0.22 %.

the limited number of absorptions of OP photons ($\mathcal{O}(10)$) limits this possibility as well. Finally, noting that the super ratio explicitly accounts for this possible effect, I conclude that this observation will not impact the final result.

Similarly, Figure 8.7 shows the super ratio comparing the observed counts in each detector, summed over polarization state. There is both a clear energy dependence and a non-zero asymmetry. Although the energy dependence is not fully understood, the value of the detector asymmetry is reproduced by the Geant4 simulation. Considering both panels of Fig. 8.7 and the much smaller EC data set, the detector asymmetry is $A_{\mathrm{det}} = 0.0419 \pm 0.0023$ compared to the simulated detector asymmetry of 0.0385 ± 0.0009. By adjusting the simulation parameters, we found that this 3.85 % asymmetry is the sum of contributions from two components. The first is that the observed trap position (see Tab. 5.3) is offset 0.61 mm from the center of the chamber along the polarization axis, increasing the effective solid angle for one detector and decreasing it for the other. By adjusting the trap position in the Geant4 simulation, we find that this produces a 2.8 % detector asymmetry. Furthermore, the number of non-functioning BB1 strips was different for the two detectors: three in the upper

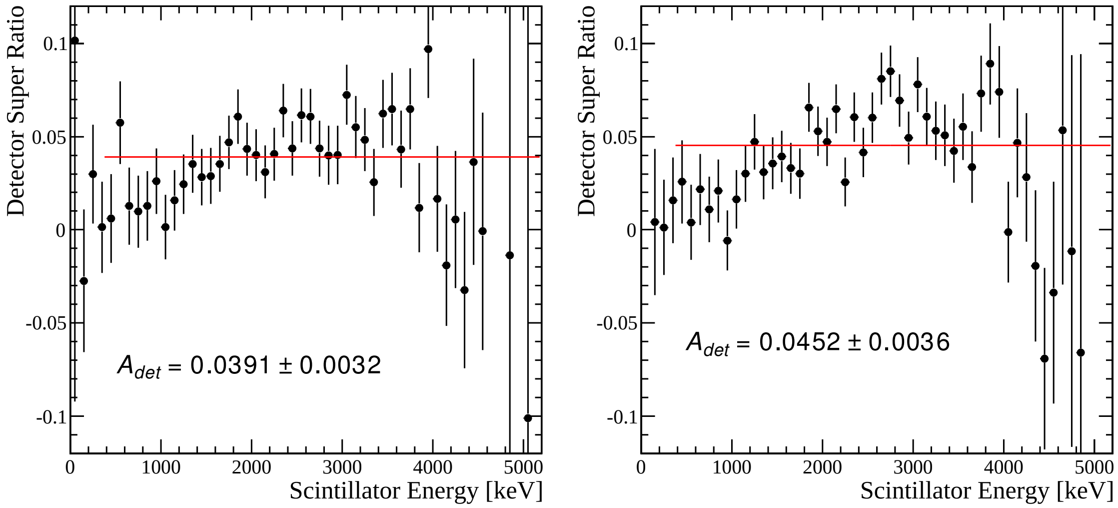

Figure 8.7: Detector super ratio. Shows the difference in detected events between the two nominally identical detectors. Layout is the same as in Fig. 8.6. The detector super ratio is significantly different from zero as a result of the trapped atoms being slightly off-center and asymmetric dead-strips on the Si-strip detectors.

detector and two in the bottom detector. Simulating with and without these dead strips, we found that this produces a 1.1 % detector asymmetry. Therefore the observed detector asymmetry shown in Fig. 8.7 is understood and reproduced in the Geant4 simulation.

To extract a value for A_β from the physics super ratio data, we compare it to a series of simulations with varying A_β and obtain the best-fit by minimizing the χ^2. However, as described in Sec. 2.2.1, recoil-order corrections to the decay rate give A_β an energy dependence. In order to properly vary A_β and its energy dependence, as well as to consistently vary all other terms in the decay rate of Eq. 2.10 and recoil-order corrections of Ref. [39], we do not vary A_β directly, but instead vary the axial-vector form-factor g_A. Since M_{GT}, g_V, and M_F are held fixed, this is nearly equivalent to varying ρ, the ratio of axial-vector to vector strengths in the decay. Recall from Eq. 2.11 that $\rho \simeq \frac{C_A M_{GT}}{C_V M_F}$ completely determines A_β in the SM. However, including recoil-order corrections, each of the factors in ρ appear separately in the decay-rate. Therefore, we fit g_A rather than ρ directly in order to include the small recoil-order terms consistently.

But why vary g_A and not M_{GT}, M_F, or g_V when any choice would amount to varying ρ? Starting with g_V, the well-tested CVC hypothesis asserts that $g_V = 1.0$. Looking ahead to the interpretation of this result, when both extracting V_{ud} and searching for right-handed currents, we will assume CVC. Hence, this has introduced no additional assumptions. Furthermore, shell model calculations from Ref. [40] have calculated both M_F and M_{GT}. In this analysis, g_A was fit such that the experimentally measured $\mathscr{F}t$ value was reproduced. Therefore, the approach described here amounts simply to repeating this procedure with g_A fit to a different observable. Despite these issues, we are *not* interpreting the result as a direct measurement of g_A, but plan to use the best-fit value of g_A to extract a value for ρ and A_β.

To compare to experimental data, two sets of simulations were performed with a single value of g_A. One simulation had the trap located according to the locations in Sets RA and RB and the other according to sets RC, RD, and RE. Referring to Tab. 4.1, this corresponds to eMCP sets EA and EB in the first case and EC and ED in the second case. The finite polarization of the atoms is accounted for by including it in the simulation directly. The simulated data is then processed using the same software as the actual data to generate the physics super ratio as a function of scintillator energy with the cuts described above. The simulated and actual data are compared and the χ^2 value calculated. This process was repeated at multiple values of g_A until the best-fit value was clear. For reasons that will be discussed below, set EA was excluded from the analysis although due to its low statistics it has essentially zero impact on the final result. The asymmetry for the remaining eMCP sets is shown overlayed with the GEANT4 simulation at the best-fit value for g_A in Figs. 8.8-8.10. There is good agreement between simulation and data with the combined $\chi^2/123 = 0.82$ corresponding to a p-value of 0.78.

As described above, the final result is determined by repeating this procedure with multiple values of g_A to determine the minimum and the result is shown in Fig. 8.11. The result is that the best-fit value of $g_A = 0.922 \pm 0.006$, corresponding to a measurement of $A_\beta = -0.5699 \pm 0.0013_{\text{stat}}$. Since the polarization of the atoms is included in the simulation, this value is A_β *not* A_{obs} and requires no further accounting for the polarization, except when propagating uncertainties.

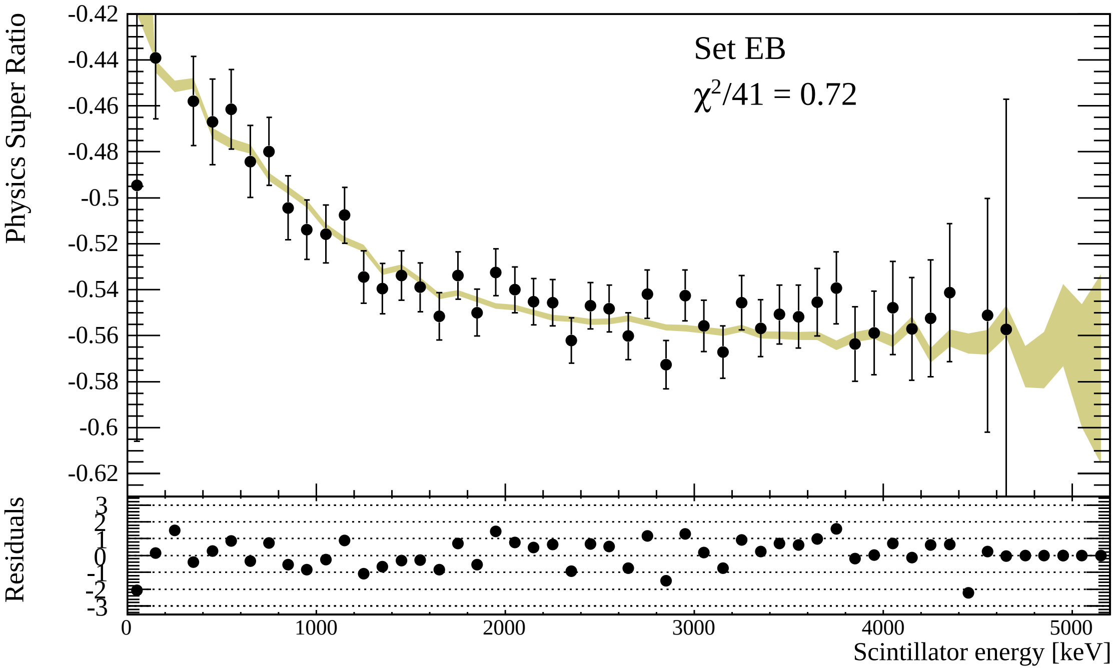

Figure 8.8: Physics super ratio asymmetry compared to GEANT4 (EB). The data points are shown with the black points with error bars. The filled band represents the simulated data with the width of the band defining the statistical uncertainty on the simulated data. There is good agreement across the whole energy region shown and the comparison is to the simulated point nearest the best-fit value $g_A = 0.923$.

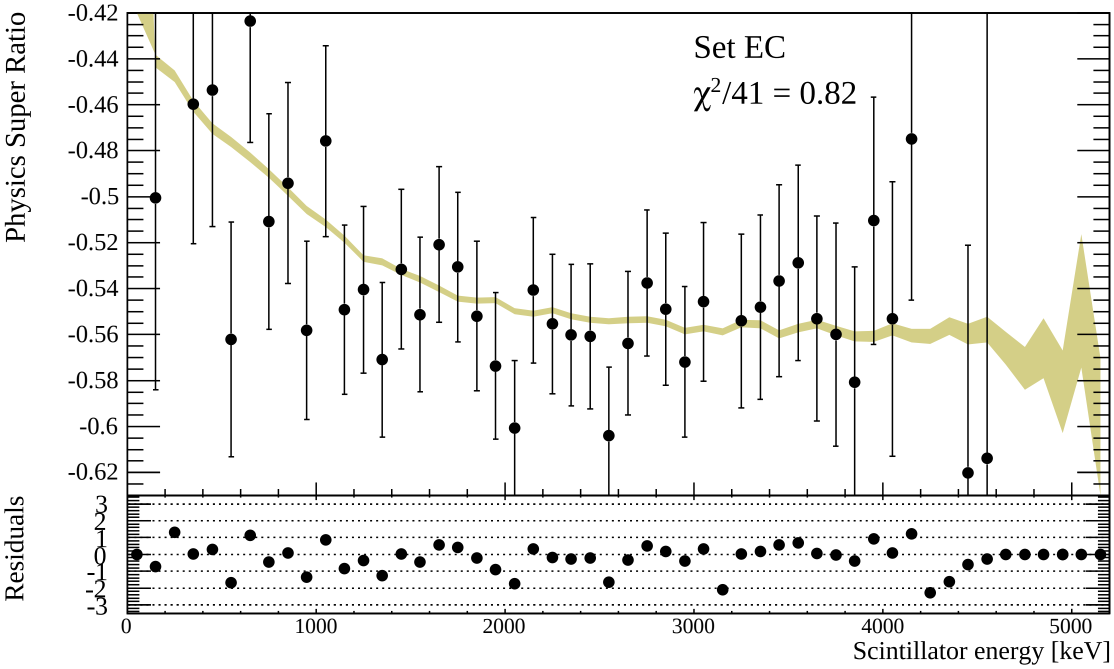

Figure 8.9: Physics super ratio compared to GEANT4 (EC). See caption for Fig. 8.8.

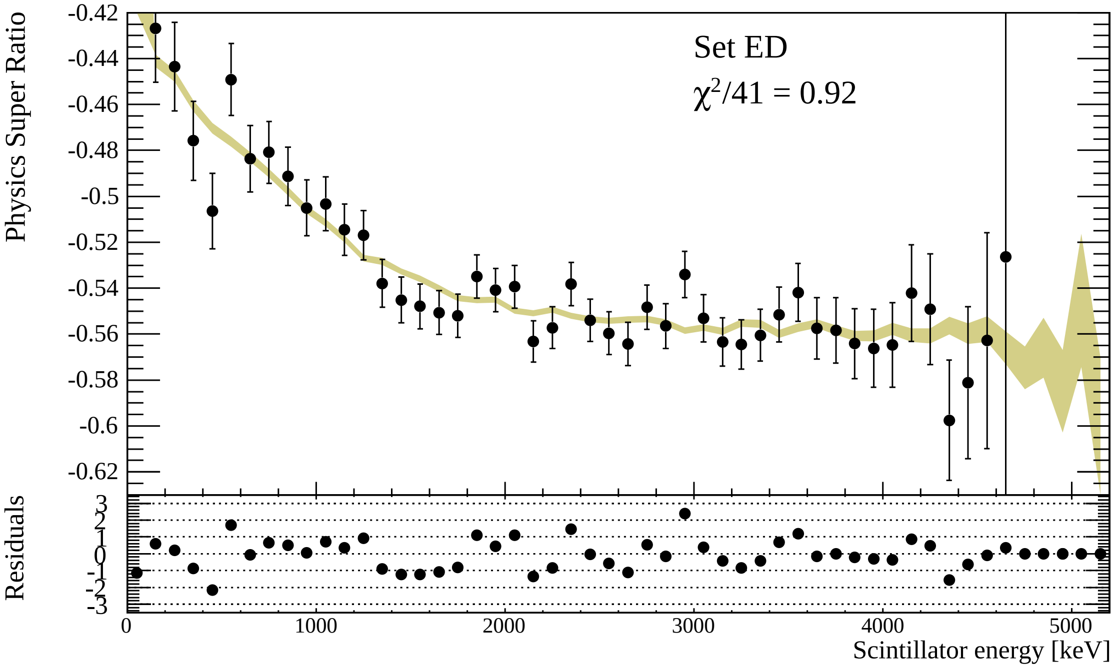

Figure 8.10: Physics super ratio compared to GEANT4 (ED). See caption for Fig. 8.8.

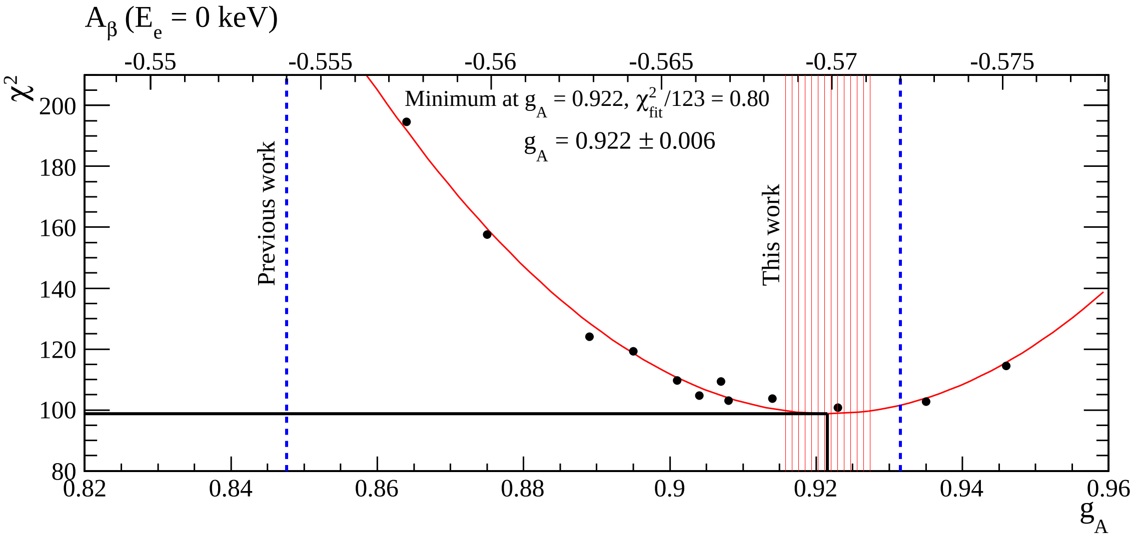

Figure 8.11: Result of fitting g_A to experimental data. The χ^2 value determines the goodness-of-fit for a specific parameter value chosen with the best value chosen by a quadratic, unweighted fit as shown as the red line. The statistical uncertainty is the amount of change of g_A required to increase the χ^2 by 1 compared to its minimum value and is also determined from the fit.

8.3 Background correction

The shakeoff electron time-of-flight spectrum shown in Fig. 8.3 contains a non-negligible amount of background events lying underneath the main shakeoff electron peak at 10 ns. Note that the time-of-flight spectrum is consistent between the upper and lower detectors after accounting for the arbitrary time delay introduced by the data acquisition electronics. We have found no selection cut that successfully eliminates this background. To consider possible sources of this background, I first note that generating a time difference between the scintillator and the eMCP of up to 70 ns, as required by the data, requires a very long electron time-of-flight. If the nuclear decay leaves the daughter $^{37}\mathrm{Ar}^-$ in an atomic excited metastable state, it will emit the shakeoff electron only after decaying to the ground state. The only known metastable state in Ar^- has the configuration $[\mathrm{Ne}]3s^2 3p^5 4s4p$ with a lifetime 260(25) ns [121]. This lifetime is inconsistent with observations and therefore metastable states in Ar^- are not the source of background.

Another possible source of background is atoms escaping the trapping region before decaying. If these atoms implant on the surface of the SiC mirrors before decaying, the probability of the β^+ entering the plastic scintillator is nearly 50 %. Furthermore, the resulting shakeoff electrons will not feel the full electric field as they are outside of the electrostatic hoops. Therefore the electrons must drift for some time before being accelerated onto the eMCP and this can lead to a longer time-of-flight. Simulation of e^- trajectories were performed with the electric field modeled in `POISSON`, a `FORTRAN`-based program to solve the Poisson equation in a cylindrically symmetric geometry. To accommodate this limitation, the electrostatic hoops and SiC mirrors were modeled as cylinders of equivalent size. The initial e^- energy is given by the distribution in Ref. [122], roughly a power-law spectrum, and the origin of the decay is uniformly distributed across the mirror surface. We find that shakeoff e^- generated from this process have a minimum time-of-flight of 15 ns [120] and therefore cannot account for the background lying underneath the main time-of-flight peak at 10 ns. This spectrum is shown as the right-most blue dotted line in Fig. 8.3, scaled to match the fraction of events expected to be produced by this process. It is interesting to note that this simulation reproduces the observed time-of-flight background spectrum well over the region it covers. Despite not accounting for the background at $t = 10$ ns, this process *is* clearly observed in the experimental data.

With the same technique, the time-of-flight spectrum for other possible surfaces is modeled as well. The next-largest contribution to the time-of-flight backgrounds appears to come from atoms decaying from the surface of the electrostatic hoop nearest the trap toward the rMCP detector, labeled H4. Shakeoff e^- originating from H4 have their time-of-flight delayed by 1.5 ns compared to e^- originating from the center of the chamber. However, the solid angle for ^{37}K leaving the trap to intersect H4 is only 2.8 % of 4π and the solid angle for β^+s originating from H4 to enter the plastic scintillator is only 0.8 % of 4π. All of this implies that the background of atoms decaying from H4 can account for only 0.05 % of events and cannot account for the short time-of-flight background. Furthermore, the remaining hoops (H3-1) all have even lower solid angle and contribute even less. The sum of contributions from hoops 1-4 is shown as the left-most blue dashed line in Fig. 8.3. Note that shakeoff electrons originating from hoops 5-7 have essentially zero efficiency for reaching the eMCP. Having considered and ruled out the most-likely sources of background, the source of background events remains an open question. Therefore, when accounting for this background below we take a very conservative approach.

Any background without an asymmetry would serve to decrease the observed asymmetry. Defining A_S as the asymmetry of the desired signal, A_N as the asymmetry of the background events, and S/N as the observed signal-to-noise ratio, the asymmetry observed in the experiment must equal:

$$A_{obs} = \frac{(S/N)\, A_S + A_N}{1 + (S/N)}. \tag{8.9}$$

This equation can be rearranged and solved for A_S, the sought-after asymmetry of the signal events. To calculate the the signal-to-noise ratio for a specified time-of-flight region, an exponential function representing the background contribution was fit around the time-of-flight peak. These choice is empirical, but appears to represent the data well. Each of the peaks in Fig. 8.3 can make a contribution to the surrounding spectrum, but modeling each as a Gaussian function shows that this contribution is negligible. With the source of background events under the main peak not known, there is no guidance from theory as to the function that would represent them best, and therefore I have modeled this as an exponential as it reproduces the observed spectrum the best. The integral of this function across the region shown is the noise with the remainder of the histogram's area making up the signal events. The exponential noise fit is shown as the red dashed lines in Fig. 8.3. This procedure was repeated for the secondary "ringing" peaks with the results discussed below. The signal-to-noise ratio observed in the main peak of Fig. 8.3 depends on the specific time-of-flight cut chosen. For the cuts pictured in Fig. 8.2, the S/N ratio ranges from 250 to 670 depending on which cut is chosen: narrower time-of-flight cuts have a higher S/N ratio. Note that although this ratio is quite high, it implies that the background can account for as much as 0.4 % of the data, which is significant compared to the statistical uncertainty reached.

Since the source of background events is ultimately unknown, the asymmetry of this background is similarly not known. One distinct possibility is that the source of background displays no asymmetry: $A_N = 0$. This possibility seems particularly likely considering that the super ratio explicitly accounts for false asymmetries produced by detector and luminosity effects. In fact, producing $A_N \neq 0$ seems rather unlikely for most possible sources of background including β-scattering, room backgrounds, and cosmic rays.

We can measure the asymmetry of the background events decaying from the SiC mirror by selecting the time-of-flight region defined by the vertical lines in Fig. 8.3. The asymmetry of these events was found to be -0.159 ± 0.022 with the result dominated by the region between 28 and 35 ns. This implies that the atoms retain a polarization of $P_{\text{nucl}} = 0.28$ as they implant on the mirror surface. However, this value may be specific to the surface of the mirror and not apply to any other surface. Furthermore, the time-of-flight background events may be decays originating from within the optical pumping region, but taking a trajectory that causes a time-of-flight that we have not been able to model. Therefore, these atoms may retain their full polarization and require *no* correction. With so much uncertainty about the asymmetry of these events, we are forced to assign 100 % uncertainty to their polarization, corresponding to $A_N = -0.29 \pm 0.29$. Note that we have excluded $A_N > 0$. This is justified as it would require atoms that escape the trap to not simply *lose* their nuclear polarization but *reverse* it completely. Since there is no mechanism for this to occur, we can safely exclude it from consideration.

Inserting these values into Eq. 8.9, we calculate a correction for each time-of-flight cut shown in Fig. 8.2 for each of the two values of A_N discussed above. The final correction is taken as the average of the correction with $A_N = 0$ and $A_N = -0.57$ and we assign a systematic uncertainty equal to half the difference between the two corrections. The statistical uncertainty on the S/N ratio is added in quadrature, but makes a negligible contribution. After applying this correction, the asymmetry is independent of the time-of-flight cut as desired and the corrections range from 0.09 % for the narrowest cuts to 0.17 % for the broadest. The success of these corrections in producing results that are independent of the region chosen is shown in Fig. 8.12. The final time-of-flight cut chosen has the median result for g_A (and therefore A_β) among the cuts accounting for time-of-flight walk at low energies, although the differences are only 2×10^{-4}. This choice has a S/N of 350 ± 80 and a correction multiplying the observed asymmetry of 1.0013 ± 0.0013. Therefore, this 0.13 % correction is known only to 100 % of its value.

We can also apply the same correction procedure to the echoes of the main peak having shakeoff electron time-of-flights 24 and 39 ns. These regions have a S/N of 5.6 ± 0.7 and 2^{+3}_{-2} making the correction significantly greater: $9 \pm 9\%$ and $21^{+32}_{-21}\%$ respectively. After making the background correction described above, the asymmetry in these peaks increases to -0.499 ± 0.041 and -0.467 ± 0.123. Note

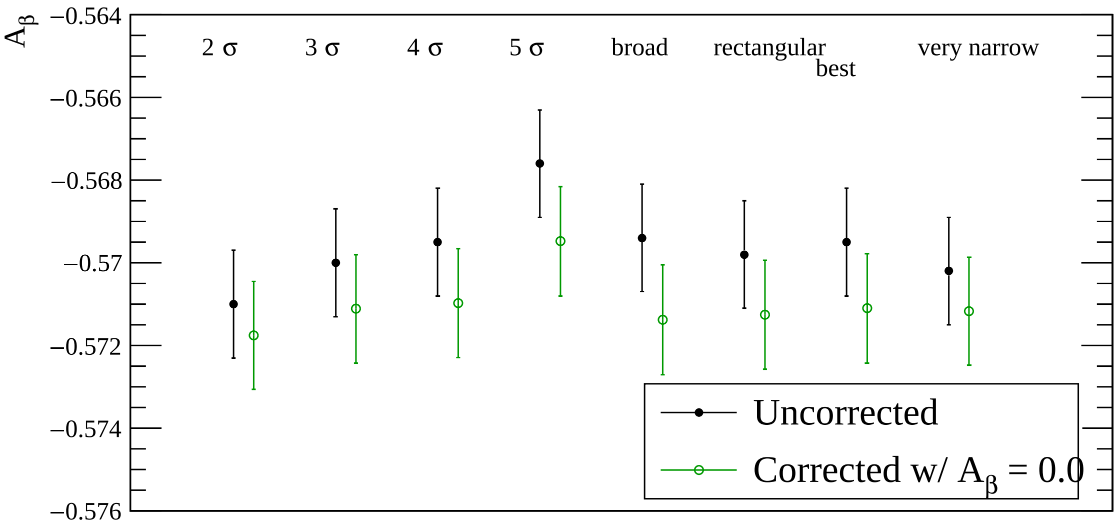

Figure 8.12: Shakeoff electron time-of-flight background correction results. Before applying the correction, the results show a dependence on the time-of-flight cut used, with narrower cuts leading to higher asymmetries. After applying the correction, the results are much more consistent. The final result is taken from the region labeled "best."

that the asymmetry remains *less* than the asymmetry in the main peak. Although only the second ringing peak agrees within the large uncertainties with the corrected asymmetry of the main peak, this result supports the conclusion that this correction is necessary and is *not* over-correcting the data.

The analysis described to this point has considered sets EB, EC, and ED. The shakeoff electron time-of-flight spectrum for set EA, with the electric field at 67 V/cm, is shown in Fig. 8.13. The same broad features are present with the ringing peaks less prominent and the spectrum shifted to longer times-of-flight as expected. Calculating the background correction for this data in the same manner as above leads to a much larger correction in this case as a result of a signal-to-noise ratio of only 19. To avoid this large correction, and because the low statistics of this data make it insignificant to the final result, set EA is not used in the final analysis.

Although no event-selection cut entirely eliminates the need for a background correction, it was found that requiring a position cut on the HEX75 detector did reduce the correction significantly. This corresponds to a cut on the shakeoff electron position. Figure 8.14b shows the position distribution of these events as well as the

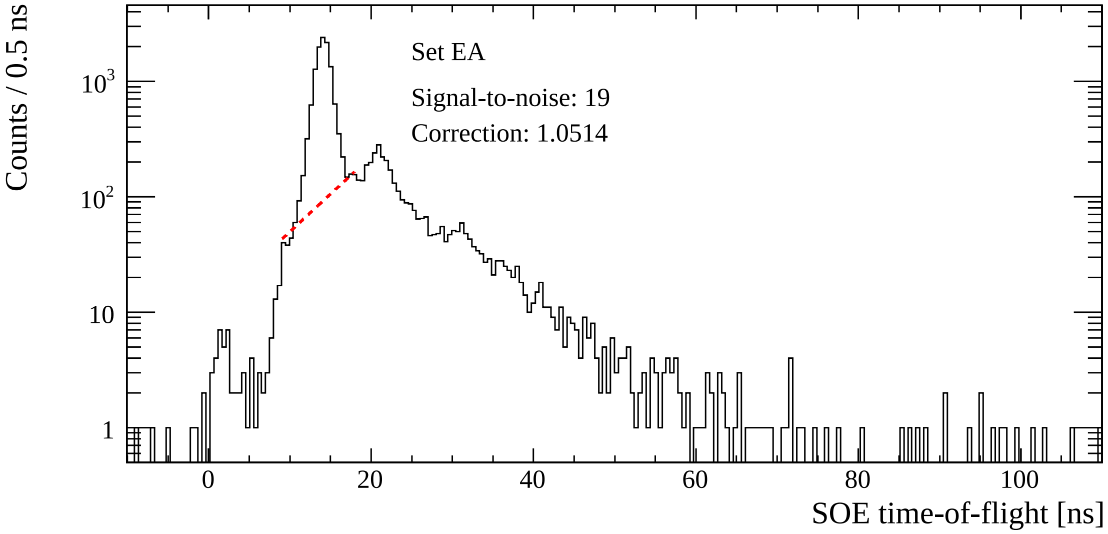

Figure 8.13: Shakeoff electron time-of-flight spectrum - EA. The signal-to-noise is much lower than in the rest of the data leading to a large 5.14 % background correction. Since the low statistics of the set will not influence the final result significantly, and to avoid making this large correction, set EA is not used in the final analysis. The equivalent spectrum for data taken with $E = 150\,\mathrm{V/cm}$ is given in Fig. 8.3.

position cut imposed. Although there are events throughout the MCP detector, the distribution is very strongly peaked and ideally this additional cut would not reject a significant number of good events. Unfortunately, the HEX75 detector had a very low efficiency to be above threshold and consequently many events that are likely good events are rejected by this selection cut[2]. The shakeoff electron time-of-flight spectrum with and without this position cut are shown in Fig. 8.14a. Two features are both notable. First, the amount of background is significantly reduced when applying the position cut. The signal-to-noise-ratio increases to 670 in this case. Second, the low efficiency has reduced the number of good events in the main peak by ≈ 50 %.

The higher-signal-to-noise in the position-cut analysis makes the background correction significantly smaller: 1.0007 ± 0.0007. However, this comes at the cost of reducing the statistical sensitivity of the measurement. Considering both of these effects, the final uncertainty including the systematic uncertainties of the next section

---

[2] Note that this is the efficiency of the delay-line anode with respect to events already triggering the MCP detector.

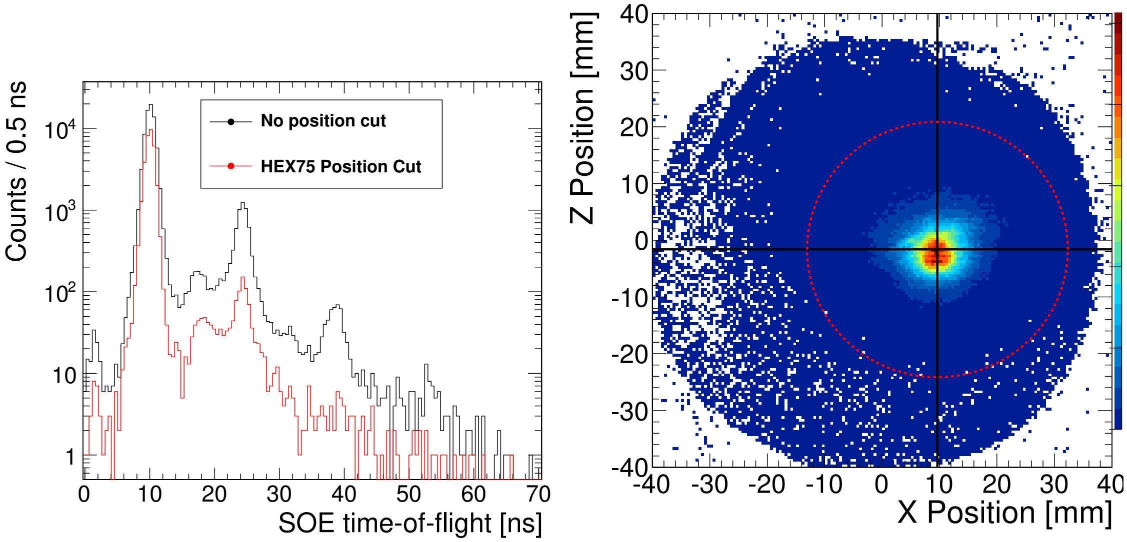

(a) Time-of-flight spectra

(b) Shakeoff e^- position spectra

Figure 8.14: Comparison of background correction with HEX75 position cut. Requiring the position cut shown on the right reduces the background correction but also reduces the statistics. This is due to a low efficiency observed in the HEX75 detector. The final result with this selection cut had a larger total uncertainty and was therefore was not used.

is *larger* in the analysis with the position cut applied. The two results *are* consistent with $A_\beta^{\text{pos. cut}} - A_\beta^{\text{no pos. cut}} = -0.0020 \pm 0.0024$. The uncertainty shown is the uncertainty on the position-cut analysis result alone in order to account for the fact that there is significant overlap between the two data sets. Since the analysis *without* a position cut has an overall smaller uncertainty, no position cut is used in the final result.

8.4 Systematic uncertainties

The first set of systematic uncertainties I will describe changes various analysis choices and measures their effect on A_β. The analysis described above measures the asymmetry using the Si-strip detectors only to discriminate against γs. Alternatively, the energy deposited in the Si-strip detector can be added to the energy observed in the scintillator, and this spectrum compared to the simulation. In this case, the same time-of-flight cuts are applied, with the energy of each region shifted up by 100 keV to account for the mean energy deposited in the Si-strip detector. The comparison of simulation and experiment is performed in the exact same was as the analysis with the scintillator energy only, with a typical comparison using this summed energy shown in Fig. 8.15a. The two analyses produced results that differed by 2×10^{-4}. Since there is no reason to prefer one analysis over the other, the final result is taken as the average of the two and half the difference is assigned as a systematic uncertainty.

The correction described in the last section significantly reduces the spread in results depending on the shakeoff electron time-of-flight. However, considering all the cuts pictured in Figs. 8.3 (except for the narrowest two horizontal lines, which clearly do not account for the walk) and 8.12, the maximum difference from the central value is 3×10^{-4} and we take this as a systematic uncertainty.

Other parameters that can be changed are the scintillator threshold, the Si-strip detector threshold, the Si-strip detector energy agreement threshold, and the maximum Si-strip detector radius. The 400 keV scintillator threshold used for the main analysis is just above the Compton edge from annihilation radiation. Raising this threshold to 1000 keV produces a 0.3×10^{-4} uncertainty. A 1×10^{-4} uncertainty was found when lowering the Si-strip detector threshold to 40 keV. Adjusting the energy agreement threshold from 3 to 5 times the average resolution produces a

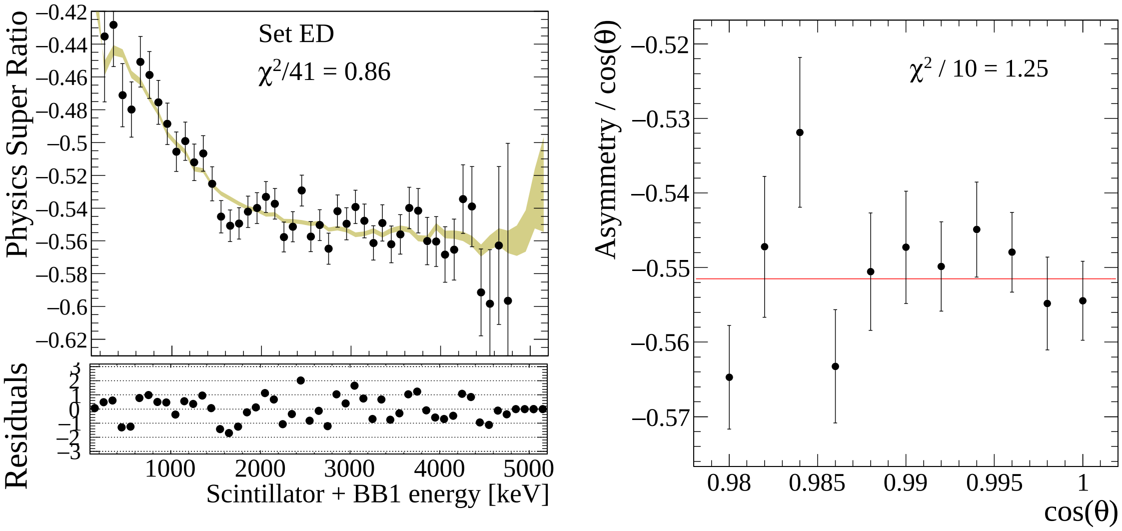

(a) Asymmetry including BB1 energy

(b) $\cos(\theta)$ dependence

Figure 8.15: Summed energy asymmetry, angle dependence. Left: Comparison of asymmetry with Si-strip energy added to scintillator energy. Right: The asymmetry agrees with the expected $\cos(\theta)$ dependence. Note that the pictured values are not compared to any GEANT4 simulation but are “raw” and “uncorrected.”

2×10^{-4} uncertainty. The maximum Si strip-detector radius of 15.5 mm is chosen to match the dimension of a stainless steel collimator. Alternative choices of 10 or 19 mm introduce an uncertainty of 3×10^{-4}. All of these systematic uncertainties are small compared to the statistical uncertainty. Furthermore, there was no difference seen when changing the scintillator calibrations by their uncertainties given in Ch. 7. Fig. 8.15b displays the observed asymmetry as a function of $\cos(\theta)$ where θ is the positron momentum's polar angle with respect to the polarization axis. The calculated angle accounts for the true position of the trapped atoms and measures the position of the β on the Si-strip detector. We observe no deviation compared to the expected $\cos(\theta)$ dependence. Note that this position-dependence is accounted for in the BB1 radius uncertainty and Fig. 8.15b is simply meant as illustration.

Tables 5.2, 5.3, and 5.4 give the trap position and its uncertainty throughout the experimental run. The super ratio significantly reduces the effects of a detector asymmetry produced by the trap being off center as long as the trap is located at the same position in the two polarization states. Although there were some significant differences between the data sets, within each set, the $\sigma^{\pm}$ polarization states consistently had the same trap parameters within uncertainties. To propagate these uncertainties to the final result, I first consider the possibility of the $\sigma^{\pm}$ polarization states having parameters adjusted from the nominal value by $\pm 1\sigma$ where σ is the stated statistical uncertainty for the parameter being studied. Second, I allow for the possibility that the two polarization states have the same value for each parameter, but shift the value by the variance between the data sets. All told there are eight parameters that are all studied independently: the trap's initial position as it is released from the MOT along all three axes (3), the sail velocity's speed and direction (3), the trap's initial width (1), and the trap's temperature (1).

The uncertainties as a result of the trap position and sail velocity were 4 and 5×10^{-4} respectively with the uncertainty from the trap size and temperature at 1×10^{-4}. The largest individual contribution comes from the large spread in possible trap positions along the $\hat{y}$-axis: 4.1×10^{-4}. The large spread in values for this parameter is perhaps conservative as it is calculated from the observed photoion time-of-flight and is correlated with small changes in the magnitude of the electric field as well as non-uniformities in the field. However, given the current data set, there is no *a priori* reason to reduce this uncertainty. Creating an uncertainty of similar magnitude is the uncertainty of the sail velocity when changing its speed in opposite directions for the two polarization states. This effectively changes the trap position for σ^+ compared to σ^- and produces an uncertainty of 3.8×10^{-4}. Note that the equivalent asymmetry produced by changing the trap's initial position is smaller. This is consistent with the observations from Tabs. 5.2, 5.3, and 5.4 that sail velocity uncertainties, when converted to an uncertainty in position, are larger than the uncertainties on the position alone.

The analysis of backscattered events presented in Ch. 6 provides a stringent test of the GEANT4 model used and constrains the possible parameter choices. The cut-for-secondaries (CFS) parameter, which has the most impact on the backscattered fraction was not found to influence the resulting asymmetry. The physics list `emlivermore` produces a result differing by 4×10^{-4} compared to the central result with the `emstandard_opt3` package and I take this as a systematic uncertainty. The `empenelope` package produces a result significantly different from the other two and, as it is an outlier, is excluded from the final analysis on this basis. Finally, increasing the range factor, which increases the minimum step size in the simulation was also found to impact the observed asymmetry. However, increasing this parameter also produces less backscattering and the large step sizes can only make the simulation less accurate. Therefore, we fix the value of $f_R = 0.002$ in the final analysis.

Finally, we can study how much of an effect the precision to which the geometry is defined can influence the result. For example, the two SiC mirrors along the $\pm\hat{z}$ direction are significant sources of β^+ scattering, and their thicknesses are defined only within $\pm 6\,\mu\text{m}$. If one of the mirrors is this much thicker than the nominal value while the opposite is this much thinner, the resulting bias in the asymmetry is 1×10^{-4}. The procedure was repeated for the Be vacuum window ($\pm 23\,\mu\text{m}$) and the Si-strip detectors ($\pm 5\,\mu\text{m}$).

The final table of systematics is shown in Tab. 8.1. Accounting for all systematic effects and corrections, the final result is:

$$A_\beta\left(0\right) = -0.5707 \pm 0.0018 \tag{8.10}$$

The uncertainty is broken down into three sources: 0.0009 ($\Delta P/P = 0.09\,\%$) from the polarization measurement, 0.0013 ($\Delta A_{\text{stat}}/A = 0.23\,\%$) from statistics on the positron asymmetry, and 0.0012 ($\Delta A_{\text{syst}}/A = 0.21\,\%$) from the systematics described here and dominated by the uncertainty on the background correction. This 0.33 % measurement of A_β is the most precise measurement of the positron asymmetry in any nuclear system to-date and is in agreement with the SM and previous measurements of the $\mathscr{F}t$ value. The value above is given at zero β kinetic energy. The mean energy lost in the mirror, Be window, and silicon-strip detector for events in the analysis window is 323 keV making the effective energy threshold 723 keV and the average kinematic factor for these events $\langle m/E_\beta \rangle = 0.16$.

As has already been noted, the polarization uncertainty is not the dominant uncertainty. The most significant systematic uncertainty arises from the uncertainty on the background correction. Discussed above, this is a result of taking a conservative approach when handling the asymmetry of the background events. If, for example, future work would show that atoms escaping the trapping region *do not* retain 100 % polarization, this uncertainty would be reduced significantly. The effects of β-scattering on the final result are propagated to the final uncertainty through the GEANT4 physics list entry of Tab. 8.1, although this is not a dominant source of uncertainty. Note that other entries in this table, labelled by a †, also change the β-scattering: changing the BB1 radius affects the degree to which βs that scatter off of the stainless steel collimator are included in the analysis, the geometry

Table 8.1: Uncertainty budget for the β-asymmetry measurement. Each entry is discussed in the text and given as the absolute uncertainty on A_β. The statistical uncertainty comes directly from a fit to Monte Carlo spectra with errors propagated to A_β. The total polarization uncertainty is listed as a single uncertainty with details given in Tab. 5.7. Entries labelled with a † indicate that the item relates to β^+-scattering and entries colored in red are greater than 0.1 %.

Source	Correction	ΔA_β [$\times 10^{-4}$]
Systematics		
Background	1.0013	7
Trap parameters		
Position		4
Sail velocity		5
Temperatue & width		1
Thresholds		
BB1 Radius†		4
BB1 Energy agreement		2
BB1 threshold		1
Scintillator threshold		0.3
GEANT4 physics list†		4
Shakeoff electon t.o.f. region		3
Geometry definition		
SiC mirror thickness†		1
Be window thickness†		0.9
BB1 thickness†		0.1
Scintillator or summed†		1
Scintillator calibration		0.1
Total systematics		12
Statistics		13
Polarization		5
Total uncertainty		18

definition has an obvious impact on scattering, and comparing the total deposited energy or scintillator energy to the simulation will account for scattering in different ways. Adding these contributions in quadrature can be used as a *de facto* measurement of the uncertainty that results from how the β scattering is modeled: 6×10^{-4} ($dA_{\text{scattering}}/A = 0.11\,\%$). All told, the final results are limited by the uncertainty in the background correction with other systematic uncertainties contributing significantly less. The final chapter of this thesis will describe possible improvements in future work that would reduce this uncertainty as well as apply this result to constraining models of BSM physics.

9. CONCLUSIONS AND FUTURE WORK

Given that the result for A_β described in the previous chapter is in agreement with the standard model and the measured $\mathscr{F}t$ value, the results are used to constrain physics beyond the standard model. The theoretical framework for this discussion was presented in Ch. 2.

9.1 Right-handed currents

The standard model $V - A$ coupling can be modified in BSM physics to include a $V + A$ component. A simple model within which to interpret results introduces only two new parameters: the mass of a new W_R boson coupling to right-handed neutrinos and the mixing angle (ζ) of W_R and the SM W_L into mass eigenstates (m_1 and m_2). All other parameters are identical to the standard model $V - A$ component including the CKM matrix elements and the overall coupling strength. A more detailed description of this model as well as a survey of constraints on this model are presented in Sec. 2.3. The result for A_β places the following limit on m_2 assuming $\zeta = 0.0$:

$$m_2 > 300\,\mathrm{GeV/c^2} \qquad 90\,\%\ \text{C.L.} \tag{9.1}$$

This limit is similar to that obtained from measurements of β particle longitudinal polarization in ^{12}N and ^{107}In, which together place the limit $m_2 > 320\,\mathrm{GeV/c^2}$ (90 % C.L.) [50]. These and other constraints are summarized in Fig. 9.1, which essentially updates Fig. 2.3 to include the results of this measurement. Figure 9.1 also includes projected limits from ^{37}K with both A_β and B_ν measured to 0.1 % of their values. As described later in this chapter, this level of precision should be attainable. Once successful, these combined measurements would be the most sensitive probe of the mass of a hypothetical W_R among all nuclear experiments. Of course, increasing precision in other experimental programs will continue to raise the bar, but ^{37}K will continue to be a useful laboratory to test the SM[1]. Furthermore, recall from Sec. 2.3.4 that muon-decay and high-energy limits on these parameters

---

[1] At this level of precision, the uncertainty in the $\mathscr{F}t$ value becomes significant and would need to be reduced. Currently, the leading source of uncertainty in this value is the branching ratio.

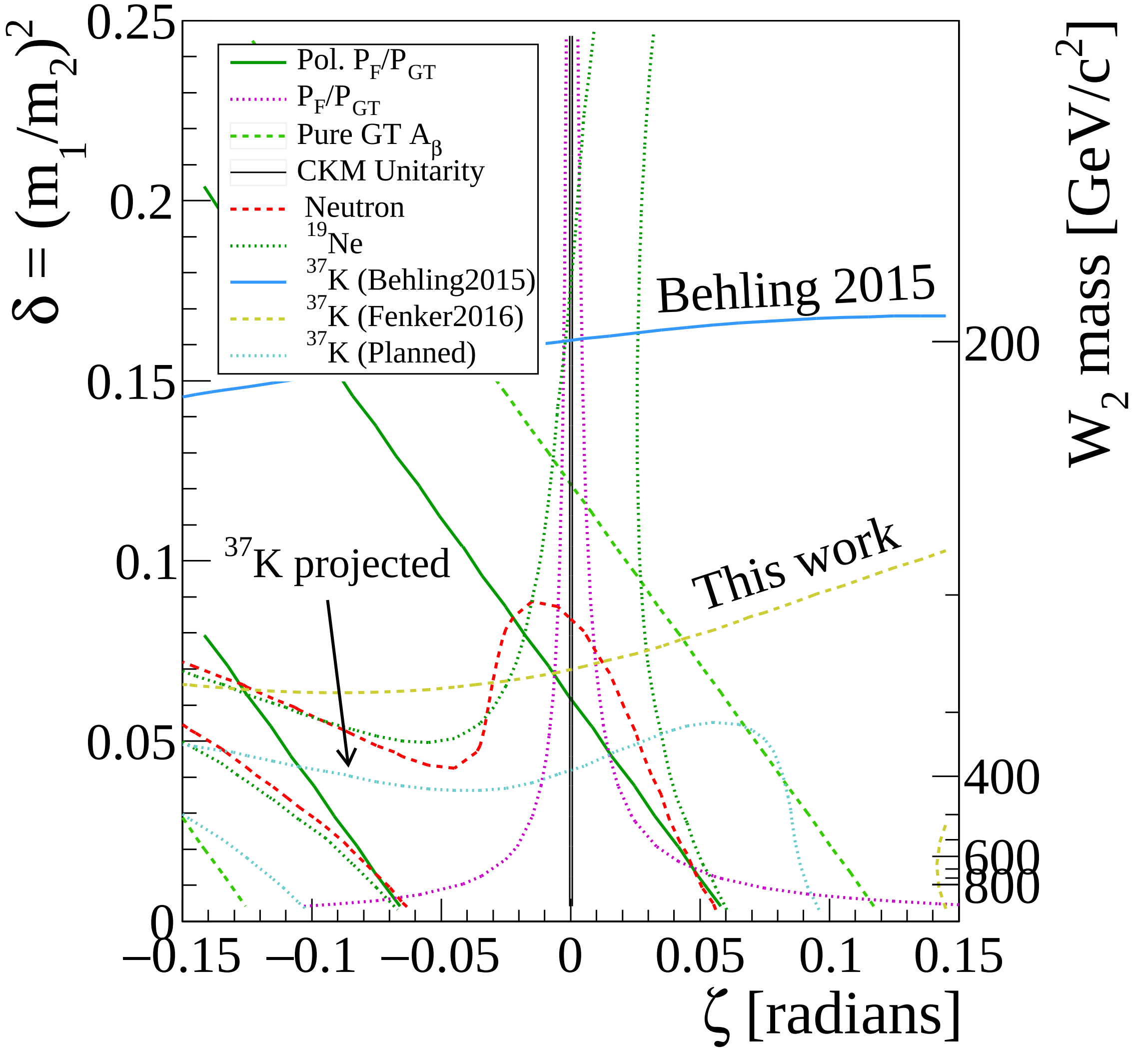

Figure 9.1: Updated exclusion plot for the minimally $L-R$ symmetric model. Results of the current work provide limits on the mass of a hypothetical W_R which are comparable to the best limits from other nuclear and neutron decays. Not shown are μ-decay and collider experiments. See Sec. 2.3.4. The projected limits from ^{37}K show the results if both A_β and B_ν are measured to 0.1 % relative uncertainty and are in agreement with the standard model and measured $\mathscr{F}t$ value. All limits shown are 90 % confidence level.

are significantly stronger than limits from β-decay and are not pictured in Fig. 9.1.

9.2 V_{ud} element of the CKM matrix

Since the fitting procedure described in Sec. 8.2 directly fit g_A, the axial-vector coupling strength, it is straightforward to extract ρ (defined in Eq. 2.4) with the recoil-order corrections of Ref. [39] included. After accounting for the background correction and systematic uncertainties, the result from from this measurement is $\rho = -0.577 \pm 0.005$. Previous measurements of correlation parameters in ^{37}K have also determined values for ρ, and taking the weighted average of all existing measurements of ρ gives [20, 25, 37]:

$$\rho = -0.575 \pm 0.005 \tag{9.2}$$

where the current measurement of A_β dominates the average. The three measurements are in agreement with one another with $\chi^2/2 = 0.93$. Using this value for ρ, the $\mathscr{F}t_0$ value defined in Eq. 2.25 is

$$\mathscr{F}t_0 = (6137 \pm 28)\,\mathrm{s}. \tag{9.3}$$

Note that the uncertainty in this quantity is still dominated by the uncertainty in ρ, meaning that increasing the precision of correlation coefficient measurements will decrease the uncertainty on $\mathscr{F}t_0$. Figure 9.2 shows the updated status of the CVC test in mirror nuclei. Currently, $\mathscr{F}t_0$ is measured more precisely in ^{37}K than in any other mirror nuclei, being slightly more precise than the value from ^{19}Ne, which has an uncertainty of 30 s [60].

With the $\mathscr{F}t_0$ value calculated, V_{ud} can be extracted from Eq. 2.26: $V_{ud}^{\mathrm{K}} = 0.9748 \pm 0.0022$. Combining this measurement with the other mirror transitions in Fig. 9.2 gives

$$V_{ud}^{\mathrm{mirror}} = 0.9730 \pm 0.0014. \tag{9.4}$$

It is remarkable that this value is only 7 times less precise than the most precise determination from pure-Fermi decays, which do not require a correlation coefficient to be measured [31]. Adopting average values for the β-asymmetry parameter and lifetime from [5], V_{ud} is extracted from neutron decay with the value $V_{ud}^{\mathrm{neutron}} =$

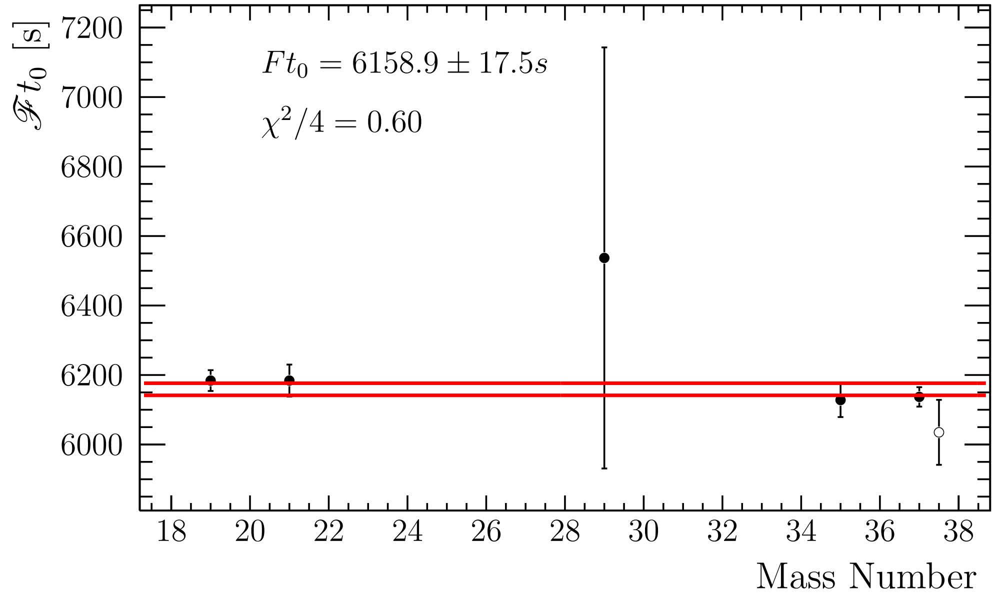

Figure 9.2: Updated status of CVC test in mirror nuclei. Includes result of present work. Open circle gives the previously measured value in ^{37}K [25].

0.9757 ± 0.0016. Although mirror nuclei and neutron results differ by 1.2 combined standard deviations, it is interesting to note that mirror nuclear decays have reached a greater precision than neutron decay in extracting a value of V_{ud}.

9.3 Future work

The present result represents a 5× improvement over the result of less than two years ago [25] and is the most precise measurement of the β-asymmetry in any nuclear system to date. However, significant progress is still possible leading to even higher precision. Improvements to the experimental system are discussed below. In addition to the physical improvements, the data set from which the results are derived contains enough data to extract additional information beyond the scope of this thesis. First, the time-of-flight of recoiling Ar^{n+} ions is sensitive to a combination of correlation coefficients and is currently under analysis. Furthermore, the Fierz interference term (b in Eq. 2.10) can be studied by further examining the asymmetry spectrum as a function of β energy. This result can be used to constrain scalar and tensor currents, neither of which is present in the standard model.

In order to be competitive in searches for new physics with experiments at the Large Hadron Collider, correlation coefficient measurements in nuclear β-decay should aim for a precision of 0.1 % or better [123]. In order to guide the discussion below, I consider the scenario where this uncertainty is made up equally of the total polarization uncertainty, the statistical uncertainty on the β-asymmetry, and the systematic uncertainty on the β-asymmetry. Although entirely arbitrary, this equal division is plausible given the results of Tab. 8.1. In any case, this scenario is simply a test case, but under its assumptions, to reach a relative uncertainty of 1×10^{-3} would require each individual source of uncertainty to reach an uncertainty relative to the central value of $\frac{\Delta X}{X} \approx 6 \times 10^{-4}$ where X is any observable. The following two subsections describe how this increase in precision could be achieved.

9.3.1 Polarization improvements

The current polarization measurement has a total uncertainty of 9×10^{-4} with a systematic uncertainty of only 5×10^{-4}. It is worth emphasizing that the measurement of the nuclear polarization described here is sensitive to $1 - P$ whereas the only the quantity P appears in the nuclear decay rate. In this light, the very precise polarization measurement is actually only a 10 % measurement of $1 - P$ due to the high polarization achieved. Based on this effect, improving the nuclear polarization will simultaneously improve the precision to which it can be measured. Improving the polarization is equivalent to reducing the two depolarizing mechanisms: incoming light polarization and a transverse magnetic field. The light polarization achieved is already quite high: $|s_3| > 0.995$ except for one branch of the beam in the σ^+ state (see Tab. 5.5), which is only slightly worse. Further optimizations of the optics setup are ongoing, but some optical elements, particularly the liquid crystal variable retarder, preserve the polarization better in one state than the other, making it difficult to optimize both polarization states simultaneously [99]. Therefore, it seems more likely that significant improvements to the polarization are more likely to come from minimizing the transverse magnetic field.

During the present experiment, magnetic fields transverse to the optical pumping axis (B_x) were minimized by a pair of Helmholtz-like coils exterior to the vacuum chamber. The DC current through these coils was optimized offline by minimizing the residual fluorescence of ^{41}K, which can be trapped in large numbers, following optical pumping. Minimizing the residual fluorescence is equivalent to minimizing the residual photoionization rate. Although the location of the trap and the magnetic field response of the surrounding materials does not depend on the species of K used[2], the distribution of trapped atoms occupies a finite volume (here $2.3\,\mathrm{mm}^3$ as the atoms are released) and moves through the vacuum chamber (here $0.4\,\mathrm{mm}$) while being optically pumped. Neither the size of the trap nor its sail velocity is expected to be identical when changing K isotope. Therefore, while being optically pumped, the two species of K probe different magnetic field regions. Since the exterior trim coils only exactly cancel stray transverse magnetic fields at one point in space, the differences between ^{41}K and ^{37}K imply that the trim coil optimization for ^{41}K is not completely optimal for ^{37}K.

This limitation can be overcome by independently controlling the DC current through each half of the trim coils. This would allow the optimization on ^{41}K to not only cancel stray magnetic fields at one point in space, but also to minimize the *gradient* of these stray fields near the center of the chamber. Therefore, the offline optimization with ^{41}K will translate better to ^{37}K. If the total transverse magnetic field can be reduced to 1/2 of its value from this experiment to $\approx 60\,\mathrm{mG}$, without any other improvements, the polarization would increase to 0.9947. If, as in this work, $1 - P$ is measured to $10\,\%$, this would correspond to a measurement of the polarization at the 5×10^{-4} level. Using independent control of the trim coils and careful offline optimizations, this reduction in the transverse magnetic field and the accompanying increase in precision should be achievable.

9.3.2 Beta-asymmetry improvements

Improving the β-asymmetry measurement to the requisite values will require improvements on a few fronts. The statistical uncertainty is limited by available beam time at TRIUMF, the production of ^{37}K from the proton beam, the collection efficiency of the first MOT, the transfer efficiency from the first MOT to the measurement chamber, and the experimental duty cycle. The available beam time and ^{37}K production are beyond the scope of this thesis while the initial collection of the atoms and transfer of the atoms have been previously optimized in Refs. [14, 15]. However, in the first MOT, there is a quartz cube coated to resist K undergoing

---

[2] In principle, the trap must be centered around the point in space where the magnetic field is $\vec{0}$.

physisorption onto the surface. This coating was done $\approx 10\,\mathrm{yr}$ ago and re-coating it may increase the collection efficiency of the first MOT by allowing the K atoms more opportunities to be trapped by the MOT before “sticking” to a surface.

In the current experimental duty cycle, the atoms are polarized only 24 % of the time. The rest of the time is divided roughly equally between collecting atoms in a DC-MOT and re-trapping the atoms in an AC-MOT. Further optimization of the *temperature* of the atom cloud would allow the MOT to stay off longer before retrapping, meaning more time is available to study polarized decays. However, the relatively narrow hyperfine splitting of ^{37}K makes many sub-Doppler cooling schemes less efficient than in other atoms. Furthermore, because of the different isotope shifts of ^{37}K compared to ^{41}K, these optimizations are best performed on accelerator-produced ^{37}K, sapping valuable beam time from the β-asymmetry measurement. In future runs, it may be worthwhile to carefully find the balance between trap-optimization and asymmetry measurement. Many systematic uncertainties, including detector thresholds and uncertainties related to the trap parameters are statistics-limited. Therefore, they too would be reduced by simply increasing the number of events observed.

To reach a greater precision, the background correction and its associated 100 % uncertainty need to be reduced. As was described earlier, using the position information from the HEX75 detector did successfully reduce the size of this correction, but had a low efficiency leading to an overall less-precise measurement. Therefore, increasing the efficiency with which the position information is gathered would significantly increase the precision achieved. The location of shakeoff e^- events was strongly peaked, suggesting that a microchannel plate with smaller diameter is likely to be sufficient in future runs. However, the location of the events was offset by 10 mm along one axis as a result of deflections from the magnetic field. With future runs expected to have an electric field of 1000 V/cm, the amount of this shift should be reduced to 4 mm, meaning that the distribution of shakeoff e^- events would be almost entirely contained within a detector with radius 20 mm. The higher electric field is not directly relevant to the β-asymmetry measurement, but is critical for a planned beta-neutrino correlation measurement. Installing a previously-used 20 mm detector would be simpler to mount and possibly prevent the large cross-talk noise between it and the recoil MCP that was observed in this experiment. Furthermore, an existing wedge-and-strip detector can be installed to provide reliable position information with good efficiency.

Although the multiple scattering of positrons is not listed directly as a systematic uncertainty, it is the underlying cause of many of the line items in Tab. 8.1. While TRINAT's unique ability to measure the backscattering fraction at low β-energy is useful, further reducing the backscattering will still be important. The most significant source of scattering in the present experiment comes from the SiC mirrors placed along the polarization axis. Since the conclusion of this run, members of the TRINAT collaboration have begun tests with thinner, pellicle mirrors. The membrane portion of these mirrors is only 25 µm thick and made of Mylar ($\rho = 1.38\,\mathrm{g/cm^3}$). This mirror is 10× thinner, has a lower density, and a lower average atomic number than the current SiC mirrors. Therefore the scattering and energy loss of βs from these mirrors is considerably less. Their extreme thinness and delicate mounting will likely necessitate changes to the AC-MOT cycle to prevent inductive heating, and this is currently being investigated. Furthermore, their optical properties must also be verified. If the mirrors can be incorporated successfully, we can expect the scattering of positrons to be less in future iterations leading to less uncertainty about how this is modelled. Another significant source of backscattering is the Si-strip detectors, however, there are currently no plans to replace these detectors in future runs.

Although not directly contributing to the uncertainty of this run, it is worth noting that the VF48 waveform digitizers used to record the strip-detector information could possibly be replaced by simpler peak-sensing ADCs. Currently, the VF48 modules increase the complexity of data acquisition, but in the end are simply used as peak-sensing ADCs. As a separate matter, including the silicon-strip detectors as an event trigger would allow future experiments to reach an even lower energy threshold by triggering off of events with so little energy ($\lesssim 500\,\mathrm{keV}$) that they are fully stopped by this detector. This would allow greater sensitivity to the energy dependence of the asymmetry and requires data acquisition development to incorporate a global `OR` between strip-detector signals as an event trigger.

Although the challenges of reaching part-per-thousand uncertainty on the β-asymmetry are large, they are not insurmountable. Modest improvements to the magnetic field setup will improve the polarization sufficiently. Combined with a new, more efficient, position-sensitive e^- detector and thinner in-vacuum mirrors, a precision of 0.1 % is attainable with sufficient beam time.

This thesis has described the most precise determination of A_β, relative to its value, in any nuclear system: $A_\beta\,(0) = -0.5507 \pm 0.0018$. The result constrains the mass of a new W boson coupling only to right-handed neutrinos to be $> 300\,\mathrm{GeV/c^2}$, comparable to the best limits from nuclear decays, but not competitive with limits from muon and high-energy collider experiments. It is also the most precise determination of the corrected partial half-life ($\mathscr{F}t_0$) in any mirror nucleus to-date and reduces the uncertainty on the value of V_{ud}^{mirror} to only $7\times$ the uncertainty of the most precise determination of V_{ud} using pure-Fermi decays. Future prospects for experiments of this kind are promising with only moderate improvements to the experiment necessary to reach an even higher precision.

REFERENCES

[1] Fermi, E. *Z. Phys.*, 88(3):161–177.

[2] Reines, F. and Cowan, C.L. *Nature*, 178(4531), 1956:446–449.

[3] Cleveland, B.T., *et al. The Astrophys. J.*, 496(1), 1998:505.

[4] Aseev, V.N., *et al. Phys. Rev. D*, 84, 2011:112003.

[5] Olive, K.A. *et al. Chin. Phys.*, C38, 2014:090001.

[6] Lee, T.D. and Yang, C.N. *Phys. Rev.*, 104, 1956:254–258.

[7] Wu, C.S., *et al. Phys. Rev.*, 105, 1957:1413–1415.

[8] Rustad, B.M. and Ruby, S.L. *Phys. Rev.*, 97, 1955:991–1002.

[9] Burgy, M.T., *et al. Phys. Rev.*, 107, 1957:1731–1733.

[10] Feynman, R.P. and Gell-Mann, M. *Phys. Rev.*, 109, 1958:193–198.

[11] Sudarshan, E.C.G. and Marshak, R.E. *Phys. Rev.*, 109, 1958:1860–1862.

[12] Garwin, R.L., Lederman, L.M., and Weinrich, M. *Phys. Rev.*, 105, 1957:1415–1417.

[13] Friedman, J.I. and Telegdi, V.L. *Phys. Rev.*, 106, 1957:1290–1293.

[14] Behr, J.A. *et al. Phys. Rev. Lett.*, 79, 1997:375–378.

[15] Swanson, T.B., *et al. J. Opt. Soc. Am. B*, 15(11), 1998:2641–2645.

[16] Trinczek, M. *et al. Phys. Rev. Lett.*, 90, 2003:012501.

[17] Gorelov, A. *et al. Phys. Rev. Lett.*, 94, 2005:142501.

[18] Melconian, D., *et al. Nucl. Instrum. Methods Phys. Res. Section A*, 538(13), 2005:93 – 99.

[19] Melconian, D.G. *Measurement of the neutrino asymmetry in the beta decay of laser-cooled, polarized 37K.* Ph. D. Thesis, Simon Fraser University, 2005.

[20] Melconian, D., *et al. Phys. Lett. B*, 649(56), 2007:370 – 375.

[21] Gorelov, A.I. *Positron-Neutrino Correlation Measurements in the Beta Decay of Magneto-Optically Trapped* ^{38m}K *Atoms.* Ph.D. Thesis, Simon Fraser University, 2008.

[22] Behr, J.A. and Gwinner, G. *J. Phys. G: Nucl. Part. Phys.*, 36(3), 2009:033101.

[23] Pitcairn, J.R.A. *et al.* *Phys. Rev. C*, 79, 2009:015501.

[24] Behr, J.A. and Gorelov, A. *J. Phys. G: Nucl. Part. Phys.*, 41(11), 2014:114005.

[25] Behling, R.S. *Measurement of the Standard Model Beta Asymmetry Parameter,* A_β *in* ^{37}K. Ph.D. Thesis, Texas A & M University, 2015.

[26] Harvey, M. and Murray, A.J. *Phys. Rev. Lett.*, 101, 2008:173201.

[27] Jackson, J.D., Treiman, S.B., and Wyld, H.W. *Phys. Rev.*, 106, 1957:517–521.

[28] Wu, C.S. and Moszkowski, S.A. *Beta Decay.* Wiley-Interscience, New York, NY, 1966.

[29] Burkhardt, H. *et al.* *Phys. Lett. B*, 206(1), 1988:169 – 176.

[30] Herczeg, P. and Khriplovich, I.B. *Phys. Rev. D*, 56, 1997:80–89.

[31] Hardy, J.C. and Towner, I.S. *Phys. Rev. C*, 91, 2015:025501.

[32] Nambu, Y. *Phys. Rev. Lett.*, 4, 1960:380–382.

[33] Severijns, N., Tandecki, M., Phalet, T., and Towner, I.S. *Phys. Rev. C*, 78, 2008:055501.

[34] Marciano, W.J. and Sirlin, A. *Phys. Rev. Lett.*, 56, 1986:22–25.

[35] Cabibbo, N. *Phys. Rev. Lett.*, 10, 1963:531–533.

[36] Kobayashi, M. and Maskawa, T. *Prog. Theor. Phys.*, 49(2), 1973:652–657.

[37] Shidling, P.D., *et al.* *Phys. Rev. C*, 90, 2014:032501.

[38] Hagberg, E., *et al.* *Phys. Rev. C*, 56, 1997:135–141.

[39] Holstein, B.R. *Rev. Mod. Phys.*, 46, 1974:789–814.

[40] Towner, I. personal communication.

[41] Platen, C., *et al.* *Z. Phys.*, 244(1):44–69.

[42] Pitt, M.L., *et al.* *Bull. Am. Phys. Soc.*, 33, 1988:1564.

[43] Minamisono, K., *et al.* *Phys. Lett. B*, 662(5), 2008:389 – 395.

[44] Klein, A., *et al.* *Nucl. Phys. A*, 607(1), 1996:1 – 22.

[45] Herczeg, P. *Phys. Rev. D*, 34, 1986:3449–3456.

[46] Herczeg, P. *Prog. Part. Nucl. Phys.*, 46(2), 2001:413 – 457.

[47] Severijns, N., Beck, M., and Naviliat-Cuncic, O. *Rev. Mod. Phys.*, 78, 2006:991–1040.

[48] Wichers, V.A., *et al. Phys. Rev. Lett.*, 58, 1987:1821–1824.

[49] Carnoy, A.S., Deutsch, J., Girard, T.A., and Prieels, R. *Phys. Rev. Lett.*, 65, 1990:3249–3252.

[50] Severijns, N. *Hyperfine Interact.*, 201(1), 2011:47–55.

[51] Severijns, N. *et al. Phys. Rev. Lett.*, 70, 1993:4047–4050.

[52] Severijns, N. *et al. Phys. Rev. Lett.*, 73, 1994:611–611.

[53] Thomas, E., *et al. Nucl. Phys. A*, 694(34), 2001:559 – 589.

[54] Severijns, N. *J. Phys. G: Nucl. Part. Phys.*, 41(11), 2014:114006.

[55] Wauters, F. *et al. Phys. Rev. C*, 82, 2010:055502.

[56] Wauters, F., *et al. Phys. Rev. C*, 80, 2009:062501.

[57] Soti, G., *et al. Phys. Rev. C*, 90, 2014:035502.

[58] Naviliat-Cuncic, O., Girard, T.A., Deutsch, J., and Severijns, N. *J. Phys. G: Nucl. Part. Phys.*, 17(6), 1991:919.

[59] Calaprice, F.P., Freedman, S.J., Mead, W.C., and Vantine, H.C. *Phys. Rev. Lett.*, 35, 1975:1566–1570.

[60] Naviliat-Cuncic, O. and Severijns, N. *Phys. Rev. Lett.*, 102, 2009:142302.

[61] Nico, J.S., *et al. Phys. Rev. C*, 71, 2005:055502.

[62] Yue, A.T., *et al. Phys. Rev. Lett.*, 111, 2013:222501.

[63] Arzumanov, S.S., *et al. JETP Lett.*, 95(5), 2012:224–228.

[64] Young, A.R., *et al. J. Phys. G: Nucl. Part. Phys.*, 41(11), 2014:114007.

[65] Vos, K.K., Wilschut, H.W., and Timmermans, R.G.E. *Rev. Mod. Phys.*, 87, 2015:1483–1516.

[66] Wauters, F., García, A., and Hong, R. *Phys. Rev. C*, 89, 2014:025501.

[67] Schumann, M., *et al. Phys. Rev. Lett.*, 100, 2008:151801.

[68] Musser, J.R. *et al. Phys. Rev. Lett.*, 94, 2005:101805.

[69] Gaponenko, A. *et al. Phys. Rev. D*, 71, 2005:071101.

[70] Bueno, J.F. *et al.* *Phys. Rev. D*, 84, 2011:032005.

[71] Khachatryan, V. *et al.* *Eur. Phys. J. C*, 74(11), 2014:1–23.

[72] Deppisch, F.F., *et al.* *Phys. Rev. D*, 90, 2014:053014.

[73] Heikinheimo, M., Raidal, M., and Spethmann, C. *Eur. Phys. J. C*, 74(10), 2014:1–5.

[74] Grinyer, J., *et al.* *Phys. Rev. C*, 91, 2015:032501.

[75] Williamson, R.S. *Magneto-optical trapping of Potassium Isotopes.* Ph.D. Thesis, University of Wisconsin Madison, 1997.

[76] *GNU Scientific Library.* `http://www.gnu.org/software/gsl/`. Accessed: 2016-11-2.

[77] Yang, F. and Hamilton, J.H. *Modern Atomic and Nuclear Physics.* World Scientific, Hackensack, NJ, revised edition, 2010.

[78] Renzoni, F., Cartaleva, S., Alzetta, G., and Arimondo, E. *Phys. Rev. A*, 63, 2001:065401.

[79] *Press Release: The 1997 Nobel Prize in Physics.* `http://www.nobelprize.org/nobel_prizes/physics/laureates/1997/press.html`. Accessed: 2015-07-15.

[80] Metcalf, H.J. and van der Straten, P. *Laser Cooling and Trapping.* Springer-Verlag, New York, NY, 1999.

[81] Williamson, R.S. and Walker, T. *J. Opt. Soc. Am. B*, 12(8), 1995:1393–1397.

[82] Anholm, M. *Characterizing the AC-MOT.* M. Sc., The University of British Columbia, 2011.

[83] Wang, B., *et al.* *Phys. Rev. A*, 75, 2007:051801.

[84] Smith, G.A., Silberfarb, A., Deutsch, I.H., and Jessen, P.S. *Phys. Rev. Lett.*, 97, 2006:180403.

[85] Julsgaard, B., Sherson, J., Srensen, J.L., and Polzik, E.S. *J. Opt. B: Quantum Semiclassical Opt.*, 6(1), 2004:5.

[86] de Clercq, E., *et al.* *J. Phys. France*, 45(2), 1984:239–247.

[87] Edmonds, A.R. *Angular Momentum in Quantum Mechanics.* Princeton University Press, Princeton, NJ, 4th edition.

[88] Nafcha, Y., Rosenbluh, M., Tremblay, P., and Jacques, C. *Phys. Rev. A*, 52, 1995:3216–3227.

[89] Jackson, J.D. *Classical Electrodynamics*. John Wiley & Sons, Inc., Hoboken, NJ, 3rd edition, 1999.

[90] Pathria, R.K. and Beale, P.D. *Statistical Mechanics*. Elsevier, San Diego, CA, 3rd edition, 2011.

[91] Tremblay, P. and Jacques, C. *Phys. Rev. A*, 41, 1990:4989–4999.

[92] Gu, S., Behr, J., Groves, M., and Dhat, D. *Opt. Commun.*, 220(46), 2003:365 – 370.

[93] Arimondo, E. volume 35 of *Progress in Optics*. Elsevier, 1996, pages 257 – 354.

[94] Jagutzki, O., *et al.* *Nucl. Instrum. Methods Phys. Res., Sect. A*, 477(13), 2002:244 – 249. 5th Int. Conf. on Position-Sensitive Detectors.

[95] Jagutzki, O., *et al.* *IEEE T. Nucl. Sci.*, 49(5), 2002:2477–2483.

[96] Landini, M., *et al.* *Phys. Rev. A*, 84, 2011:043432.

[97] *Midas documentatio.* `https://midas.triumf.ca/MidasWiki/index.php/Midas_documentation`. Accessed: 2015-05-15.

[98] *VF48 Manual.* `http://www.triumf.info/wiki/DAQwiki/index.php/VF48`. Accessed: 2015-11-11.

[99] Fenker, B. *et al.* *New J. Phys.*, 18(7), 2016:073028.

[100] Kobayashi, S., Yamamoto, Y., Ito, M., and Kimura, T. *IEEE J. Quantum Elec.*, 18(4), 1982:582–595.

[101] Tanaka, U. and Yabuzaki, T. In *Frequency-Stabilized Lasers and Their Applications*, volume 1837. SPIE, 1992, page 70.

[102] Warner, C.L., Behr, J.A., and Gorelov, A. *Rev. Sci. Instrum.*, 85(11), 2014:113106.

[103] Aymar, M., Luc-Koenig, E., and Farnoux, F.C. *J. Phys. B: At. Mol. Phys.*, 9(8), 1976:1279.

[104] Rossi, D.M. *et al.* *Phys. Rev. C*, 92, 2015:014305.

[105] Agostinelli, S. *et al.* *Nucl. Instrum. Methods Phys. Res., Sect. A*, 506(3), 2003:250 – 303.

[106] Bevington, P.R. and Robinson, D.K. *Data Reduction and Error Analysis for the Physical Sciences*. McGraw-Hill, New York, NY, 2003.

[107] Wilkinson, D. *Nucl. Phys. A*, 143(2), 1970:365 – 372.

[108] Ivanchenko, V.N., Kadri, O., Maire, M., and Urban, L. *J. Phys. Conf. Ser.*, 219(3), 2010:032045.

[109] Soti, G., *et al.* *Nucl. Instrum. Methods Phys. Res., Sect. A*, 728, 2013:11 – 22.

[110] Apostolakis, J., *et al.* In *Computing in High Energy and Nuclear Physics*. 2007.

[111] Chauvie, S., *et al.* In *Nuclear Science Symposium Conference Record, 2004 IEEE*, volume 3. 2004, pages 1881–1885 Vol. 3.

[112] Bar, J., Sempau, J., Fernndez-Varea, J., and Salvat, F. *Nucl. Instrum. Methods Phys. Res., Sect. B*, 100(1), 1995:31 – 46.

[113] Lewis, H.W. *Phys. Rev.*, 78, 1950:526–529.

[114] Goudsmit, S. and Saunderson, J.L. *Phys. Rev.*, 57, 1940:24–29.

[115] Tabata, T., Ito, R., and Okabe, S. *Nucl. Instrum. Methods*, 94(3), 1971:509 – 513.

[116] Gay, T.J. and Dunning, F.B. *Rev. Sci. Instrum.*, 63(2), 1992:1635–1651.

[117] Plaster, B. *et al.* *Phys. Rev. C*, 86, 2012:055501.

[118] Aad, G. *et al.* *Phys. Lett. B*, 716(1), 2012:1 – 29.

[119] Mendenhall, M.P. *et al.* *Phys. Rev. C*, 87, 2013:032501.

[120] Behr, J. personal communication.

[121] Ben-Itzhak, I., Heber, O., Gertner, I., and Rosner, B. *Phys. Rev. A*, 38, 1988:4870–4871.

[122] Levinger, J.S. *Phys. Rev.*, 90, 1953:11–25.

[123] Cirigliano, V., González-Alonso, M., and Graesser, M.L. *J. High Energy Phys.*, 2013(2), 2013:1–18.